Investigation of banglenes as neurotrophic agents and development of a new fluorescent protein-based FRET pair

by

Khyati Gohil

A thesis submitted in partial fulfillment of the requirements for the degree of

Doctor of Philosophy

Department of Chemistry
University of Alberta

Abstract

This thesis describes efforts towards understanding the neurotrophic activity of banglenes and the development of a new fluorescent protein-based FRET pair.

Neurotrophic small molecule natural products are functional analogs of signaling proteins called neurotrophins, which cause a pro-growth, pro-survival, or pro-differentiation responses in neuronal cells. While these phenotypic responses are desirable to combat neurodegenerative disease progression, neurotrophin proteins possess pharmacokinetic properties that present challenges to their administration in whole organisms, whether in biomedical studies or as therapeutics. Therefore, neurotrophic small molecules such as the *cis*- and *trans*-banglenes offer attractive alternatives.

The first part of this thesis describes the synthesis and testing of banglene derivatives to establish a structure-activity response for the banglene family. Further, it describes studies to provide insights into the mechanism of action of banglenes.

Notably, *trans*-banglene demonstrates neuritogenic effect alone and substantially potentiates nerve growth factor (NGF) induced neuritogenesis. The neuritogenic studies demonstrate that (–) *trans*-banglene is primarily the active enantiomer, while its (+) enantiomer is minimally effective. Further, the structure-activity relationship studies show that select modifications on the cyclohexene ring of *trans*-banglene do not impair its neuritogenic activity.

The combination of (–) *trans*-banglene and NGF induces NGF secretion in PC-12 cells which might be in part responsible for its neuritogenic effect. However, (–) *trans*-banglene's

potentiation of NGF-induced neuritogenesis was unaffected by the presence of kinase inhibitors designed to inhibit NGF-induced neurotrophic signaling. Collectively, these results suggest a dual-mode of action for (–) *trans*-banglene (neurotrophic alone and strong potentiating of NGF activity), and that its potentiating action is unaffected by the presence of inhibitors of specific kinases involved in canonical NGF signal transduction pathways.

The second part of this thesis describes the development of new green-red fluorescent protein-based Förster resonance energy transfer (FRET) pair as an alternative to the classically employed cyan fluorescent protein-yellow fluorescent protein pair. This FRET pair constitutes of mScarlet-I and its blue shifted version gScarlet. Indicators to detect protease activity, Ca^{2+} and K^{+} were developed using the gScarlet–mScarlet-I pair.

An attempt was made to increase the FRET efficiency of these indicators by increasing the intramolecular association between gScarlet and mScarlet-I. This strategy proved useful in improving the response of the protease indicator, but it did not improve the response of the Ca^{2+} and K^{+} indicators.

Finally, the comparison of gScarlet–mScarlet-I indicators to the best existing FRET pairs-mClover3-mRuby3 and cpVenus-mScarlet-I demonstrates comparable responses, establishing gScarlet–mScarlet-I as a reliable FRET pair which can be utilised to create FRET-based indicators for various cellular applications.

Preface

Chapter 2 and chapter 3 (except section 3.5.2 and 3.6) of this thesis were published as - Gohil, K.; Kazmi, M.Z.H.; Williams, F. J. "Structure-Activity Relationship and Bioactivity Studies of Neurotrophic Trans-Banglene." *Org. Biomol. Chem.* **2022**, *20* (11), 2187–2193. I performed the synthesis of most banglene derivatives, except 2-34 to 2-37 which were synthesized by Zain Kazmi. Lotus Separations separated the enantiomers of *t*-BG and the PhenoLogix applications team at Phenomenex developed the chiral HPLC method for separating enantiomers of banglene derivatives. Dr. Florence Williams directed the research and co-wrote the manuscript.

Chapter 4 is a collaborative effort with Dr. Yi Shen and Dr. Sheng-Yi Wu. Dr. Sheng-Yi Wu guided me in designing the constructs and assisted me in the experimental research described in section 4.4.2 and 4.6. Dr. Yi Shen initiated the project and engineered green scarlet as described in section 4.2.2. Dr. Robert Campbell supervised the research.

Acknowledgements

First, I would like to express my greatest gratitude to my supervisors, Dr. Florence Williams, and Dr. Robert Campbell for providing me with this opportunity to accomplish one of my biggest professional goals. Their advice on both research and life has been priceless. Without their guidance, time, patience, and continued encouragement, I would not be able to accomplish this research.

I would like to express my gratitude and appreciation to the thesis examining committee members: Dr. Christopher Cairo, Dr. Matthew Macauley, Dr. Julianne Gibbs and Dr. Tim Storr for their valuable time and feedback.

I would like to thank the excellent research service staff at the University of Alberta. I am grateful for the help of all the people in the University of Alberta molecular biology services unit, NMR, mass spectrometry, analytical labs, chemistry shipping/receiving and the storeroom for their continued assistance. I am extremely grateful to Gareth Lambkin for his advice, encouragement and for always helping me troubleshoot issues.

I would like to thank all members of the Williams and Campbell lab for their scientific, technical, and emotional support in making my time in the lab a wonderful experience. A very special thank you to Andreas Dorian and Zain Kazmi- I am grateful to have met you both, thanks for keeping me sane, grounded, and happy. I am also grateful to Dr. Yi Shen, Dr. Sheng-Yi Wu, Dr. Kei Takashahi-Yamashiro, Dr. Safeenaz Alladin-Mustan and Dr. Rochelin Dalangin for helping me transition labs and always reminding me that life is more than experimental results.

I am forever in debt of my parents, especially my mother for all her sacrifices to give me the best in life. Without her, I would never have achieved anything in life. I am also indebted to the rest of my family, especially my brother and to the one we lost too soon. Their encouragement and faith in many ways has helped me through my graduate journey.

I am especially grateful to the set of friends, or perhaps more aptly put, the family that I am privileged to have built here. Lastly, I would like to thank Dr. Boo, you have been a constant supportive presence since we met; you are instrumental in making me feel at home away from home.

Table of Contents

List of tables

List of figures

List of schemes

List of abbreviations

AChE	Acetylcholinesterase
AD	Alzheimer's disease
Akt	Protein kinase B
ATP	Adenosine triphosphate
BBB	Blood brain barrier
BDNF	Brain derived neurotrophic factor
BFP	Blue fluorescent protein
CaM	Calmodulin
CaMK	Calmodulin-dependent protein kinase
CFP	Cyan fluorescent protein
cis-Banglene	*c*-BG
cpFP	Circularly permuted fluorescent protein
CREB	cAMP response element-binding protein
DAG	Diacylglycerol
DMEM	Dulbecco's modified Eagle's medium
dNTP	Deoxyribonucleic acid triphosphate
EC	Extinction coefficient
ee	Enantiomeric excess
EGTA	Ethylene glycol tetraacetic acid
ELISA	Enzyme-linked immunosorbent assay
Erk	Extracellular signal-regulated kinase
FBS	Fetal bovine serum
FLIM	Fluorescence-lifetime imaging microscopy
FP	Fluorescent protein
FRET	Förster resonance energy transfer
Frs2	Fibroblast growth factor receptor substrate 2
GAP43	Growth-associated protein 43
GFP	Green fluorescent protein
Grb	growth factor receptor bound protein

HDAC	Histone deacetylase
HS	Horse serum
HWE	Horner-Wadsworth-Emmons
iAkt	Triciribine
iErk	SCH772984
IP3	Inositol triphosphate
iPKC	Gö 6983
JNK	c-Jun N-terminal kinase
Kbp	K^+ binding protein
Klc-1	Kinesin-light chain 1
MAP2	Microtubule associated protein-2
MAPK	Mitogen activated protein kinase
MEF2	Myocyte enhancer factor-2
Mek	Mitogen activated Erk kinase
MMP-7	Matrix metalloproteinase-7
NeUN	Neuronal nuclear protein
NFκB	nuclear factor kappa B
NGF	Nerve growth factor
NT	Neurotrophin
NT-3	Neurotrophin 3
NT-4/5	Neurotrophin 4/5
OBX	Olfactory bulbectomy
OFP	Orange fluorescent protein
p75 NTR	p75 neurotrophin receptor
Pgp	P-glycoprotein
PI3K	Phosphoinositide-3-kinase
PKC	Protein kinase C
PLCγ	Phosphoinositide phospholipase Cγ
QY	Quantum yield
Raf	Rapidly accelerated fibrosarcoma protein
Ras	Rat sarcoma protein

RFP	Red fluorescent protein
RP-HPLC	Reverse-phase high performance liquid chromatography
SAR	Structure-activity relationship
SDS-PAGE	Sodium dodecyl sulphate polyacrylamide gel electrophoresis
Shc	Src homolgy
SNT	Single neurite tracer
TBS	Tris buffered saline
TMD	Transmembrane domain
trans-Banglene	*t*-BG
Trk	Tropomyosin/ tyrosine receptor kinase
YFP	Yellow fluorescent protein

Chapter 1: Neurotrophins and neurotrophic molecules

1.1 Neurotrophins

Neurotrophins (NTs) are soluble growth factors which act as paracrine or autocrine factors for cells expressing NT binding receptors. NTs are secreted both by neuronal and non-neuronal cells such as glial, cardiovascular, endocrine, immune, and many neoplastic cells. NTs were first identified as survival factors for neurons and since then have been most widely investigated for their effects on the central and peripheral nervous systems, where they are responsible for regulation of neuronal differentiation, proliferation, migration, and synaptic plasticity.[1]

Four mammalian NTs have been identified till date - the nerve growth factor (NGF), brain-derived neurotrophic factor (BDNF), neurotrophin 3 (NT-3), and neurotrophin 4/5 (NT-4/5). NTs are synthesized as pre-pro-peptides, the N-terminal (pre) signal sequence mediates translocation into the endoplasmic reticulum where the pro-peptides are subsequently processed and secreted as mature NTs. All mature NTs are structurally and functionally very similar. They are all non-covalently associated dimeric proteins with a characteristic cysteine knot. The dimeric interface consists of highly conserved hydrophobic residues and the cysteine knot is a tertiary structure that is formed by three disulfide bonds (**figure 1-1**).[1,2]

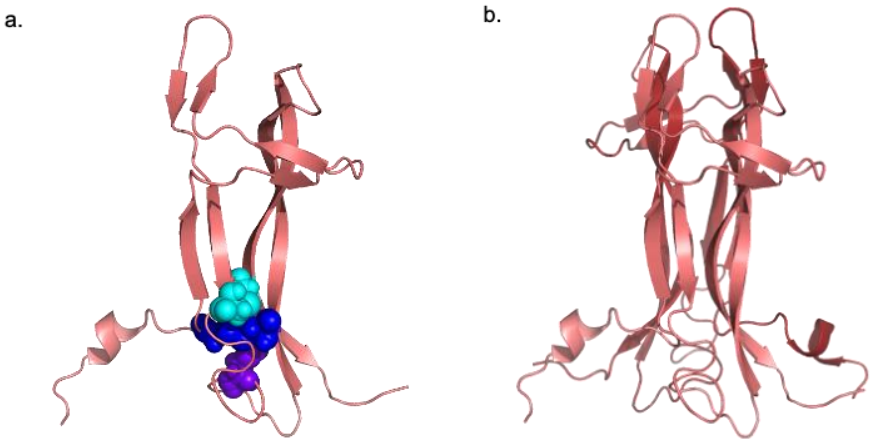

Figure 1-1. Structure of a representative NT- nerve growth factor (NGF). (a) Monomer of NGF showing the three cysteine pairs that form the knot. (b) Homodimer of NGF. PDB id. 5lsd.[3]

NTs mediate their effects through two classes of cell surface receptors- a cognate member of the tropomyosin-related kinase (Trk) family of receptor tyrosine kinases and the p75 neurotrophin receptor (p75 NTR), which belongs to the tumor necrosis superfamily.[1]

NTs are secreted by post-synaptic target tissues and neurons; a retrograde transport is established transporting NTs from the nerve terminal to the axon and the cell body. During development, neurons that establish this retrograde transport survive and the others degenerate.[4,5]

1.2 Nerve growth factor

Nerve growth factor (NGF) was the first NT to be discovered and was characterized in the 1940s by Rita Levi-Montalcini, Viktor Hamburger and Stanley Cohen.[6] It is highly expressed in target tissues that express its cognate receptor, with the highest level of NGF mRNA detected in hippocampal and cortical cholinergic neurons.[6]

Like all other NTs it is expressed as pre-pro-NGF, and the pro-domain is essential to ensure correct folding of the mature NGF. Pro-NGF can be proteolytically cleaved by furin and pro-protein convertases in the endoplasmic reticulum and Golgi apparatus. Any un-processed pro-NGF can be cleaved extracellularly by plasmin and matrix metalloproteases.[7]

Pro-NGF levels are very low in young uninjured organs, but an upregulation is seen with age. Following an injury to the central nervous system, pro-NGF is detected for several days, suggesting an impairment to the proteolysis of pro-NGF.[6] In a study using a seizure model of CNS injury, it was found that matrix metalloproteinase-7 (MMP-7) was downregulated, and the cellular inhibitor of MMP-7 was upregulated, leading to stabilization of pro-NGF.[8]

Mature NGF and pro-NGF bind differently to NT receptors. Mature NGF binds with a high affinity to its cognate receptor TrkA as well as to p75 NTR whereas pro-NGF binds with high affinity to the p75 receptor.[6]

1.3 Trk receptors

The Trk receptor family are transmembrane receptors consisting of TrkA, TrkB and TrkC. Each Trk receptor selectively binds to a NT with binding affinities of 10^{-9}-10^{-10} M. NGF

binds preferentially to TrkA, BDNF and NT-4/5 bind to TrkB and NT-3 binds to TrkC and also with lesser affinity to TrkA and TrkB. [1]

The structural arrangement of TrkA, B and C receptors is highly conserved and consists of a N-terminal ligand binding extracellular region, a hydrophobic trans-membrane domain and a C-terminal cytoplasmic region that has a highly conserved catalytic kinase domain. There are five domains in the extracellular region of Trk- a cysteine-rich domain followed by a domain that has three leucine-rich repeats, another cysteine-rich cluster, and two Ig-like domains (Ig C1 and Ig C2 domains). Trks bind to mature NTs through the Ig-C2 domain (**figure 1-2**). Most studies on NT-Trk binding have been carried out with NGF and TrkA and have been extrapolated to other NTs and Trks.

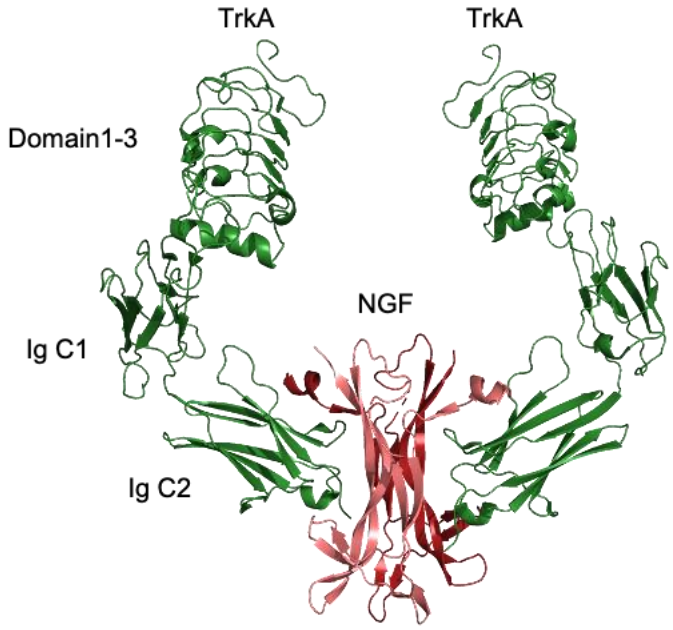

Figure 1-2. Structure of extracellular segment of TrkA receptor bound to NGF. TrkA shown in green and NGF structure represented in red. PDB id. 2ifg [3]

Binding of NGF to TrkA leads to receptor dimerization, followed by a conformational change in the intracellular kinase domain.[9] The dimerization-activation of TrkA has been an area of interest and there are no conclusions yet on whether this process is dependent on the presence of ligand binding.[10]

Two models exist to explain TrkA homodimerization and subsequent activation, the first model is based on the crystal structure of NGF bound to TrkA, which suggests that induction of dimerization and activation is ligand mediated.[10] This model assumes that the receptor-receptor interactions are absent without a ligand. The second model postulates that TrkA exists as preformed inactive dimer in the absence of NGF.[11]

The current model put forth by Franco and co-workers suggests that NGF binding induces dimerization of Trk monomers or preformed Trk dimers followed by a conformational change leading to kinase activation. They proposed this model based on structural studies validated by monitoring TrkA phosphorylation and cell differentiation following site-directed mutagenesis on the TrkA transmembrane domain (TMD).

First, they solved the structure of human TrkA–TMD dimers in detergent micelles using NMR and identified the dimerization interface. Then they strategically mutated TMD residues and found that there are two interfaces of TrkA dimers an active and an inactive interface. In the inactive interface, even though TrkA dimers are present no downstream signalling leading to cell differentiation is seen. The active interface is the dimer interface which causes downstream signalling leading to cell differentiation. The inactive interface pivots to an active interface upon NGF binding (**figure 1-3**). Alanine 428 was identified as the residue that plays a critical role in the transition of inactive to active interface upon NGF binding. In their experiments, they did not detect TrkA dimers in the absence of NGF even when TrkA receptors were overexpressed, thereby suggesting that NGF binding promoted dimerization of TrkA receptors. Finally, they observed that TrkA dimerization was not enough to activate TrkA signalling and that the conformational change is essential for TrkA autophosphorylation.[12]

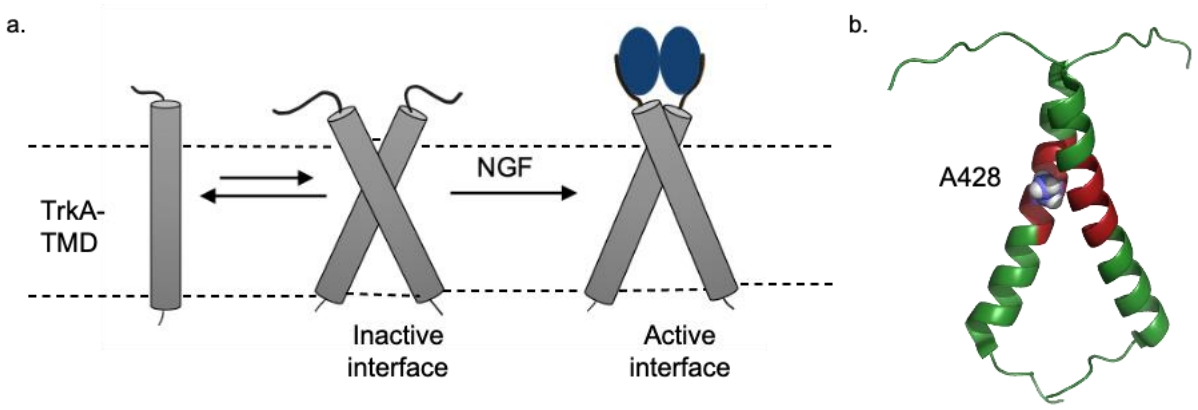

Figure 1-3. TrkA dimerization (a) Schematic representation of TrkA activation showing the inactive and active dimer interface. (b) Structure of TrkA-TMD domain. The dimerization motif is shown in red and residue A428 is highlighted. PDB id. 2n90.[12]

There are several tyrosine residues in the kinase domain that serve as phosphorylation-dependent docking sites for cytoplasmic adaptors and enzymes that propagate neurotrophic signalling.[9]

1.4 NGF-TrkA signalling pathways

NT signalling regulates several processes during development, adulthood, and upon injury to nervous system. These processes include neuronal differentiation, neurite outgrowth, axon pruning, cell survival and apoptosis.[13]

The binding of a NT and homodimerization of Trk brings the cytoplasmic tails of each monomer in close proximity favouring autophosphorylation. Different downstream signalling cascades get activated following autophosphorylation with the phosphorylated residues providing docking sites for adaptor proteins. NGF binding and activation of TrkA initiates three main pathways - the MAPK/Erk (mitogen-activated protein kinase/extracellular signal-regulated kinase), PI3K (phosphoinositide 3-kinase)/Akt (protein kinase B), and PLCγ (phosphoinositide phospholipase Cγ) pathways (**figure 1-4**).[13]

Phosphorylation of tyrosines on TrkA creates binding sites for proteins containing the Src-homology-2 domain (Shc). Phosphorylation of the tyrosine Y490 activates binding of an

adaptor called proteins of the Src homology (Shc) or Fibroblast growth factor receptor substrate 2 (Frs2). The Shc domain recruits adapter protein growth factor receptor bound protein (Grb2) which leads to activation of the rat sarcoma protein (Ras). Ras activates downstream signalling of the Raf (rapidly accelerated fibrosarcoma protein)-Erk-MAPK and PI3K signalling. [13]

For MAPK activation, Ras activates the serine/threonine protein kinase Raf which phosphorylates mitogen activated Erk kinase (Mek 1/2) which in turn phosphorylates and activate Erk 1/2 transcription factor and MAP kinase isoforms. Activated MAPKs and Erk1/2 are able to signal through cAMP response element-binding protein (CREB), ETS like protein 1 (Elk1) and myocyte enhancer factor-2 (MEF2) to regulate target gene expression influencing neuronal differentiation and survival.[13]

Grb2 recruitment of PI3K regulates cell survival by signal transduction through the serine/threonine protein kinase Akt which in turn regulates phosphorylation of several proteins and transcription factors important for cell survival like the BCL2 associated agonist of cell death (Bad) and the glycogen synthase kinase.[13]

Phosphorylation of Y785 in human Trk activates the PLCγ pathway, which leads to the production of inositol triphosphate (IP3) and diacylglycerol (DAG). DAG stimulates protein kinase C (PKC) isoforms and IP3 promotes the release of Ca^{2+} from internal stores and subsequent activation of Ca^{2+}/calmodulin (Ca^{2+}/CaM)-dependent protein kinases (CaMKII, CaMKK and CaMKIV).[14]

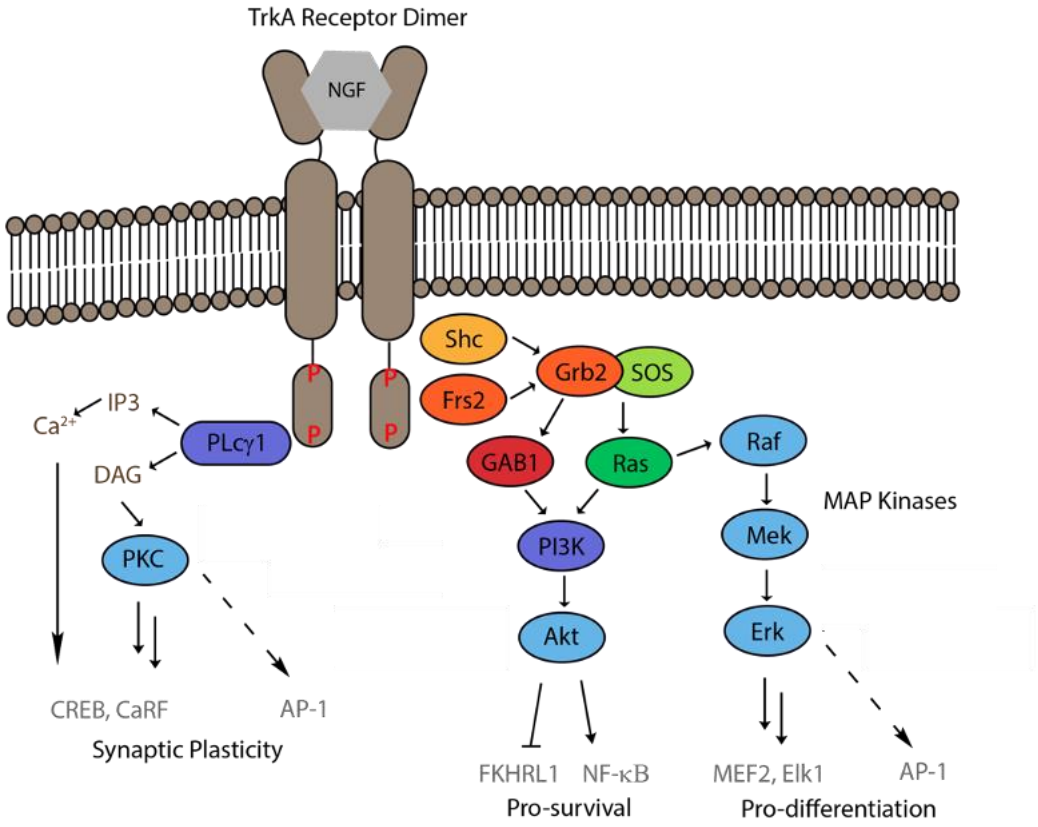

Figure 1-4. Simplified schematic showing NGF induced TrkA signalling. Blue/Purple: kinases. Green: GTPases. Tan letters: second messenger small molecules. Grey letters: transcription factors. SOS: Son of sevenless homolog 1. CaRF: Calcium responsive factor. AP-1: Activator protein 1. FKHRL: Forkhead family transcription factor. NFκB- Nuclear factor kappa-light-chain-enhancer of activated B cells. MEF2: Myocyte enhancer factor 2. Elk1: ETS domain-containing protein 1. [13]

1.5 p75 neurotrophin receptor

p75 neurotrophin receptor (p75 NTR) is a ~75 kDa protein and is a member of the tumor necrosis factor receptor superfamily. It consists of four cysteine rich domains in its extracellular region through which it binds to both pro-NTs and mature NTs, a transmembrane domain and a cytoplasmic death domain. p75 NTR is best known as a critical regulator of developmental apoptosis in a variety of neuronal and non-neuronal cells.[7]

p75 receptor can bind to both pro-NTs and mature NTs and initiate pathways associated with cell death. A high concentration of mature NTs is required to trigger cell death through

the p75 NTR, but pro-NTs act as potent activators of p75 NTR at sub nanomolar concentrations.[7]

Pro-NTs induce programmed cell death by binding to a high affinity protein complex containing p75 NTR and its co-receptor Sortilin. Sortilin is a Vps10p domain trafficking protein which functions as a non-G protein coupled receptor. Pro-NTs bind to Sortilin via their pro-domain and to p75 NTR by their mature domain, thus facilitating the association of these two receptors to initiate programmed cell death.[6] Sortilin is known to increase the affinity of p75 NTR to bind to pro-NTs by about 100-fold.[15]

Although p75 NTR does not have a catalytic domain, it can trigger apoptotic pathways by a regulated two-step intramembrane proteolysis similar to β-amyloid precursor protein (APP) and Notch facilitated by metalloproteinases and γ-secretase. It is unclear whether the proteolysis is ligand dependent or independent. The soluble intra-cellular domain of the p75 NTR is believed to facilitate the nuclear localization of transcription factors that can trigger apoptosis pathways. One major pathway associated with p75 NTR is the JNK (c-Jun N-terminal kinase)-p53 pathway which causes a transcriptional upregulation of pro-apoptotic genes leading to the release of cytochrome-c from the mitochondria and caspase-dependent apoptosis.[13]

Apart from its regulation of cell death, p75 NTR regulates different signalling pathways depending on the presence of different ligands and co-receptors. For example, in the presence of pro-NGF and sortilin it triggers cell death pathways whereas in the presence of TrkA and NGF it can lead to cell survival and differentiation. p75 NTR can also inhibit axonal regeneration by forming a ternary complex with Nogo receptor (Nogo-R) and Lingo-1 (LRR and Ig domain-containing, Nogo Receptor-interacting protein).[7,16]

p75 NTR can have a pro-survival effect in the presence of Trk. p75 NTR can form a heterodimer with Trk and potentiate Trk function by promoting ligand binding and increasing Trk signalling.[17] This interaction prolongs the cell surface expression of Trk and increases the affinity of NGF binding to Trk. This is advantageous as NTs are typically present in limiting amounts in target tissues.[18] The p75 NTR-TrkA complex formation and

activation of TrkA signalling pathway leads to cleavage of p75 NTR and the intracellular domain leads to the activation of the pro-survival Akt pathway.[17,19]

Independent of Trk interactions, the cleaved intracellular domain of p75 NTR can potentiate NT induced survival signalling by modulating nuclear factor kappa B (NFκB) which can lead to upregulation of cytokines and pro-survival genes. [7]

p75 NTR can be thought of as a neurotrophic/ apoptotic switch and its effect on cell survival is very variable and dependent on the absence or presence of Trk. It can be generalized that selective activation of p75 NTR in the absence of Trk receptor activation would promote cell death.

p75 NTR also plays an important role in regulating synaptic function (specifically weakening synaptic connections), synaptic plasticity and neurite outgrowth. The mechanism for its regulation of synaptic function is not fully known, but it seems to be associated with an alteration in glutamate receptors.[7] p75 NTR affects neurite outgrowth by modulating RhoA, unliganded p75 NTR promotes RhoA activation causing a decrease in neurite outgrowth and binding of NTs prevents this activation.[20]

1.6 Neurotrophic small molecules

Considering the importance of NTs in regulating neuronal development and maintenance, it is not surprising that NTs can influence the manifestation of neurodegenerative diseases. For many years it was believed that a decrease in NGF is correlated with the loss of cholinergic neurons in Alzheimer's disease (AD), although there have been conflicting reports on the associated changes in NGF and BDNF levels in AD affected tissue.[21] On the other hand, a downregulation of Trk receptors and p75 NTR is consistently observed with progression of AD.[22,23]

There have been attempts to use exogenous NTs as therapeutics for neurodegenerative diseases or to promote regeneration of axons from mechanical injuries. But they have not been successful in clinical trials due to poor pharmacokinetic properties such as short half-lives (BDNF serum half-life ~ 10 min), poor blood-brain barrier permeability, poor serum stability, poor receptor selectivity (binding to Trk or p75 NTR) and the resulting conflicting

pharmacology. [24,25] Some of these issues can be extended to other polypeptide factors that possess neurotrophic function such as the ciliary neurotrophic factor, glial cell line–derived neurotrophic factor, insulin-like growth factor, and basic fibroblast growth factor.[5]

These pharmacokinetic issues can be addressed by neurotrophic small molecules, which mimic the function or stimulate production of neurotrophin proteins. Many of these small molecules have the advantage of being more stable in blood and plasma, are amenable to synthetic modification to improve activity, and can be administered through different delivery routes. There are numerous, structurally diverse neurotrophic small molecules (>100 examples), and they constitute a unique opportunity to overcome the therapeutic limitations of NTs and can also be valuable as chemical tools to study NT signalling pathways.[26]

In this section, I have highlighted some examples which demonstrate the diversity in the structure and proposed mechanism of actions of neurotrophic small molecules.

1.6.1 Model systems to study neurotrophic activity

Most often, neurotrophic activity of small molecules is first assessed in a model cell line such as PC-12, Neuro2a, SH-SY5Y, P19 etc.[26,27] Neurotrophic activity can be described as the ability to promote neuronal growth, survival and differentiation. As a first step, a change in the phenotype of these cells caused by potential neurotrophic molecules is monitored.[26] Alongside, changes in certain neuronal growth associated marker proteins, perturbation of neurotrophic signalling pathways and ability to rescue cells from cell death can also be monitored.[26]

PC-12 is a cell line derived from a transplantable rat pheochromocytoma of the adrenal medulla. It differentiates easily into neuronal like cells upon induction by NGF. The differentiated PC-12 cells form elongated projections, which are commonly referred to as neurites. The process of formation of these neurites is called neuritogenesis. PC-12 cells express TrkA and p75 NTR and their associated signalling pathways, making them a widely used cell model to study the effects of molecules on these receptors and pathways.[28]

Neuro-2a cells are mouse neuroblasts cells derived from the neural crest. It is a widely used cell line to study neuronal differentiation, neurite growth, synaptogenesis and signaling pathways. Neuro-2a cells respond quickly to serum deprivation and other environmental stimuli and differentiate into cells with neurite outgrowth. They differentiate in the presence of NTs, forskolin (a natural inducer of cAMP), retinoic acid and 2,4-dinitrophenol.[29]

SH-SY5Y are a subclone of the SK-N-SH neuroblastoma cells which can be differentiated into neuron like phenotype. The most common differentiating agent used for SH-SY5Y cells is retinoic acid, other differentiating agents used include phorbol esters such as 12-O-tetradecanoyl-phorbol-13 acetate, staurosporine (a PKC inhibitor), NGF and BDNF. SH-SY5Y cells differentiate primarily to exhibit a cholinergic neuronal phenotype as an increase in the expression of choline acetyl transferase activity and vesicular monoamine transporters is observed. Since SH-SY5Y cells are human-derived, they express several human-specific proteins and protein isoforms that would not be inherently present in rodent cell lines or primary cultures. However, these cells lack functional NT receptors and require pre-treatment with retinoic acid to increase the expression of these receptors. These cells express a number of mature neuronal markers, including βIII-tubulin, microtubule-associated protein-2 (MAP2), synaptophysin and NeuN (neuronal nuclear protein).[30]

Apart from these cell lines, the activity of neurotrophic molecules can also be assessed in primary cultured neurons and in rat or mouse model systems. *In vivo*, these molecules are assessed for their ability to induce neurogenesis, which can be described as the formation of new axons and dendrites with functional synaptic connections.[26,31,32] There are very few neurotrophic molecules that have been used in clinical studies.[33,34]

1.6.2 Neurotrophic molecules affecting MAPK and PI3K signaling

Since MAPK and PI3K signaling pathways are activated by NTs, the perturbation of these pathways is generally assessed if a molecule presents neurotrophic activity in a phenotypic assay. This is achieved by monitoring the phosphorylation levels of key kinases involved and/or by inhibiting the activity of kinases involved in these pathways. Many neurotrophic molecules affect these pathways, for example Spicatoside A, Quercetin, Berberine, Honokiol

etc.[26] Two such neurotrophic molecules that affect these signalling pathways are discussed below.

1.6.2.1 Diarylheptanoids

A diarylheptanoid (**1-1**, **figure 1-5**) extracted from rhizomes of *Alpinia officinarum*, a genus of *Zingiberaceae*, is known to cause neuronal differentiation in Neuro-2a cells, rat hippocampal neurons and adult male mice. This molecule is structurally analogous to curcumin. In Neuro-2a cells, compound **1-1** at 4 μM caused a modest increase in length of neurites by ~ 15% over no treatment, and the increase was comparable to that caused by retinoic acid which served as the positive control. In hippocampal neurons compound **1-1** promoted axon and neurite growth. In adult mice, administration of compound **1-1** at 28 mg/kg for 14 days did not affect the proliferation of progenitor cells, but it promoted the differentiation of newborn progenitor cells by ~10% over control. Compound **1-1** promotes differentiation and neurite growth by activating MAPK/Erk and PI3K/Akt signaling pathways as observed by an increase in the phosphorylation levels of Erk 1/2, Mek1/2 and Akt. Compound **1-1** did not cause any change in the phosphorylation levels of JNK or PKC.[35]

1.6.2.2 Talaumidin

Talaumidin (**1-2**) is a 2,5-biaryl-3,4-dimethyltetrahydrofuran lignan isolated from *Aristolochia arcuate*. Talaumidin by itself does not have any neurotrophic activity but it promotes NGF mediated neurite outgrowth in PC-12 cells (1- 30 μM) and primary culture rat cortical neurons (10 μM), and it also protects rat neurons against cell death by serum deprivation.[36]

The tetrahydrofuran in talaumidin has four stereogenic centers. Harada and co-workers studied the structure activity relationship of talaumidin. First, they synthesized seven diastereomers of talaumidin along with an enantiomer (–) talaumidin. All stereoisomers resulted in a moderate increase in neuritogenesis when dosed along with NGF. Harada and co-workers observed that the isomer **1-3** with all *cis* configuration of substituents on the tetrahydrofuran ring demonstrated the highest neurotrophic activity. Upon exploring the neurotrophic effect of synthesized derivatives with and without benzene rings on the

terahydrofuran and different substitutions on the tetrahydrofuran, Harada and coworkers observed that the two benzene rings were essential for neurotrophic activity as removal of one (**1-5**) resulted in loss of neurotrophic activity.[36,37]

Koriyama and co-workers demonstrated that talaumidin could promote staurosporine mediated neurite outgrowth in the non-retinal cell line RGC-5 through the PI3K-Akt signalling pathway and that MAPK-Erk signalling is not involved.[38]

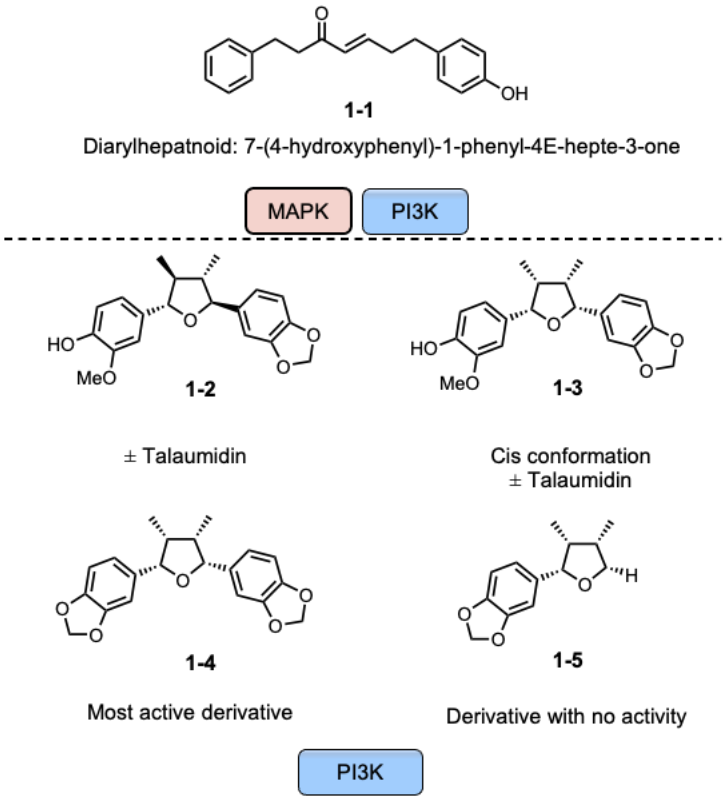

Figure 1-5. Structure of diarylheptanoid and talaumidin derivatives. The pathways that they perturb are mentioned in the coloured boxes.

1.6.3 Neurotrophic molecules interacting with TrkA receptors

Since NTs bind to Trk receptors and subsequently activate them, an agonist of Trk would cause a similar induction of neurotrophic signalling pathways downstream of Trk. Two such neurotrophic compounds that interact with Trk to cause its activation are gambogic amide and sarcodonin G.

1.6.3.1 Gambogic amide

Gambogic amide (**1-6**, **figure 1-6**) is derived from gambogic acid which is extracted as a resin from the *Garcinia hanburryi* tree. Gambogic amide demonstrated neurotrophic activity by selectively binding to TrkA, triggering its phosphorylation and activating the PI3K/Akt and MAPK pathways. It caused neurite outgrowth in PC-12 cells at a concentration of 0.5 μM and promoted neuronal survival of primary hippocampal neurons against glutamate toxicity and in an oxygen-glucose deprivation model.[39]

Jang and co-workers identified gambogic amide as a hit in a screen designed to identify compounds that mimic NGF and activate TrkA. The screening was done in two stages, in the first stage the protective activity of molecules against staurosporine-induced apoptosis was screened in two different cell lines, one that stably expressed TrkA and another that did not express TrkA. The candidates that selectively protected the TrkA expressing cell line were selected and then screened for their ability to induce neurite outgrowth.[39]

Further, through an in-vitro binding assay with numerous truncated TrkA tagged with GFP, Jang and co-workers demonstrated that the cytoplasmic juxtamembrane region and not the extracellular membrane of TrkA was critical for binding gambogic amide. The K_d for the binding of gambogic amide to TrkA is ≈ 75 nM and it specifically binds to TrkA and not TrkB, TrkC or p75 NTR. Pronounced phosphorylation of TrkA, Erk1/2 and Akt is observed following the TrkA dimerization caused by gambogic amide.[39]

Gao and co-workers could not demonstrate how gambogic amide causes TrkA dimerization, however, they suggested that it could cause a conformational change in TrkA reducing the autoinhibitory effect by the Ig C2 domain, which can block TrkA dimerization in the absence of NGF.[40] This mechanism was proposed based on the structural information available for Trk activation. Based on Franco and co-workers' structural studies, it is highly likely that gambogic amide binds to the extracellular juxtamembrane and enhances dimerization and more importantly causes the conformational change necessary for effective Trk activation.[12]

1.6.3.2 Sarcodonin G

The elucidation of the mechanism of action of sarcodonin G **(1-7)** is an interesting example of neurotrophic effect arising from molecular interactions with NGF and TrkA.

Sarcodonin G is a cyathane diterpenoid isolated from the mushroom *Sarcodon scabrosus* which possess neurotrophic activity in the presence of NGF. Its mechanism was elucidated through two of its derivatives (**figure 1-6**), both of which have opposing activities, derivative **1-8** has superior activity as compared to its parent (**1-7**), whereas derivative **1-9** acts as an inhibitor. At 10 μM in PC-12 cells and 20 μM in primary cultured rat cortical neurons derivative **1-8** promoted neurite outgrowth whereas derivative **1-9** suppressed neurite extension. Interestingly at lower concentrations (1-5 μM) derivative **1-9** promoted neurite outgrowth in PC-12 cells. The neuritogenic activity of derivative **1-8** was also confirmed by an observed upregulation in neuronal markers- growth-associated protein 43 (GAP43) and βIII-tubulin. Through molecular dynamic simulations, Cao and co-workers hypothesize that derivatives **1-8** and **1-9** stabilize the interaction between Ig C2 domain of TrkA and NGF by penetrating the interfaces in a symmetrical pattern. They suggested that derivative **1-9** has a tighter interaction with the NGF-TrkA complex, and that the kinetics of reversible association/dissociation are disrupted with increasing concentrations of derivative **1-9,** resulting in the inhibitory effects.[41]

Further, they found that this stabilization of the NGF/TrkA complex was followed by a subsequent increase in phosphorylation of TrkA at Y490 and Y785 which further led to activation of the PKC and MAPK pathways. [41]

It would be interesting to see how the interaction of gambogic amide and sarcodonin G to Trk is affected in the presence of p75 NTR- Trk complex.

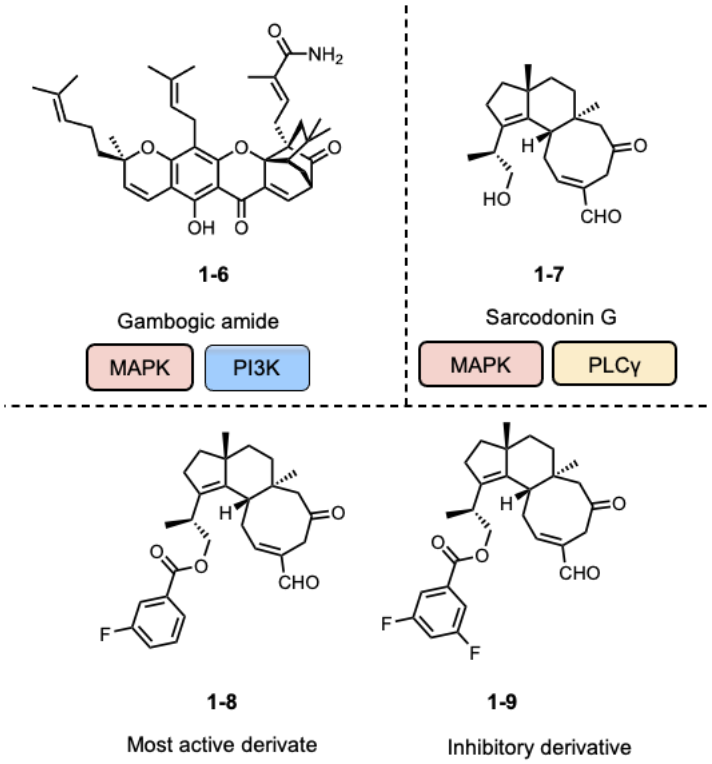

Figure 1-6. Structure of Gambogic amide and Sarcodonin G derivatives. The pathways that they perturb are mentioned in the coloured boxes.

1.6.4 Neurotrophic molecules that induce NGF secretion

Cyathane diterpenoids such as erinacines, scabronines and cyrneines isolated from mushrooms, present neurotrophic activity in part by inducing NGF synthesis.[42–45]

1.6.4.1 Erinacines

Erinacines A-F at a concentration of 1-5 mM stimulated NGF production in mouse astroglial cells. The amount of NGF induced by erinacines is substantially higher than that induced by epinepherine which is a known potent NGF stimulator.[46–48] Erinacine A (**1-10**, **figure 1-7**) when administered at 8mg/kg to rats leads to an increase in NGF in certain regions of the central nervous system.[49]

The mechanism of action of erinacine A was elucidated by Zhang and co-workers, who demonstrated that 30 μM of erinacine A potentiated neuritogenesis caused by 2 ng/mL of

NGF in PC-12 cells. Surprisingly, they could not detect any NGF secretion by PC-12 cells induced by erinacine A. Zhang and co-workers concluded that erinacine A potentiates NGF activity by increasing the phosphorylation levels of TrkA and Erk 1/2 and does not increase NGF expression levels at least in the PC-12 model system.[49]

1.6.4.2 Scabronine G

Scabronine G (**1-11**) isolated from *Sarcodon scabrosus* enhances the secretion of NGF in human astrocytoma cells (1321N1). This secretion of NGF induced by scabronine G has been linked to the activation of a specific isoform PKC- ζ. When the culture medium in which 1321N1 cells were conditioned with Scabronine G was added to PC-12 cells it led to a substantial increase in neuritogenesis. Surprisingly this activity was not solely due to the secreted NGF present in the conditioned media, as no decrease in activity was observed when an anti-NGF antibody was used to block the activation of TrkA by secreted NGF. Further, pre-treatment with a MEK inhibitor did cause a decrease in neuritogenesis in PC-12 cells, suggesting that scabronine G has a dual mechanism of action- it increases NGF levels in astrocytoma cells and activates the MAPK pathway in PC-12 cells.[42,50]

In 2011, Shi and co-workers demonstrated that 25 μM of scabronine G potentiates neuritogenesis caused by 20 ng/mL of NGF in PC-12 cells.[45] Interestingly, scabronine M (**1-12, figure 1-7**), which is structurally related to scabronine G, substantially inhibits NGF mediated neuritogenesis at 10 μM in PC-12 cells by reducing TrkA and Erk 1/2 phosphorylation. It was hinted that the epoxy group in scabronine M was responsible for this inhibitory effect.[51]

1.6.4.3 6-Shogaol

6-Shogaol (**1-13, figure 1-7**) is a compound isolated from the rhizomes of *jahe gajah* (*Zingiber officinale*). It has numerous pharmacological activities, including neuroprotective and anti-neuroinflammatory activities. 6-shogaol at a concentration of 500 ng/ml induced neuritogenesis in PC-12 cells which was comparable to the neuritogenesis induced by 50 ng/ml NGF. It's neuritogenic activity was attributed to its ability to induce low levels of NGF biosynthesis (1.7-fold compared to no treatment) and as a NGF mimic.

Its neurotrophic activity was attenuated by pre-treatment with Trk, Mek 1/2 and PI3K inhibitors. Previously, it was demonstrated that 6-shogaol protects PC-12 and human neuroblastoma cells from β-amyloid insult and cholinergic primary neurons from oxidative stress.[52]

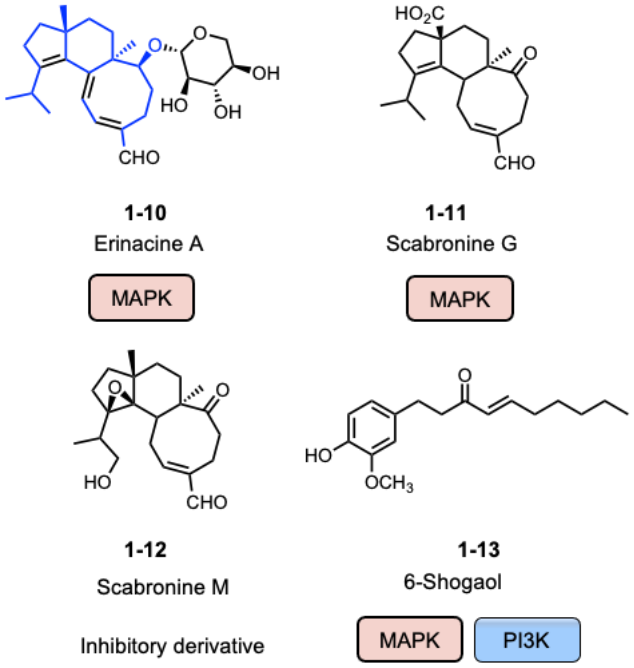

Figure 1-7. Structure of erinacine A, scabronine derivatives and 6-shogaol. Cyathane diterpenoid skeleton shown in blue. The pathways that they perturb are mentioned in the coloured boxes.

1.6.5 Molecules with dual neurotrophic and acetylcholinesterase inhibition activity

Many natural products that demonstrate neurotrophic activity also have other biological effects. These effects can work synergistically, and the molecule can have the potential to modulate neurodegenerative diseases by multiple mechanisms.

1.6.5.1 Huperzine A

Some molecules which are known inhibitors of acetylcholinesterase have also shown neurotrophic effect. One example is the potent acetylcholinesterase (AChE) inhibitor huperzine A (**1-14**, **figure 1-8**), a lycopodium alkaloid isolated from a Chinese herb

Huperzia serrata. At a concentration of 10 μM, it increases TrkA and p75 NTR levels in PC-12 cells and preventes oxidative damage in SH-SY5Y cells. When administered to mice at 0.2 mg/kg, it upregulates protein levels of NGF and BDNF, activates the MAPK pathway and promotes hippocampal neurogenesis. In an $A\beta_{1-40}$-infused rat AD model, huperzine A improved the processing of amyloid precursor protein by increasing the levels of PKC α, although the precise mechanism of this is unknown.

Huperzine A is an approved drug in China to treat cognitive deficiencies associated with AD and many clinical trials have been conducted to understand its impact on AD, although there is no firm conclusion from the outcomes of these trials.[33,34,53,54]

1.6.5.2 Lactucopicrin

A second example is lactucopicrin (**1-15**) a sesquiterpene lactone isolated from *Cichorium intybus L.* It increased neurite outgrowth in Neuro-2a cells when dosed at a concentration of 0.25-1 μM. At ~ 1μM it inhibited AChE activity in Neuro-2a cells. It's neuritogenic activity was attributed to three mechanisms- first, as an AChE inhibitor it increased intracellular Ca^{2+} concentration which further led to activation of calmodulin-dependent protein kinase-II (CaMKII) and Erk1/2. Second, it increased the phosphorylation levels of Trk and Akt. Interestingly inhibition of PI3K did not affect lactucopicrin mediated neuritogenesis which suggests that lactucopicrin increases Akt phosphorylation levels independent of PI3K signalling. Third, it induced NT secretion (NGF, BDNF and NT3) in rat C6 glioma cells.[55]

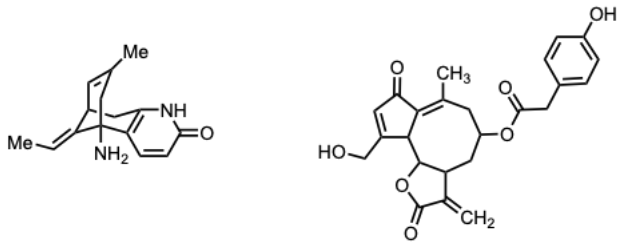

1-14
Huperizine A

1-15
Lactucopicrin

Figure 1-8. Structure of huperzine A and lactucopicrin.

1.6.6 Histone deacetylase inhibitors with neurotrophic activity

Another class of molecules that has been assessed for their neurotrophic activity are the histone deacetylase inhibitors.

Histones are a family of highly basic proteins which provide structural support to DNA in the nucleus and help condense it into chromatin. The nucleosome which is the fundamental unit of eukaryotic chromatin is made of DNA wrapped around eight core histone proteins called a histone octamer. Histones regulate gene transcription through their N-terminal modifications, the most common modification being methylation and acetylation. Histone deacetylases (HDACs) are enzymes which attenuate transcriptional activity by deacetylating histones and various transcription factors resulting in a more compact chromatin.[56] HDAC inhibitors (HDACi) are recognized as potential anticancer agents and interestingly some of these inhibitors also induce neuritogenesis and neuroprotection.[57]

1.6.6.1 Valproic acid

One such HDACi is valproic acid which is a short chain fatty acid. It promotes neuronal differentiation in various cells such as PC-12 cells, N1E–115 neuroblastoma cells, SH-SY5Y cells, rat neurons and *in vivo* in rats. Valproic acid causes neurogenesis through activation of Erk pathway and down regulation of JNK pathway. It also upregulated BDNF expression in rat cortical neurons by hypermethylating the histone associated in the BDNF promoter.[58–60] BDNF plays an important role in promoting neuronal survival and synaptic plasticity.[61]

1.6.6.2 Suberoylanilide hydroxamic acid

Another example is suberoylanilide hydroxamic acid (vorinostat) which functions as a pan histone deacetylase inhibitor. At 1 μM concentration it increased differentiation in a subclone of PC-12 cells by activating TrkA followed by induction of MAPK and PI3K pathways. It did not potentiate the effect of NGF, suggesting that it affects TrkA activation independently. It also induces hyperacetylation of α-tubulin and histones H3 and H4. Increase in acetylation of histones and transcription factors in neurons has been shown to promote differentiation of neurons. [57,62,63]

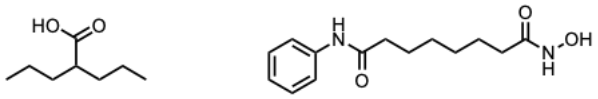

1-16

Valproic acid

1-17

Suberoylanilide hydroxamic acid

Figure 1-9. Structure of Valproic acid and Suberoylanilide hydroxamic acid

1.6.7 Neurotrophic activity of Clovanemagnolol

Clovanemagnolol (**1-18**, **figure 1-10**) is a sesquiterpene-neolignan isolated from the bark of *Magnolina obovata* and was identified in a screen for compounds as a molecule with potential neuroregenerative properties. At a concentration of 0.1 mM clovanemagnolol led to pronounced neurite outgrowth in fetal rat cerebral hemispheres. At the same concentration, it increased choline acetyltransferase activity and led to increased biosynthesis of the neurotransmitter acetylcholine.[64]

Cheng and co-workers demonstrated that, in primary cultures of hippocampal and embryonic cortical neurons, at a low concentration of 0.01 μM clovanemagnolol enhanced neurite outgrowth but at micromolar concentration, it decreased neurite outgrowth.[65]

Zlotkowski and co-workers tried to elucidate its mechanism of action using *Caenorhabditis elegans* as a model system. First they verified the phenotypic changes caused by clovanemagnolol and derivatives in *C.elegans*. After identifying the derivative that caused substantial outgrowth, they converted it into a probe (**1-19**) that they then used in a pull-down assay to identify which protein the molecule binds to. In this pull-down assay, kinesin-light-chain 1 (Klc-1) was identified as the enriched protein. They verified the importance of Klc-1 by using mutant *C.elegans* lacking Klc-1, which showed substantial reduction in axonal branching. Further, clovangemagnolol did not rescue axonal branching in mutant (– Klc-1) *C.elegans,* but it did increase axonal branching in wild type *C.elegans*.[66] Through this study, Zlotkowski and co-workers not only identified a possible binding partner for clovanemagnolol but also demonstrated the potential of using these neurotrophic molecules as probes to identify proteins with previously unknown biological effects.[66]

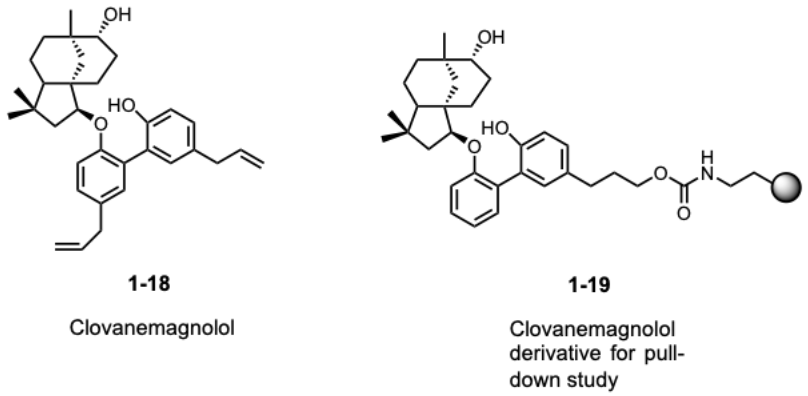

1-18

Clovanemagnolol

1-19

Clovanemagnolol derivative for pull-down study

Figure 1-10. Structure of clovanemagnolol and its derivative

1.7 Summary and conclusions

This chapter describes neurotrophin proteins and their receptors, with special emphasis on NGF. The biological importance of NGF in neuronal survival and development and the complex interactions with various NT receptors has been described. Further, several examples of neurotrophic small molecules and the signalling pathways they perturb are described.

Neurotrophic natural products have commonly been identified by assessing individual components from an extract of a natural source and by testing the activity of structurally similar molecules. Some neurotrophic molecules have also been identified from high throughput phenotypic screens. Some of these molecules possess interesting synergistic activities such as HDAC inhibition and AChE inhibition (section 1.6.5-1.6.6). It would be interesting to study further how these different mechanisms affect each other.

Detailed mechanism of action and cellular binding partners for many neurotrophic small molecules have not yet been determined. More often than not, determining the mechanism of action of these neurotrophic molecules follows a similar path of checking the activity of few key kinases in the Trk induced signalling pathways. Given the complexity of these pathways and their downstream effects and interdependence on other cellular pathways, a broader approach is required to understand the mechanism of actions of these molecules.

Also, it is important to elucidate how these molecules affect these kinases (Erk, Akt, PKC etc.), is their activity affected by elements upstream in the signalling pathway or do these molecules act as agonists of these kinases?

By focusing on Trk signalling, these studies sometimes tend to overlook the feedback from p75 NTR signalling pathways. The same applies for studies where neurotrophic molecules bind to Trk receptors. For example, even though it is established that gambogic amide binds to TrkA, we still need to understand how the presence of different levels of p75 NTR and sortilin affect its binding and activity.[39] This is especially important in a clinical context since the expression of receptors varies with different stages of neurodegenerative disease progression and even in different regions of the brain. These questions require more rigorous investigation into the biological activity of neurotrophic small molecules.

One way of achieving this is to convert neurotrophic molecules into chemical probes which can be used to assess which cellular components these molecules bind to. Clovanemagnolol is an excellent example of such a probe development which allowed the determination of novel proteins which affect neuronal function and survival.[66] This requires a synthetic route to access these molecules followed by determination of their structure-activity relationship, which identifies attachment positions for tags that convert these molecules into probes.

One of the reasons why the mechanism of neurotrophic molecules has not been explored is the complexity of neurotrophic signalling pathways and the difficulty of studying them in primary neuronal models.[26] Although cell lines offer an attractive alternative, they need to be chosen wisely as this choice biases the identified mechanism. For example, erinacine A increases NGF secretion in mouse astroglia cells and rat brains, but this secretion was not observed in PC-12 cells.[49,67]

In conclusion, neurotrophic small molecules present with the potential of protecting neuronal tissue and modulating neurogenesis, which can be of clinical significance in neurodegenerative diseases. Neurotrophic small molecules can also be used to identify new therapeutic targets by understanding how these molecules interact with cellular macromolecules to drive neurodifferentiation and neuroprotection.

1.8 Thesis structure

This thesis describes two individual studies. The first part of this thesis describes studies undertaken to investigate the properties of a particular neurotrophic small molecule. Given the vast choice of neurotrophic natural products to select from, I decided to explore the neurotrophic potential of banglenes. Banglenes are phenylbutenoid dimers extracted from Javanese ginger and have demonstrated neurotrophic activity in multiple *in-vitro* models and *in-vivo* in mouse model.[68] Despite their promising bioactivity, there were significant gaps in understanding the structural features responsible for its neurotrophic effect and its mechanism of action had not been explored. In chapter 2 and 3 these two gaps are addressed.

The second part of this thesis describes the development of a new fluorescent protein-based Förster resonance energy transfer (FRET) pair. The most popular fluorescent protein pair used in genetically encodable FRET indicators is the cyan fluorescent protein-yellow fluorescent protein pair. However, this pair has certain limitations, and to overcome some of their limitations green-red fluorescent protein pairs have been developed. These existing green-red fluorescent protein-based indicators usually have responses lower than cyan fluorescent protein-yellow fluorescent protein-based indicators.[69] In Chapter 4 of this thesis, I describe the engineering of a new green-red fluorescent protein-based FRET pair and describe a strategy to improve the response of the resultant indicators.

1.9 References

(1) Bothwell, M. NGF, BDNF, NT3, and NT4. *Handb. Exp. Pharmacol.* **2014**, *220*, 3–15.

(2) Al-Qudah, M. A.; Al-Dwairi, A. Mechanisms and Regulation of Neurotrophin Synthesis and Secretion. *Neurosci. J.* **2016**, *21* (4), 306–313.

(3) Paoletti, F.; Chiara, C. de; Kelly, G.; Covaceuszach, S.; Malerba, F.; Yan, R.; Lamba, D.; Cattaneo, A.; Pastore, A. Conformational Rigidity within Plasticity Promotes Differential Target Recognition of Nerve Growth Factor. *Front. Mol. Biosci.* **2016**, *3* (DEC), 83.

(4) Yamashita, N.; Kuruvilla, R. Neurotrophin Signaling Endosomes: Biogenesis, Regulation, and Functions. *Curr. Opin. Neurobiol.* **2016**, *39*, 139–145.

(5) Skaper, S. D. The Neurotrophin Family of Neurotrophic Factors: An Overview. *Methods Mol. Biol.* **2012**, *846*, 1–12.

(6) Hempstead, B. L. Deciphering Proneurotrophin Actions. *Handb. Exp. Pharmacol.* **2014**, *220*, 17–32.

(7) Kraemer, B. R.; Yoon, S. O.; Carter, B. D. The Biological Functions and Signaling Mechanisms of the P75 Neurotrophin Receptor. *Handb. Exp. Pharmacol.* **2014**, *220*, 121–164.

(8) Le, A. P.; Friedman, W. J. Matrix Metalloproteinase-7 Regulates Cleavage of pro-Nerve Growth Factor and Is Neuroprotective Following Kainic Acid-Induced Seizures. *J. Neurosci.* **2012**, *32* (2), 703–712.

(9) Deinhardt, K.; Chao, M. V. Trk Receptors. *Handb. Exp. Pharmacol.* **2014**, *220*, 103–119.

(10) Wlesmann, C.; Ultsch, M. H.; Bass, S. H.; De Vos, A. M. Crystal Structure of Nerve Growth Factor in Complex with the Ligand-Binding Domain of the TrkA Receptor. *Nat. 1999 4016749* **1999**, *401* (6749), 184–188.

(11) Shen, J.; Maruyama, I. N. Nerve Growth Factor Receptor TrkA Exists as a Preformed, yet Inactive, Dimer in Living Cells. *FEBS Lett.* **2011**, *585* (2), 295–299.

(12) Franco, M. L.; Nadezhdin, K. D.; Goncharuk, S. A.; Mineev, K. S.; Arseniev, A. S.; Vilar, M. Structural Basis of the Transmembrane Domain Dimerization and Rotation in the Activation Mechanism of the TRKA Receptor by Nerve Growth Factor. *J. Biol. Chem.* **2020**, *295* (1), 275–286.

(13) Reichardt, L. F. Neurotrophin-Regulated Signalling Pathways. *Philos. Trans. R. Soc. B Biol. Sci.* **2006**, *361* (1473), 1545–1564.

(14) Lee, F. S.; Rajagopal, R.; Kim, A. H.; Chang, P. C.; Chao, M. V. Activation of Trk Neurotrophin Receptor Signaling by Pituitary Adenylate Cyclase-Activating Polypeptides *. *J. Biol. Chem.* **2002**, *277* (11), 9096–9102.

(15) Skeldal, S.; Sykes, A. M.; Glerup, S.; Matusica, D.; Palstra, N.; Autio, H.; Boskovic, Z.; Madsen, P.; Castrén, E.; Nykjaer, A.; Coulson, E. J. Mapping of the Interaction Site between Sortilin and the P75 Neurotrophin Receptor Reveals a Regulatory Role for the Sortilin Intracellular Domain in P75 Neurotrophin Receptor Shedding and Apoptosis *. *J. Biol. Chem.* **2012**, *287* (52), 43798–43809.

(16) Mi, S.; Lee, X.; Shao, Z.; Thill, G.; Ji, B.; Relton, J.; Levesque, M.; Allaire, N.; Perrin, S.; Sands, B.; Crowell, T.; Cate, R. L.; McCoy, J. M.; Pepinsky, R. B. LINGO-1 Is a Component of the Nogo-66 Receptor/P75 Signaling Complex. *Nat. Neurosci.* **2004**, *7* (3), 221–228.

(17) Franco, M. L.; Nadezhdin, K. D.; Light, T. P.; Goncharuk, S. A.; Soler-Lopez, A.; Ahmed, F.; Mineev, K. S.; Hristova, K.; Arseniev, A. S.; Vilar, M. Interaction between the Transmembrane Domains of Neurotrophin Receptors P75 and TrkA Mediates Their Reciprocal Activation. *J. Biol. Chem.* **2021**, *297* (2),1000926.

(18) Makkerh, J. P. S.; Ceni, C.; Auld, D. S.; Vaillancourt, F.; Dorval, G.; Barker, P. A. P75 Neurotrophin Receptor Reduces Ligand-Induced Trk Receptor Ubiquitination and Delays Trk Receptor Internalization and Degradation. *EMBO Rep.* **2005**, *6* (10), 936–941.

(19) Ceni, C.; Kommaddi, R. P.; Thomas, R.; Vereker, E.; Liu, X.; McPherson, P. S.; Ritter, B.; Barker, P. A. The P75NTR Intracellular Domain Generated by Neurotrophin-Induced Receptor Cleavage Potentiates Trk Signaling. *J. Cell Sci.* **2010**, *123* (13), 2299–2307.

(20) Yamashita, T.; Tucker, K. L.; Barde, Y. A. Neurotrophin Binding to the P75 Receptor Modulates Rho Activity and Axonal Outgrowth. *Neuron* **1999**, *24* (3), 585–593.

(21) Gao, L.; Zhang, Y.; Sterling, K.; Song, W. Brain-Derived Neurotrophic Factor in Alzheimer's Disease and Its Pharmaceutical Potential. *Transl. Neurodegener.* **2022**, *11* (1), 1–34.

(22) Mufson, E. J.; Counts, S. E.; Ginsberg, S. D.; Mahady, L.; Perez, S. E.; Massa, S. M.; Longo, F. M.; Ikonomovic, M. D. Nerve Growth Factor Pathobiology During the Progression of Alzheimer's Disease. *Front. Neurosci.* **2019**, *13* (JUL).

(23) Latina, V.; Caioli, S.; Zona, C.; Ciotti, M. T.; Amadoro, G.; Calissano, P. Impaired NGF/TrKA Signaling Causes Early AD-Linked Presynaptic Dysfunction in Cholinergic Primary Neurons. *Front. Cell. Neurosci.* **2017**, *11*, 68.

(24) Saragovi, H. U.; Galan, A.; Levin, L. A. Neuroprotection: Pro-Survival and Anti-Neurotoxic Mechanisms as Therapeutic Strategies in Neurodegeneration. *Front. Cell. Neurosci.* **2019**, *13*, 231.

(25) Cai, J.; Hua, F.; Yuan, L.; Tang, W.; Lu, J.; Yu, S.; Wang, X.; Hu, Y. Potential Therapeutic Effects of Neurotrophins for Acute and Chronic Neurological Diseases. *Biomed Res. Int.* **2014**, .

(26) Xu, J.; Lacoske, M. H.; Theodorakis, E. A. Neurotrophic Natural Products: Chemistry and Biology. *Angew. Chem. Int. Ed. Engl.* **2014**, *53* (4), 956.

(27) Balon, K.; Wiatrak, B. PC12 and THP-1 Cell Lines as Neuronal and Microglia Model in Neurobiological Research. *Appl. Sci.* **2021**, *11* (9), 3729.

(28) Greene, L. A.; Tischler, A. S. Establishment of a Noradrenergic Clonal Line of Rat Adrenal Pheochromocytoma Cells Which Respond to Nerve Growth Factor. *Proc. Natl. Acad. Sci.* **1976**, *73* (7), 2424–2428.

(29) Tremblay, R. G.; Sikorska, M.; Sandhu, J. K.; Lanthier, P.; Ribecco-Lutkiewicz, M.; Bani-Yaghoub, M. Differentiation of Mouse Neuro 2A Cells into Dopamine Neurons. *J. Neurosci. Methods* **2010**, *186* (1), 60–67.

(30) Kovalevich, J.; Langford, D. Considerations for the Use of SH-SY5Y Neuroblastoma Cells in Neurobiology. *Methods Mol. Biol.* **2013**, *1078*, 9.

(31) Duque, A.; Arellano, J. I.; Rakic, P. An Assessment of the Existence of Adult Neurogenesis in Humans and

Value of Its Rodent Models for Neuropsychiatric Diseases. *Mol. Psychiatry.* **2021**, 1–6.

(32) Azari, H.; Reynolds, B. A. In Vitro Models for Neurogenesis. *Cold Spring Harb. Perspect. Biol.* **2016**, *8* (6).

(33) Yang, G.; Wang, Y.; Tian, J.; Liu, J. P. Huperzine A for Alzheimer's Disease: A Systematic Review and Meta-Analysis of Randomized Clinical Trials. *PLoS One* **2013**, *8* (9).

(34) Venkatesan, R.; Ji, E.; Kim, S. Y. Phytochemicals That Regulate Neurodegenerative Disease by Targeting Neurotrophins: A Comprehensive Review. *Biomed Res. Int.* **2015**.

(35) Tang, G.; Dong, X.; Huang, X.; Huang, X. J.; Liu, H.; Wang, Y.; Ye, W. C.; Shi, L. A Natural Diarylheptanoid Promotes Neuronal Differentiation via Activating ERK and PI3K-Akt Dependent Pathways. *Neuroscience* **2015**, *303*, 389–401.

(36) Harada, K.; Kubo, M.; Fukuyama, Y. Chemistry and Neurotrophic Activities of (–)-Talaumidin and Its Derivatives. *Front. Chem.* **2020**, *8*, 301.

(37) Harada, K.; Kubo, M.; Horiuchi, H.; Ishii, A.; Esumi, T.; Hioki, H.; Fukuyama, Y. Systematic Asymmetric Synthesis of All Diastereomers of (-)-Talaumidin and Their Neurotrophic Activity. *J. Org. Chem.* **2015**, *80* (14), 7076–7088.

(38) Koriyama, Y.; Furukawa, A.; Sugitani, K.; Kubo, M.; Harada, K.; Fukuyama, Y. Talaumidin Promotes Neurite Outgrowth of Staurosporine-Differentiated RGC-5 Cells Through PI3K/Akt-Dependent Pathways. *Adv. Exp. Med. Biol.* **2018**, *1074*, 649–653.

(39) Jang, S. W.; Okada, M.; Sayeed, I.; Xiao, G.; Stein, D.; Jin, P.; Ye, K. Gambogic Amide, a Selective Agonist for TrkA Receptor That Possesses Robust Neurotrophic Activity, Prevents Neuronal Cell Death. *Proc. Natl. Acad. Sci. U. S. A.* **2007**, *104* (41), 16329.

(40) Arevalo, J. C.; Conde, B.; Hempstead, B. L.; Chao, M. V.; Martin-Zanca, D.; Perez, P. TrkA Immunoglobulin-Like Ligand Binding Domains Inhibit Spontaneous Activation of the Receptor. *Mol. Cell. Biol.* **2000**, *20* (16), 5908–5916.

(41) Cao, C. Y.; Zhang, C. C.; Shi, X. W.; Li, D.; Cao, W.; Yin, X.; Gao, J. M. Sarcodonin G Derivatives Exhibit Distinctive Effects on Neurite Outgrowth by Modulating NGF Signaling in PC12 Cells. *ACS Chem. Neurosci.* **2018**, *9* (7), 1607–1615.

(42) Obara, Y.; Nakahata, N.; Kita, T.; Takaya, Y.; Kobayashi, H.; Hosoi, S.; Kiuchi, F.; Ohta, T.; Oshima, Y.; Ohizumi, Y. Stimulation of Neurotrophic Factor Secretion from 1321N1 Human Astrocytoma Cells by Novel Diterpenoids, Scabronines A and G. *Eur. J. Pharmacol.* **1999**, *370* (1), 79–84.

(43) Obara, Y.; Hoshino, T.; Marcotullio, M. C.; Pagiotti, R.; Nakahata, N. A Novel Cyathane Diterpene, Cyrneine A, Induces Neurite Outgrowth in a Rac1-Dependent Mechanism in PC12 Cells. *Life Sci.* **2007**, *80* (18), 1669–1677.

(44) Ma, B. J.; Shen, J. W.; Yu, H. Y.; Ruan, Y.; Wu, T. T.; Zhao, X. Hericenones and Erinacines: Stimulators of Nerve Growth Factor (NGF) Biosynthesis in Hericium Erinaceus. *Mycology* **2010**, *1* (2), 92–98.

(45) Shi, X. W.; Liu, L.; Gao, J. M.; Zhang, A. L. Cyathane Diterpenes from Chinese Mushroom Sarcodon Scabrosus and Their Neurite Outgrowth-Promoting Activity. *Eur. J. Med. Chem.* **2011**, *46* (7), 3112–3117.

(46) Kawagishi, H.; Simada, A.; Shizuki, K.; Mori, H.; Okamoto, K.; Sakamoto, H.; Furukawa, S. Erinacine D, a

Stimulator of NGF-Synthesis, from the Mycelia of Hericium Erinaceum. *Heterocycl. Commun.* **1996**, *2* (1), 51–54.

(47) Kawagishi, H.; Shimada, A.; Hosokawa, S.; Mori, H.; Sakamoto, H.; Ishiguro, Y.; Sakemi, S.; Bordner, J.; Kojima, N.; Furukawa, S. Erinacines E, F, and G, Stimulators of Nerve Growth Factor (NGF)-Synthesis, from the Mycelia of Hericium Erinaceum. *Tetrahedron Lett.* **1996**, *37* (41), 7399–7402.

(48) Kawagishi, H.; Shimada, A.; Shirai, R.; Okamoto, K.; Ojima, F.; Sakamoto, H.; Ishiguro, Y.; Furukawa, S. Erinacines A, B and C, Strong Stimulators of Nerve Growth Factor (NGF)-Synthesis, from the Mycelia of Hericium Erinaceum. *Tetrahedron Lett.* **1994**, *35* (10), 1569–1572.

(49) Shimbo, M.; Kawagishi, H.; Yokogoshi, H. Erinacine A Increases Catecholamine and Nerve Growth Factor Content in the Central Nervous System of Rats. *Nutr. Res.* **2005**, *25* (6), 617–623.

(50) Obara, Y.; Kobayashi, H.; Ohta, T.; Ohizumi, Y.; Nakahata, N. Scabronine G-Methylester Enhances Secretion of Neurotrophic Factors Mediated by an Activation of Protein Kinase C-ζ. *Mol. Pharmacol.* **2001**, *59* (5), 1287–1297.

(51) Liu, L.; Shi, X. W.; Zong, S. C.; Tang, J. J.; Gao, J. M. Scabronine M, a Novel Inhibitor of NGF-Induced Neurite Outgrowth from PC12 Cells from the Fungus Sarcodon Scabrosus. *Bioorg. Med. Chem. Lett.* **2012**, *22* (7), 2401–2406.

(52) Seow, S. L. S.; Hong, S. L.; Lee, G. S.; Malek, S. N. A.; Sabaratnam, V. 6-Shogaol, a Neuroactive Compound of Ginger (Jahe Gajah) Induced Neuritogenic Activity via NGF Responsive Pathways in PC-12 Cells. *BMC Complement. Altern. Med.* **2017**, *17* (1), 1–11.

(53) Tang, L. L.; Wang, R.; Tang, X. C. Effects of Huperzine A on Secretion of Nerve Growth Factor in Cultured Rat Cortical Astrocytes and Neurite Outgrowth in Rat PC12 Cells. *Acta Pharmacol. Sin.* **2005**, *26* (6), 673–678.

(54) Ma, T.; Gong, K.; Yan, Y.; Zhang, L.; Tang, P.; Zhang, X.; Gong, Y. Huperzine A Promotes Hippocampal Neurogenesis in Vitro and in Vivo. *Brain Res.* **2013**, *1506*, 35–43.

(55) Venkatesan, R.; Shim, W. S.; Yeo, E. J.; Kim, S. Y. Lactucopicrin Potentiates Neuritogenesis and Neurotrophic Effects by Regulating Ca2+/CaMKII/ATF1 Signaling Pathway. *J. Ethnopharmacol.* **2017**, *198*, 174–183.

(56) Bannister, A. J.; Kouzarides, T. Regulation of Chromatin by Histone Modifications. *Cell Res.* **2011**, *21* (3), 381–395.

(57) Shukla, S.; Tekwani, B. L. Histone Deacetylases Inhibitors in Neurodegenerative Diseases, Neuroprotection and Neuronal Differentiation. *Front. Pharmacol.* **2020**, *11*, 537.

(58) Van Bergeijk, J.; Haastert, K.; Grothe, C.; Claus, P. Valproic Acid Promotes Neurite Outgrowth in PC12 Cells Independent from Regulation of the Survival of Motoneuron Protein. *Chem. Biol. Drug Des.* **2006**, *67* (3), 244–247.

(59) Hasan, M. R.; Kim, J. H.; Kim, Y. J.; Kwon, K. J.; Shin, C. Y.; Kim, H. Y.; Han, S. H.; Choi, D. H.; Lee, J. Effect of HDAC Inhibitors on Neuroprotection and Neurite Outgrowth in Primary Rat Cortical Neurons Following Ischemic Insult. *Neurochem. Res.* **2013**, *38* (9), 1921–1934.

(60) Hao, Y.; Creson, T.; Zhang, L.; Li, P.; Du, F.; Yuan, P.; Gould, T. D.; Manji, H. K.; Chen, G. Mood Stabilizer Valproate Promotes ERK Pathway-Dependent Cortical Neuronal Growth and Neurogenesis. *J. Neurosci.* **2004**, *24* (29), 6590–6599.

(61) Miranda, M.; Morici, J. F.; Zanoni, M. B.; Bekinschtein, P. Brain-Derived Neurotrophic Factor: A Key Molecule for Memory in the Healthy and the Pathological Brain. *Front. Cell. Neurosci.* **2019**, *13*, 363.

(62) Shukla, S.; Shariat-Madar, Z.; Walker, L. A.; Tekwani, B. L. Mechanism for Neurotropic Action of Vorinostat, a Pan Histone Deacetylase Inhibitor. *Mol. Cell. Neurosci.* **2016**, *77*, 11–20.

(63) Gaub, P.; Tedeschi, A.; Puttagunta, R.; Nguyen, T.; Schmandke, A.; Di Giovanni, S. HDAC Inhibition Promotes Neuronal Outgrowth and Counteracts Growth Cone Collapse through CBP/P300 and P/CAF-Dependent P53 Acetylation. *Cell Death Differ.* **2010**, *17* (9), 1392–1408.

(64) Fukuyama, Y.; Otoshi, Y.; Miyoshi, K.; Nakamura, K.; Kodama, M.; Nagasawa, M.; Hasegawa, T.; Okazaki, H.; Sugawara, M. Neurotrophic Sesquiterpene-Neolignans from Magnolia Obovata: Structure and Neurotrophic Activity. *Tetrahedron* **1992**, *48* (3), 377–392.

(65) Khaing, Z.; Kang, D.; Camelio, A. M.; Schmidt, C. E.; Siegel, D. Hippocampal and Cortical Neuronal Growth Mediated by the Small Molecule Natural Product Clovanemagnolol. *Bioorg. Med. Chem. Lett.* **2011**, *21* (16), 4808–4812.

(66) Zlotkowski, K.; Eliasen, A. M.; Mitra, A.; Siegel, D. Small-Molecule Mechanism of Action Studies in Caenorhabditis Elegans. *Chembiochem* **2013**, *14* (17), 2338–2344.

(67) Zhang, C. C.; Cao, C. Y.; Kubo, M.; Harada, K.; Yan, X. T.; Fukuyama, Y.; Gao, J. M. Chemical Constituents from Hericium Erinaceus Promote Neuronal Survival and Potentiate Neurite Outgrowth via the TrkA/Erk1/2 Pathway. *Int. J. Mol. Sci.* **2017**, *18* (8).

(68) Matsui, N.; Kido, Y.; Okada, H.; Kubo, M.; Nakai, M.; Fukuishi, N.; Fukuyama, Y.; Akagi, M. Phenylbutenoid Dimers Isolated from Zingiber Purpureum Exert Neurotrophic Effects on Cultured Neurons and Enhance Hippocampal Neurogenesis in Olfactory Bulbectomized Mice. *Neurosci. Lett.* **2012**, *513* (1), 72–77.

(69) Lam, A. J.; St-Pierre, F.; Gong, Y.; Marshall, J. D.; Cranfill, P. J.; Baird, M. A.; McKeown, M. R.; Wiedenmann, J.; Davidson, M. W.; Schnitzer, M. J.; Tsien, R. Y.; Lin, M. Z. Improving FRET Dynamic Range with Bright Green and Red Fluorescent Proteins. *Nat. Methods* **2012**, *9* (10), 1005.

Chapter 2: Synthesis of banglenes and banglene derivatives

2.1 Origin and bioactivity of banglenes

Zingiber purpureum (also known as *Zingiber cassumunar*), is a perennial plant widely grown in South-East Asia. The rhizome of this plant is commonly called Bangle and is used in traditional medicinal systems to treat various ailments such as rheumatism, fever etc.[1]

Several phytochemicals such as curcuminoids, terpenoids and phenylbutenoids have been extracted from this rhizome and their biological effects have been studied. Phenylbutenoids are characteristic to the *Zingiberaceae* family but have mainly been isolated from *Z. purpureum.*[1] Some of these phenylbutenoids are reported to inhibit P-glycoprotein and cyclooxygenase-2, and also demonstrate neurotrophic activity.[2,3,4]

The phenylbutenoid dimers *cis* and *trans* banglenes (***c*-BG** and ***t*-BG**, **figure 2-1**) isolated from methanolic extracts of Bangle using silica gel chromatography and purified by reverse-phase high performance liquid chromatography (RP-HPLC) have demonstrated neurotrophic activity.[2] These two phenylbutenoid dimers are diastereomers of each other, being *cis/ trans* isomers with respect to the cyclohexene ring.

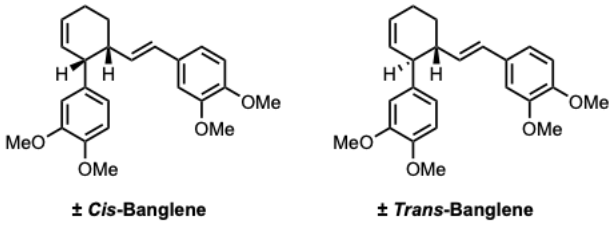

Figure 2-1. Phenylbutenoid dimers extracted from *Z. purpureum*

The Fukuyama and Matsui group evaluated the neurotrophic activity of extracted (±) ***c*-BG** and (±) ***t*-BG**.[2] First, they studied their effect on PC-12 cells, where (±) ***c*-BG** and (±) ***t*-BG** dose-dependently induced neurite outgrowth. Next, they examined the effects on primary cultured rat cortical neurons, where (±) ***c*-BG** and (±) ***t*-BG** increased the number and length of neurite outgrowths and were also neuroprotective. After demonstrating the neurotrophic and neuroprotective activity *in vitro*, their activity was investigated *in vivo* in

olfactory bulbectomized (OBX) mouse model system, which is an experimental model for depression. This stress induced depression is known to alter adult hippocampal neurogenesis in rodents.[5] After olfactory bulbectomy, it was found that the number of newly generated neurons significantly decreased after 30 days. Individual treatment with 50 mg/kg p.o. of (±) ***c*-BG** or (±) ***t*-BG** once a day for 14 days significantly enhanced hippocampal neurogenesis by approximately 3-fold.[2] The concentrations at which the neurotrophic effects of banglenes were observed are listed in **table 2-1**.

Model system	**Response monitored**	**Conc. of (±) *t*-BG**	**Conc. of (±) *c*-BG**
PC-12 cells	Neurite outgrowth	10–30 μM	30 μM
Primary rat cortical neurons	Number of neurites	0.3–3 μM	0.03-3 μM
	Neurite length		
	Viability	30 μM	3–30 μM
OBX mice	Neurogenesis	50 mg/kg p.o.	

Table 2-1. Summary of neurotrophic effects of banglenes.

Matsui and co-workers *in vivo* studies demonstrated that banglenes are orally available and can cross the blood brain barrier (BBB). Banglenes were detected at measurable levels in brain tissue (250-400 ng/ g) and in plasma (~50ng/mL) within an hour of administration.[2] With these studies, Matsui and co-workers suggested that banglenes can be valuable as potential leads for developing therapeutics for neurodegenerative diseases.

Further, Nakai et al. studied the therapeutic effect of ethanolic extract of bangle containing 0.63% (±) ***c*-BG** and 0.3% (±) ***t*-BG** in senescence accelerated mice, which is an experimental model for age related AD. These mice were fed bangle extract as a powder for 30 days. After performing the Morris water maze behavioural test, they found that the bangle containing diet improved spatial learning of the mice. They were also able to demonstrate significant neurogenesis in the dentate gyrus of the model mice.[6]

Additionally, the Fukuyama group assessed the safety of *Z. purpureum* extracts and demonstrated no-adverse effects to human subjects taking 850 mg/day for four weeks, which corresponds to 50 mg of ***c*-BG** and ***t*-BG**.[7]

2.2 Objectives for investigating banglenes neurotrophic activity

The studies describe above show that banglenes are an appealing small molecule scaffold with neurotrophic properties. Their neurotrophic potential has been demonstrated in both *in vitro* and *in vivo* model systems, namely PC-12 cells, primary rat cortical neurons and OBX mice. Moreover, they are synthetically accessible and their favourable pharmacokinetic properties and safety profiles have already been established in animal studies .[8–11]

Despite demonstrated neurotrophic activity, bioavailability and safety data, there are still gaps in the mechanistic and molecular understanding of banglene activity. In this thesis I aim to address this gap by assessing the structural features responsible for the neurotrophic activity of the banglenes and by providing insights into its mechanism of action.

2.3 Structural features of banglene scaffold

The banglene scaffold can be broken down into key structural features- three rings which are further referred to as ring A, B or C and two alkenes which are referred to as the cyclohexene (or ring B) alkene and the styrenyl alkene connecting ring B and C (**figure 2-2**).

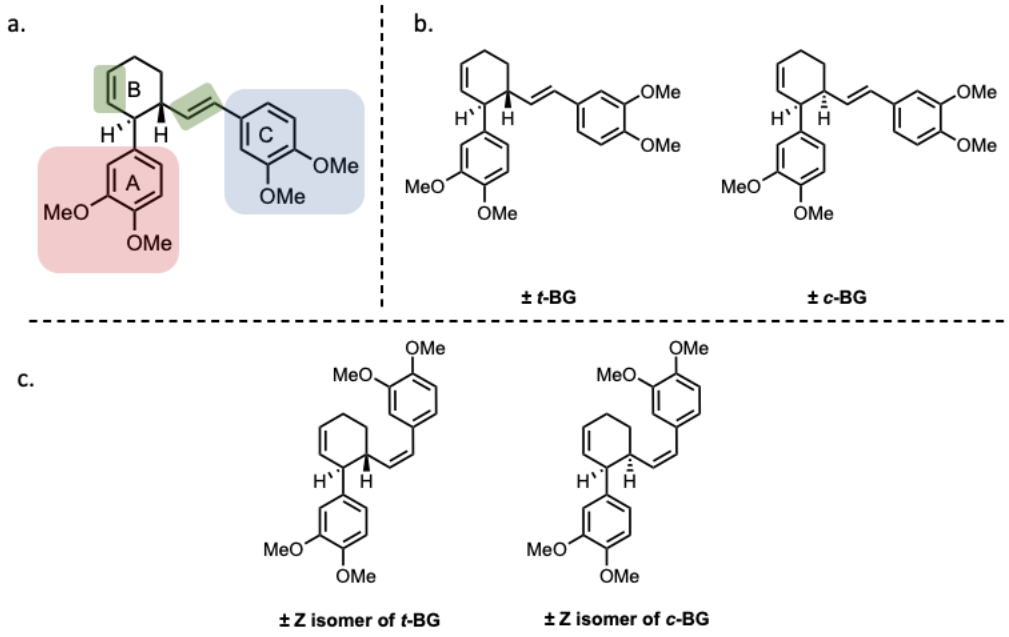

Figure 2-2. (a) Structural features of trans banglene (b) E (c) Z diastereomers of banglenes

Analyzing the structure, there are 8 possible stereoisomers, first the *cis* and *trans* relationship of the cyclohexene substituents, which respectively lead to ***c*-BG** and ***t*-BG**. Further, the styrenyl alkene can be in an E or Z geometry depending on the relationship of rings B and C. Finally, all 4 diastereomers will have their enantiomers. All these structural features add a certain complexity to the scaffold which needed to be systematically investigated to understand their contributions towards bioactivity.

2.4 Synthesis routes to access banglene isomers

The Fukuyama and Matsui group utilised extracts from bangle for all their studies. However, in the 70% aqueous ethanol extract of bangle, the total percentage of *cis* and *trans* banglene is only 1.6%, this makes extracting banglenes a rather low yielding process.[12] An ideal alternative is to access banglenes synthetically, some of the routes to synthesize banglenes are discussed in this section.

2.4.1 Synthesis of banglenes through Diels-Alder dimerization

The first synthetic route to access banglenes was described by Byrne and co-workers in 1980 by a Diels-Alder dimerization of diene **2-1** in the presence of catalytic amounts of hydroquinone (**scheme 2-1**). They were able to crystallize the (±) ***c*-BG** as fine needles from ether/ hexanes.[9]

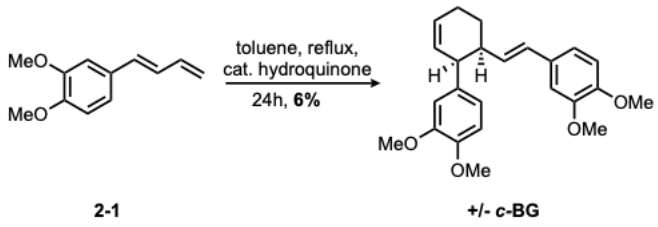

Scheme 2-1. Synthesis of *cis*-Banglene by Diels-Alder dimerization

Byrne and co-workers also attempted to synthesise banglenes derivatives by using two different dienes (**scheme 2-2**) which led to a mixture of ***c*-BG,** derivative **2-3** and derivative **2-4**, which were then separated by preparative liquid chromatography.[9]

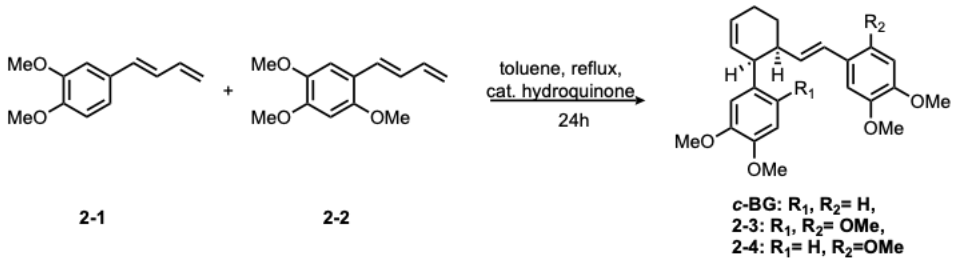

Scheme 2-2. Synthesis banglene derivatives by Diels-Alder dimerization

2.4.2 Synthesis of banglenes through Wittig reaction

An alternative synthesis (**scheme 2-3**) was investigated by Byrne and co-workers, where they synthesized a *cis/ trans* mixture of aldehydes **2-6** and **2-7** by a Diels-Alder reaction between diene **2-1** and acrolein (**scheme 2-3a**). Since they had difficulty in isolating the *cis*-aldehyde **(2-6)**, they replaced acrolein with acrylic acid, and the corresponding Diels-Alder products were methylated to yield methyl esters **(2-10)** which were easier to separate by preparative liquid chromatography. The separated *cis*-methyl ester **2-10** was then reduced to an alcohol by lithium aluminium hydride, followed by a Collin's oxidation to access the *cis* aldehyde **2-6**. They were unsuccessful at subsequently accessing (±) ***c*-BG** through a Wittig reaction with aldehyde **2-6** (**scheme 2-3b**).[9]

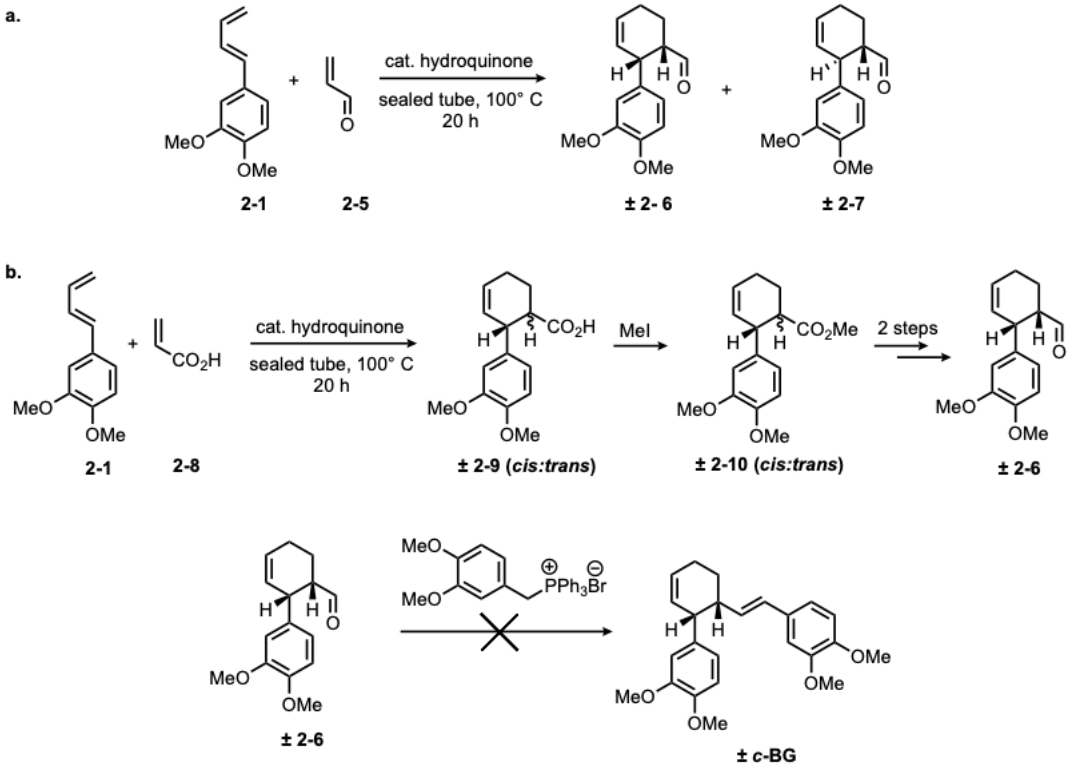

Scheme 2-3. Synthetic routes to access aldehydes for synthesis of c-BG

Haeil Park and co-workers were able to synthesize (±) ***t*-BG** and 15 other banglene derivatives by accessing the aldehydes in a similar fashion as shown **scheme 2-3** followed by a Wittig reaction (**scheme 2-4**). In their synthesis, their Diels-Alder cyclization between diene **2-1** and acrolein gave them access to *cis*-aldehyde (±) **2-6**, this is in contradiction to the report from Byrne and co-workers where they got a 1:1.4 mixture of *cis: trans* aldehydes.[8,10] The authors hint that possibly in their subsequent step, n-BuLi could have isomerized the *cis* aldehydes to give the final ***t*-BG** product. It is surprising how the styrenyl alkene in their final banglene product has an E stereochemistry, as the Wittig reaction would result in some amount of product having the styrenyl alkene with a Z geometry.

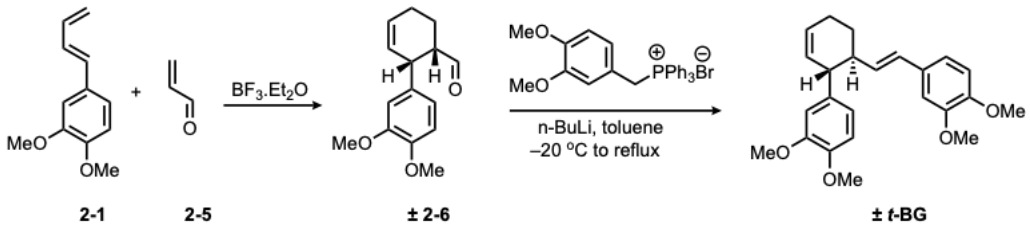

Scheme 2-4. Synthesis of (±) *t*-BG through a Wittig reaction

2.4.3 Enantioselective synthesis of banglene isomers

A five step enantioselective synthesis of both ***c*-BG** and ***t*-BG**, as well as their Z isomers, was reported by Seo, Lim and co-workers.[13] In their synthesis, diene **2-1** underwent a Diels-Alder cycloaddition with enantiopure acrylamide **2-11** to form the cyclohexene ring. A subsequent two-step conversion of the chiral oxazolidinone auxiliary in **2-12** resulted in the *cis* aldehyde **2-6** which then undergoes the final Horner- Wadsworth-Emmons (HWE) olefination with the phosphonate **2-14** to yield (+) ***c*-BG** along with its Z isomer, and the E: Z selectivity ratio was 95:5 (**scheme 2-5a**).

In order to synthesize (+) ***t*-BG**, they epimerized *cis* aldehyde **2-6** to *trans* aldehyde **2-7** using potassium carbonate in methanol, and then carried out the olefination using the same HWE conditions (**scheme 2-5b**). However, this led to a 24% yield of (+) ***t*-BG** which Seo, Lim and coworkers wanted to improve.[10]

Therefore, they used an alternative route (**scheme 2-5c**) where *trans* aldehyde **2-7** was converted to its alkyne analogue by Corey-Fuchs reaction. Hydrostannylation of **2-15** with tributylstannane led to the vinyl stannane **2-16** with a E: Z selectivity ratio of 80:20. This E/Z mixture of **2-16** was then used to perform a Stille coupling with 3,4 dimethoxyphenyl triflate (**2-17**) to furnish (+) ***t*-BG** and its Z isomer in a 4:1 ratio which was further separated by chiral HPLC.[10]

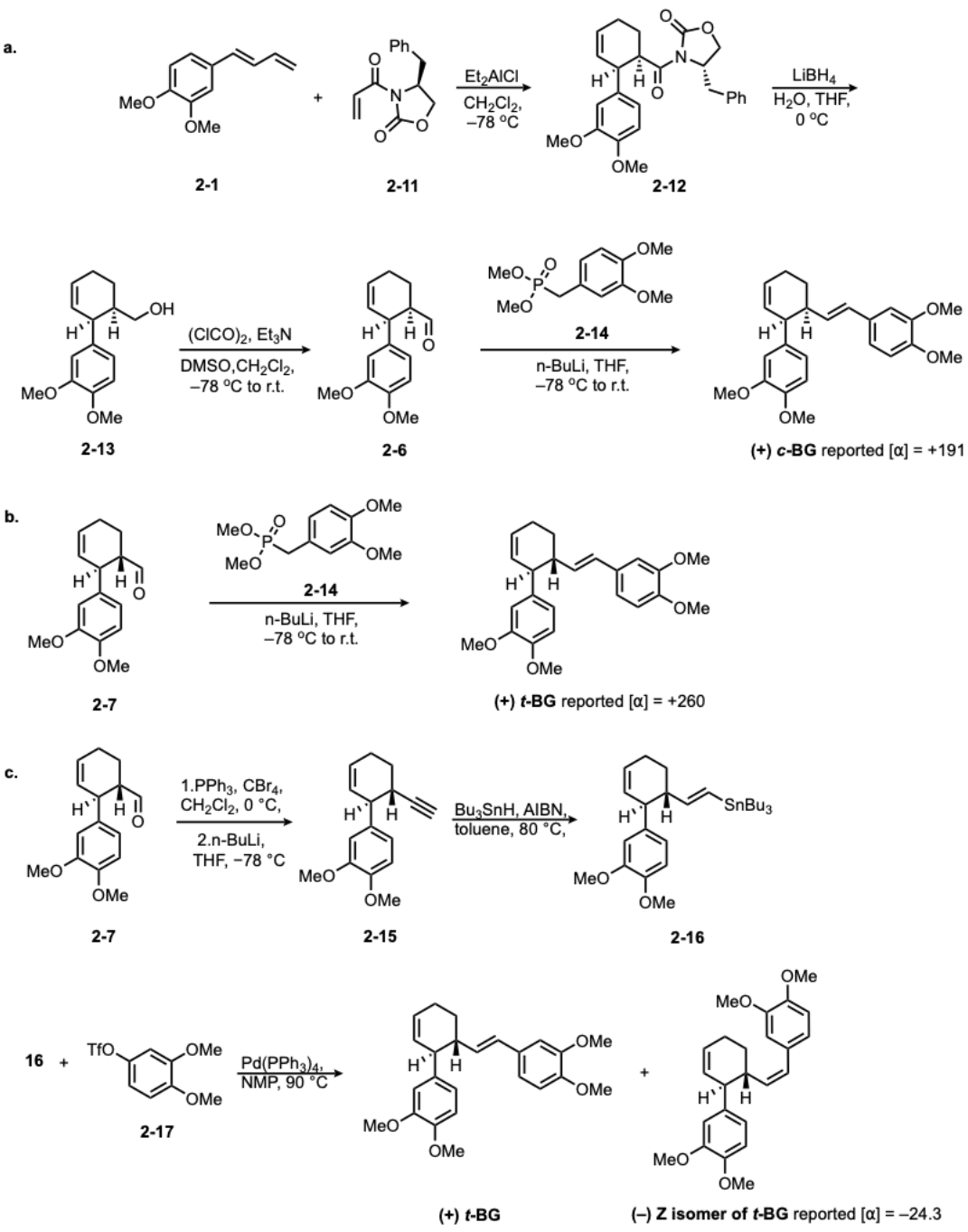

Scheme 2-5. Enantiospecific route to access various isomers of banglenes

2.5 Synthesis of banglene isomers and their derivatives

It was important to synthesise ***c*-BG** and ***t*-BG** to test them for their neurotrophic activity, as previously neurotrophic activity had only been studied with banglenes isolated from the rhizome extract.[2] Trace amounts of other components in the extract could affect the bioactivity, and the only data that confirms the diastereomeric enrichment of isolated banglenes was a HPLC trace. Given the lack of additional confirmatory analytical data, it was necessary to test the neurotrophic activity of synthetically accessed banglenes.

Derivatives of banglene were synthesised to establish a structure-activity relationship (SAR). Three strategies were chosen to establish the SAR, first was to vary the substitutions on ring A and C, second was to modify the cyclohexene alkene and the styrenyl alkene and third was to change the geometry of the styrenyl alkene. The derivatives synthesised are shown in **figure 2-3** and their synthesis is described in the section below.

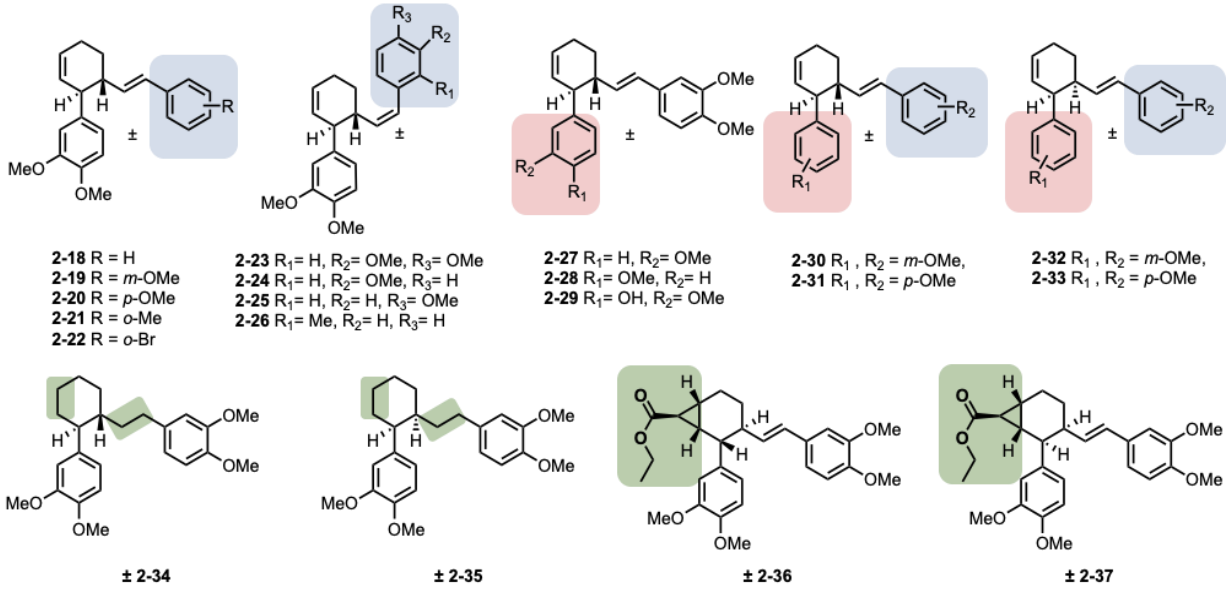

Figure 2-3. Banglene derivatives synthesized to investigate their neurotrophic activity. Derivatives are colour-coded corresponding to their structural change, red = ring A, blue = ring C, green = modifications of the alkenes

2.5.1 Synthesis of banglene derivatives with same substitution pattern on A and C rings

Banglenes have the same substitution pattern on both ring A and C *(meta* and *para* methoxy groups). The easiest way to access this pattern was through a Diels-Alder dimerization as shown in **scheme 2-3**. Other derivatives with same substitution patterns on A and C rings (**2-30–2-33**, **figure 2-3**) were also synthesized using this synthetic route (**scheme 2-6**) by changing the starting aldehyde.

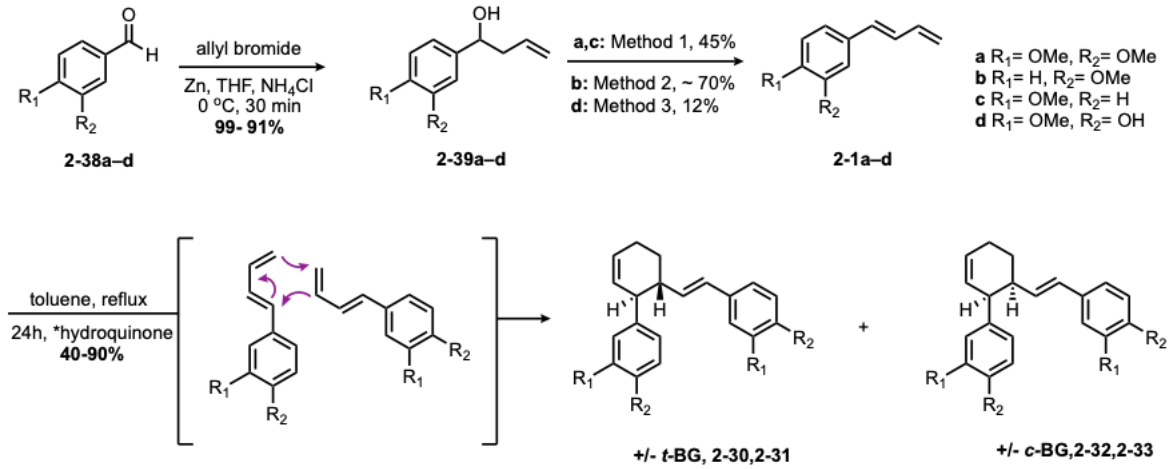

Method 1: $MeSO_2Cl$, DIPEA, toluene, reflux, 1h; Method 2: $POCl_3$, Pyridine, toluene, reflux, o/n; Method 3: p-TSA, toluene, reflux, 50 min
* cat. hydroquinone was added for the final synthesis of **28-31**

Scheme 2-6. Synthesis of racemic banglene derivatives with same substitution on A and C ring.

First, a zinc mediated nucleophilic allylation of the substituted benzylaldehydes **(2-38a–d)**, generated allyl alcohols **2-39a–d**. The alcohols **2-39a** and **c** were converted to diene **2-1a** and **c** through mesylation and base-promoted elimination. The conversion of **2-39b** to **2-1b** using method 1 was very low yielding and it was difficult to separate the diene from the alcohol. Therefore, method 2 was used to maximize the conversion to diene **2-1b** such that the crude mixture could be used in the next step without purification. **2-39d** was converted to **2-1d** through an acid-promoted elimination.

The dienes **2-1a–c** were then dimerized through a Diels-Alder cycloaddition to provide a 1:1 mixture of (±) ***t*-BG***:* (±) ***c*-BG** and derivatives **2-30–2-33**. Though a precedented reaction, it was surprising to note the lack of any endo/exo selectivity for this cyclization. However, this is consistent with a study in 2020 that found that in Diels-Alder reactions between 1,3 butadiene and mono-substituted alkenic dienophiles, the kinetic endo: exo ratios were close to 1:1.[14] (±) ***t*-BG** and (±) ***c*-BG** were separated by reverse phase HPLC on a C8 column. **2-30–2-33** were separated through reverse phase HPLC on a chiral amylose column.

Byrne and co-workers had used catalytic amounts of hydroquinone to drive the Diels-Alder dimerization of diene **2-1a**.[9] In my hands the dimerization of **2-1a** proceeded with similar conversions without the use of hydroquinone. Whereas, for the dimerization of **2-1b** and **c** the addition of 0.12 equiv. of hydroquinone was necessary.

2.5.2 Synthesis of banglene derivatives with different substitution pattern on A and C ring

There are two routes available to synthesize derivatives where ring A and C have different substitution pattern (**2-18–2-29**, **figure 2-3**), one is through a Wittig reaction as shown in **scheme 2-4**, which leads to racemic E diastereomers along with minor Z diastereomers. The second route is through an HWE reaction as shown in **scheme 2-5a**, through which I successfully synthesized enantioenriched (+) ***c*-BG**. I was unable to follow the same route and carry out the HWE reaction with the *trans* aldehyde to access (+) ***t*-BG** , although Lim and co-workers had some success with it.[11] For this reason, I synthesized derivatives through a Wittig reaction as shown in **scheme 2-7** which is adapted from Haeil Park's work.[10]

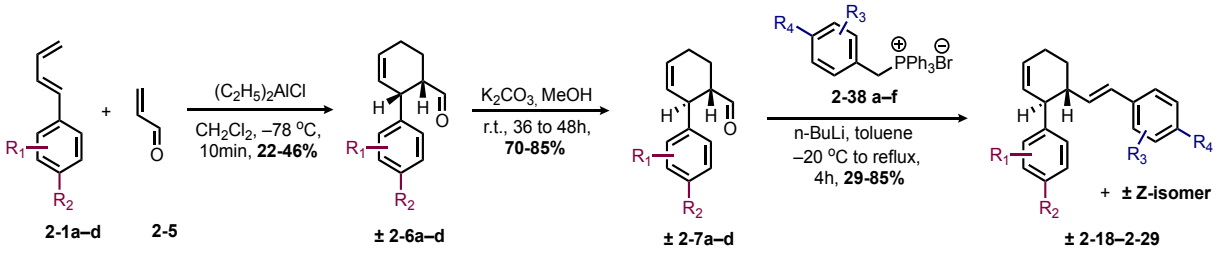

Scheme 2-7. Synthetic route to access derivatives with distinct A and C ring modifications using a Wittig olefination

Dienes **2-1a–d** were accessed from the corresponding aryl aldehydes as described in **scheme 2-6**. A Diels-Alder cycloaddition between **2-1a–d** and acrolein then generated the aldehyde scaffold for **2-6a–d** as the *cis* diastereomer. Epimerization of the *cis* aldehydes to the thermodynamically favored *trans* diastereomers **2-7a–d** was facilitated by potassium carbonate, and the final banglene derivatives were generated by a subsequent Wittig reaction with different triphenyl phosphonium salts **(2-38 a–f)**. Phosphonium salts were generated by converting the corresponding substituted benzyl alcohols to the benzyl bromides using phosphorous tribromide. The benzylic bromide intermediate was then reacted with triphenylphosphine to generate the triphenylphosphonium bromide salt used in the Wittig reaction. The enantiomers for derivatives **2-18–2-29** were separated by chiral chromatography.

2.5.3 Synthesis of alkene modified derivatives of banglene *

The synthesis of derivatives **2-34–2-35** was achieved through a palladium-catalysed hydrogenation of (±) ***c*-BG** and (±) ***t*-BG**. Further the cyclohexene ring was derivatized by generating compound **2-36–2-37** through a rhodium-catalysed cyclopropanation using an alpha-diazo ester.[15]

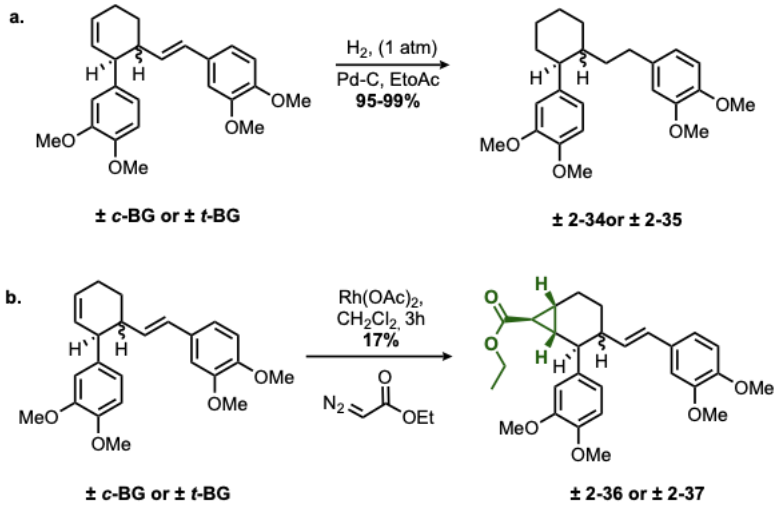

Scheme 2-8. Synthesis of derivatives through (a) Hydrogenation and (b) cyclopropanation

*Z.H.K synthesized 2-34 – 2-37

2.6 Summary

This chapter describes the efforts of the Matsui and Fukayama groups in investigating the neurotrophic effects of banglenes in various model systems, establishing the premise for its use as potential therapeutic agent. The chapter further describes our efforts building upon Matsui and Fukuyama's foundational work, three different synthetic routes are outlined that provided access to all stereoisomers of the banglenes as well as 20 derivatives designed to probe the structure-activity relationship of the banglene scaffold.

2.7 Experimental methods

2.7.1 General method information

All reactions were performed under a nitrogen atmosphere unless stated otherwise. Dichloromethane (CH_2Cl_2) and toluene were passed through a column of activated molecular sieves (4Å, LC technologies SP-1 solvent purification system). HPLC purification was performed using an Agilent 1260 preparatory system, using one of the following: a C8 Zorbax column (PrepHT, 21.2x150mm, 7 μm particle size), Lux® 5 μm i-Amylose-3 column (250 x 10 mm, 5 μm particle size) or Daicel CHIRALPAK AD-H (250 x 30 mm). Chiral HPLC analysis was performed using a normal-phase Agilent 1260 system, with UV detection using a standard diode-array- detector, and one of the following: a Daicel CHIRALPAK IG column (150 x 4.6 mm, 5 μm particle size), IC Daicel CHIRALPAK IC column (150 x 4.6 mm, 5 μm particle size), or a Daicel CHIRALPAK AD-H (250 x 4.6 mm).

NMR spectra were obtained from one of the following Varian spectrometers: DD2 MR 400MHz, VNMRS 500MHz, VNMRS 600MHz, VNMRS 700MHz. NMR spectra chemical shifts (δ) are reported in ppm and are referenced to residual protonated solvent (^{1}H) or deuterated solvent (^{13}C) chemical shifts. Coupling constants (J) are reported in Hertz (Hz). The following abbreviations are used: s = singlet, d = doublet, t = triplet, q = quartet, dd = doublet of doublets, dq = doublet of quartets, ddd = doublet of doublet of doublets, tdd = triplet of doublet of doublets, m = multiplet, app. = apparent, br. = broad. HSQC was used to determine ^{13}C NMR multiplicities, which are reported as follows: C = no attached

hydrogens, CH = one attached hydrogen, CH_2 = two attached hydrogens, CH_3 = three attached hydrogens.

HRMS were obtained from a Kratos Analytical MS50G EI-MS. FTIR were obtained using a Thermo Nicolet 8700 with an attached continuum microscope. Optical rotation data was obtained using a Perkin Elmer 241 Polarimeter at 589 nm at 25 °C, using a 10 cm path-length cell.

2.7.2 Synthesis of allyl alcohols

The corresponding aldehydes **2-38a–d** (30 mmol) were dissolved in tetrahydrofuran (25 mL). Allyl bromide (8 mL, 90 mmol) and saturated aqueous NH_4Cl solution (125 mL) were then added, and the reaction mixture was cooled to 0 °C. Zinc power (12 g, 180 mmol) was added, and the reaction mixture was stirred at 0 °C for 30 minutes. The precipitate was filtered, and the filtrate was extracted with ethyl acetate (25 mLx4). The organic layers were combined and washed with brine (25 mLx1), then dried over Na_2SO_4, filtered, and then concentrated in vacuo. The resulting product was used without further purification.

1-(3,4-Dimethoxyphenyl)but-3-en-1-ol (2-38a): White solid (91%). **^{1}H NMR** ($CDCl_3$, 400 MHz) δ: 6.94–6.83 (m, 3H), 5.85–5.76 (m,1H), 5.20–5.14 (m, 2H), 4.70 (td, J = 6.5 Hz, 3.0 Hz, 1H), 3.90 (s, 3H), 3.88 (s, 3H), 2.51 (t, J = 6.9 Hz, 2H), 1.96 (d, J = 3.0 Hz, 1H). **^{13}C NMR** ($CDCl_3$, 176 MHz) δ: 149.1, 148.2, 134.6, 118.4, 118.1, 111.0, 109.0, 73.3, 56.0, 55.9, 43.9. Characterization data is consistent with literature.[16]

1-(3-Methoxyphenyl)but-3-en-1-ol (2-38b): Yellow oil (99%). **^{1}H NMR** ($CDCl_3$, 400 MHz) δ: 7.29–7.25 (t, J = 8.0, 1H), 6.95–6.93 (m, 2H), 6.82 (ddd, J = 8.4 Hz, 2.6 Hz, 1.2 Hz, 1H), 5.87–5.77 (m, 1H), 5.20–5.14 (m, 1H), 4.73 (dd, J = 7.7 Hz, 4.2 Hz, 1H), 3.82 (s, 3H), 2.56–2.45 (m, 2H), 2.03 (s, 1H). **^{13}C NMR** ($CDCl_3$, 176 MHz) δ: 159.8, 145.7, 134.5, 129.5, 118.5, 118.2, 113.1, 111.4, 73.3, 55.3, 43.9. Characterization data is consistent with literature.[17]

1-(4-Methoxyphenyl)but-3-en-1-ol (2-38c): Yellow oil (99%). **^{1}H NMR** ($CDCl_3$, 700 MHz) δ: 7.29–7.28 (app. d, J = 8.3 Hz, 2H), 6.89–6.88 (app. d, J = 8.7 Hz, 2H), 5.83–5.77 (m, 1H), 5.17–5.12 (m, 2H), 4.70 (t, J = 6.5 Hz, 1H), 3.81 (s, 3H), 2.52–2.49 (app. t, J = 6.5

Hz, 2H), 1.94 (s, 1H). **^{13}C NMR** ($CDCl_3$, 176 MHz) δ: 159.0, 136.0, 134.6, 127.0, 118.2, 113.8, 72.9, 55.3, 43.7. Characterization data is consistent with literature.[17]

1-(3-hydroxy-4-methoxy)but-3-en-1-ol (2-38d): Colourless oil (99%). **^{1}H NMR** ($CDCl_3$, 600 MHz) δ: 6.93–6.82 (m, 3H), 5.84–5.78 (m, 1H), 5.58 (s, 1H), 5.19–5.13 (m, 2H), 4.69–4.66 (td, J = 4.8 Hz, 3.0 Hz, 1H), 3.91 (s, 3H), 2.51–2.49 (m, 2H), 1.99 (d, J = 3.0 Hz, 1H). **^{13}C NMR** ($CDCl_3$, 125 MHz) δ: 146.6, 145.1, 136.0, 134.6, 118.9, 118.3, 114.1, 108.3, 73.3, 55.9, 43.9. Characterization data is consistent with literature.[1] (this compound decomposes at room temperature).

2.7.3 Synthesis of dienes (2-39a,c)

In a flame dried RBF, the corresponding alcohol **2-39** (14 mmol) was dissolved in toluene (40 mL). N,N-diisopropylethylamine (72 mmol) and methanesulfonyl chloride (22 mmol) were slowly added and the reaction mixture was heated at reflux for 1 hour. The mixture was diluted with CH_2Cl_2 (45 mL), washed with sodium bicarbonate (15 mLx3), water (15 mLx3), and brine (15 mLx2). Then the organic layer dried over Na_2SO_4, filtered, and then concentrated in vacuo. The resultant oil was purified by column chromatography (silica; isocratic: 8% ethyl acetate/hexane).

4-((*E*)-Buta-1,3-dienyl)-1,2-dimethoxybenzene (2-39a): Yellow oil (45%). R_f = 0.1. **^{1}H NMR** ($CDCl_3$, 500 MHz) δ: 6.97–6.94 (m, 2H), 6.82 (d, *J* = 8.2 Hz, 1H), 6.67 (dd, *J* = 15.4 Hz, 10.6 Hz, 1H), 6.53–6.45 (m, 2H), 5.29 (d, *J* = 16.7 Hz, 1H), 5.13 (d, *J* = 10.0 Hz, 1H), 3.91 (s, 3H), 3.89 (s, 3H). **^{13}C NMR** ($CDCl_3$, 126 MHz) δ: 149.1, 148.9, 137.3, 132.7, 130.3, 128.0, 119.9, 116.7, 111.2, 108.7, 60.0, 55.9. Characterization data are consistent with literature.[18]

(*E*)-1-(buta-1,3-dien-1-yl)-4-methoxybenzene (2-39c): Yellow oil (45%). R_f = 0.3. **^{1}H NMR** ($CDCl_3$, 400 MHz) δ: 7.34 (d, *J* = 8.7 Hz, 2H), 6.86 (d, *J* = 8.8 Hz, 2H), 6.67 (dd, *J* = 15.6 Hz, 10.5 Hz, 1H), 6.53–6.45 (m, 2H), 5.28 (d, *J* = 16.9 Hz, 1H), 5.11 (d, *J* = 10.1 Hz, 1H), 3.81 (s, 3H). **^{13}C NMR** ($CDCl_3$, 176 MHz) δ: 159.3, 137.4, 132.4, 129.9, 127.6, 116.4, 114.1, 55.3. Characterization data are consistent with literature.[19]

2.7.4 Synthesis of 2-3b: (E)-1-(buta-1,3-dien-1-yl)-3-methoxybenzene

In a flame dried RBF, 1-(3 methoxy)-but-3-en-1-ol (**2-39b**, 170 mg, 1.0 mmol) was dissolved in 4 mL toluene, followed by the addition of 3Å molecular sieves. Pyridine (0.6 mL, 7.0 mmol) and phosphoryl chloride (0.16 mL, 2.10 mmol) were slowly added, and the reaction mixture was heated at reflux overnight. The reaction mixture was diluted with CH_2Cl_2 (15 mL), washed with 0.01 M HCl (5 mLx2), $NaHCO_3$ (sat. aq.) (5 mLx1), water (5 mLx2), and brine (10 mLx1). The organic layer was dried over Na_2SO_4, filtered, and then concentrated in vacuo. The resultant oil was purified with column chromatography (silica; isocratic: 15% ethyl acetate/hexane, $R_f = 0.3$) to remove residual starting alcohol, and the yellow oil (107 mg, 70% 3b) was then carried forward to synthesise **2-30** and **2-32**.

2.7.5 Synthesis of 2-3d: (E)-4-(Buta-1, 3-dienyl)-2-methoxyphenol

In a flame dried RBF, alcohol **39d** (4.50 mmol) was dissolved in toluene (40.0 mL), followed by the addition of p-toluenesulphonic acid (0.09 mmol). The reaction mixture was then heated at reflux for 50 mins. The reaction solution was washed with aq. sat. sodium bicarbonate (10 mLx2), brine (10 mL) and then the organic layer was dried over Na_2SO_4, filtered, and concentrated in vacuo. The resulting residue was purified by column chromatography (silica; 5-10 % ethyl acetate/hexane, $R_f = 0.4$ in 10% ethyl acetate/hexane).

Low melting white solid (12%). **^{1}H NMR** ($CDCl_3$, 400 MHz,): 6.94–6.88 (m, 3H), 6.70–6.64 (m, 1H), 6.55–6.46 (m, 2H), 5.77 (s, 1H), 5.31 (dd, J = 17.6 Hz, 1.6 Hz, 1H), 5.14 (dd, J = 10.0 Hz, 2.0 Hz, 1H), 3.90 (s, 3H). **^{13}C NMR** ($CDCl_3$, 125 MHz) δ: 146.8, 145.7, 137.4, 132.9, 129.9, 127.6, 120.5, 116.5, 114.7, 108.4, 55.9. Characterization data are consistent with literature.[10]

2.7.6 Synthesis of banglenes (c-BG, t-BG) and banglene derivatives 2-30–2-33

In a flame dried RBF, the corresponding diene (0.62 mmol) was dissolved in toluene (2 mL). Hydroquinone (0.12 mmol) was added only for synthesis of **(2-30–2-33**), and the reaction was allowed to stir at reflux, for 18 hours. Toluene was removed in vacuo, and the resulting residue was purified by column chromatography (silica). The *cis/ trans* diastereomers were then separated by preparative HPLC.

product	silica column conditions	product mass (% yield)	HPLC separation conditions	HPLC injection	isolated components		
						amount	R_t (min)
***c*–BG** ***t*-BG**	20% EtOAc/hex R_f= 0.3	390 mg (40%)	C8 column. 50→100% ACN/H_2O (20 min)	350 mg	***t*–BG** ***c*-BG**	164 mg 166 mg	10.8 11.3
2-30 **2-32**	20% EtOAc/hex R_f= 0.4	90 mg (90%)	i-amylose-3 column. 97% hex/EtOH (15 min)	70 mg	**2-30** **2-32**	10 mg 5 mg	9.4 8.6
2-31 **2-33**	5% EtOAc/hex R_f= 0.2	47 mg (47%)	i-amylose-3 column. 97% hex/EtOH (15 min)	40 mg	**(-) 2-31** **(+) 2-33**	5 mg 4 mg	14.5 11.3

(±) **3(*S/R*)-(3,4-Dimethoxyphenyl)-4(*S/R*)-[(*E*)-3,4-dimethoxystyryl]cyclohex-1-ene (*c*–BG):** Colourless oil. **^{1}H NMR** ($CDCl_3$, 700MHz) δ : 6.79 (d, *J* = 8.2 Hz, 1H), 6.75–6.72 (m, 4H), 6.69 (d, *J* = 1.9 Hz, 1H), 6.24 (d, *J* = 15.8 Hz, 1H), 5.97 (tdd, *J* = 2.3 Hz, 4.4 Hz, 10.0 Hz, 1H), 5.79 (tdd, *J* = 2.3 Hz, 4.4 Hz, 10 Hz, 1H), 5.58 (dd, *J* = 9.2 Hz, 15.8 Hz), 3.85 (s, 3H), 3.84 (s, 3H), 3.82 (s, 3H), 3.74 (s, 3H), 3.50 (br. s, 1H), 2.70 (dddd, *J* = 3.1 Hz, 5.5 Hz, 9.1 Hz, 10.9 Hz, 1H), 2.27–2.16 (m, 2H), 1.68–1.59 (m, 2H). **^{13}C NMR** ($CDCl_3$, 176 MHz) δ: 149.0, 148.3, 148.2, 147.6, 133.9, 132.5, 131.1, 129.2, 128.6, 128.1, 122.0, 118.8, 113.7, 111.2, 110.4, 108.8, 56.0, 55.9, 55.8, 45.8, 42.7, 24.9, 24.4. Characterization data are consistent with literature.[11]

(±) **3(*S/R*)-(3,4-Dimethoxyphenyl)-4(*R/S*)-[(*E*)-3,4-dimethoxystyryl]cyclohex-1-ene (*t*–BG):** Yellow oil. **^{1}H NMR** ($CDCl_3$, 700MHz) δ: 6.82 (d, *J* = 1.8 Hz, 1H), 6.8 (dd, *J* = 1.9 Hz, 8.3 Hz, 1H), 6.77 (t, *J* = 7.8 Hz, 2H), 6.72 (dd, *J* = 1.9 Hz, 8.2 Hz, 1H), 6.7 (d, *J* = 1.9 Hz, 1H), 6.09 (d, *J* = 15.9 Hz, 1H), 6.02 (dd, *J* = 7.6 Hz, 15.9 Hz), 5.90 (tdd, *J* = 2.5 Hz, 4.3 Hz, 10.0 Hz, 1H), 5.68 (dq, *J* = 10.2 Hz, 2.2 Hz, 1H), 3.87 (s, 3H), 3.86 (s, 3H), 3.85 (s, 3H),

3.82 (s, 3H), 3.18 (dq, J = 8.6 Hz, 2.8 Hz), 2.36 (dq, J = 9.0 Hz, 2.8 Hz 1H), 2.24–2.20 (m, 2H), 1.92 (dq, J = 13.3 Hz, 4.1 Hz), 1.70–1.65 (m, 1H). **^{13}C NMR** ($CDCl_3$, 176 MHz) δ: 149.0, 148.6, 148.3, 147.4, 137.6, 132.2, 131.0, 130.3, 128.9, 127.6, 120.5, 118.8, 111.7, 111.2, 110.9, 108.8, 55.98, 55.92, 55.89, 55.88 48.1, 45.5, 27.9, 24.2. Characterization data are consistent with literature.[11]

(±) **3(*S/R*)-(3-methoxyphenyl)-4(*R/S*)-[(*E*)-3-methoxystyryl]cyclohex-1-ene (2-30):** Yellow oil. **^{1}H NMR** ($CDCl_3$, 600MHz) δ: 7.18 (q, J = 7.7 Hz, 2H), 6.86 (d, J = 7.7 Hz, 1H), 6.80–6.78 (m, 2H), 6.74–6.72 (m, 3H), 6.17–6.16 (m, 2H), 5.90 (tdd, J = 2.4 Hz, 4.4 Hz, 10 Hz, 1H), 5.70 (dq, J = 10.0 Hz, 2.2 Hz, 1H), 3.79 (s, 3H), 3.77 (s, 3H), 3.23 (dq, J = 11.0 Hz, 2.7 Hz, 1H), 2.45–2.41 (1.0 Hz, 2H), 2.26–2.19 (m, 2H), 1.92 (tdd, J = 3.2 Hz, 5.2 Hz, 12.6 Hz, 1H), 1.70–1.64 (m, 1H). **^{13}C NMR** ($CDCl_3$, 176 MHz) δ: 159.8 (C), 159.6 (C), 146.6 (C), 139.4 (C), 134.4 (CH), 129.9 (CH), 129.4 (CH), 129.2 (CH), 129.1 (CH), 127.6 (CH), 121.1 (CH), 118.7 (CH), 114.2 (CH), 112.4 (CH), 111.5 (CH), 111.5 (CH), 55.2 (CH_3), 55.2 (CH_3), 48.4 (CH), 45.2 (CH), 27.8 (CH_2), 24.5 (CH_2). **HRMS** (EI, $C_{22}H_{24}O_2$, M^+): calcd.: 320.1776, found: 320.1782. **FTIR** (cast film): 3021, 2928, 2834, 1599, 1488, 1264, 1156, 1050, 777 cm^{-1}.

(–) **3(*R*)-(4-methoxyphenyl)-4(*S*)-[(*E*)-4-methoxystyryl]cyclohex-1-ene (2-31):** Yellow oil. $[\alpha]^{25}_D$ –237 (c = 0.7, CH_2Cl_2). **^{1}H NMR** ($CDCl_3$, 700MHz) δ: 7.19 (d, J = 8.7 Hz, 2H), 7.10 (d, J = 8.6 Hz, 2H), 6.82–6.80 (m, 4H), 6.11 (d, J = 15.9 Hz, 2H), 6.02 (dd, J = 7.6 Hz, 15.9 Hz, 1H), 5.88 (tdd, J = 2.5 Hz, 4.2 Hz, 10.0 Hz, 1H), 5.65 (dq, J = 9.8 Hz, 2.2 Hz, 1H), 3.78 (s, 3H), 3.78 (s, 3H), 3.18 (dq, J = 11.0 Hz, 2.7 Hz 1H), 2.35 (dq, J = 2.7 Hz, 8.9 Hz, 1H), 2.23–2.18 (m, 2H), 1.91 (dq, J = 12.5 Hz, 4.2 Hz, 1H), 1.68–1.63 (m, 1H). **^{13}C NMR** ($CDCl_3$, 176 MHz) δ: 158.7 (C), 158.0 (C), 137.2 (C), 132.1 (C), 130.8 (CH), 130.5 (CH), 129.4 (CH), 128.5 (CH), 127.4 (CH), 127.1 (CH), 113.9 (CH), 113.6 (CH), 55.3 (CH_3), 55.3 (CH_3), 47.7 (CH), 45.5 (CH), 27.9 (CH_2), 24.6 (CH_2). **FTIR** (cast film): 3020, 2927, 2835, 1609, 1511, 1249, 1175, 1037 cm^{-1}. **HRMS** (EI, $C_{22}H_{24}O_2$, M^+): calcd.: 320.1776, found: 320.1774. **FTIR** (cast film): 3018, 2929, 2835, 1609, 1511, 1249, 1176, 1037 cm^{-1}.

(±) **3(*S/R*)-(3-methoxyphenyl)-4(*S/R*)-[(*E*)-3-methoxystyryl]cyclohex-1-ene (2-32):** Colourless oil. **^{1}H NMR** ($CDCl_3$, 700MHz) δ: 7.20–7.17 (m, 1H), 7.15 (t, J = 7.9 Hz, 1H),

6.79 (dd, *J* = 7.5 Hz, 13.2 Hz, 2H), 6.67–6.75 (m, 2H), 6.73–6.71 (m, 2H), 6.27 (d, *J* = 15.8 Hz, 1H), 5.98 (tdd, *J* = 2.4 Hz, 3.4 Hz, 10.1 Hz, 1H), 5.82–5.76 (m, 2H), 3.77 (s, 3H), 3.74 (s, 3H), 3.57 (br. s, 1H), 2.76 (dddd, *J* = 3.1 Hz, 5.6 Hz, 9.1 Hz, 10.4 Hz, 1H), 2.28–2.17 (m, 2H), 1.74–1.64 (m, 2H). **^{13}C NMR** ($CDCl_3$, 176 MHz) δ 159.7 (C), 159.2 (C), 143.1 (C), 139.5 (C), 134.3 (CH), 129.4 (CH), 129.0 (CH), 128.9 (CH), 128.5 (CH), 128.2 (CH), 122.6 (CH), 118.8 (CH), 115.8 (CH), 112.5 (CH), 111.7 (CH), 111.4 (CH), 55.2 (CH_3), 46.0 (CH), 42.5 (CH), 24.6 (CH_2), 24.6 (CH_2). **HRMS** (EI, $C_{22}H_{24}O_2$, M^+): calcd.: 320.1776, found: 320.1775. **FTIR** (cast film): 3021, 2926, 2835, 1599, 1486, 1264, 1155, 1049, 776 cm^{-1}.

(+) **3(*S*)-(4-methoxyphenyl)-4(*R*)-[(*E*)-4-methoxystyryl]cyclohex-1-ene (2-33):** Colorless oil. $[\alpha]^{25}_D$ (+)212 (*c* = 0.6, CH_2Cl_2). **^{1}H NMR** ($CDCl_3$, 700MHz) δ: 7.14 (d, *J* = 8.6 Hz, 1H), 7.10 (d, *J* = 8.6 Hz, 1H), 6.82 (d, *J* = 8.7 Hz, 2H), 6.79 (d, *J* = 8.8 Hz, 2H), 6.25 (d, *J* = 15.9 Hz, 1H), 5.95 (tdd, *J* = 2.4 Hz, 3.8 Hz, 10.0 Hz, 1H), 5.8 (tdd, *J* = 2.2 Hz, 4.5 Hz, 10.0 Hz, 1H), 5.60 (dd, *J* = 9.1 Hz, 15.9 Hz, 1H), 3.79 (s, 3H), 3.78 (s, 3H), 3.52 (br. s, 1H), 2.70 (dddd, *J* = 3.3 Hz, 5.5 Hz, 9.0 Hz, 10.5 Hz, 1H), 2.27–2.14 (m, 2H), 1.68–1.58 (m, 2H). **^{13}C NMR** ($CDCl_3$, 176 MHz) δ: 158.7 (C), 158.1 (C), 133.4 (C), 132.1 (C), 131.0 (CH), 130.9 (CH), 129.4 (CH), 128.4 (CH), 127.9 (CH), 127.1 (CH), 113.9 (CH), 113.1 (CH), 55.3 (CH_3), 55.3 (CH_3), 43.3 (CH), 42.8 (CH), 24.8 (CH_2), 24.4 (CH_2). **HRMS** (EI, $C_{22}H_{24}O_2$, M^+): calcd.: 320.1776, found: 320.1775. **FTIR** (cast film): 3018, 2929, 2835, 1609, 1511, 1249, 1176, 1037 cm^{-1}.

2.7.7 Synthesis of *cis*-aldehydes (2-6a-d)

In a flame dried RBF, the corresponding diene (4 mmol) was dissolved in CH_2Cl_2 (12 mL) and cooled to –78 °C. Acrolein (6 mmol) was added, followed by the dropwise addition of Et_2AlCl (3.8 mmol). The reaction mixture was stirred at –78 °C for 10 minutes and then warmed to 0 °C. The reaction was quenched with 1N HCl (15 mL) and extracted with CH_2Cl_2 (20 mLx2). The combined organic layers were washed with $NaHCO_3$(sat. aq.) (15 mLx2), then brine(10mLx1), dried over Na_2SO_4, filtered, and then concentrated in vacuo. The crude residue was purified with column chromatography (silica; isocratic: 20 % ethyl acetate/hexane).

(±) (1*S*, 2*R*)-2-(3,4-Dimethoxyphenyl)cyclohex-3-ene-1-carboxyaldehyde (2-6a): White semi-solid (46%). R_f = 0.36. **^{1}H NMR** ($CDCl_3$, 600 MHz) δ: 9.50 (d, *J* = 2.1 Hz, 1H), 6.80 (d, *J* = 8.2 Hz, 1H), 6.76 (dd, *J* = 8.2 Hz, 2.1 Hz, 1H), 6.72 (d, *J* = 1.9 Hz, 1H), 5.99–5.97 (m, 1H), 5.83–5.80 (m, 1H), 3.93–3.91 (m,1H), 3.85 (s, 6H), 2.76–2.72 (m, 1H), 2.32–2.26 (m, 1H), 2.19–2.12 (m, 1H), 1.88–1.85 (m, 2H). **^{13}C NMR** ($CDCl_3$, 126 MHz) δ: 205.0, 148.8, 148.1, 132.6, 128.5, 128.1, 121.4, 112.6, 111.1, 55.9, 50.9, 41.2, 23.7, 18.9. Characterization data are consistent with literature.[11]

(±) (1*S*, 2*R*)-2-(3-Dimethoxyphenyl)cyclohex-3-ene-1-carboxyaldehyde (2-6b): Yellow oil (22%), R_f = 0.6. **^{1}H NMR** ($CDCl_3$, 500MHz) δ: 9.51 (d, *J* = 2.1 Hz, 1H), 7.23–7.20 (m, 1H), 6.81 (d, *J* = 7.7 Hz, 1H), 6.77–6.76 (m, 2H), 6.00–5.97 (m, 1H), 5.84–5.81 (m,1H), 3.95–3.94 (m, 1H), 3.79 (s, 3H), 2.77–2.74 (m, 1H), 2.30–2.26 (m, 1H), 2.18–2.12 (m, 1H), 1.92–1.85 (m, 2H). **^{13}C NMR** ($CDCl_3$, 126MHz) δ: 204.7 (CH), 159.7 (C) ,141.8 (C), 129.4 (CH), 128.8 (CH), 127.8 (CH), 121.7 (CH), 115.5 (CH), 112.0 (CH), 55.2 (CH_3), 50.7 (CH), 41.5 (CH), 23.6 (CH_2), 19.0 (CH_2). HRMS (EI, $C_{14}H_{16}O_2$, M^+): calcd.: 216.1150, found: 216.1148.

(±) **(1*S*, 2*R*)-2-(4-Dimethoxyphenyl)cyclohex-3-ene-1-carboxyaldehyde (2-6c):** Yellow oil (44%). R_f = 0.3. **^{1}H NMR** ($CDCl_3$, 700MHz) δ: 9.51 (d, *J* = 1.9 Hz, 1H), 7.13 (d, *J* = 8.6 Hz, 2H), 6.83 (d, *J* = 8.7 Hz, 2H), 5.98–5.96 (m, 1H), 5.80 (m, 1H), 3.95–3.92 (m, 1H), 3.78 (s, 3H), 2.75–2.72 (m, 1H), 2.31–2.25 (m, 1H), 2.18–2.11 (m,1H), 1.89–1.80 (m, 2H). **^{13}C NMR** ($CDCl_3$, 126MHz) δ: 158.7, 132.1, 130.3, 128.4, 128.2, 113.8, 112.9, 55.3, 51.0, 40.8, 23.7, 18.6. HRMS (EI, $C_{14}H_{16}O_2$, M^+): calcd.: 216.1150, found: 216.1153.

(±) **(1*S*, 2*R*)-2-(4-hydroxy-3-methoxyphenyl)-cyclohex-3-ene-1-carboxaldehyde (2-6d):** Yellow oil (30%). **^{1}H NMR** ($CDCl_3$, 400 MHz) δ: 9.49 (d, *J* = 2 Hz, 1H), 6.82 (d, *J* = 8.4 Hz, 1H), 6.72–6.68 (m, 2H), 5.98–5.93 (m, 1H), 5.81–5.77 (m, 1H), 5.65 (br. s, 1H), 3.91–3.87 (m, 1H), 3.83 (s, 3H), 2.74–2.69 (m, 1H), 2.30–2.24 (m, 1H), 2.17–2.12 (m, 1H), 1.87–1.81 (m, 2H). **^{13}C NMR** ($CDCl_3$, 125 MHz) δ: 205.2, 146.5, 144.7, 131.9, 128.5, 128.2, 122.1, 114.4, 111.9, 55.9, 50.9, 41.2, 23.6, 18.8. Characterization data are consistent with literature.[10]

2.7.8 Epimerization of *cis*-aldehydes to *trans*-aldehydes (2-7a-c)

The corresponding *cis*-aldehyde **2-5** (1.4 mmol) was dissolved in methanol (15 mL), followed by the addition of K_2CO_3 (1.6 mmol). The reaction solution was stirred at room temperature for 48 hours. The reaction mixture was diluted with CH_2Cl_2 (20 mL) and washed with water (10 mL) and brine (10 mL). The organic layer was dried over Na_2SO_4 and concentrated in vacuo.

(±) **(1*R*, 2*R*)-2-(3,4-Dimethoxyphenyl)cyclohex-3-ene-1-carboxyaldehyde (2-7a)**: Yellow oil (85%, 87:13 **7a:6a**). **^{1}H NMR** ($CDCl_3$, 500 MHz) δ: 9.69 (d, *J* = 1.5 Hz, 1H), 6.81–6.72 (m, 3H), 5.92 (dq, *J* = 10.0 Hz, 3.3 Hz, 1H), 5.70 (dq, *J* = 2.5 Hz, 10.0 Hz, 1H), 3.86 (d, *J* = 5.6 Hz, 6H), 3.76–3.72 (m, 1H), 2.60 (dddd, *J* = 1.6 Hz, 3.5 Hz, 7.6 Hz, 9.4 Hz, 1H), 2.23–2.18 (m, 2H), 2.01–1.95 (m, 1H), 1.81–1.74 (m, 1H). **^{13}C NMR** ($CDCl_3$, 126 MHz) δ: 205.0, 148.8, 148.1, 132.6, 128.5, 128.1, 121.4, 112.6, 111.1, 55.9, 50.9, 41.2, 23.7, 18.9. Characterization data are consistent with literature.[11]

(±) **(1*R*, 2*R*)-2-(3-Dimethoxyphenyl)cyclohex-3-ene-1-carboxyaldehyde (2-7b):** Yellow oil (71%, 90:10 **7b:6b**). **^{1}H NMR** ($CDCl_3$, 500MHz) δ: 9.70 (d, *J* = 1.3 Hz, 1H), 7.23 (t, *J* = 7.8 Hz, 1H), 6.83 (d, *J* = 7.7 Hz, 1H), 6.79–6.75 (m, 2H), 5.90 (dq, *J* = 9.5Hz, 3.3 Hz, 1H), 5.68 (dq, *J* = 10.0 Hz, 2.4 Hz, 1H), 3.80 (s, 3H), 3.77–3.73 (m, 1H), 2.61 (ddt, *J* = 1.3 Hz, 3.5 Hz, 8.5 Hz, 1H), 2.20–2.15 (m, 2H), 2.0–1.93 (m, 1H), 1.80–1.72 (m,1H). **^{13}C NMR** ($CDCl_3$, 126MHz) δ: 203.8 (CH), 159.8 (C), 145.3 (C), 129.6 (CH), 128.7 (CH), 127.8 (CH), 120.7 (CH), 114.2 (CH), 111.9 (CH), 55.3 (CH_3), 53.9 (CH), 41.4 (CH), 23.5 (CH_2), 20.9 (CH_2). **HRMS** (EI, $C_{14}H_{16}O_2$, M^+): calcd.: 216.1150, found: 216.1150.

(±) **(1*R*, 2*R*)-2-(4-Dimethoxyphenyl)cyclohex-3-ene-1-carboxyaldehyde (2-7c):** Yellow oil (87%, 90:10 **7c:6c**). **^{1}H NMR** ($CDCl_3$, 500MHz) δ: 9.69 (d, *J* = 1.2 Hz, 1H), 7.15 (d, *J* = 8.5 Hz, 2H), 6.85 (d, *J* = 8.6 Hz, 2H), 5.88 (dq, *J* = 9.5 Hz, 3.3 Hz, 1H), 5.66 (dq, *J* = 9.5 Hz, 2.4 Hz, 1H), 3.79 (s, 3H), 3.74–3.70 (m, 1H), 2.56 (ddt, *J* = 1.5 Hz, 4.3 Hz, 8.5 Hz, 1H), 2.21–2.15 (m, 2H), 1.95 (dq, 1H, *J* = 13.5 Hz, 4.3 Hz), 1.78-1.71 (m,1H). **^{13}C NMR** ($CDCl_3$, 126MHz) δ: 204.0 (CH), 158.4 (C) ,135.6 (C), 129.3 (CH_2), 129.2 (CH_2), 127.5 (CH), 114.0 (CH), 55.3 (CH_3), 54.2 (CH), 40.7 (CH_2), 23.5 (CH_2), 21.0 (CH_2). **HRMS** (EI, $C_{14}H_{16}O_2$, M^+): calcd.: 216.1150, found: 216.1148.

2.7.9 Synthesis of Wittig Salts (2-38a-f)

In a flame dried RBF, the corresponding substituted benzyl bromide (5.4 mmol) was dissolved in toluene (20 mL), followed by addition of triphenylphosphine (5.4 mmol). The reaction solution was then heated at reflux overnight. The organic layer was concentrated in vacuo to afford a crude white solid which was then purified by recrystallization in ethanol (**2-38a**), or ethanol/diethyl ether (**2-38b-f**).

3,4-Methoxybenzyltriphenylphosphonium bromide (2-38a): White powder (61%). **^{1}H NMR** ($CDCl_3$, 400MHz) δ: 7.78–7.74 (m, 9H), 7.65–7.62 (m, 6H), 6.86 (s, 1H), 6.62–6.61 (m, 2H), 5.37 (d, *J* = 13.8 Hz, 2H), 3.80 (s, 3H), 3.55 (s, 3H). **^{13}C NMR** ($CDCl_3$, 126MHz) δ: 148.9, 148.8, 134.8 (d, *J* = 3.1 Hz), 134.6 (d, *J* = 9.5 Hz), 130.0 (d, *J* = 12.6 Hz), 123.7 (d, *J* = 6.2 Hz), 119.0 (d, *J* = 9.0 Hz), 118.3, 117.8, 115.0, (d, *J* = 4.8 Hz), 111.0 (d, *J* = 3.4 Hz), 56.1, 55.80, 30.5, 30.2. **^{31}P{^{1}H} NMR** ($CDCl_3$, 201.64 MHz) δ: 22.5 (s). Characterization data is consistent with literature.[20]

Benzyltriphenylphosphonium bromide (2-38b): White powder (76%). **^{1}H NMR** ($CDCl_3$, 400MHz) δ: 7.78–7.72 (m, 9H), 7.65–7.60 (td, *J* = 7.8 Hz, 3.6 Hz, 6H), 7.23–7.19 (m, 1H), 7.14–7.09 (m, 4H), 5.43 (d, *J* = 14.4 Hz, 2H). **^{13}C NMR** ($CDCl_3$, 176 MHz) δ: 135.0 (d, *J* = 3.1 Hz), 134.5 (d, *J* = 9.8 Hz), 131.6 (d, *J* = 5.6 Hz), 130.2 (d, *J* = 12.3 Hz), 128.9 (d, *J* = 3.4 Hz), 128.4 (d, *J* = 3.9 Hz), 127.2 (d, *J* = 8.7 Hz), 118.0 (d, *J* = 85.6 Hz), 31.0 (d, *J* = 46.6 Hz). **^{31}P{^{1} H}** NMR ($CDCl_3$, 162 MHz) δ: 23.2 (s). Characterization data is consistent with literature.[21]

3-Methoxybenzyltriphenylphosphonium bromide (2-38c): White powder (65%). **^{1}H NMR** ($CDCl_3$, 400MHz) δ: 7.78–7.73 (m, 9H), 7.63 (td, *J* = 7.7 Hz, 3.4 Hz, 6H), 7.02 (t, *J* = 8.0 Hz, 1H), 6.82 (q, *J* = 1.8 Hz, 1H), 6.76 (dt, *J* = 8.2 Hz, 2.1 Hz, 1H), 6.63 (d, *J* = 7.5, 1H), 5.40 (d, *J* = 14.4 Hz, 2H), 3.55 (s, 3H). **^{13}C NMR** ($CDCl_3$, 176 MHz) δ: 159.7, 135.0 (d, *J* = 3.1 Hz), 134.6 (d, *J* = 9.8 Hz), 130.1 (d, *J* = 12.6 Hz), 129.7 (d, *J* = 3.1 Hz), 123. 5 (d, *J* = 5.9 Hz), 118.2, 117.7, 116.3 (d, *J* = 5.3 Hz), 115.4 (d, *J* = 3.9 Hz), 55.5, 31.9 (d, *J* = 46.8 Hz). **^{31}P{^{1}H}** NMR ($CDCl_3$, 161.913 MHz) δ: 23.23 (s). Characterization data is consistent with literature.[22]

4-Methoxybenzyltriphenylphosphonium bromide (2-38d): White powder (65%). **^{1}H NMR** ($CDCl_3$, 400MHz) δ: 7.77–7.71 (m, 9H), 7.64–7.61 (m, 6H), 7.03 (dd, *J* = 2.5 Hz, 8.8 Hz, 2H), 6.65 (d, *J* = 8.6 Hz, 2H), 5.35 (dd, *J* = 3.2 Hz, 14.0 Hz, 2H), 3.72 (s, 3H). **^{13}C NMR** ($CDCl_3$, 176 MHz) δ: 159.7, 134.9 (d, *J* = 3.1 Hz), 134.5 (d, *J* = 9.5 Hz), 132.8 (d, *J* = 5.3 Hz), 130.2 (d, *J* = 12.6 Hz), 118.3, 117.8, 114.3 (d, *J* = 3.1 Hz), 55.3, 30.2 (d, *J* = 46.6 Hz). **^{31}P{^{1}H}** NMR ($CDCl_3$, 161.913 MHz) δ: 22.4 (s). Characterization data is consistent with literature.[23]

2-Methylbenzyltriphenylphosphonium bromide (2-38e): White powder (71%). **^{1}H NMR** ($CDCl_3$, 400MHz) δ: 7.81–7.76 (m, 3H), 7.72–7.61 (m, 12H), 7.15 (t, *J* = 7.3 Hz, 1H), 7.09 (d, *J* = 7.2 Hz, 1H), 7.0–6.96 (m, 2H), 5.37 (d, *J* = 14.1 Hz, 2H), 1.68 (s, 3H). **^{13}C NMR** ($CDCl_3$, 176 MHz) δ: 138.6, 135.1 (d, *J* = 2.8 Hz), 134.4 (d, *J* = 9.8 Hz), 131.6, 131.0, 130.22 (d, *J* = 12.6 Hz), 128.8, 126.7, 125.7, 122.0, 118.2, 117.8, 28.5 (d, *J* = 46.6 Hz). **^{31}P{^{1}H}** NMR (CDCl3, 161.913 MHz) δ: 22.2 (s). Characterization data is consistent with literature.[24]

2-Bromobenzyltriphenylphosphonium bromide (2-38f): White powder (87%). **^{1}H NMR** ($CDCl_3$, 400MHz) δ: 7.81–7.77 (m, 3H), 7.75–7.70 (m, 6H), 7.66–7.59 (m, 7H), 7.37 (d, *J* = 7.9 Hz, 1H), 7.20 (t, *J* = 7.5 Hz, 1H), 7.13 (tt, *J* = 7.7 Hz, 2.0 Hz, 1H), 5.75 (d, *J* = 14.3 Hz, 2H). **^{13}C NMR** ($CDCl_3$, 126 MHz) δ: 135.2 (d, *J* = 2.8 Hz), 134.5 (d, *J* = 9.8 Hz), 133.5 (d, *J* = 4.9 Hz), 132.9, 130.2 (d, *J* = 12.6 Hz), 128.5 (d, *J* = 3.6 Hz), 118.0, 117.3, 31.1 (d, *J* = 48.2 Hz). Characterization data is consistent with literature.[25]

2.7.10 Synthesis of banglenes and derivatives (2-18–2-29) via a Wittig reaction

In a flame dried RBF, the corresponding Wittig salt **2-7** (0.6 mmol) was dissolved in toluene (5 mL) and tetrahydrofuran (5 mL) and cooled to –70 °C. n-Butyl lithium (0.73 mmol) was added slowly, and the reaction mixture was allowed to stir at –70 °C for 1 hour. The reaction solution was then warmed up to –20° C, the corresponding aldehyde (**2-6**) was added, and the reaction was then heated at reflux for 3 hours. The reaction mixture was quenched with saturated aqueous NH_4Cl (5 mL), and then concentrated in vacuo. The crude oil was dissolved in ethyl acetate (30 mL), washed with water (10 mLx2), and $NaHCO_3$ (sat.

aq.) (10 mLx2), was dried over Na_2SO_4 and then concentrated in vacuo. The resulting oil was purified with column chromatography.

(±) **3(*S/R*)-(3,4-dimethoxyphenyl)-4(*R/S*)-[(*E*)-styryl]cyclohex-1-ene (2-18):**

product	silica column conditions	product mass (% yield)	separation method	HPLC injection	isolated components			ee
						amount	R_t (min)	
2-18E **2-18Z**	20% EtOAc/hex R_f = 0.4	93 mg (48%)	i-amylose-3 column. 97% hex/EtOH (15 min)	80 mg	(+) **2-18E**	10 mg	5.8	99%
					(–) **2-18E**	19 mg	8.0	>99%
					(+) **2-18Z**	*not isolated*	5.5	-
					(–) **2-18Z**		7.2	-

^{1}H NMR ($CDCl_3$, 500MHz) δ: 7.26–7.25 (m, 4H, *overlaps with CDCl₃*), 7.16 (m, 1H), 6.78 (d, *J* = 8.2 Hz, 1H), 6.72 (dd, *J* = 2.0 Hz, 8.1 Hz, 1H), 6.70 (d, *J* = 1.9 Hz, 1H), 6.16 (d, *J* = 3.3 Hz, 2H), 5.90 (tdd, *J* = 2.4 Hz, 4.1 Hz, 10.0 Hz, 1H), 5.68 (dq, *J* = 10.0 Hz, 2.2 Hz, 1H), 3.85 (s, 3H), 3.82 (s, 3H), 3.78 (s, 3H), 3.19 (dq, *J* = 11.2 Hz, 2.7 Hz, 1H), 2.41–2.35 (m, 1H), 2.27–2.17 (m, 2H), 1.95–1.91 (m, 1H), 1.72–1.64 (m, 1H). **^{13}C NMR** ($CDCl_3$, 126 MHz) δ: 148.6 (C), 147.4 (C), 137.8 (C), 137.5 (C), 134.1 (CH), 130.3 (CH), 129.3 (CH), 128.5 (CH), 127.6 (CH), 126.9 (CH), 126.0 (2xCH), 120.4 (CH), 111.7 (CH), 110.9 (CH), 55.9 (CH_3), 55.9 (CH_3), 48.0 (CH), 45.5 (CH), 27.8 (CH_2), 24.6 (CH_2).

(+) **2-18E:** White oil; $[\alpha]^{25}_D$ (+)296 (*c* = 0.10, CH_2Cl_2). **HRMS** (EI, $C_{22}H_{24}O_2$, M^+): calcd.: 320.1776, found: 320.1771. **FTIR** (cast film): 3022, 2929, 2835, 1516, 1261, 1139, 1030 cm^{-1}.

(–) **2-18E:** White oil; $[\alpha]^{25}_D$ –290 (*c* = 0.99, CH_2Cl_2). **HRMS** (EI, $C_{22}H_{24}O_2$, M^+): calcd.: 320.1776, found: 320.1774. **FTIR** (cast film): 3022, 2929, 2835, 15l16, 1261, 1139, 1030 cm^{-1}.

(±) **3(*S/R*)-(3,4-dimethoxyphenyl)-4(*R/S*)-[(*E*)-3-methoxystyryl]cyclohex-1-ene (2-19)**:

product	silica column conditions	product mass (% yield)	separation method	HPLC injection	isolated components			ee
						amount	R_t (min)	
2-19E **2-24Z**	15% EtOAc/hex R_f = 0.3	123 mg (58%)	i-amylose-3 column. 95% hex/EtOH (15 min)	110 mg	(+) **2-19E**	13 mg	5.8	99%
					(–) **2-19E**	25 mg	7.8	>99%
					(+) **2-24Z**	9 mg	5.2	>99%
					(–) **2-24Z**	9 mg	6.3	>99%

^{1}H NMR ($CDCl_3$, 700MHz) δ: 7.17 (t, *J* = 7.9 Hz, 1H), 6.87 (bd, *J* = 7.7 Hz, 1H), 6.80 (t, *J* = 2.0 Hz, 1H), 6.78 (d, *J* = 8.2 Hz, 1H), 6.74–6.72 (m, 2H), 6.80 (d, *J* = 1.9 Hz, 1H), 6.18–6.12 (m, 2H), 5.90 (tdd, *J* = 2.4 Hz, 4.4 Hz, 10.0 Hz, 1H), 5.68 (dq, *J* = 10.0 Hz, 2.2 Hz, 1H), 3.85 (s, 3H), 3.83 (s, 3H), 3.79 (s, 3H), 3.19 (dq, *J* = 11.0 Hz, 2.7 Hz, 1H), 2.40–2.36 (m, 1H), 2.28–2.18 (m, 2H), 1.93 (tdd, *J* = 3.1 Hz, 5.2 Hz, 12.8 Hz 1H), 1.71–1.65 (m, 1H). **^{13}C NMR** ($CDCl_3$, 176 MHz) δ: 159.8 (C), 148.7 (C), 147.4 (C), 139.3 (C), 137.5 (C), 134.5 (CH), 130.3 (CH), 129.4 (CH), 129.2 (CH), 127.6 (CH), 120.4 (CH), 118.7 (CH), 112.4 (CH), 111.7 (CH), 111.5 (CH), 110.9 (CH), 55.9 (CH_3), 55.9 (CH_3), 55.2 (CH_3), 48.0 (CH), 45.5 (CH), 27.8 (CH_2), 24.5 (CH_2).

(+) **2-19:** White oil; $[\alpha]^{25}_D$ (+)300 (*c* = 1.00, CH_2Cl_2). **HRMS** (EI, $C_{23}H_{26}O_3$, M^+): calcd.: 350.1882, found: 350.1878. **FTIR** (cast film): 3018, 2931, 2835, 1598, 1515, 1464, 1261, 1155, 1030 cm^{-1}.

(–) **2-19:** White oil; $[\alpha]^{25}_D$ -294 (*c* = 1.00, CH_2Cl_2). **HRMS** (EI, $C_{23}H_{26}O_3$, M^+): calcd.: 350.1882, found: 350.1875. **FTIR** (cast film): 3019, 2931, 2835, 1598, 1515, 1464, 1261, 1155, 1030 cm^{-1}.

(±) **3(*S/R*)-(3,4-dimethoxyphenyl)-4(*R/S*)-[(*Z*)-3-methoxystyryl]cyclohex-1-ene (2-24):** **^{1}H NMR** ($CDCl_3$, 500MHz) δ: 7.10 (t, *J* = 7.9 Hz, 1H), 6.73 (d, *J* = 8.2 Hz, 1H), 6.69 (dd, *J* = 2.2 Hz, 8.2 Hz, 1H), 6.64 (dd, *J* = 2.0 Hz, 8.2 Hz, 1H), 6.54 (d, *J* = 2.0 Hz, 1H), 6.45 (br. d, *J* = 7.6 Hz, 1H), 6.42 (br. s, 1H), 6.31 (d, *J* = 11.7 Hz, 1H), 5.83 (tdd, *J* = 2.4 Hz, 4.3 Hz, 10 Hz, 1H), 5.64 (dq, *J* = 10.0 Hz, 2.2 Hz, 1H), 5.56 (dd, *J* = 10.5 Hz, 11.6 Hz, 1H), 3.83 (s, 3H), 3.72 (s, 3H), 3.72 (s, 3H), 3.14 (dq, *J* = 11.2 Hz, 2.8 Hz, 1H), 2.85 (dq, *J* = 2.5 Hz, 10.0

Hz, 1H), 2.23–2.12 (m, 2H), 1.82 (tdd, *J* = 3.1 Hz, 5.2 Hz, 13.0 Hz, 1H), 1.67–1.59 (m, 1H). **^{13}C NMR** ($CDCl_3$, 126 MHz) δ: 159.3 (C), 148.8 (C), 147.4 (C), 139.1 (C), 137.3 (C), 136.9 (CH), 130.4 (CH), 128.8 (CH), 128.8 (CH), 127.3 (CH), 120.9 (CH), 120.4 (CH), 113.9 (CH), 111.9 (CH), 111.2 (CH), 110.8 (CH), 55.9 (CH3), 55.7 (CH_3), 55.1 (CH_3), 48.1 (CH), 40.6 (CH), 28.5 (CH_2), 24.3 (CH_2).

(+) **2-24:** White solid; $[\alpha]^{25}_D$ (+)23 (*c* = 0.85, CH_2Cl_2). **HRMS** (EI, $C_{23}H_{26}O_3$, M^+): calcd.: 350.1882, found: 350.1876. **FTIR** (cast film): 3000, 2930, 2834, 1576, 1515, 1464, 1260, 1140, 1030 cm^{-1}.

(–) **2-24:** White solid; $[\alpha]^{25}_D$ –12 (*c* = 0.78, CH_2Cl_2). **HRMS** (EI, $C_{23}H_{26}O_3$, M^+): calcd.: 350.1882, found: 350.1882. **FTIR** (cast film): 2999, 2931, 2834, 1577, 1515, 1464, 1260, 1140, 1030 cm^{-1}.

(±) **3(*S/R*)-(3,4-dimethoxyphenyl)-4(*R/S*)-[(*E*)-4-methoxystyryl]cyclohex-1-ene (2-20)**:

product	silica column conditions	product mass (% yield)	separation method	HPLC injection	isolated components				ee
						mass	R_{ta} (min)	R_{tb} (min)	
2-20E **2-25Z**	20% EtOAc/hex R_f = 0.4	100 mg (48%)	*sequential runs:* i-amylose-3 column. a. 95% hex/EtOH (30 min) b. 97% hex/EtOH (20 min)	90 mg	(+) **2-20E**	13 mg	16.3	10.6	>99%
					(–) **2-20E**	20 mg	20.1	-	99%
					(+) **2-25Z**	9 mg	16.3	11.9	98%
					(–) **2-25Z**	109mg	16.3	9.3	99%

^{1}H NMR ($CDCl_3$, 700MHz) δ: 7.20 (d, *J* = 8.7 Hz, 2H), 6.79 (dd, *J* = 17.0 Hz, 8.5 Hz, 3H), 6.72 (dd, *J* = 1.8 Hz, 8.1 Hz, 1H), 6.70 (d, *J* = 1.8 Hz, 1H), 6.11 (d, *J* = 15.9 Hz, 1H), 6.02 (dd, 7.5 Hz, 15.9 Hz, 1H), 5.89 (tdd, *J* = 2.5 Hz, 4.5 Hz, 10.0 Hz, 1H), 5.68 (dq, *J* = 9.8 Hz, 2.3 Hz, 1H), 3.86 (s, 3H), 3.82 (s, 3H), 3.79 (s, 3H), 3.17 (dq, *J* = 11.2 Hz, 2.8 Hz, 1H), 2.35 (dq, *J* = 2.6 Hz, 8.9 Hz, 1H), 2.24–2.18 (m, 2H), 1.92 (tdd, *J* = 3.1 Hz, 5.3 Hz, 12.8 Hz, 1H), 1.69–1.64 (m, 1H). **^{13}C NMR** ($CDCl_3$, 176 MHz) δ: 158.7 (C), 148.6 (C), 147.4 (C), 137.7 (C), 132.0 (C), 130.7 (CH), 130.4 (CH), 128.6 (CH), 127.6 (CH), 127.1 (2 CH), 120.4 (CH), 113.9 (2 CH), 111.8 (CH), 110.9 (CH), 55.9 (CH_3), 55.9 (CH_3), 55.3 (CH_3), 48.1 (CH), 45.4 (CH), 27.9 (CH_2), 24.6 (CH_2).

(+) **2-20:** White oil; $[\alpha]^{25}_D$ (+)335 (*c* = 1.00, CH_2Cl_2). **HRMS** (EI, $C_{23}H_{26}O_3$, M^+): calcd.: 350.1882, found: 350.1875. **FTIR** (cast film): 3018, 2931, 2835, 1607, 1512, 1250, 1139, 1031 cm^{-1}.

(–) **2-20:** White oil; $[\alpha]^{25}_D$ –303 (*c* = 1.00, CH_2Cl_2). **HRMS** (EI, $C_{23}H_{26}O_3$, M^+): 350.1882, found: 350.1879. **FTIR** (cast film): 3018, 2931, 2835, 1607, 1512, 1250, 1139, 1031 cm^{-1}.

(±) **3(*S/R*)-(3,4-dimethoxyphenyl)-4(*R/S*)-[(*Z*)-4-methoxystyryl]cyclohex-1-ene (2-25):** **^{1}H NMR** ($CDCl_3$, 500MHz) δ: 6.78 (d, *J* = 8.6 Hz, 2H), 6.73 (t, *J* = 5.5 Hz, 3H), 6.66 (dd, *J* = 2.0 Hz, 8.2 Hz, 1H), 6.55 (d, *J* = 1.9 Hz, 1H), 6.27 (d, *J* = 11.7 Hz, 1H), 5.84 (tdd, *J* = 2.4 Hz, 4.3 Hz, 10.0 Hz, 1H), 5.65 (dq, *J* = 10.0 Hz, 2.2 Hz, 1H), 5.49 (dd, *J* = 10.4 Hz, 11.6 Hz, 1H), 3.84 (s, 3H), 3.77 (s, 3H), 3.72 (s, 3H), 3.14 (dq, *J* = 11.1 Hz, 2.8 Hz, 1H), 2.81 (dq, *J* = 2.3 Hz, 10.0 Hz, 1H), 2.23–2.12 (m, 2H), 1.82 (tdd, *J* = 3.1 Hz, 5.3 Hz, 13.0 Hz, 1H), 1.67–1.59 (m, 1H). **^{13}C NMR** ($CDCl_3$, 126 MHz) δ: 158.1(C), 148.8 (C), 147.4 (C), 137.4 (C), 135.5 (CH), 130.4 (CH), 130.3 (C), 129.5 (CH), 128.3 (CH), 127.4 (CH), 120.5 (CH), 113.3 (CH), 111.3 (CH), 110.8 (CH), 56.0 (CH_3), 55.7 (CH_3), 55.2 (CH_3), 48.1 (CH), 40.5 (CH), 28.4 (CH_2), 24.4 (CH_2).

(+) **2-25:** White solid; $[\alpha]^{25}_D$ (+)16 (*c* = 1.10, CH_2Cl_2). **HRMS** (EI, $C_{23}H_{26}O_3$, M^+): calcd.: 350.1882, found: 350.1876. **FTIR** (cast film): 350.1882, found: 350.1878. **FTIR** (cast film): 2999, 2929, 2835, 1607, 1512, 1249, 1139, 1031 cm^{-1}.

(–) **2-25:** White solid; $[\alpha]^{25}_D$ –8 (*c* = 1.10, CH_2Cl_2). **HRMS** (EI, $C_{23}H_{26}O_3$, M^+): 350.1882, found: 350.1878. **FTIR** (cast film): 2999, 2929, 2835, 1607, 1512, 1249, 1139, 1031 cm^{-1}.

(±) **3(*S/R*)-(3,4-dimethoxyphenyl)-4(*R/S*)-[(*E*)-2-methylstyryl]cyclohex-1-ene (2-21):**

product	silica column conditions	product mass (% yield)	separation method	HPLC injection	isolated components	amount	R_t (min)	ee
2-21E 2-26Z	20% EtOAc/hex R_f = 0.4	141 mg (70%)	i-amylose-3 column. 97% hex/EtOH (20 min)	140 mg	**(+) 2-21E**	20 mg	10.7	98%
					(–) 2-21E	24 mg	12.6	99%
					(+) 2-26Z	20 mg	9.7	99%
					(–) 2-26Z	19 mg	11.7	99%

^{1}H NMR ($CDCl_3$, 700MHz) δ: 7.33 (d, *J* = 8.4 Hz, 1H), 7.12–7.07 (m, 3H), 6.78 (d, *J* = 8.2 Hz, 1H), 6.73 (dd, *J* = 8.4 Hz, 2.0 Hz, 1H), 6.71 (d, *J* = 2.1 Hz, 1H), 6.31 (d, *J* = 15.7 Hz, 1H), 5.98 (dd, *J* = 7.9 Hz, 15.9 Hz, 1H), 5.89 (tdd, *J* = 2.5 Hz, 4.6 Hz, 2.5 Hz, 1H), 5.69 (dq, 10.1 Hz, 2.2 Hz, 1H), 3.85 (s, 3H), 3.84 (s, 3H), 3.19 (dq, *J* = 8.8 Hz, 2.8 Hz, 1H), 2.40 (dq, *J* = 2.6 Hz, 9.3 Hz, 1H), 2.29–2.19 (m, 2H), 2.15 (s, 3H), 2.0 (tdd, *J* = 3.1 Hz, 5.4 Hz, 12.9 Hz, 1H), 1.73–1.67 (m, 1H). **^{13}C NMR** ($CDCl_3$, 176 MHz) δ: 148.7 (C), 147.4 (C), 137.6 (C), 137.1 (C), 135.5 (C), 135.1 (CH), 130.5 (CH), 130.1(CH), 127.5 (CH), 127.5 (CH), 126.8 (CH), 125.9 (CH), 125.5 (CH), 120.6 (CH), 111.7 (CH), 111.0 (CH), 56.0 (CH_3), 55.9 (CH_3), 48.2 (CH), 46.0 (CH), 28.2 (CH_2), 24.7 (CH_2), 19.8 (CH_3).

(+) **2-21.** Colourless oil; $[\alpha]^{25}_D$ (+)266 (*c* = 1, CH_2Cl_2). **HRMS** (EI, $C_{23}H_{26}O_2$, M^+): calcd.: 334.1933, found: 334.1930. **FTIR** (cast film): 3018, 2931, 2835, 1515, 1261, 1030 cm^{-1}.

(–) **2-21.** Colourless oil; $[\alpha]^{25}_D$ –201 (*c* = 1, CH_2Cl_2). **HRMS** (EI, $C_{23}H_{26}O_2$, M^+): 334.1933, found: 334.1928. **FTIR** (cast film): 3018, 2931, 2835, 1515, 1261, 1030 cm^{-1}.

(±) **3(*S/R*)-(3,4-dimethoxyphenyl)-4(*R/S*)-[(*Z*)-2-methylstyryl]cyclohex-1-ene (2-26):** **^{1}H NMR** ($CDCl_3$, 700MHz) δ: 7.07 (t, *J* = 7.4 Hz, 1H), 7.04 (d, *J* = 7.3, 1H) 7.0 (t, *J* = 7.4 Hz, 1H), 6.71 (d, *J* = 8.0 Hz, 1H), 6.58 (dt, *J* = 1.7 Hz, 8.4 Hz, 2H), 6.38 (d, *J* = 2.0 Hz, 1H), 6.27 (d, *J* = 11.3 Hz, 1H), 5.78 (dq, *J* = 9.8 Hz, 3.2 Hz, 1H), 5.60–5.57 (m, 2H), 3.85 (s, 3H), 3.64 (s, 3H), 3.10 (dq, *J* = 9.0 Hz, 2.8 Hz, 1H), 2.58 (dq, *J* = 2.8 Hz, 10.3 Hz, 1H), 2.16–2.13 (m, 2H), 1.87 (s, 3H), 1.81–1.77 (m, 1H), 1.66–1.60 (m, 1H). **^{13}C NMR** ($CDCl_3$, 176 MHz) δ: 148.8 (C), 147.4 (C), 137.6 (C), 137.0 (C), 136.3 (CH_2), 130.6 (CH_2), 129.3 (CH), 128.8 (CH_2), 128.4 (CH), 127.1 (CH), 126.6 (CH), 125.0 (CH), 120.5 (CH_2), 110.9 (CH), 110.8 (CH), 56.0 (CH_3), 55.7 (CH_3), 48.2 (CH), 40.7 (CH), 28.7 (CH_2), 24.4 (CH_2), 19.5 (CH_3).

(+) **2-26.** White solid; $[\alpha]^{25}_D$ (+)64 (*c* = 1.00, CH_2Cl_2). **HRMS** (EI, $C_{23}H_{26}O_2$, M^+): calcd.: 334.1933, found: 334.1934. **FTIR** (cast film): 3018, 2924, 2835, 1516, 1261, 1031 cm^{-1}.

(–) **2-26.** White solid; $[\alpha]^{25}_D$ –43 (*c* = 1.00, CH_2Cl_2). **HRMS** (EI, $C_{23}H_{26}O_2$, M^+): calcd.: 334.1933, found: 334.1928. **FTIR** (cast film): 3018, 2928, 2834, 1516, 1261, 1031 cm^{-1}.

(±) **3(*S/R*)-(3,4-dimethoxyphenyl)-4(*R/S*)-[(*E*)-2-bromostyryl]cyclohex-1-ene (2- 22):**

product	silica column conditions	product mass (% yield)	separation method	HPLC injection	isolated components			ee
						amount	R_t (min)	
2-22E **2-22Z**	20% EtOAc/hex R_f = 0.3	71 mg (29%)	i-amylose-3 column. 97% hex/EtOH (30 min)	70 mg	(+) **2-22E**	18 mg	13.1	>99%
					(–) **2-22E**	18 mg	17.0	99%
					(+) **2-22Z**	*not isolated*	11.4	-
					(–) **2-22Z**		14.8	-

^{1}H NMR ($CDCl_3$, 700MHz) δ: 7.48 (dd, *J* = 7.9 Hz, 1.2 Hz, 1H), 7.40 (dd, *J* = 7.8Hz, 1.5 Hz, 1H), 7.20 (dt, *J* = 0.8 Hz, 7.5 Hz, 1H), 7.03 (dt, *J* = 1.5 Hz, 7.7 Hz, 1H), 6.80 (d, *J* = 8.2 Hz, 1H), 6.74 (dd, *J* = 8.1 Hz, 2.0 Hz, 1H), 6.72 (d, *J* = 2.1 Hz, 1H), 6.53 (d, *J* = 15.8 Hz, 1H), 6.10 (dd, *J* = 7.6 Hz, 15.9 Hz, 1H), 5.9 (tdd, *J* = 2.5 Hz, 4.6 Hz, 10.0 Hz, 1H), 5.68 (dq, *J* = 10.0 Hz, 2.2 Hz, 1H), 3.85 (s, 3H), 3.85 (s, 3H), 3.22 (dq, *J* = 11.1 Hz, 2.8 Hz, 1H), 2.46 (dq, *J* = 2.1 Hz, 9.0 Hz, 1H), 2.29–2.19 (m, 2H), 1.97 (tdd, *J* = 3.1 Hz, 5.1 Hz, 12.9 Hz, 1H), 1.74–1.68 (m, 1H). **^{13}C NMR** ($CDCl_3$, 176 MHz) δ: 148.8 (C), 147.5(C), 137.7 (C), 137.4 (C), 137.2 (CH), 132.8 (CH), 130.4 (CH), 128.3 (CH), 128.2 (CH), 127.5 (CH), 127.3 (CH), 126.9 (CH), 123.3 (C), 120.5 (CH), 111.6 (CH), 111.1 (CH), 55.9 (CH_3), 55.9 (CH_3), 48.0 (CH), 45.3 (CH), 27.7 (CH_2), 24.6 (CH_2).

(+) **2-22E:** Colourless oil; $[\alpha]^{25}_D$ (+)214 (*c* = 1.00, CH_2Cl_2). **HRMS** (EI, $C_{22}H_{23}BrO_2$, M^+): calcd.: 400.0861, found: 400.0861. **FTIR** (cast film): 3018, 2930, 2834, 1515, 1465, 1261, 1139, 1029 cm^{-1}.

(–) **2-22E:** Colourless oil; $[\alpha]^{25}_D$ –230 (*c* = 0.99, CH_2Cl_2). **HRMS** (EI, $C_{22}H_{23}BrO_2$, M^+): calcd.: 400.0861, found: 400.0871. **FTIR** (cast film): 3018, 2930, 2834, 1515, 1465, 1261, 1139, 1029 cm^{-1}.

(±) **3(*S/R*)-(3,4-dimethoxyphenyl)-4(*R/S*)-[(*Z*)-3,4-dimethoxystyryl]cyclohex-1-ene (2-23):**

product	silica column conditions	product mass (% yield)	separation method	HPLC injection	isolated components					ee
						$mass_a$	R_{ta} (min)	$mass_b$	R_{tb} (min)	
t-BG 2-23	20% EtOAc/hex R_f = 0.3	527 mg (77%)	*sequential runs:* a. AD-H column. 18% ^{i}PrOH/CO_2 b. C8 column. 50→100% ACN/H_2O (30 min)	479 mg	**(+) t-BG**	144 mg	12.0	67 mg	11.9	99%
					(–) t-BG	146 mg	15.2	50 mg	11.9	93%
					(+) 2-23Z	44 mg	9.4	12 mg	10.1	98%
					(–) 2-23Z	50 mg	10.8	18 mg	10.1	96%

**HPLC Method B used to remove minor impurities*

^{1}H NMR ($CDCl_3$, 700MHz) δ: 6.72 (d, *J* = 8.2 Hz, 1H), 6.70 (d, *J* = 8.1 Hz, 1H), 6.65 (dd, *J* = 2.1 Hz, 8.2 Hz, 1H), 6.56 (d, *J* = 2.1 Hz, 1H), 6.43–6.41 (m, 2H), 6.27 (d, *J* = 11.5 Hz, 1H), 5.84 (tdd, *J* = 2.4 Hz, 4.2 Hz, 10.1 Hz, 1H), 5.65 (dq, *J* = 2.2 Hz, 9.8 Hz, 1H), 5.51 (dd, *J* = 10.4 Hz, 11.5 Hz), 3.84 (s, 3H), 3.83 (s, 3H), 3.76 (s, 3H), 3.73 (s, 3H), 3.15 (dq, *J* = 8.8 Hz, 2.8 Hz, 1H), 2.84 (dq, *J* = 2.5 Hz, 10.1 Hz, 1H), 2.19–2.15 (m, 2H), 1.83 (tdd, *J* = 3.1 Hz, 5.0 Hz, 12.8 Hz, 1H), 1.67–1.61 (m, 1H). **^{13}C NMR** ($CDCl_3$, 176 MHz) δ: 148.7, 148.4, 147.6, 147.4, 137.4, 135.9, 130.7, 130.5, 128.5, 127.3, 120.8, 120.3, 111.8, 111.3, 110.8, 110.8, 55.9, 55.8, 55.7, 48.1, 40.7, 28.6, 24.5. Characterization data is consistent with literature.[11]

(+) ***t*-BG:** Colourless oil: $[\alpha]^{25}_D$ (+)325 (*c* = 1.00, CH_2Cl_2).

(–) ***t*-BG:** Colourless oil: $[\alpha]^{25}_D$ –275 (*c* = 1.00, CH_2Cl_2).

(+) **2-23:** Colourless oil: $[\alpha]^{25}_D$ (+)6.4(*c* = 1.00, CH_2Cl_2).

(–) **2- 23:** Colourless oil: $[\alpha]^{25}_D$ –3.3 (*c* = 1.90, CH_2Cl_2).

(±) **3(*S/R*)-(3-methoxyphenyl)-4(*R/S*)-[(*E*)-3,4-dimethoxystyryl]cyclohex-1-ene (2-27):**

product	silica column conditions	product mass (% yield)	separation method	HPLC injection	isolated components		
						amount	R_t (min)
2-27E 2-27Z	15% EtOAc/hex R_f= 0.2	66 mg (52%)	i-amylose-3 column. 97% hex/EtOH (20 min)	50 mg	**(±) 2-27E**	22 mg	7.8
					(±) 2-27Z	*not isolated*	

2-27 E: White oil. **^{1}H NMR** ($CDCl_3$, 700MHz) δ: 7.19 (t, *J* = 7.8 Hz, 1H), 6.82–6.73 (m, 6H), 6.13 (d, *J* = 15.9 Hz, 1H), 6.03 (dd, *J* = 7.6 Hz, 16.0 Hz 1H), 5.90 (tdd, *J* = 2.4 Hz, 4.0 Hz, 10.0 Hz, 1H), 5.68 (dq, *J* = 10.0 Hz, 2.1 Hz, 1H), 3.88 (s, 3H), 3.86 (s, 3H), 3.77 (s, 3H), 3.23 (dq, *J* = 9.4 Hz, 2.7 Hz, 1H), 2.41 (dq, *J* = 2.6 Hz, 9.3 Hz, 1H), 2.26–2.18 (m, 2H), 1.92 (dq, *J* = 12.5 Hz, 4.2 Hz, 1H), 1.70–1.64 (m, 1H). **^{13}C NMR** ($CDCl_3$, 176 MHz) δ: 159.5 (C), 149.0 (C), 148.3 (C), 146.7 (C), 132.2 (CH), 131.1 (C), 130.0 (CH), 129.0 (CH), 128.9 (CH), 127.6 (CH), 121.1 (CH), 118.9 (CH), 114.3 (CH), 111.5 (CH), 111.2 (CH), 108.8 (CH), 56.0 (CH_3), 55.8 (CH_3), 55.2 (CH_3), 48.5 (CH), 45.1 (CH), 27.8 (CH_2), 24.5 (CH_2). **HRMS** (EI, $C_{23}H_{26}O_3$, M^+): calcd.: 350.1882, found: 350.1874. **FTIR** (cast film): 3019, 2931, 2835, 1601, 1515, 1465, 1263, 1157, 1028 cm^{-1}.

(±) **(3(*S/R*)-(4-methoxyphenyl)-4(*R/S*)-[(*E*)-3,4-dimethoxystyryl]cyclohex-1-ene (2-28):**

product	silica column conditions	product mass (% yield)	separation method	HPLC injection	isolated components		
						amount	R_t (min)
2-28E **2-28Z**	20% EtOAc/hex R_f = 0.2	206 mg (85%)	i-amylose-3 column. 97% hex/EtOH (10 min)	100 mg	**(±) 2-28E**	22 mg	9.2
					(±) 2-28Z	*not isolated*	

^{1}H NMR ($CDCl_3$, 500MHz) δ: 7.12–7.09 (m, 2H), 6.83–6.76 (m, 5H), 6.11 (d, *J* = 16.0 Hz, 1H), 6.02 (dd, *J* = 7.4 Hz, 16.0 Hz, 1H), 5.89 (dq, *J* = 10.0, 3.3 Hz, 1H), 5.66 (dq, *J* = 10 Hz, 2.2 Hz, 1H), 3.88 (s, 3H), 3.86 (s, 3H), 3.78 (s, 3H), 3.20 (dq, *J* = 11.0 Hz, 2.8 Hz, 1H), 2.36 (dq, *J* = 2.9 Hz, 9.8 Hz, 1H), 2.24–2.19 (m, 2H), 1.91 (dq, *J* = 12.5 Hz, 4.2 Hz, 1H), 1.70–1.63 (m, 1H). **^{13}C NMR** ($CDCl_3$, 126 MHz) δ: 158.0 (C), 149.0 (C), 148.3 (C), 137.1 (C), 132.3 (C), 131.1 (CH), 130.5 (CH), 129.4 (2 CH), 128.8 (CH), 127.4 (CH), 118.8 (CH), 113.6 (2 CH), 111.2 (CH), 108.8 (CH), 56.0 (CH_3), 55.9 (CH_3), 55.263 (CH_3), 47.6 (CH), 45.5 (CH), 27.9 (CH_2), 24.6 (CH_2). **HRMS** (EI, $C_{23}H_{26}O_3$, M^+): calcd.: 350.1882, found: 350.1878. **FTIR** (cast film): 3018, 2931, 2835, 1608, 1513, 1262, 1139, 1029 cm^{-1}.

(±) **3(*S/R*)-(3-methoxy-4-hydroxyphenyl)-4(*R/S*)-[(*E*)-3,4-dimethoxystyryl]cyclohex-1-ene (2-29)**:

product	silica column conditions	product mass (% yield)	separation method	HPLC injection	isolated components		
						amount	R_t (min)
2-29E **2-29Z**	10 → 25% EtOAc/hex R_f= 0.2	40 mg (32%)	C8 column. 50→100% ACN/H_2O (30 min)	40 mg	**(±) 2-29E**	8 mg	18.0
					(±) 2-29Z	*not isolated*	

^{1}H NMR ($CDCl_3$, 500MHz) δ: 6.83–6.76 (m, 4H), 6.70–6.67 (m, 2H), 6.10 (d, *J* = 16.0 Hz, 1H), 6.02 (dd, *J* = 16.0 Hz, 7.5 Hz, 1H), 5.91–5.87 (m, 1H), 5.67 (dq, *J* = 10.5 Hz, 2.5 Hz, 1H), 5.45 (s, 1H), 3.87 (s, 3H), 3.86 (s, 3H), 3.82 (s, 3H), 3.17–3.15 (m, 1H), 2.35–2.33 (m, 1H), 2.22–2.20 (m, 2H), 1.93–1.90 (m, 1H), 1.69–1.64 (m, 1H). Characterization data are consistent with literature.[11]

Synthesized directly from cis aldehyde **2-6d*

2.7.11 Synthesis of 2-34 and 2-35:

Pd/C (5 mg) was added to a flame dried flask under N_2 followed by (±) ***t*-BG** or (±) ***c*-BG** (25.0 mg, 0.06 mmol) in ethyl acetate. After a quick exposure to vacuum, then N_2, the flask was placed under reduced pressure. A hydrogen (H_2) balloon was inserted, and the reaction was then stirred for 18 hours. The contents of the flask were filtered through celite and rinsed with CH_2Cl_2. The solvent was concentrated in vacuo, providing products **2-34** and **2-35** without the need for further purification.

(±) **4-((1*R*,2*S*)-2-(3,4-dimethoxyphenylethy)cyclohexyl)-1,2-dimethoxy benzene (2-34):** White solid **(**99%). **^{1}H NMR** ($CDCl_3$,700 MHz) δ: 6.75 (d, *J* = 7.7 Hz, 1H), 6.70 (d, *J* = 7.7 Hz, 1H), 6.62 (dd, *J* = 7.7 Hz, 1.4 Hz, 1H), 6.59 (d, *J* = 1.4 Hz, 1H), 6.51 (dd, *J* = 7.7 Hz, 1.4 Hz, 1H), 6.46 (d, *J* = 1.4 Hz, 1H), 3.84 (s, 3H), 3.82 (s, 3H), 3.81 (s, 3H), 3.77 (s, 3H), 2.56–2.52 (m, 1H), 2.32–2.27 (m, 1H), 2.17–2.14 (m, 1H), 2.06–2.02 (m, 1H), 1.82–.77 (m, 3H), 1.52–1.42 (m, 2H), 1.39–1.31 (m, 3H), 1.20–1.16 (m, 1H), 1.10, 1.04 (m, 1H). **^{13}C NMR** ($CDCl_3$,175 MHz) δ: 148.7, 148.6, 147.0, 146.9, 139.4, 135.4, 120.0, 119.5,

111.6, 111.0, 110.6, 55.9, 55.8, 55.7, 55.7, 50.4, 41.5, 36.3, 35.9, 32.2, 32.1, 26.9, 26.5. **HRMS** (EI, $C_{24}H_{32}O_4$, M^+): calcd: 385.2301, found: 385.2342.

(±) **4-((1S,2S)-2-(3,4-dimethoxyphenylethy)cyclohexyl)-1,2-dimethoxy benzene (2-35):** White solid (95%). **^{1}H NMR** ($CDCl_3$,700 MHz) δ: 6.77 (d, *J* = 8.4 Hz, 1H), 6.69 (d, *J* = 8.4 Hz, 1H), 6.67 (dd, *J* = 8.4, 1.4 Hz, 1H), 6.65 (d, *J* = 1.4 Hz, 1H), 6.49 (dd, *J* = 7.7, 1.4 Hz, 1H), 6.45 (d, *J* = 1.4 Hz, 1H), 3.85 (s, 3H), 3.82 (app s, 6H), 3.77 (s, 3H), 2.80-2.77 (m, 1H), 2.48-2.45 (m, 1H), 2.14-2.11 (m, 1H), 1.89-1.85 (m, 3H), 1.75-1.67 (m, 2H), 1.59-1.46 (m, 4H), 1.41-1.37 (m, 1H), 1.31-1.26 (m, 1H) ppm. **^{13}C-NMR** ($CDCl_3$,175 MHz) δ: 148.6, 148.5, 146.9, 146.9, 138.5, 135.3, 120.0, 119.2, 111.6, 111.2, 111.0, 110.7, 55.9, 55.9, 55.8, 55.7, 45.9, 39.3, 33.6, 29.6, 27.3, 26.5, 25.7, 20.6 **HRMS** (EI, $C_{24}H_{32}O_4$, M^+): calcd: 385.2301, found: 385.2342.

2.7.12 Synthesis of 2-36 and 2-37

Rhodium acetate dimer (1 mg) and a solution of (±) ***t*-BG** (50 mg, 0.13 mmol) or (±) ***c*-BG** (24 mg, 0.06 mmol) in CH_2Cl_2 (0.50 mL) was added to a flame dried round bottom flask. The reaction solution was stirred while ethyl diazoacetate (33 wt% CH_2Cl_2 solution, 16 mL dissolve in 0.5 mL CH_2Cl_2 for ***t*-BG** and 8 mL dissolve in 0.5 mL CH_2Cl_2 for ***c*-BG** was added dropwise. The reaction was stirred at rt for 3 hours and then concentrated in vacuo. The residue was dissolved in acetonitrile and was purified by HPLC

product	separation method	product mass (% yield)	R_t (min)
2-36	C8 column. 50→100% ACN/H_2O (20 min)	9.4 mg (16%)	17.8
2-37		4.5 mg (15%)	9.9

(±) **1-((1*R*,2*S*,3*S*,6*R*,7*S*)-3-(3,4-dimethoxyphenethyl)-2-(3,4-dimethoxyphenyl) bicyclo [4.1.0]heptan-7-yl)-2-methoxyethanone (2-36):** Yellow oil (16%). **^{1}H NMR** ($CDCl_3$,700 MHz) δ: 6.80 (m, 2H), 6.73–6.72 (m, 2H), 6.70–6.69 (m, 2H), 5.92 (d, *J* = 16.1 Hz, 1H), 5.73 (dd, *J* = 16.1 Hz, 7.7 Hz, 1H), 4.10–4.05 (m, 2H), 3.83 (s, 6H), 3.83 (s, 3H), 3.82 (s, 3H), 2.55 (dd, *J* = 10.5 Hz, 0.7 Hz, 1H), 2.16–2.14 (m, 1H), 2.05–1.98 (m, 2H), 1.86–1.84 (m, 1H), 1.75–1.69 (m, 2H), 1.59 (app t, *J* = 4.2 Hz, 1H), 1.23 (t, *J* = 7 Hz,

3H),1.16 (dd, *J* = 12.6 Hz, 4.2 Hz, 1H). **^{13}C NMR** ($CDCl_3$,175 MHz) δ: 174.1, 148.9, 148.7, 148.3, 147.3, 139.0, 131.8, 130.8, 129.0, 120.2, 118.7, 111.4, 111.1, 111.0, 108.7, 60.4, 55.9, 55.9, 55.8, 55.7, 28.2, 25.7, 25.4, 23.3, 22.5, 14.3. **HRMS** (EI, $C_{28}H_{35}O_6$, $[M+H]^+$: calcd: 467.2355, found: 467.2439.

(±) **1-((1*R*,2*R*,3*S*,6*R*,7*S*)-3-(3,4-dimethoxyphenethyl)-2-(3,4-dimethoxyphenyl) bicyclo [4.1.0]heptan-7-yl)-2-methoxyethanone (2-37):** Yellow oil (15%). **^{1}H NMR** ($CDCl_3$, 700 MHz) δ: 6.88 (dd, *J* = 7.7 Hz, 2.1 Hz, 1H), 6.81 (d, *J* = 7.7 Hz, 1H), 6.76 (d, *J* = 2.1 Hz, 2H), 6.74 (dd, *J* = 7.7 Hz, 2.1 Hz, 2H), 6.17 (d, *J* = 16.1 Hz, 1H), 5.60 (dd, *J* = 16.1 Hz, 9.1 Hz, 1H), 4.12 (q, *J* = 7 Hz, 2H), 3.86 (s, 3H), 3.85 (s, 3H), 3.83 (s, 3H), 3.74 (s, 3H), 3.23 (app. d, *J* = 4.9 Hz, 1H), 2.29–2.23 (m, 2H), 1.89 (appt, *J* = 4.2 Hz, 2H), 1.82–1.78 (m, 1H), 1.60 (t, *J* = 4.2 Hz, 1H), 1.52–1.48 (m, 1H), 1.27–1.21 (m, 4H). **^{13}C NMR** ($CDCl_3$,175 MHz) δ: 174.2, 148.9, 148.4, 148.1, 147.5, 134.9, 131.3, 130.7, 129.1, 121.3, 118.8, 113.3, 111.2, 110.5, 108.6, 60.4, 55.9, 55.8, 55.8, 55.7, 43.7, 40.0, 28.3, 26.2, 23.1, 20.9, 20.8, 14.3. **HRMS** (EI, $C_{28}H_{36}O_6$, $[M+H]^+$: calcd: 467.2355, found: 467.2442.

2.8 References

(1) Han, A.-R.; Kim, H.; Piao, D.; Jung, C.-H.; Seo, E. K.; Jung, D. ; Seo, C.-H. ; Phytochemicals, E. K.; Of Zingiber, B.; Molecules, R.; Sülsen, P. Phytochemicals and Bioactivities of Zingiber Cassumunar Roxb. *Mol.* **2021**, *26* (8), 2377.

(2) Matsui, N.; Kido, Y.; Okada, H.; Kubo, M.; Nakai, M.; Fukuishi, N.; Fukuyama, Y.; Akagi, M. Phenylbutenoid Dimers Isolated from Zingiber Purpureum Exert Neurotrophic Effects on Cultured Neurons and Enhance Hippocampal Neurogenesis in Olfactory Bulbectomized Mice. *Neurosci. Lett.* **2012**, *513* (1), 72–77.

(3) Chu, J.; Suh, D. H.; Lee, G.; Han, A. R.; Chae, S. W.; Lee, H. J.; Seo, E. K.; Lim, H. J. Synthesis and Biological Activity of Optically Active Phenylbutenoid Dimers. *J. Nat. Prod.* **2011**, *74* (8), 1817–1821.

(4) Nakamura, S.; Iwami, J.; Matsuda, H.; Wakayama, H.; Pongpiriyadacha, Y.; Yoshikawa, M. Structures of New Phenylbutanoids and Nitric Oxide Production Inhibitors from the Rhizomes of Zingiber Cassumunar Chart 1. Structures of New Constituents from the Rhizomes of Zingiber Cassumunar. *Chem. Pharm. Bull* **2009**, *57* (11), 1267–1272.

(5) Morales-Medina, J. C.; Iannitti, T.; Freeman, A.; Caldwell, H. K. The Olfactory Bulbectomized Rat as a Model of Depression: The Hippocampal Pathway. *Behav. Brain Res.* **2017**, *317*, 562–575.

(6) Nakai, M.; Iizuka, M.; Matsui, N.; Hosogi, K.; Imai, A.; Abe, N.; Shiraishi, H.; Hirata, A.; Yagi, Y.; Jobu, K.; Yokota, J.; Kato, E.; Hosoda, S.; Yoshioka, S.; Harada, K.; Kubo, M.; Fukuyama, Y.; Miyamura, M. Bangle (Zingiber Purpureum) Improves Spatial Learning, Reduces Deficits in Memory, and Promotes Neurogenesis in the Dentate Gyrus of Senescence-Accelerated Mouse P8. *J. Med. Food* **2016**, *19* (5), 435–441.

(7) Kato, E.; Kubo, M.; Okamoto, Y.; Matsunaga, Y.; Kyo, H.; Suzuki, N.; Uebaba, K.; Fukuyama, Y. Safety Assessment of Bangle (Zingiber Purpureum Rosc.) Rhizome Extract: Acute and Chronic Studies in Rats and Clinical Studies in Human. *ACS Omega* **2018**, *3* (11), 15879-15889.

(8) Amatayakul, T.; C, J. R.; Dechatiwongse, T.; F Giles, R. G.; Ku, K.; ast ton, C. L.; WhiteB, A. H. Chemistry and Crystal Structures of Some Constituents of Zingiber Cassumunar*. *Aust. J. Chem* **1979**, *32*, 71–88.

(9) Amatayakul, T.; Cannon, J. R.; Dampawan, P.; Dechatiwongse, T.; Giles, R. G. F.; Huntrakul, C.; Kusamran, K.; Mokkhasamit, M.; Raston, C. L.; Reutrakul, V.; White, A. H. Syntheses of Some Constituents of Zingiber Cassumunar. *Aust. J. Chem* **1980**, *33*, 2756.

(10) Kim, S. S.; Fang, Y.; Park, H. Synthesis and Anti-Inflammatory Activity of Phenylbutenoid Dimer Analogs. *Bull. Korean Chem. Soc.* **2015**, *36* (6), 1676–1680.

(11) Chu, J.; Suh, D. H.; Lee, G.; Han, A. R.; Chae, S. W.; Lee, H. J.; Seo, E. K.; Lim, H. J. Synthesis and Biological Activity of Optically Active Phenylbutenoid Dimers. *J. Nat. Prod.* **2011**, *74* (8), 1817–1821.

(12) Kubo, M.; Kaga, S.; Harada, K.; Okamoto, Y.; Kato, E.; Hosoda, S.; Fukuyama, Y. Studies on Extraction Conditions to Increase the Content of Neurotrophic Compounds in the Bangle (Zingiber Purpureum) Extract. *Nat. Prod. Commun.* **2017**, *12* (8), 1934578X1701200835.

(13) Chu, J.; Suh, D.; Lee, G.; Han, A.; Chae, S.; Lee, H.; Seo, E.; Lim, H. Synthesis and Biological Activity of Optically Active Phenylbutenoid Dimers. *J. Nat. Prod.* **2011**, *74* (8), 1817–1821.

(14) Lording, W. J.; Fallon, T.; Sherburn, M. S.; Paddon-Row, M. N. The Simplest Diels–Alder Reactions Are Not Endo -Selective. *Chem. Sci.* **2020**, *11* (43), 11915–11926.

(15) Díaz, E.; Reyes, E.; Uria, U.; Carrillo, L.; Tejero, T.; Merino, P.; Vicario, J. L. Carboxylates as Nucleophiles in the Enantioselective Ring-Opening of Formylcyclopropanes under Iminium Ion Catalysis. *Chem. – A Eur. J.* **2018**, *24* (35), 8764–8768.

(16) Fuchs, M.; Schober, M.; Pfeffer, J.; Kroutil, W.; Birner-Gruenberger, R.; Faber, K. Homoallylic Alcohols via a Chemo-Enzymatic One-Pot Oxidation–Allylation Cascade. *Adv. Synth. Catal.* **2011**, *353* (13), 2354–2358.

(17) Huang, X. R.; Pan, X. H.; Lee, G. H.; Chen, C. C2-Symmetrical Bipyridyldiols as Promising Enantioselective Catalysts in Nozaki–Hiyama Allylation. *Adv. Synth. Catal.* **2011**, *353* (11–12), 1949–1954.

(18) Fillion, E.; Dumas, A. M.; Hogg, S. A. Modular Synthesis of Tetrahydrofluorenones from 5-Alkylidene Meldrum's Acids. *J. Org. Chem.* **2006**, *71* (26), 9899–9902.

(19) Davenport, E.; Fernandez, E. Transition-Metal-Free Synthesis of Vicinal Triborated Compounds and Selective Functionalisation of the Internal C–B Bond. *Chem. Commun.* **2018**, *54* (72), 10104–10107.

(20) Diaz-Muñoz, G.; Isidorio, R. G.; Miranda, I. L.; de Souza Dias, G. N.; Diaz, M. A. N. A Concise and Efficient Synthesis of Tetrahydroquinoline Alkaloids Using the Phase Transfer Mediated Wittig Olefination Reaction. *Tetrahedron Lett.* **2017**, *58* (33), 3311–3315.

(21) Schmid, P.; Maier, M.; Pfeiffer, H.; Belz, A.; Henry, L.; Friedrich, A.; Schönfeld, F.; Edkins, K.; Schatzschneider, U. Catalyst-Free Room-Temperature IClick Reaction of Molybdenum(Ii) and Tungsten(Ii) Azide Complexes with Electron-Poor Alkynes: Structural Preferences and Kinetic Studies. *Dalt. Trans.* **2017**, *46* (39), 13386–13396.

(22) Ngwendson, J. N.; Schultze, C. M.; Bollinger, J. W.; Banerjee, A. Effect of Base on Alkyltriphenylphosphonium Salts in Polar Aprotic Solvents. *Can. J. Chem.* **2011**, *86* (7), 668–675.

(23) Mohideen, M.; Zulkepli, S.; Nik-Salleh, N. S.; Zulkefeli, M.; Weber, J. F. F. A.; Rahman, A. F. M. M. Design, Synthesis, in Vitro Cytotoxicity Evaluation and Structure-Activity Relationship of Goniothalamin Analogs. *Arch. Pharm. Res.* **2013**, *36* (7), 812–831.

(24) Moghaddam, F. M.; Farimani, M. M. A Simple and Efficient Total Synthesis of (±)-Danshexinkun A, a Bioactive Diterpenoid from Salvia Miltiorrhiza. *Tetrahedron Lett.* **2010**, *51* (3), 540–542.

(25) Montgomery, T. P.; Grandner, J. M.; Houk, K. N.; Grubbs, R. H. Synthesis and Evaluation of Sterically Demanding Ruthenium Dithiolate Catalysts for Stereoretentive Olefin Metathesis. *Organometallics* **2017**, *36* (20), 3940–3953.

Chapter 3: Investigation of neurotrophic activity of banglenes and banglene derivatives

After synthesizing banglenes and their derivatives, next, I optimized an assay to test their neurotrophic effect. I used the PC-12 cell line as a model system to assess the ability of banglenes to cause neuritogenesis and to explore their impact on NGF signaling pathways. The Fukuyama and Matsui groups had also used PC-12 cells to establish the bioactivity of *cis* and *trans* banglenes (*c*-BG and *t*-BG).

3.1 PC-12 cell line as a neurotrophic model system

Neurite formation is a fundamental step in neuronal development and can be considered a distinct morphogenetic marker of neuronal differentiation. The phenotypic hallmark of neurodegenerative disorders is degeneration of neurons. Thus, identifying bioactive agents that can activate and drive neurogenesis is often of clinical significance.[1] The assessment of the neurotrophic effect of such bioactive agents can be done *in vivo* or through model systems such as primary cell cultures or neuronal cell lines. The cell lines commonly used for neurobiological studies include PC-12, SH-SY5Y, P19, Neuro-2a etc.[2]

The rat pheochromocytoma PC-12 cell line is commonly used to study neurotoxicity, neuroprotection, neurosecretion and neuro-differentiation.[3,4] Although these cells originate from a rat adrenal tumor, they mimic differentiated cultured neurons.[5] They have a distinct morphology based on the conditions in which they are cultured (**figure 3-1**). In serum containing culture medium, these cells are highly proliferative and have a round morphology. Upon induction by the neurotrophin protein-Nerve growth factor (NGF), these cells stop dividing and acquire some characteristics of sympathetic ganglion neurons, such as forming long branching neurites and being electrically excitable.[4] The electrical excitability of these cells is because they synthesize and store catecholamines such as dopamine and norepinephrine, which are released upon depolarization in a calcium dependent manner.[6] NGF triggered neurite generation in PC-12 cells is a slow, RNA synthesis dependent process which begins after a lag of 24 hours and can take 2-7 days. The phenotypic changes observed in PC-12 cells upon induction by NGF are reversible, upon removal of NGF the cells go back to their un-differentiated state.[5]

Apart from NGF, PC-12 cells can be induced to differentiate by dexamethasone, sodium nitrite, saturosporine etc. However, NGF continues to be the most widely employed agent of choice to differentiate PC-12 cells.[7] The differentiation of PC-12 cells can be assessed by quantitative morphological methods, such as the measurement of cell size, neurite number and neurite length.[8] This quantifiable and clear morphological change upon application of a neurotrophic trigger has resulted in PC-12 cell line being widely used to study neurotrophic small molecules.[9]

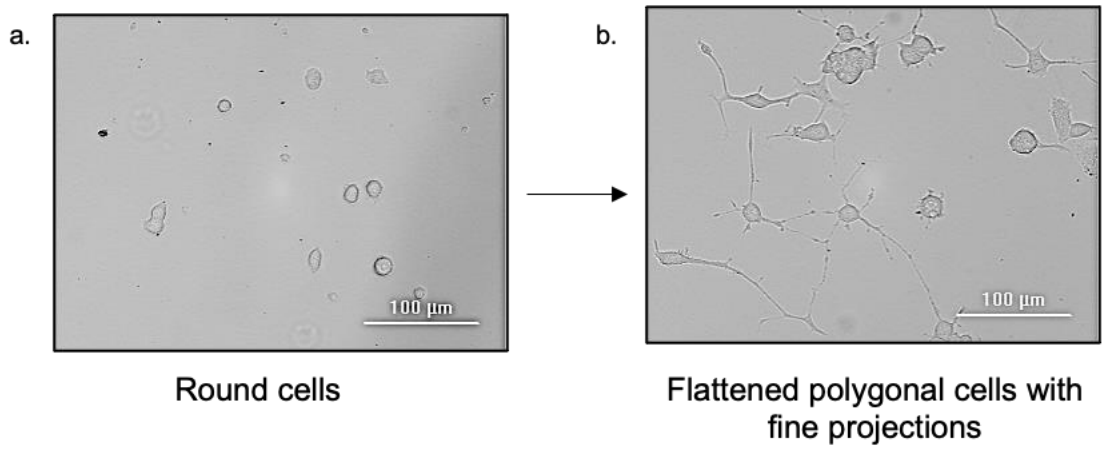

Figure 3-1. Morphology of PC-12 cells in (a) serum containing medium and (b) induced by NGF

There are certain limitations to the use of PC-12 cells as a model to study neuritogenesis. First, it is difficult to halt cell division of PC-12 cells and obtain a stable population of differentiated cells.[8] This limitation can be accounted for in the assay design by including a negative and a positive control which can establish the range of cells that undergo proliferation vs. differentiation. Concurrent with the first limitation, once NGF is removed from the medium, over 75% of PC-12 cells lose their neurite outgrowths and start proliferating within three days. For this reason, most neuritogenesis studies with PC-12 cells have an end point preferably within the first 24-48 hours after the addition of a neuritogenesis inducer. If the end point is greater than 48 hours then NGF is routinely supplemented.[10,11]

Despite being an imperfect representative model of neurons, this cell line is popular because it is easy to culture and there is immense background knowledge on its proliferation and differentiation.[5–7]

3.2 Setup and optimization of neuritogenesis assay

There are various parameters which affect the reproducibility and robustness of a cellular assay. Some of these parameters are selection of an appropriate cell line, environmental factors such as growing medium, cell density, temperature, time of incubation, and the surface of culturing plasticware. The optimization for some of these parameters has been described in this section.

3.2.1 Cell line selection and assay method

American type culture collection (ATCC) has two different variants of PC-12 cells- one is the traditional PC-12 cells that grow in suspension and second is the adherent phenotype that has increased growth rate. The original suspension variant of PC-12 cells was used for all neurotrophic assays described in this chapter. This line had undergone quality control tests by ATCC to check for their differentiation potential on induction by NGF.[12]

An assay method was setup as shown in **figure 3-2** to assess the neuritogenic potential of banglene and its derivatives.

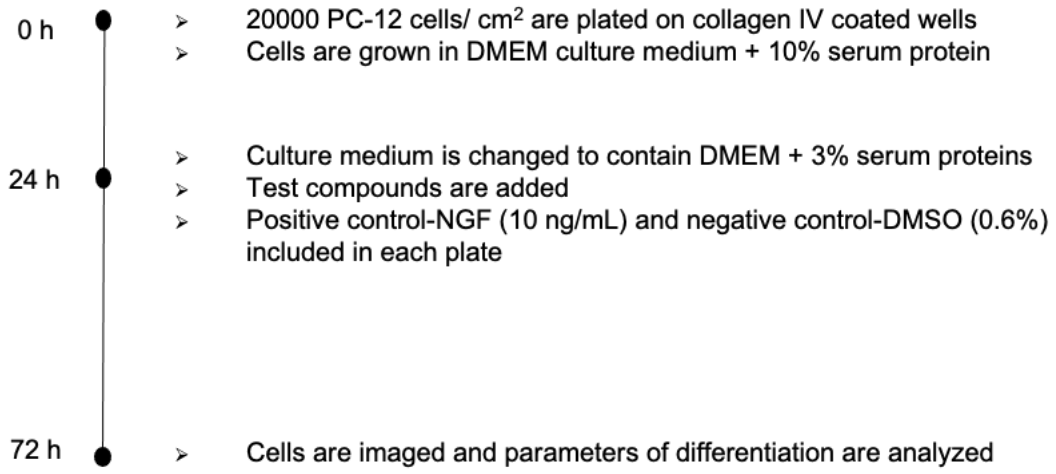

Figure 3-2. Basic setup of assay method for validation of neuritogenic activity in PC-12 cells.

This assay method was similar to the one used by the Fukuyama and Matsui groups to assess the neuritogenesis of banglenes. Briefly, a set number of PC-12 cells were plated on collagen type IV coated wells and grown in culture medium containing 10% serum proteins. The high serum concentration ensured that these cells did not differentiate as the conditions favoured proliferation and the collagen allowed a surface for cells to adhere. After 24 hours, the growth medium was replaced with medium containing decreased amount of serum proteins (3%) and then test compounds were added. DMSO was selected as the negative control as it was the vehicle in which test compounds were dissolved. The total amount of DMSO in a well was kept at a maximum 0.6%. Since NGF is the most commonly used agent to differentiate PC-12 cells, it was selected as the positive control. It is reported that the apparent minimum amount of NGF required to differentiate PC-12 cells is 10 ng/mL and that the percentage of neurite bearing cells is nearly the same in the presence of 10-100 ng/mL of NGF.[13] Based on this, 10ng/mL of recombinant human β NGF was selected as the positive control to induce neurite outgrowth. Later, I observed that 0.6% DMSO reduced NGF mediated neuritogenesis (**appendix 3, figure S22**), thus I adjusted the positive control to be 10 ng/mL of NGF + 0.6% DMSO. 72 hours after incubation of test and control compounds, these cells were then imaged and analysed for their neuritogenic activity.

3.2.2 Optimization of coating and other factors

The PC-12 suspension cells grow as small irregularly shaped cells which often cluster together, and some cells are lightly attached to non-coated flask surfaces. Adherence of these cells is important for differentiation and development of neurites. The substratum surface does not only affect cell adhesion but also affects the outgrowth of processes and survival *in vitro*.[14] Various coating materials have been used previously to support PC-12 neurite outgrowths such as laminin, fibronectin, poly-D-lysine, poly-L-lysine, polyornithine and Collagen I and IV. Out of these, studies have shown that Collagen type IV and laminin promote PC-12 cell adhesion better than fibronectin.[14,15] Besides these two, a combination of poly-L-lysine along with fibronectin or laminin also promotes adhesion better than these components alone.[15] Given these studies and ATCC recommendations, collagen type IV was selected as the coating of choice. The concentration of collagen type IV needed to coat was highly variable in various protocols, hence I tested a concentration range of 0-4 µg/cm^2 to assess the effect on neurite outgrowth. In the absence of collagen IV, cells did not adhere to the plate and no neurite outgrowth was observed. At a concentration of 2-4 µg/cm^2 substantial neurite outgrowth was seen upon induction with NGF (**figure 3-3**) and this range was selected for all further experiments.

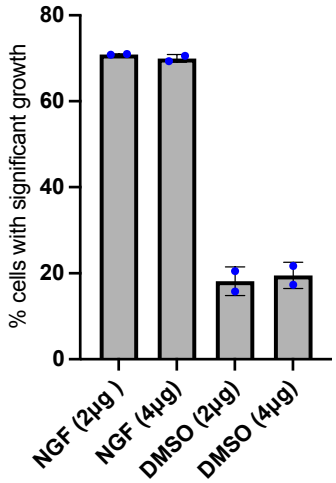

Figure 3-3. Comparison of neurite outgrowth on plates coated with different concentration of collagen type IV.

The passage number of PC-12 cells is another important factor which determines the sensitivity of the cells to induction by neurotrophic agents. Mejía and co-workers have shown that there are differences in morphology between PC-12 cells in an early passage (passage 5) vs. in a late passage (passage 16). They showed that proliferating cells from the later passage are more heterogenous with a fibroblast like morphology and no change in morphology was observed upon induction by NGF.[16] Kinarivala and co-workers have reported that passage variation can result in false identification of neuroprotective compounds, as cells from later passages (> 17) were more resilient to cell death caused by serum deprivation.[17] Given these studies, I used PC-12 cells from passage 4-5 in the neuritogenic assay.

Since the assay lasts 72 hours, there was a high possibility of evaporation of media during the incubation period especially in 96 well plates. This can change the effective concentration of the test molecules and can affect the cell metabolism rate. As a means to minimize evaporation, no cells were plated in the outer boundary wells of a plate and instead these boundary wells were flooded with buffer.[18]

3.2.3 Optimization of imaging and analysis methods

Since the assessment of neuritogenic potential of banglenes was highly dependent on the morphological change of PC-12 cells, it was important to establish a robust method for imaging and analysis. The most common method for quantifying neurite outgrowth is to take phase contrast images of cells post differentiation and then assess the quantity of differentiated cells by visual detection and manual measurement. The length of neurite outgrowths can be quantified from images in a semi-automated fashion using ImageJ plugins such as simple neurite tracer (SNT) or NeuronJ. [15,19–22]

I followed this process, which although fairly simple, had its disadvantages. It was very time and labour intensive and was prone to errors as PC-12 cells tend to proliferate and differentiate in clumps, which makes distinguishing individual neurites for measurement challenging. Additionally, it is rare to locate a field of view with only single cells, which would minimize the underreporting of neurites due to clumping. Another challenge in this original analysis method, is that it is very dependent on the contrast between cells and

background. A high level of contrast was difficult to achieve without staining the cells. In an attempt to increase the contrast, cells were fixed and stained with 0.1% methylene blue. This did increase the ability to differentiate neurites from the background but made the image segmentation of cell bodies harder as they had clumped together, thus this method was not followed. Also, neurites tend to be on a different plane than cell bodies making it difficult to find a good focal plane with sufficient contrast.

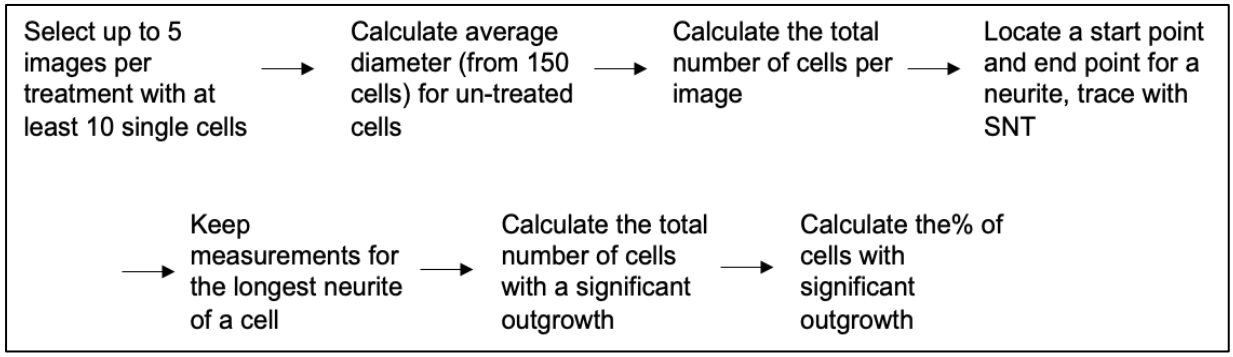

Figure 3-4. Schematic of image analysis for cells with significant neurite outgrowth.

The analysis of neurite growth parameters as shown in **figure 3-4** using ImageJ plugins had its own set of challenges. The SNT plugin traces neurites by connecting the dots between the start point and end point selected as input. Neurites from differentiated PC-12 cells have different lengths, some of them as short as 7 µm which makes it difficult to input an accurate start and end point. In an effort to minimize error, it was easiest to measure the longest neurite of a cell, but this required measuring multiple branching neurites to decide the longest one. Sometimes with longer neurites with multiple branch points, this tracing is not accurate, and would need to be redone by manually adding more path points. Once all the lengths of the longest neurites were measured, a cell was considered to have significant neurite outgrowth if it was longer than the diameter of the cell.[2,4,8,15,19,22,23] This threshold although commonly used seems arbitrary because average neurite lengths of neurites in PC-12 cells increase rapidly up to 14 days before plateauing and the day at which neurite length were measured in previously published assays varied from 2 to 7 days.[3] This semi-automated method of analysis is cheap and easy to implement, however it limited the number of cells that could be analysed and introduced a bias while selecting fields of view with single cells.

Automated image analysis using fluorescent markers to visualize cell bodies and neurite growth was the next method tried to overcome the challenges posed by manual imaging and analysis. First, I fixed the cells and stained the nucleus with Hoechst stain. The cell body and neurites were labelled using an anti-β-tubulin III antibody followed by a secondary antibody conjugated to Alexa Fluor 488. The fluorescence labelling ensured a high signal to noise ratio for further analysis. Following immunofluorescence staining, the plates were imaged at 10 × magnification using a high content analysis system from Molecular Devices. The autofocus was set manually using the plate bottom and well bottom and the exposure time was determined for each wavelength. This system also allowed for a z-stack of images to be taken which were then combined to form a 2D projection image. Twenty-five images were taken such as to cover the entire well, this provided fairly unbiased data from which cell-based measurements could be taken. The cell segmentation was done by the analysis software based on the input parameters such as intensity above background, maximum and minimum width or area of nucleus, cell body and neurites (segmentation shown in **figure 3-5**). Several images were selected and analysed at random to fine tune the parameters. After segmentation, cell specific measurements were obtained such as mean, median and maximum process length, cell body area and number of processes and branches per cell. Image specific measurements were also obtained such as total number of cells, cells with significant outgrowth per image and total processes per image. The algorithm determined a neurite outgrowth as a significant outgrowth based on a threshold neurite length given by the user. Two values were tried, one where a neurite was defined as a process with length greater than the average cell diameter and the second where the neurite had a length greater than the average cell radius. Since the presence of a process would denote a change in phenotype, processes with length greater than average cell radius were selected as a significant growth.

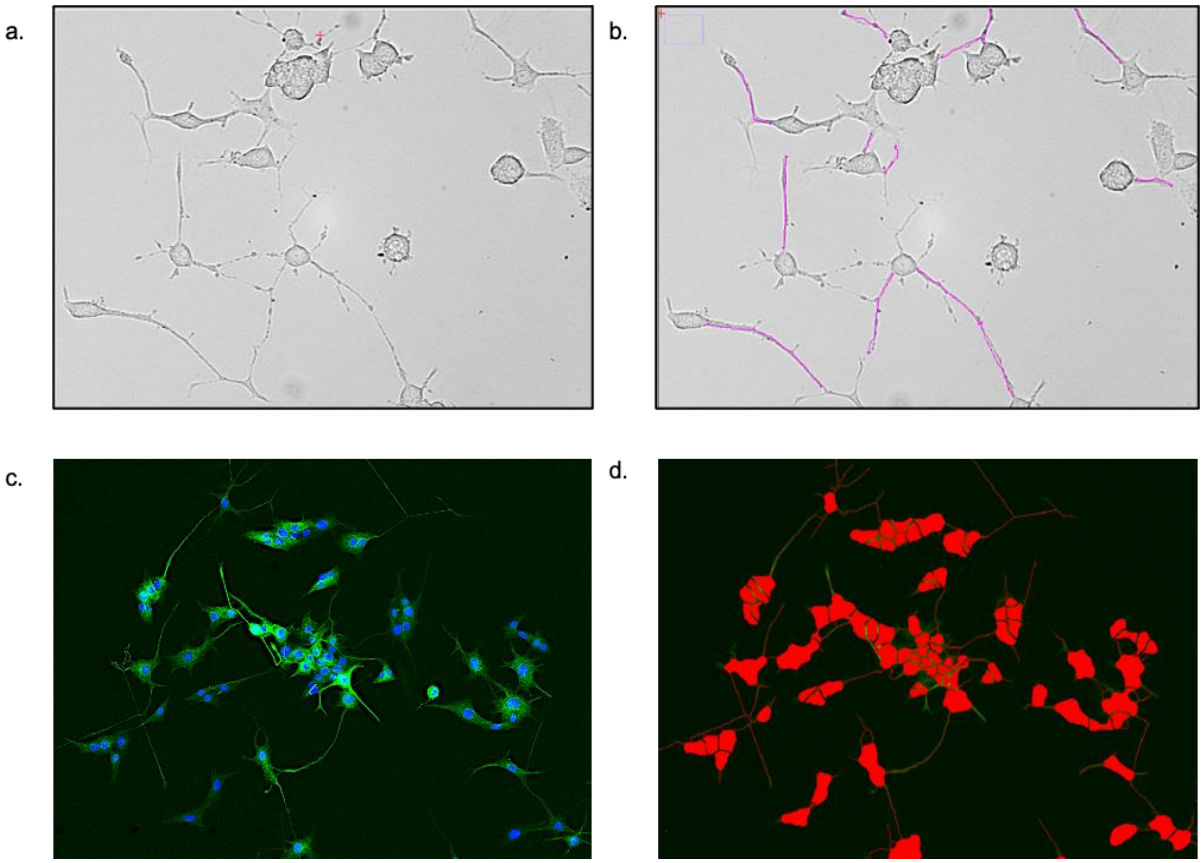

Figure 3-5. Comparison between manual (a,b) and automated (c,d) imaging and analysis. Panels b and d show tracing of neurites for images in panel a and c respectively.

The automated imaging and analysis method made the process faster and resulted in a more wholistic representation of data. It removed the user bias originating from selecting which cells to image and could collect data from cell clusters as well as single cells.

3.3 Effect of banglenes in PC-12 neuritogenesis assay

After optimizing all the parameters for the neuritogenesis assay, banglenes were tested in PC-12 cells. First (±) *c*-BG and (±) *t*-BG were tested individually at 30 µM, as at this concentration they demonstrated neurotrophic active in the study by the Matsui and Fukayama group. Unfortunately, (±) *c*-BG at 30 µM crashes out in medium (**figure 3-6b**). This precipitation was also observed in media without added serum proteins. All further

studies were therefore conducted with (±) *t*-BG, which did not demonstrate any solubility issues at 30 μM.

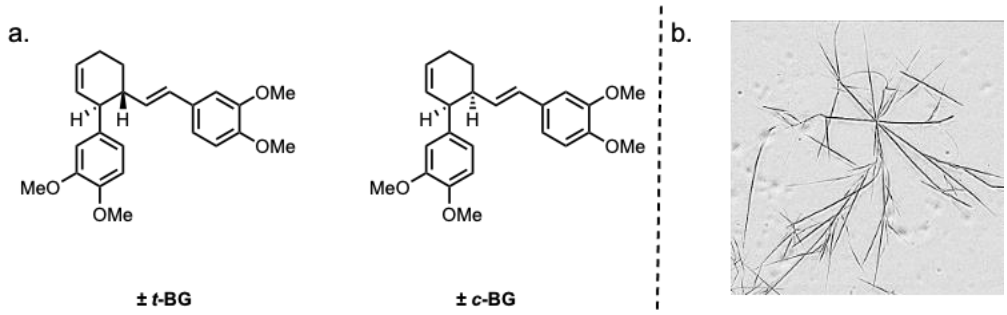

Figure 3-6. (a) Structures of *cis* and *trans* baglene (b) Image of *c*-BG crystal at 10X magnification taken 24 h after addition of *cis*-BG in DMEM medium with 5% HS and 5% FBS.

I was able to observe a roughly 2.5-fold increase in neuritogenesis when cells were treated with 30 μM of (±) *t*-BG (**figure 3-7**). This increase in neuritogenesis was modest compared to that observed following treatment with 10 ng/mL of NGF but had high statistical significance.

Many neurotrophic molecules potentiate NGFs neuritogenic ability when dosed along with NGF.[24–36] Given the modest increases in neuritogenesis with (±) *t*-BG alone, I tested it in combination with NGF, and this resulted in a strong augmentation of neuritogenesis. Concurrent to increases in neuritogenesis, I also saw increases in cell body area as the differentiating cells flattened.

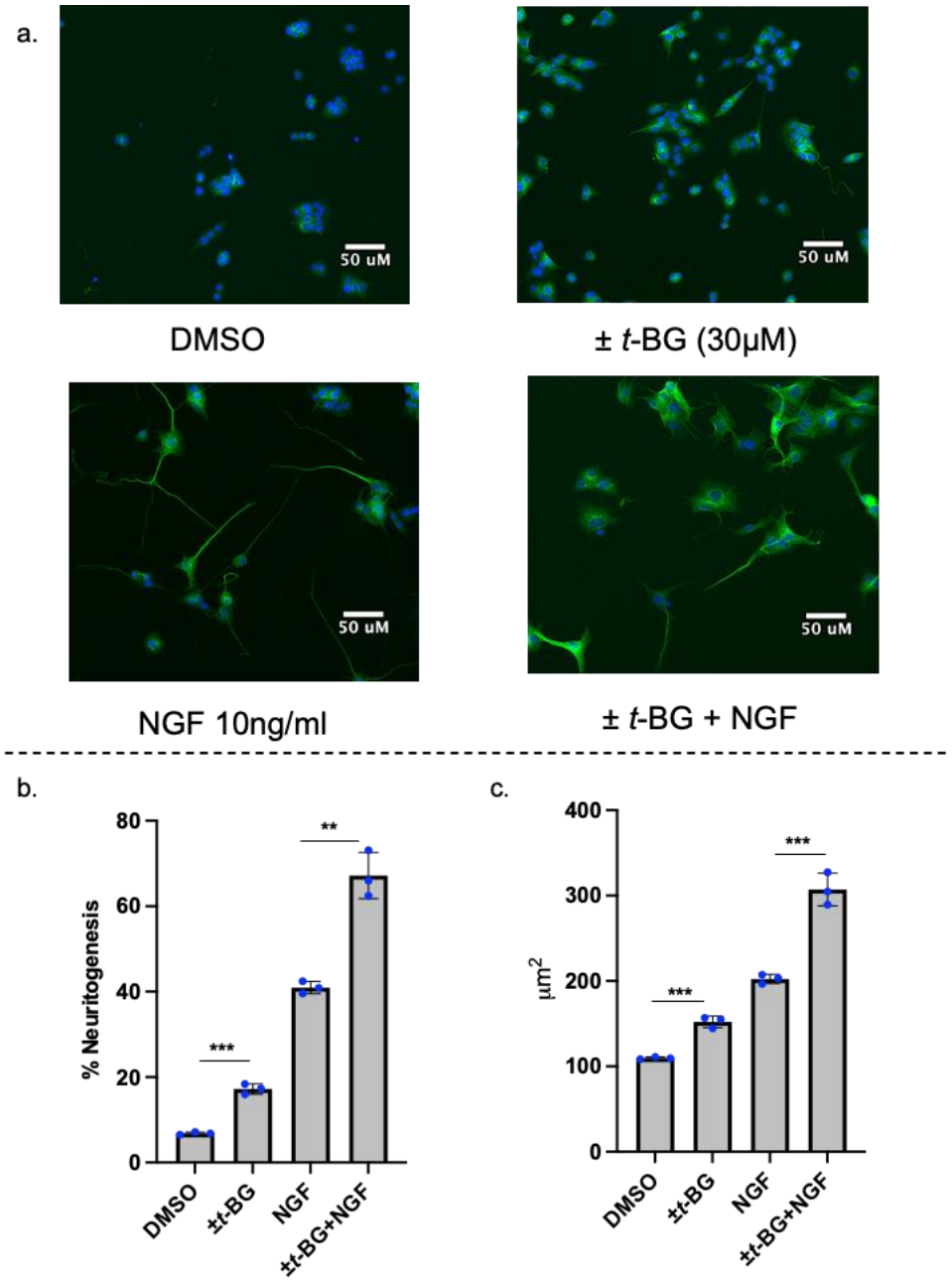

Figure 3-7. Effect of NGF and (±) t-BG on PC-12 cell line post 48h incubation (a) Neuritogenesis cell assays in PC-12 cell line. Cells were treated as follows: DMSO (control, 0.6%), (±) t-BG (30 μM + 0.6%DMSO), NGF (10 ng/mL + 0.6% DMSO), and (±) t- BG + NGF (30 μM t-BG + 10 ng/mL NGF + 0.6% DMSO). Nucleus = blue and cell body = green (b) %Neuritogenesis post treatment was calculated as a percentage of total number of cells

that had neurites > 5 μm. (c) Average cell body area measured for each treatment. p-value measured by unpaired t-test ***p < 0.001, **p < 0.01.

After establishing the NGF potentiating effect of (±) *t*-BG, next I tested the neuritogenesis activity of its individual stereoisomers.

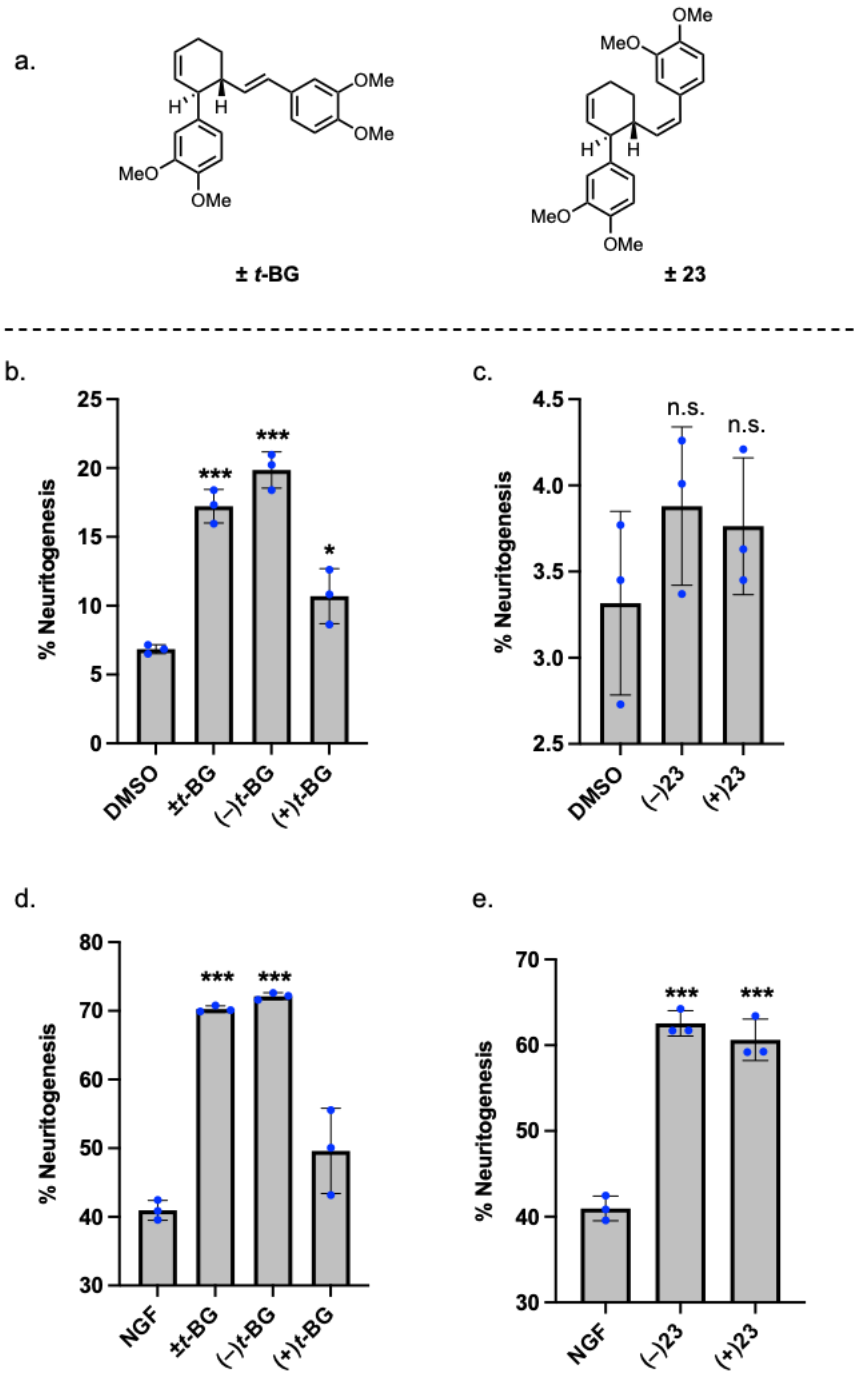

Figure 3-8. Quantification of neuritogenesis caused by *t*-BG isomers in PC-12 cell assays (a) Structure of test compounds. (b) & (c) Trend of neuritogenesis after treatment with 30 μM of racemic (±) *t*-BG or individual enantiomers (–) *t*-BG, (+) *t*-BG, (–) 23, (+) 23. (d) & (e) NGF neuritogenesis potentiation: all compounds were tested at 30 μM in the presence of 10 ng/mL of NGF. %Neuritogenesis post treatment was calculated as a percentage of total number of cells that had neurites > 5 μm. p-value measured by ANOVA followed by Dunnett's multiple comparison test vs. DMSO (b. and c.) and vs. NGF (a and d) *$p < 0.05$, ***$p < 0.001$.

As shown in **figure 3-8b** and **c**, all stereoisomers of *t*-BG exhibited differences in activity when tested alone. (–) *t*-BG caused the highest neuritogenesis while (+) *t*-BG had a minimal effect. The Z alkene isomers of *t*-BG: (–) **23** and (+) **23** did not increase differentiation by themselves.

When dosed in combination with NGF (**figure 3d-e**), (–) *t*-BG is observed to be the active enantiomer, while (+) *t*-BG causes minimal neuritogenesis. Interestingly, Z alkene isomers (+) **23** and (–) **23**, both exhibited potentiating effects in the presence of NGF, although they augment NGF neuritogenesis nearly 1.5 times lower as compared to (–) *t*-BG.

After determining that (–) *t*-BG is likely the active enantiomer, the dose dependency of its neuritogenic activity was established (**figure 3-9**). By itself, (–) *t*-BG showed an increase in neuritogenesis from 15 μM. At a concentration of 60 μM the compound had solubility issues (cLogP = 5.12, predicted by Chemicalize) which is why the maximum concentration dosed is 30 μM. It was challenging to estimate the EC_{50} of (–) *t*-BG with these four data points, as there was no plateau at the higher end of dosing (**figure 3-9a**). More data points need to be measured between 7.5-45 μM, solubility allowing, to generate a curve from which an accurate EC_{50} can then be calculated. When dosed in combination with fixed concentration of 10 ng/mL NGF, the trend is similar, with substantial NGF potentiation starting at 15 μM and a calculated EC_{50} of 14 ± 1 μM.

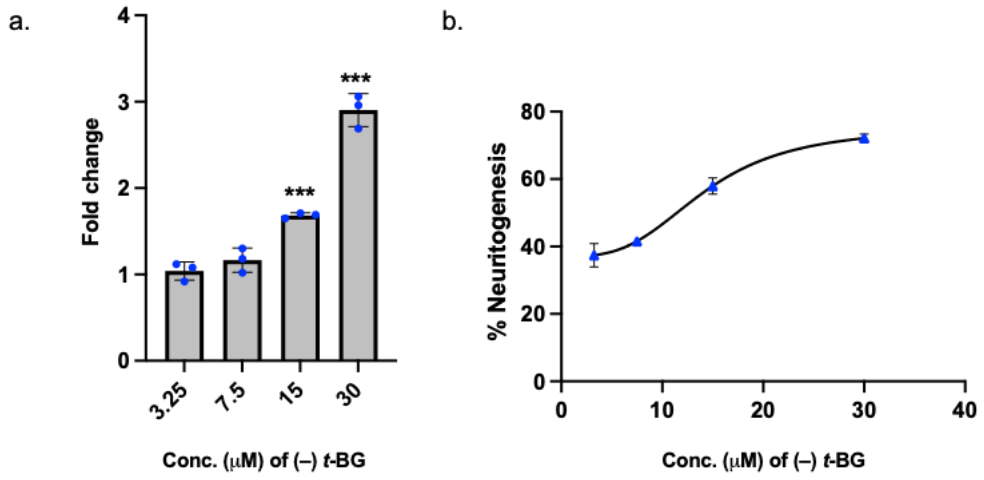

Figure 3-9. Dose dependent neuritogenic response of (–) *t*-BG (a) Fold change of neuritogenesis after treatment with increasing (μM) concentrations of (–) *t*-BG for 48 h. % Neuritogenesis was calculated as a percentage of total number of cells that had neurites > 5 μm. Fold change was calculated as %neuritogenesis (Compound) / % neuritogenesis (DMSO). p-value measured by unpaired t-test vs. DMSO ***$p < 0.001$. (b) Dose response curve of the potentiating effect of (–) *t*-BG when dosed along with 10 ng/mL of NGF. Curve simulated by GraphPad Prism using a dose-response curve model with variable slope (four parameters) with least squares fit.

Collectively, these modulated responses show that the activity of *t*-BG is structure dependent, increasing the likelihood of a specific recognition event in the PC-12 cell. Prior to this work, the enantiomers of *t*-BG had only been tested for P-glycoprotein antagonist activity.[37]

3.4 Structure-activity relationship of banglene derivatives

The long-term goal of this project is to design mechanistic probe variants of *t*-BG which can subsequently be utilized in cellular assays to identify a cell recognition partner and its localization in the cell. In order to achieve this, it was necessary to recognize which structural feature of the banglene scaffold would tolerate modifications without loss of activity. I conducted a preliminary SAR study to identify these sites. Since the neuritogenic response was the most pronounced for the combined treatment of *t*-BG and NGF, the initial screen to test derivatives was performed in combination with NGF.

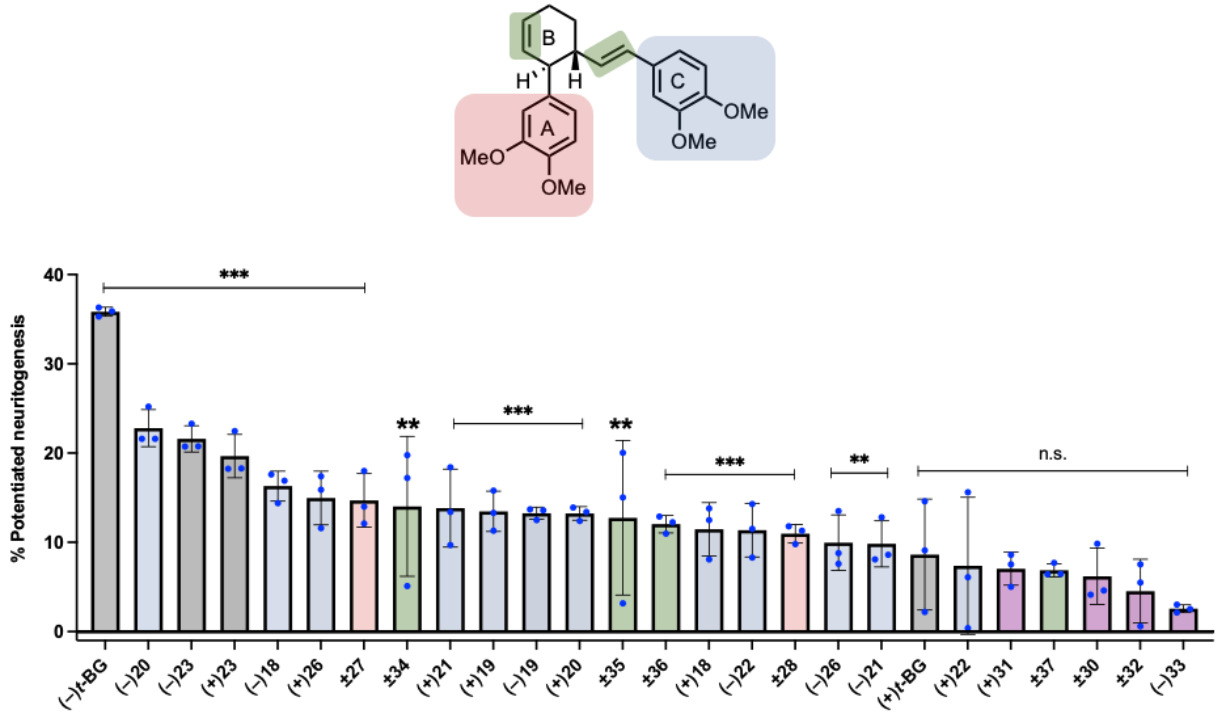

Figure 3-10. Neuritogenesis potentiated by banglene analogues in the presence of NGF. All compounds were tested at 30 µM along with 10 ng/mL of NGF and 0.6% DMSO. %Neuritogenesis post treatment was calculated as a percentage of total number of cells that had neurites > 5 µm. %Potentiated neuritogenesis = % neuritogenesis (30 µM compound +10 ng/mL NGF) – %neuritogenesis (10 ng/mL NGF). p-value measured by ANOVA followed by Dunnett's multiple comparison test vs. NGF *p < 0.05, **p < 0.01, ***p < 0.001. Colours reflect the location of *t*-BG modification for each derivative tested. Blue = A ring; green = B ring; red = C ring; purple = both A and C rings.

Following the screening, the data was analyzed to calculate the amount of neuritogenesis potentiated by the derivatives. This was done by subtracting the percentage of neuritogenesis caused by NGF alone from the percentage of neuritogenesis caused by the combination of derivatives and NGF.

As can be seen in **figure 3-10**, (–) *t*-BG elicited the largest increase in neuritogenesis. Many derivatives were identified that cause a substantial NGF potentiating effect, although none of them had activity as high as (–) *t*-BG. Modifications were tolerated either on ring A or

ring C, but if modifications were made on both rings, it resulted in a loss of activity. Some modifications of the two alkenes were also tolerated.

Modifications on ring A are tolerated as shown in **figure 3-11**. The potentiated neuritogenic activity of (±) **27** and (±) **28** is half of (–) *t*-BG. (±) **29** was the only derivative that had a hydroxyl group and when tested at 30 µM it resulted in high levels of cell death.

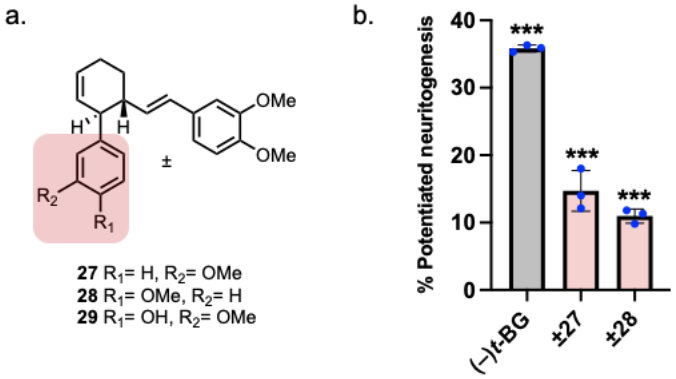

Figure 3-11. Potentiated neuritogenic activity of derivatives with modifications on ring A. (a) Structure of derivatives with modified ring A.(b) Trend of potentiated neuritogenesis of ring A modified derivatives (subset of **figure 3-10**).

Looking at modifications on ring C (**figure 3-12**), derivative (–) **20**, has NGF potentiating activity that is statistically similar to both the Z alkene derivatives. This group of derivatives also has the highest NGF potentiating activity of all derivatives tested. Derivatives **24** and **25** had solubility issues at 30 µM concentration and were not tested. Both enantiomers of derivative **18** had similar activity. For derivative **22**, interestingly (–) **22** shows significant but low NGF potentiating activity, whereas (+) **22** is not active. Its Z alkene isomers (+/–) **26** on the other hand shows similar activity to (–) **22**.

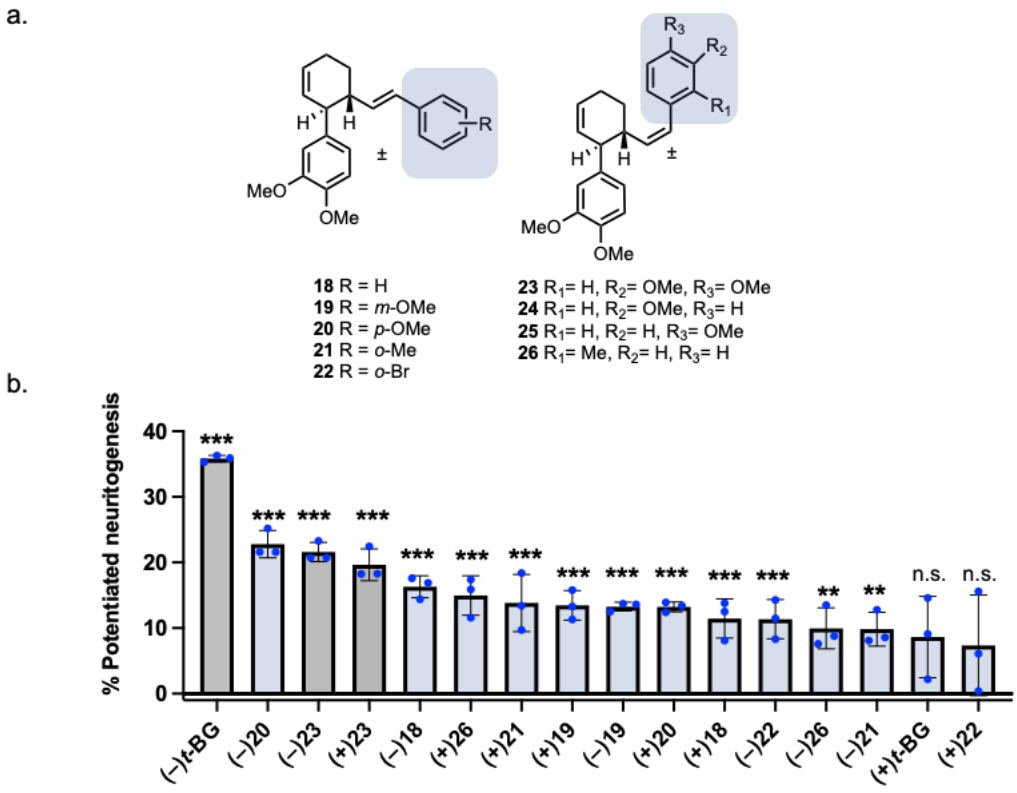

Figure 3-12. Potentiated neuritogenic activity of derivatives with modifications on ring C. (a) Structure of derivatives with ring C modified (b) Trend of potentiated neuritogenesis of ring C modified derivatives (subset of **figure 3-10**).

Derivatives with modification on both ring A and C did not have any neuritogenic activity (**figure 3-13**). This indicates that it is important to have the 3,4-dimethoxy substitution in at-least one of the rings. Derivatives **32** and **33** despite having rings A and C *cis* to the cyclohexene were still soluble at 30 µM in cell media with added serum proteins.

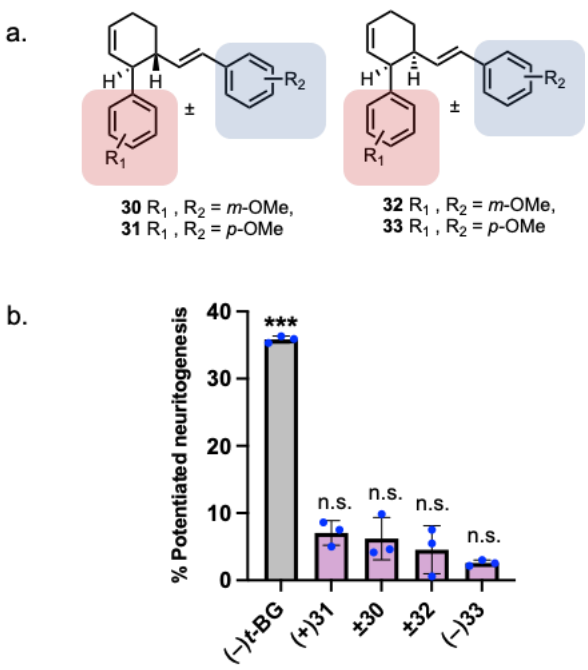

Figure 3-13. Potentiated neuritogenic activity of derivatives with modifications on both ring A and C. (a) Structure of derivatives with ring A and C modified (b) Trend of potentiated neuritogenesis of ring A and C modified derivatives (subset of **figure 3-10**).

Derivatives (±) **34** and (±) **35** where both the alkene rings were hydrogenated retained activity. With ring A and C substitutions being the same as *t*-BG for these derivatives, it is likely that the conformational flexibility of **34** and **35** is what causes the activity to decrease by roughly half. Cyclopropanation of the B ring, which in contrast retains rigidity similar to that of an alkene, was tolerated for *trans* derivative (±) **36** but also resulted in a similar decrease in potentiating effects. Derivative (±) **37** did not have any potentiating activity, likely due to rings A and C being *cis* to the cyclohexene (**figure 3-14**).

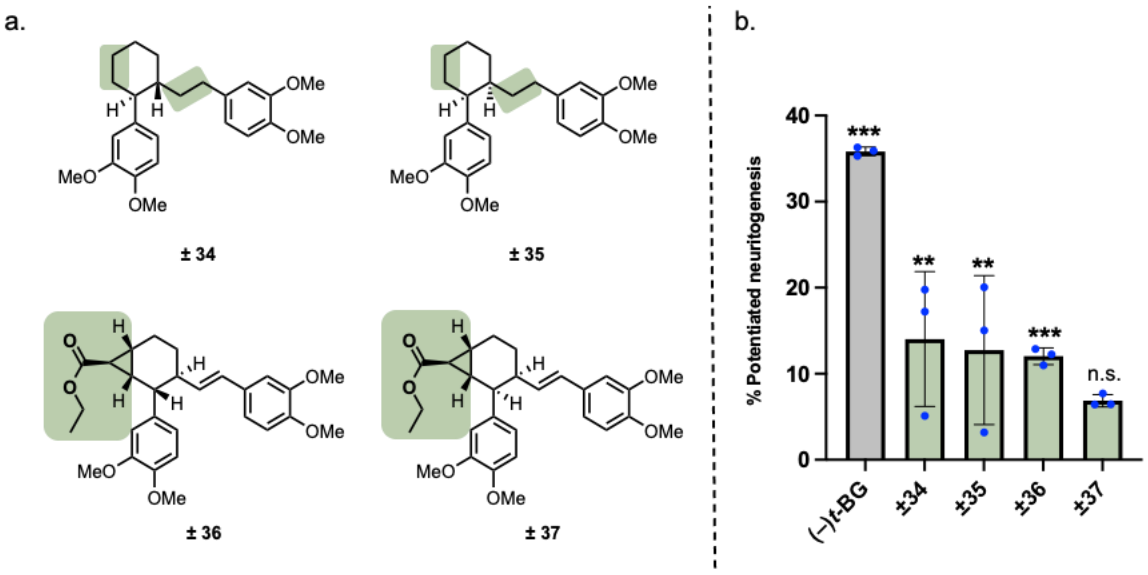

Figure 3-14. Potentiated neuritogenic activity of derivatives with modifications of banglene alkenes (a) Structure of derivatives with hydrogenated alkenes and cyclopropanation of ring B (b) Trend of potentiated neuritogenesis for derivatives (±)34 – (±)37 (subset of **figure 3-10**).

With the results of this initial screen, I examined a few derivatives to understand their neuritogenic activity in the absence of NGF (**figure 3-15**). The most active derivative, (–) **20**, its ring A analogue (±) **28**, hydrogenated *trans* derivative (±) **34**, and cyclopropyl ester derivative (±) **36** were tested. Interestingly, only compounds **34** and **36** demonstrated neuritogenic activity in this assay. Therefore, modifications to the substitution patterns on the A and C rings appear to abrogate neuritogenic activity, despite being tolerated for NGF potentiation responses. Further, the lack of neuritogenic activity of Z-alkene derivatives (–) **23** and (+) **23** also demonstrates that neuritogenic activity is sensitive to styrenyl alkene geometry.

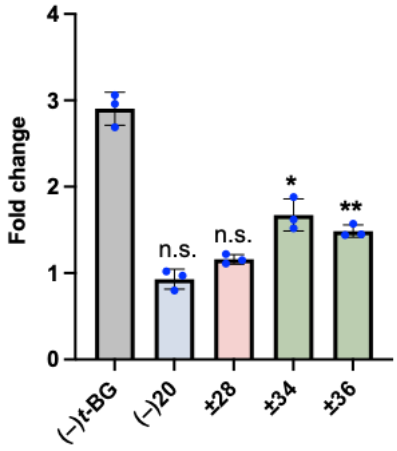

Figure 3-15. Fold change of neuritogenesis caused by treatment with 30 μM of banglene derivatives + 0.6% DMSO. % Neuritogenesis was calculated as a percentage of total number of cells that had neurites > 5 μm. Fold change was calculated as %neuritogenesis (Compound) / %neuritogenesis (DMSO), p-value measured by unpaired t-test, values compared to control (DMSO), *p < 0.05, **p < 0.01, ***p < 0.001

From these two SAR screens, it can be seen that the degree of potentiating activity for banglene derivatives is not proportional to neuritogenic activity in the absence of NGF. Although derivative (–) **20** has the highest NGF potentiating activity, it does not cause substantial neurite outgrowth on its own. Since (±) **34** and (±) **36** are active in the presence and absence of NGF, ring B seems to be the most desirable site for modification to generate mechanistic probes. Further, in a study published in 2020, a neurotrophic molecule was designed in which the tricyclic core of neovibsanin was fused to ring B of *t*-BG.[38] This hybrid new molecule had a neurotrophic activity lower than *t*-BG but emphasizes the ability of ring B to be modified.

The ester containing derivative (±) **36** provides a good starting point to access a mechanistic probe, due to the ester functional handle. Derivative **36** can potentially be used in a pull-down assay by ligating it to a solid support through an amide bond. This strategy tests for cellular recognition partner(s).

3.5 Studies to determine the mechanism of action

3.5.1 Investigating neuritogenesis caused by antioxidants

Some neurotrophic molecules such as flavonoids that trigger neuritogenesis also act as antioxidants. It is believed that in some part this neuritogenic activity can be attributed to their antioxidant nature. However, some of these molecules, such as luteolin, (–) epicatechin or α-phenyl-N-tert-butylnitron caused neurite outgrowth by activating the Erk signaling pathway.[39–41] The antioxidant activity of luteolin is linked to its Erk activation, as inhibition of Erk resulted in attenuation of luteolin induced binding of nuclear factor E2-related factor 2 to antioxidant response element.[39] Similarly, α-phenyl-N-tert-butylnitron induced Erk activation was counteracted upon addition of the antioxidant N-acetylcysteine.[40]

Since *t*-BG possesses two electron-rich aromatic rings, it may also act as an antioxidant. Prior to demonstrating that the individual enantiomers of *t*-BG have differing activity, I had first investigated whether the neurotrophic activity of (±) *t*-BG was likely due to its antioxidant behaviour. Two antioxidants were selected to test in the PC-12 neuritogenesis assay. Tocopherol acetate was selected due to its lipophilicity and resveratrol was selected due to the electron rich styrenyl aromatic rings. While trans-resveratrol treatment resulted in minor increases in neuritogenesis levels in an NGF potentiation assay, neither antioxidant appeared to have similar levels of neuritogenic activity compared to *t*-BG in the same assay (**Figure 3-16**).

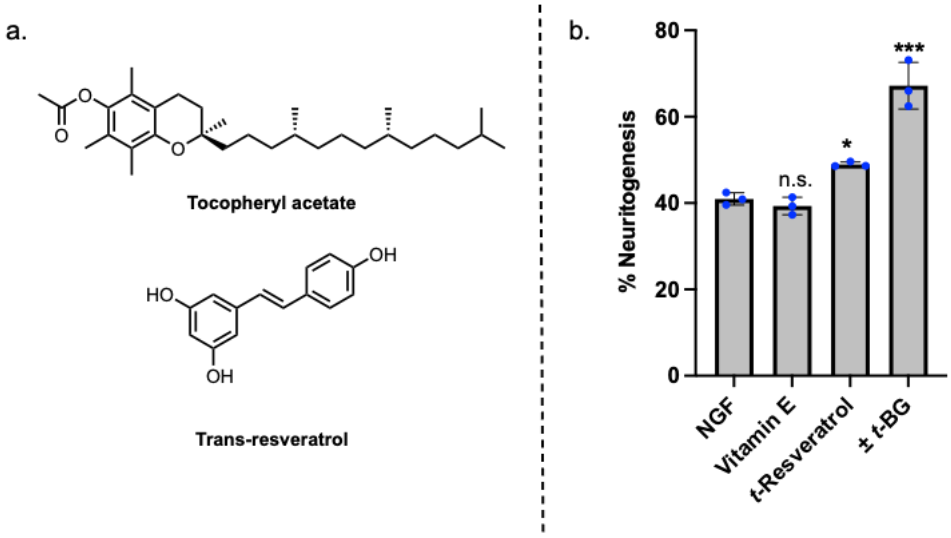

Figure 3-16. Effect of common antioxidants on PC-12 neuritogenesis. (a) Structure of antioxidants. (b) Quantification of neuritogenesis in PC-12 cell assays common antioxidants when tested at 30 μM in the presence of 10 ng/mL of NGF. p-value measured by ANOVA followed by Dunnett's multiple comparison test vs. NGF *$p < 0.05$, ***$p < 0.001$.

3.5.2 Investigating induction of NGF release

A well-understood mechanism of neuritogenesis and neuroprotection caused by various neurotrophic molecules is their ability to induce NGF secretion.[42–47] Some examples of neurotrophic molecules that trigger NGF release are shown in **table 3-1**.

Neurotrophic molecule	Model cell system	NGF detected as
Hericenones C–E (+ NGF)	PC-12	Protein
	mouse astroglial cells	
Huperzine A	SHSY5Y	mRNA and protein
Fellutamide B	L-M fibroblast	Protein
Scabronine G	1321N1	Protein
Lyconadins D-E	1321N1	mRNA

Table 3-1. Neurotrophic molecules inducing NGF secretion.

The release of NGF protein in these studies was done by commercially available enzyme linked immunosorbent assays (ELISA). However, the antibodies used in these assays can also detect pro-NGF with a lower sensitivity.[48] This is important when detecting NGF protein levels in PC-12 cell media, as they release pro-NGF in cell media. Soligo and co-workers have recently demonstrated that NGF primed PC-12 cells (exponentially grown PC-12 cells in the presence of 50 ng/mL NGF) are known to release pro-NGF upon treatment with NGF in serum free media and that this secreted pro-NGF does not get processed into mature NGF.[49] It is believed that pro-NGF is prone to cleavage in the presence of serum, although there is no reported evidence supporting this cleavage.[50,51]

Hericenone C–E when dosed with 5 ng/mL of NGF are the only neurotrophic small molecules reported to induce NGF synthesis in PC-12 cells. Phan and co-workers

demonstrated that this secreted NGF was in part responsible for Hericenone C–E's neuritogenic effect.[47]

Given this example, I investigated whether (–) *t*-BG induces NGF secretion in PC-12 cells using an ELISA. An ELISA kit for detection of secreted NGF was used with the assumption that both NGF and pro-NGF would be detected. As seen in **figure 3-17b**, both (–) *t*-BG and the second most active derivative (–) **20**, when dosed along with NGF, caused a measurable increase in the concentration of secreted NGF (or pro-NGF).

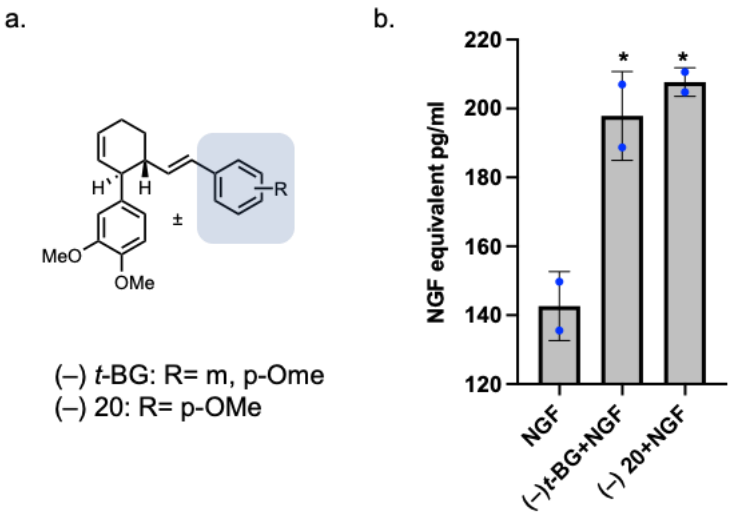

Figure 3-17. NGF levels as measured by ELISA. Analysis of cell media 48 h after dosing 30 µM of test compounds with 10 ng/mL NGF. p-value measured by unpaired t-test vs. NGF, *$p < 0.05$.

Since the detection of secreted NGF was done in cell medium containing serum protein, it is likely that only mature NGF was detected. This secreted NGF can be in part responsible for (–) *t*-BG's potentiation of NGF's neuritogenic effect.

However, if the pro-NGF secreted by PC-12 cells is not fully processed into mature NGF in the cell media then pro-NGF signalling pathways can be activated. Pro-NGF signalling, unlike mature NGF signalling has not been fully elucidated. There is growing evidence showing that the effects of pro-NGF are dependent on the receptor balance of TrkA, p75 NTR and Sortilin.[52] Sortilin is the molecular switch that can trigger either a pro-apoptotic or

neurotrophic response in a cell. Sortilin can form a complex with p75 NTR and when pro-NGF binds to this sortilin/p75 NTR complex, it causes a pro-apoptotic response. In the absence of this complex, pro-NGF has been shown to bind to TrkA after recruitment of p75 NTR.[53] A study in 2017 showed that under normal circumstances, when cells express both TrkA and p75 NTR, and in environmental conditions that support growth, pro-NGF has a neurotrophic effect. When there are low levels of TrkA receptors, pro-NGF primarily has a pro-apoptotic response.[54]

Unprimed PC-12 cells, like the ones used in assessing (–) *t*-BG's neuritogenic effect tend to have lower amounts of TrkA compared to p75 NTR.[51] In this case we should observe an apoptotic response and not a neurotrophic response from any secreted and un-processed pro-NGF. This is contradictory to the observed increase in neuritogenesis caused by the combination of (–) *t*-BG and NGF.

A corollary of this NGF (or pro-NGF) secretion mechanism is that if the combination of *t*-BG + NGF was active *in vivo*, then in a system such as uninjured brain where the proteolysis machinery of pro-NGF remained functional, we would potentially observe an increase in NGF protein levels.

3.5.3 Effect on canonical neurotrophic pathways

Since (–) *t*-BG potentiates the effects of NGF and induces the release of NGF (or pro-NGF) when administered with NGF, it is possible that this response is facilitated by NGF-mediated signal transduction pathways. NGF neurotrophic signal transduction is initiated by the binding of NGF to tropomyosin receptor kinase A (TrkA, **figure 3-18a**). Upon binding of NGF, TrkA dimerizes and undergoes autophosphorylation, which in turn initiates signal transduction through protein kinase C (Pkc), protein kinase B (Akt/Pkb), and/or mitogen activated protein kinases (Raf, Mek, Erk). TrkA activation of these kinases is associated with neural plasticity, cell survival, and differentiation responses, respectively.[55]

To investigate the effect that the combination of (–) *t*-BG and NGF has on TrkA initiated signal transduction in each of these parallel pathways, neuritogenesis levels were measured in the presence of three chemical inhibitors, triciribine (iAkt), Gö 6983 (iPkc), and

SCH772984 (iErk). Triciribine inhibits the phosphorylation, and subsequent activation, of Akt1/2/3.[56] Triciribine binds to the Akt pleckstrin homology (PH) domain and prevents the localization of Akt to the plasma membrane, which is required for phosphorylation and activation of Akt by Pdk1. Gö 6983 is a Pkc inhibitor, and acts as a competitive inhibitor of ATP binding.[10,57] Gö 6983 has been shown to be pan-specific, inhibiting the α, b, γ, and δ isoforms of Pkc. SCH772984 is also a competitive inhibitor of ATP binding, but for Erk1/2. Despite similar mechanisms, Gö 6983 and SCH772984 have demonstrated high specificity for their target kinases, with the latter having been tested on over 300 different kinases.[58]

As seen in **figure 3-18b**, inhibition of Pkc and Erk activity by Gö 6983 (iPkc) and SCH772984 (iErk) resulted in a substantial decrease in NGF induced neuritogenesis observed in PC-12 cells. However, inhibition of Akt activity by triciribine treatment (iAkt) did not result in a similar decrease in neuritogenesis levels. There are competing hypotheses for the activity of Akt in PC-12 cells. Many groups have shown that Akt affects neurite elongation and branching while others have shown that instead Akt only affects cell survival. There is also evidence that Akt negatively regulates neurite elongation promoted by growth factors.[59–61] Given these conflicting reports, PC-12 cells may not be the most appropriate model to study the role of Akt in neurotrophin triggered differentiation.

Interestingly, (–) *t*-BG treatment rescued NGF induced neuritogenesis levels in the presence of these inhibitors and further resulted in potentiated neuritogenesis that was statistically similar to levels observed in the absence of the inhibitors. A similar trend was observed for neurite elongation (**figure 3-18c**.).

The total outgrowth per cell was also calculated as this would include the addition of all neurites and not just the measurement of longest one (**figure 3-18d**). This was important as these kinases can affect neurite initiation and these newly formed neurites may not have reached a significant elongation length. Addition of the inhibitors with NGF resulted in a trend similar to neuritogenesis, where iPkc and iErk reduce the total outgrowth per cells and iAkt has no effect. However, a substantial decrease in total outgrowth per cell was observed with iAkt and iErk on the combined treatment of (–) *t*-BG and NGF. The decrease caused

by iAkt is surprising as it caused no decrease in total outgrowth per in cells treated with only NGF; this data should be interpreted cautiously.

Average branches of neurites per cell were quantified as shown in **figure 3-18e**. iPkc and iErk led to a reduction in the number of branches on both cells treated with NGF and those treated with (–) *t*-BG+NGF. The effect of iAkt was conflicting as it increased the average number of branches for cells treated with NGF but decreased it for cells treated with (–) *t*-BG and NGF.

This data indicates that the NGF potentiating neuritogenic activity of (–) *t*-BG is not expressly reliant on Pkc or Erk activity. However, iErk does affect the mean total outgrowth per cell which would hint that it affects neurite initiation. The data for iAkt is conflicting for phenotypic changes associated with neurite outgrowth and it would be better to test its effect on cell survival.

The lack of sensitivity on the neuritogenic response post the combined treatment of (–) *t*-BG and NGF to pan-Pkc and Erk1/2 inhibitors suggests the mechanism may not be a result of direct TrkA activation. One important factor to be noted is that the concentration of iPkc and iErk used in the inhibition assay caused a decrease in NGF mediated neuritogenesis by ~10%. It might be important to establish a dose response curve of these inhibitors and concentrations that lead to a more substantial decrease in neuritogenesis should be used. Any increase in the concentration of inhibitors should be done after assessing its effect on cell survival. Another way of understanding if the combined treatment of (–) *t*-BG and NGF perturbs these kinases would be to assess the phosphorylation levels of these kinases.

An alternate interpretation of these results would be that the combined treatment of (–) *t*-BG and NGF either activates elements of neuritogenic signalling response pathways downstream of Pkc and Erk or that it affects a system which is independent of canonical NGF signalling transduction pathways.

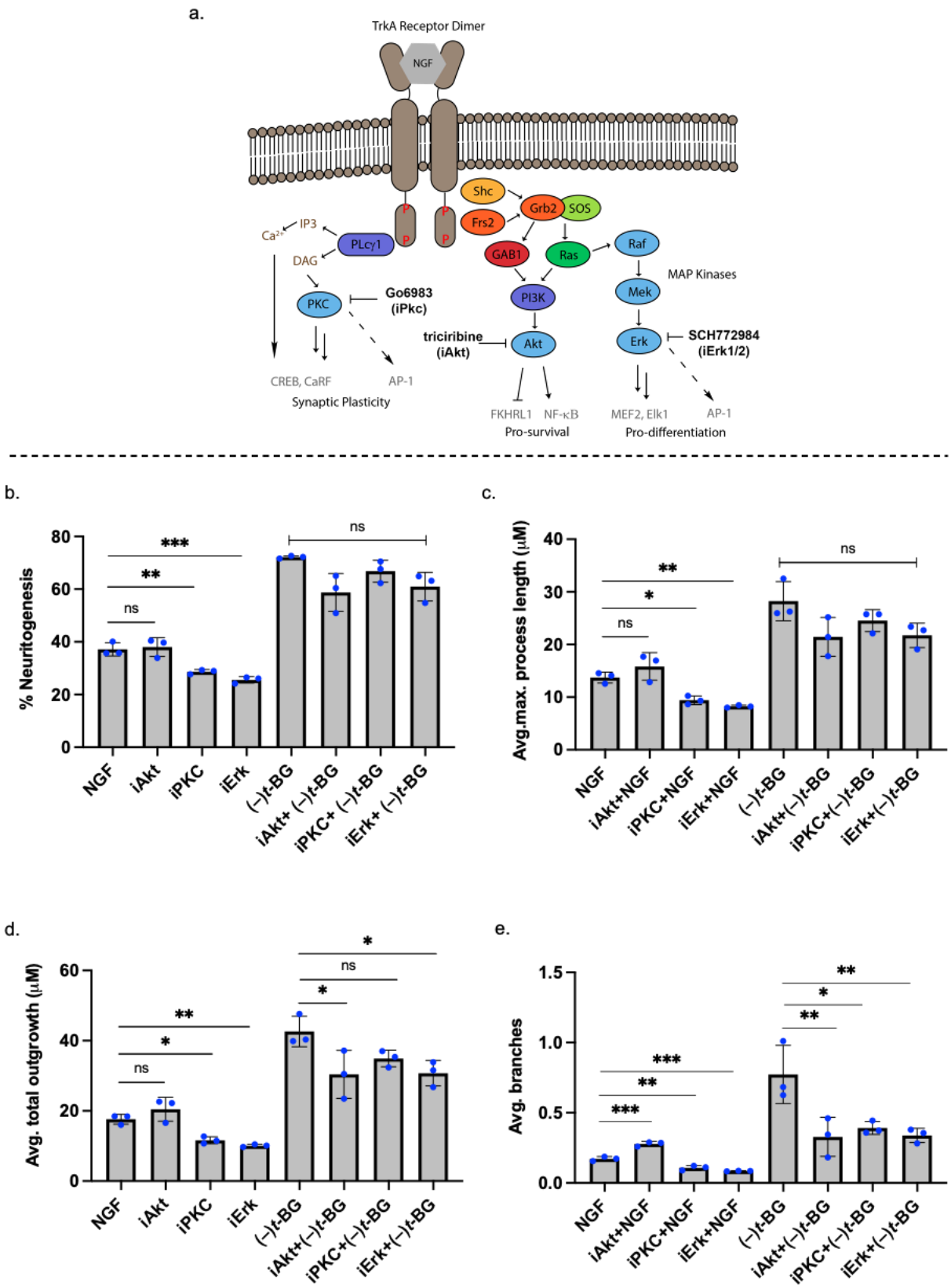
a.
TrkA Receptor Dimer
NGF
Shc
Grb2
SOS
Frs2
GAB1
Ras
Raf
MAP Kinases
Mek
Erk
SCH772984
(iErk1/2)
PI3K
Akt
triciribine
(iAkt)
PLCγ1
IP3
DAG
PKC
Go6983
(iPkc)
CREB, CaRF
AP-1
Synaptic Plasticity
FKHRL1
NF-κB
Pro-survival
MEF2, Elk1
AP-1
Pro-differentiation
b.
% Neuritogenesis
c.
Avg.max. process length (μM)
d.
Avg. total outgrowth (μM)
e.
Avg. branches
NGF
iAkt
iPKC
iErk
(−)t-BG
iAkt+ (−)t-BG
iPKC+ (−)t-BG
iErk+ (−)t-BG
iAkt+NGF
iPKC+NGF
iErk+NGF
iAkt+(−)t-BG
iPKC+(−)t-BG
iErk+(−)t-BG
ns

Figure 3-18. Investigating the effect of (–) *t*-BGs on neurotrophic signalling pathway (a) NGF-mediated signal transduction pathways with sites of inhibitor action. Effect of pathway inhibitors on (b) % neuritogenesis (c) average length of longest neurite process (d) average of total neurite outgrowth per cell (e) average number of branches per cell. Cells were treated with NGF (10 ng/mL + 0.6% DMSO) or (–) *t*-BG (30 μM +10 ng/mL NGF+ 0.6%DMSO) in the presence or absence of inhibitors. p-value measured by ANOVA followed by Dunnett's multiple comparison test *p < 0.05, **p < 0.01, ***p < 0.001.

3.6 PC-12 cell viability studies

Neurotrophin proteins affect neuronal survival, function, and development. If a molecule acts as a functional mimic of neurotrophin proteins, it can have the potential to affect cell survival.

(±) *t*-BG was shown to be neuroprotective against serum withdrawal in primary cultured rat neurons.[23] To understand the effect of (±) *t*-BG and its individual enantiomers on PC-12 cell a viability assay was setup. The assay conditions are identical to the scheme in **figure 3-2,** where a set number of PC-12 cells were plated on collagen coated wells and grown for 24 hours in DMEM culture medium containing 10% serum proteins. After 24 hours, the cells were serum starved by changing the culture medium to DMEM containing 3% serum proteins. At this 24-hour time point the test compounds (30 μM with or without 10 ng/mL NGF) and controls (10 ng/mL NGF and 0.6% DMSO) were added. After incubation for 48 hours the cells were lysed, and the amount of ATP present was quantified. The ATP released was quantified through a luciferin-luciferase assay where the readout was a luminescent signal. The amount of ATP detected acted as a proxy to quantify metabolically active cells.

As shown in **figure 3-19a**, there was no change in viability between the negative control of 0.6% DMSO and treatment with (±) *t*-BG or (–/+) *t*-BG. This indicates that (±) and (–/+) *t*-BG are not toxic to PC-12 cells at 30 μM. This also suggests that (±) and (–/+) *t*-BG do not offer any protection to cells against death caused by serum deprivation.

NGF on the other shows increased cell viability as compared to DMSO. In PC-12 cells, NGF is known to protect cells from serum deprivation, which would align with this

result.[13,62] A combination of (±) *t*-BG or (–/+) *t*-BG with NGF shows lower cell viability as compared to only NGF. This is surprising as this suggests that (±) *t*-BG and (–/+) *t*-BG are reducing the neuroprotective ability of NGF. This decrease in cell viability could perhaps be explained by the apoptotic effect of secreted pro-NGFs. Masoudi and co-workers have showed that in unprimed PC-12 cells, 0.4 nM of pro-NGF can increase serum deprivation driven cell death. Masoudi and co-workers attributed this pro-NGF mediated increase in apoptosis to a decrease in the ratio of TrkA to p75 NTR in unprimed PC-12 cells.[51]

The combination of (+) *t*-BG and NGF causes a decrease in cell viability as compared to NGF alone. This is interesting as (+) *t*-BG did not potentiate NGF mediated neuritogenesis.

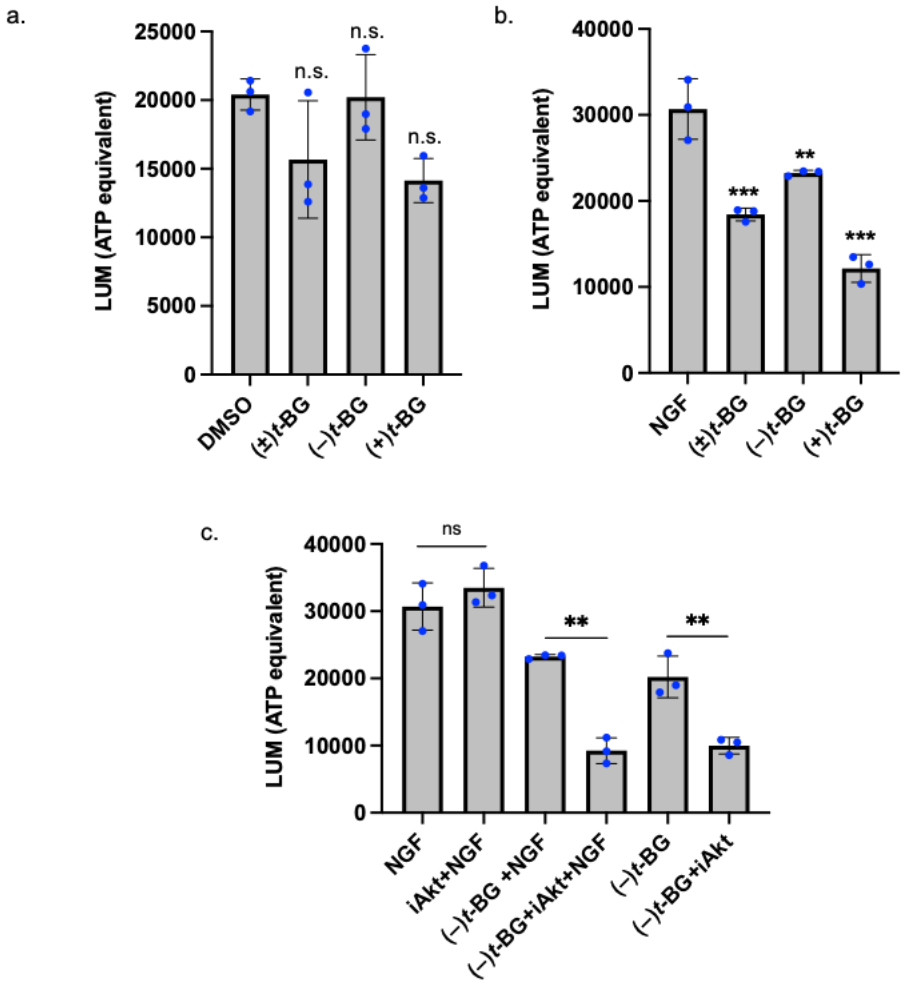

Figure 3-19. Cell viability studies in PC-12. Cell viability was determined using CellTiter-Glo® luminescent cell viability assay. (a) Cell viability after dosing 30 µM each of (±) *t*-

BG, (–) *t*-BG and (+) *t*-BG. 0.6% DMSO was added as control (b) Cell viability after dosing with a combination of 10 ng/mL NGF+0.6% DMSO and 30 μM of test compounds. 10 ng/mL NGF+0.6% DMSO was added as control. (c) Effect of iAkt on cell viability after treatment with NGF, (–) *t*-BG+NGF and (–) *t*-BG. p-value measured by ANOVA followed by Dunnett's multiple comparison test for (a, vs. DMSO) and (b, vs. NGF), p-value determined by unpaired t-test for (c) *p < 0.05, **p < 0.01, ***p < 0.001.

Since inhibition of Akt by triciribine (iAkt) had no effect on neuritogenesis caused by NGF, I checked if triciribine inhibited the neuroprotective ability of NGF. Surprisingly there is no change in cell viability between treatment with NGF and NGF+iAkt. On the other hand, iAkt reduced cell viability for treatment with only (–) *t*-BG and also the combined treatment of (–) *t*-BG + NGF. This indicates that (–) *t*-BG can affect cell survival through the PI3K-Akt pathway, but it is difficult to interpret this result as the positive control with NGF failed.

3.7 Summary and conclusions

This chapter describes the neuritogenic effect of *t*-BG on PC-12 cells. Further, it describes SAR studies for banglene derivatives and provides insights into the mechanism of action of *t*-BG.

It was found that (±) *t*-BG caused modest neuritogenesis independently and substantially potentiates NGF mediated neuritogenesis in PC-12 cells. Only one of its enantiomers (–) *t*-BG demonstrated neuritogenic activity alone and potentiated NGF's neuritogenic activity. This structural dependency hints at a distinct cellular target.

The SAR studies for banglene derivatives showed that even though most derivatives potentiated NGF's neuritogenic effect, not all of them were active by themselves. Such differences in structure-activity response constitute evidence of dual-function, and further, may be the result of a dual-mechanism for (–) *t*-BG's neuritogenic action. The SAR studies led to the discovery of cyclopropyl ester derivative (±) **36** which exhibited neuritogenic activity independently and in combination with NGF. This derivative is particularly promising as the ester of (±) **36** is primed for the conjugation of mechanistic reporters or cross-linking functionality that can facilitate cellular target identification.

The exact mechanism of (–) *t*-BG remains unclear. When (–) *t*-BG is dosed in combination with NGF, it increased the levels of NGF (or pro-NGF) released by PC-12 cells. This release of NGF (or pro-NGF) may be responsible in part for the NGF potentiating ability of (–) *t*-BG. Further, an increase in pro-NGF levels could explain the drop in cell viability when dosed with (±) or (+/–) *t*-BG.

Upon further exploration of (–) *t*-BGs effects, it was found that in PC-12 cells, the combined treatment of (–) *t*-BG and NGF did not seem to intercept any TrkA initiated signal transduction. Inhibition of Erk, Akt and PKC did not cause any decrease in neuritogenesis caused by the combination of (–) *t*-BG and NGF.

Lastly it was found that (±) and (–) *t*-BG independently do not provide any protection to cell death by serum deprivation. In contrast, (±) and (–) *t*-BG decrease the protection provided by NGF to cells against death by serum deprivation.

Increased neuritogenesis and decreased viability can be thought of as opposing effects and require further investigation. These studies highlight the inherent complexity of neurotrophic signalling mechanisms. PC-12 cell line is an easy model to observe the neuritogenesis caused by neurotrophic molecules, however it might not be the best model system to study the mechanism of action of (–) *t*-BG. The conflicting reports on the actions of pro-NGF and Akt make it difficult to understand their perturbation by (–) *t*-BG. Given that *t*-BG show neurotrophic activity in primary cultured rat neurons, it might be more physiologically relevant to conduct further studies in a primary model system.

3.8 Experimental methods

3.8.1 Cell line maintenance

PC-12 cells (CRL-1721) were obtained from ATCC and maintained in Dulbecco's modified Eagle's medium (DMEM) (Gibco™ LS11965092) containing 5% horse serum (HS) (Gibco™ LS10438018), 5% fetal bovine serum (FBS) (Gibco™ LS26050070) and 100 U/mL penicillin with 100 µg/mL streptomycin (1% Pen-Strep) (Gibco™ LS15140148). Cells were cultured for a month to reach passage 4 and then used for neuritogenesis assays. Living cells were counted using trypan blue exclusion staining.

3.8.2 Coating with collagen IV

The assay to determine neuritogenesis was carried out in 96 well plates (Ibidi USA μ-Plate 96 Well, ibiTreat -#1.5 polymer coverslip, #89626). Each well was coated with 4-6 $\mu g/cm^2$ of Collagen IV (Sigma-C5533 - Collagen from human placenta Bornstein and Traub Type IV) dissolved in Hanks' balanced salt solution (HBSS). After overnight incubation at 8°C, the plates were sterilized with 70% ethanol and then washed with HBSS (3 times) to remove any residual ethanol.

3.8.3 Neuritogenesis assay [23]

Passage 4 PC-12 cells (at 70% confluency) were seeded in the collagen-IV coated wells at a density of 2×10^4 cells/cm^2 and cultured in DMEM medium containing 5% HS, 5% FBS and 1% Pen-Strep for 24 hours, then the medium was changed to DMEM containing 2% HS, 1% FBS and a given treatment was added (see below). The cells were cultured for a further 48 hours and then visualized and/or stained for analysis.

Treatments: All the test compounds and commercial inhibitors were dissolved in DMSO and added as a solution. Compounds were tested at 30 μM concentration, unless otherwise noted. The final concentration of DMSO does not exceed 0.6% in any test. Recombinant human β NGF (SRP3015-Sigma-Aldrich) (10 ng/mL) with 0.6% DMSO was used as the positive control and 0.6% DMSO as the negative control.

For testing the perturbation of pathways associated with Nerve growth factor (NGF) mediated signalling, the following chemical inhibitors were used – triciribine hydrate (iAkt, 5 μM; Sigma T3830), Gö 6983 (iPkc, 0.5 μM; Sigma G1918), and SCH772984 (iErk, 10 μM; AbMole BioScience M2084).

All compounds and controls were tested as triplicate independent experiments. Importantly, to reduce inter-assay variations caused by evaporation of cell culture medium, cells were cultured only in wells B2-G11, the wells on the outer boundary of the plate were flooded with 300 μl of HBSS over the time course of the entire assay.

3.8.4 Immunofluorescence staining procedure [19,21]

48 hours after addition of test compounds and controls, the cells were fixed with 4:1 ratio of 20% formaldehyde and 5% sucrose for 30 min. After aspirating, the fixative was washed with HBSS (2 times), and the residual formaldehyde was treated with 0.1% $NaBH_4$ for 7 min and washed with HBSS (2 times). The cells were blocked and permeabilized with 5% goat serum in 0.3% Triton X-100 for 25 min. Cells were incubated with primary mouse anti-β-tubulin III antibody (Sigma T8578), 1:1000 diluted in antibody buffer (5% goat serum in 0.1% Triton X-100) overnight at 4°C. The primary antibody was aspirated and washed with HBSS (2 times). Neurites were stained with secondary antibody goat anti-mouse, Alexa Fluor Plus 488, Secondary Antibody (Invitrogen™ A28175) and the nuclei were stained with 0.5 µg/well of Hoechst 33342 (Invitrogen™ LSH3570) for 1h at 37°C. After the secondary antibody was aspirated and washed with HBSS (2 times), mounting solution (80% glycerol and 0.5% n-propyl gallate) was added.

3.8.5 Imaging acquisition parameters and data analyses

Images were acquired on a high content analysis system (Metaxpress XLS, Molecular Devices) with a Nikon 10× Plan Fluor lens. 25 sites per well (covering the entire well) with 0 µm between images in X and Y direction were taken with a 100 ms exposure time for DAPI filter set and an 1800 ms exposure time for Alexa 488 filter set. A digital confocal mode was used to image neurites with five Z sections separated by 2 µm steps which were combined into a single stack for analysis. Proper image acquisition was confirmed in several wells to ensure that gain and exposure levels didn't result in images with saturated regions. The images were segmented and analyzed using Metaxpress' Neurite Outgrowth module, the parameters were set as shown:

Segemented region	Parameter	Measurement
Cell bodies	Approximate maximum width	25 μm
	Minimum area	90 μm^2
Nuclear stain	Approximate minimum width	4 μm
	Approximate maximum width	15 μm
Outgrowth	Maximum width	4 μm
	Minimum cell growth to log as significant	5 μm

Table 3-2. Image segmentation parameters

For each well, the data generated for 25 images was added up to give the total number of cells and the total number of cells with significant outgrowth. An average cell body area was also calculated. Statistical analyses and graphing were done using GraphPad Prism version 9.2.0. p-values were determined by One-way ANOVA followed by Dunnett's multiple comparisons test or unpaired t-tests as mentioned in figures. Bar graphs have been plotted to show data as mean ± standard deviation.

3.8.6 NGF ELISA assay

The Rat beta-NGF sandwich ELISA kit (Millipore) was used to determine the pro-NGF concentration in the cell-free culture medium. 2×10^4 cells/cm^2 PC-12 cells were seeded in the collagen-IV coated and cultured in DMEM medium containing 5% HS, 5% FBS and 1% Pen-Strep for 24 hours, then the medium was changed to DMEM containing 2% HS, 1% FBS and NGF (10 ng/mL +0.6% DMSO) was added alone or in combination with 30 μM (–) *t*-BG or (–) 20 . The cells were cultured for a further 48 hours and then the culture medium was then collected and added into a microplate pre-coated with rat beta-NGF antibody. Anti-mouse NGF monoclonal antibody was then added to each well as a detection antibody. After 2.5 h, biotinylated detection antibody was added and incubated for 1h. HRP-Streptavidin was then added, and samples were incubated for 45 min. The TMB solution was added and incubated for 30 min after which the stop solution was added, and colour intensity of the

sample was measured at 450 nm. The level of pro-NGF was determined from a NGF standard curve plotted with known concentrations of NGF.

3.8.7 Viability determination

Cell viability measurements were done using the CellTiter-Glo® luminescent cell viability assay. The assay was set up similar to section 8.3. 48 h post treatment with controls or test molecules, 100 µL of the CellTiter-Glo reagent was added and the plate was mixed for 2 mins in an orbital shaker to cause cell lysis. The plate was incubated at room temperature for 10 mins to stabilize the luminescence signal and then the luminescence was recorded.

3.9 References

(1) Bennison, S. A.; Blazejewski, S. M.; Smith, T. H.; Toyo-oka, K. Protein Kinases: Master Regulators of Neuritogenesis and Therapeutic Targets for Axon Regeneration. *Cell. Mol. Life Sci.* **2020**, *77* (8), 1511–1530.

(2) Balon, K.; Wiatrak, B. PC12 and THP-1 Cell Lines as Neuronal and Microglia Model in Neurobiological Research. *Appl. Sci.* **2021**, *11* (9), 3729.

(3) Wiatrak, B.; Kubis-Kubiak, A.; Piwowar, A.; Barg, E. PC12 Cell Line: Cell Types, Coating of Culture Vessels, Differentiation and Other Culture Conditions. *Cells* **2020**, *9* (4).

(4) Teng, K. K.; Angelastro, J. M.; Cunningham, M. E.; Greene, L. A. Cultured PC12 Cells: A Model for Neuronal Function, Differentiation, and Survival. *Cell Biol. Four-Volume Set* **2006**, *1*, 171–176.

(5) Greene, L. A.; Tischler, A. S. Establishment of a Noradrenergic Clonal Line of Rat Adrenal Pheochromocytoma Cells Which Respond to Nerve Growth Factor. *Proc. Natl. Acad. Sci.* **1976**, *73* (7), 2424–2428.

(6) Westerink, R. H. S.; Ewing, A. G. The PC12 Cell as Model for Neurosecretion. *Acta Physiol. (Oxf).* **2008**, *192* (2), 273.

(7) Barbosa, D. J.; Capela, J. P.; De Lourdes Bastos, M.; Carvalho, F. In Vitro Models for Neurotoxicology Research. *Toxicol. Res. (Camb).* **2015**, *4* (4), 801–842.

(8) Hu, R.; Cao, Q.; Sun, Z.; Chen, J.; Zheng, Q.; Xiao, F. A Novel Method of Neural Differentiation of PC12 Cells by Using Opti-MEM as a Basic Induction Medium. *Int. J. Mol. Med.* **2018**, *41* (1), 195.

(9) Xu, J.; Lacoske, M. H.; Theodorakis, E. A. Neurotrophic Natural Products: Chemistry and Biology. *Angew. Chem. Int. Ed. Engl.* **2014**, *53* (4), 956.

(10) Cho, J. Y.; Katz, D. R.; Skubitz, K. M.; Chain, B. M. Conventional Protein Kinase C Plays a Critical Role in Negative Regulation of CD98-Induced Homotypic Aggregation. *Tissue Antigens* **2010**, *75* (1), 19–29.

(11) Guroff, G. PC12 Cells as a Model of Neuronal Differentiation. *Cell Cult. Neurosci.* **1985**, 245–272.

(12) PC-12 | ATCC https://www.atcc.org/products/crl-1721 (accessed 2022 -01 -10).

(13) Greene, L. A. Nerve Growth Factor Prevents the Death and Stimulates the Neuronal Differentiation of Clonal PC12 Pheochromocytoma Cells in Serum-Free Medium. *J. Cell Biol.* **1978**, *78* (3), 747.

(14) Tomaselli, K. J.; Damsky, C. H.; Reichardt, L. F. Purification and Characterization of Mammalian Integrins Expressed by a Rat Neuronal Cell Line (PC12): Evidence That They Function as Alpha/Beta Heterodimeric Receptors for Laminin and Type IV Collagen. *J. Cell Biol.* **1988**, *107* (3), 1241–1252.

(15) Orlowska, A.; Perera, P. T.; Al Kobaisi, M. A.; Dias, A.; Nguyen, H. K. D.; Ghanaati, S.; Baulin, V.; Crawford, R. J.; Ivanova, E. P. The Effect of Coatings and Nerve Growth Factor on Attachment and Differentiation of Pheochromocytoma Cells. *Mater.* **2017**, *11* (1), 60.

(16) Morales-Medina, J. C.; Iannitti, T.; Freeman, A.; Caldwell, H. K. The Olfactory Bulbectomized Rat as a Model of Depression: The Hippocampal Pathway. *Behav. Brain Res.* **2017**, *317*, 562–575.

(17) Kinarivala, N.; Shah, K.; Abbruscato, T. J.; Trippier, P. C. Passage Variation of PC12 Cells Results in Inconsistent Susceptibility to Externally Induced Apoptosis. *ACS Chem. Neurosci.* **2017**, *8* (1), 82.

(18) Mansoury, M.; Hamed, M.; Karmustaji, R.; Al Hannan, F.; Safrany, S. T. The Edge Effect: A Global Problem. The Trouble with Culturing Cells in 96-Well Plates. *Biochem. Biophys. Reports* **2021**, *26*, 100987.

(19) Harrill, J. A.; Mundy, W. R. Quantitative Assessment of Neurite Outgrowth in PC12 Cells. *Methods Mol. Biol.* **2011**, *758*, 331–348.

(20) Weber, S.; Fernández-Cachón, M. L.; Nascimento, J. M.; Knauer, S.; Offermann, B.; Murphy, R. F.; Boerries, M.; Busch, H. Label-Free Detection of Neuronal Differentiation in Cell Populations Using High-Throughput Live-Cell Imaging of PC12 Cells. *PLoS One* **2013**, *8* (2), e56690.

(21) Radio, N. M.; Breier, J. M.; Shafer, T. J.; Mundy, W. R. Assessment of Chemical Effects on Neurite Outgrowth in PC12 Cells Using High Content Screening. *Toxicol. Sci.* **2008**, *105* (1), 106–118.

(22) Das, K. P.; Freudenrich, T. M.; Mundy, W. R. Assessment of PC12 Cell Differentiation and Neurite Growth: A Comparison of Morphological and Neurochemical Measures. *Neurotoxicol. Teratol.* **2004**, *26* (3), 397–406.

(23) Matsui, N.; Kido, Y.; Okada, H.; Kubo, M.; Nakai, M.; Fukuishi, N.; Fukuyama, Y.; Akagi, M. Phenylbutenoid Dimers Isolated from Zingiber Purpureum Exert Neurotrophic Effects on Cultured Neurons and Enhance Hippocampal Neurogenesis in Olfactory Bulbectomized Mice. *Neurosci. Lett.* **2012**, *513* (1), 72–77.

(24) Burch, P.; Binaghi, M.; Scherer, M.; Wentzel, C.; Bossert, D.; Eberhardt, L.; Neuburger, M.; Scheiffele, P.; Gademann, K. Total Synthesis of Gelsemiol. *Chem. – A Eur. J.* **2013**, *19* (8), 2589–2591.

(25) Cho, Y. S.; Carcache, D. A.; Tian, Y.; Li, Y. M.; Danishefsky, S. J. Total Synthesis of (±)-Jiadifenin, a Non-Peptidyl Neurotrophic Modulator. *J. Am. Chem. Soc.* **2004**, *126* (44), 14358–14359.

(26) Clement, C. M.; Dandepally, S. R.; Williams, A. L.; Ibeanu, G. C. A Synthetic Analog of Verbenachalcone Potentiates NGF-Induced Neurite Outgrowth and Enhances Cell Survival in Neuronal Cell Models. *Neurosci. Lett.* **2009**, *459* (3), 157–161.

(27) Williams, B.; Dwyer, D. S. Structure-Based Discovery of Low Molecular Weight Compounds That Stimulate Neurite Outgrowth and Substitute for Nerve Growth Factor. *J. Neurochem.* **2009**, *110* (6), 1876.

(28) Chan, G. K. L.; Hu, W. W. H.; Zheng, Z. X.; Huang, M.; Lin, Y. X. Y.; Wang, C. Y.; Gong, A. G. W.; Yang, X. Y.; Tsim, K. W. K.; Dong, T. T. X. Quercetin Potentiates the NGF-Induced Effects in Cultured PC 12 Cells: Identification by HerboChips Showing a Binding with NGF. *Evid. Based. Complement. Alternat. Med.* **2018**.

(29) Tang, W.; Hioki, H.; Harada, K.; Kubo, M.; Fukuyama, Y. Clerodane Diterpenoids with NGF-Potentiating Activity from Ptychopetalum Olacoides. *J. Nat. Prod.* **2008**, *71* (10), 1760–1763.

(30) Jessen, H. J.; Barbaras, D.; Hamburger, M.; Gademann, K. Total Synthesis and Neuritotrophic Activity of Farinosone C and Derivatives. *Org. Lett.* **2009**, *11* (15), 3446–3449.

(31) Liu, L.; Shi, X. W.; Zong, S. C.; Tang, J. J.; Gao, J. M. Scabronine M, a Novel Inhibitor of NGF-Induced Neurite Outgrowth from PC12 Cells from the Fungus Sarcodon Scabrosus. *Bioorg. Med. Chem. Lett.* **2012**, *22* (7), 2401–2406.

(32) Imagawa, H.; Saijo, H.; Kurisaki, T.; Yamamoto, H.; Kubo, M.; Fukuyama, Y.; Nishizawa, M. Total

Synthesis of(±)-Neovibsanin B. *Org. Lett.* **2009**, *11* (6), 1253–1255.

(33) Cao, C. Y.; Zhang, C. C.; Shi, X. W.; Li, D.; Cao, W.; Yin, X.; Gao, J. M. Sarcodonin G Derivatives Exhibit Distinctive Effects on Neurite Outgrowth by Modulating NGF Signaling in PC12 Cells. *ACS Chem. Neurosci.* **2018**, *9* (7), 1607–1615.

(34) Harada, K.; Kubo, M.; Horiuchi, H.; Ishii, A.; Esumi, T.; Hioki, H.; Fukuyama, Y. Systematic Asymmetric Synthesis of All Diastereomers of (-)-Talaumidin and Their Neurotrophic Activity. *J. Org. Chem.* **2015**, *80* (14), 7076–7088.

(35) Jessen, H. J.; Barbaras, D.; Hamburger, M.; Gademann, K. Total Synthesis and Neuritotrophic Activity of Farinosone C and Derivatives. *Org. Lett.* **2009**, *11* (15), 3446–3449.

(36) Phan, C. W.; Lee, G. S.; Hong, S. L.; Wong, Y. T.; Brkljača, R.; Urban, S.; Abd Malek, S. N.; Sabaratnam, V. Hericium Erinaceus (Bull.: Fr) Pers. Cultivated under Tropical Conditions: Isolation of Hericenones and Demonstration of NGF-Mediated Neurite Outgrowth in PC12 Cells via MEK/ERK and PI3K-Akt Signaling Pathways. *Food Funct.* **2014**, *5* (12), 3160–3169.

(37) Chu, J.; Suh, D. H.; Lee, G.; Han, A. R.; Chae, S. W.; Lee, H. J.; Seo, E. K.; Lim, H. J. Synthesis and Biological Activity of Optically Active Phenylbutenoid Dimers. *J. Nat. Prod.* **2011**, *74* (8), 1817–1821.

(38) Yanagimoto, T.; Kishimoto, S.; Kasai, Y.; Matsui, N.; Kubo, M.; Yamamoto, H.; Fukuyama, Y.; Imagawa, H. Design and Synthesis of Dual Active Neovibsanin Derivatives Based on a Chemical Structure Merging Method. *Bioorg. Med. Chem. Lett.* **2020**, *30* (20), 127497.

(39) Lin, C. W.; Wu, M. J.; Liu, I. Y. C.; Su, J. D.; Yen, J. H. Neurotrophic and Cytoprotective Action of Luteolin in PC12 Cells through ERK-Dependent Induction of Nrf2-Driven HO-1 Expression. *J. Agric. Food Chem.* **2010**, *58* (7), 4477–4486.

(40) Tsuji, M.; Inanami, O.; Kuwabara, M. Induction of Neurite Outgrowth in PC12 Cells by α-Phenyl-N-Tert-Butylnitron through Activation of Protein Kinase C and the Ras-Extracellular Signal-Regulated Kinase Pathway *. *J. Biol. Chem.* **2001**, *276* (35), 32779–32785.

(41) Vauzour, D.; Vafeiadou, K.; Rodriguez-Mateos, A.; Rendeiro, C.; Spencer, J. P. E. The Neuroprotective Potential of Flavonoids: A Multiplicity of Effects. *Genes Nutr.* **2008**, *3* (3–4), 115–126.

(42) Cao, C. Y.; Zhang, C. C.; Shi, X. W.; Li, D.; Cao, W.; Yin, X.; Gao, J. M. Sarcodonin G Derivatives Exhibit Distinctive Effects on Neurite Outgrowth by Modulating NGF Signaling in PC12 Cells. *ACS Chem. Neurosci.* **2018**, *9* (7), 1607–1615.

(43) Ishiuchi, K.; Kubota, T.; Ishiyama, H.; Hayashi, S.; Shibata, T.; Mori, K.; Obara, Y.; Nakahata, N.; Kobayashi, J. Lyconadins D and E, and Complanadine E, New Lycopodium Alkaloids from Lycopodium Complanatum. *Bioorg. Med. Chem.* **2011**, *19* (2), 749–753.

(44) Obara, Y.; Kobayashi, H.; Ohta, T.; Ohizumi, Y.; Nakahata, N. Scabronine G-Methylester Enhances Secretion of Neurotrophic Factors Mediated by an Activation of Protein Kinase C-ζ. *Mol. Pharmacol.* **2001**, *59* (5), 1287–1297.

(45) Hines, J.; Groll, M.; Fahnestock, M.; Crews, C. M. Proteasome Inhibition by Fellutamide B Induces Nerve Growth Factor Synthesis. *Chem. Biol.* **2008**, *15* (5), 501.

(46) Tang, L. L.; Wang, R.; Tang, X. C. Huperzine A Protects SHSY5Y Neuroblastoma Cells against Oxidative Stress Damage via Nerve Growth Factor Production. *Eur. J. Pharmacol.* **2005**, *519* (1–2), 9–15.

(47) Phan, C. W.; Lee, G. S.; Hong, S. L.; Wong, Y. T.; Brkljača, R.; Urban, S.; Abd Malek, S. N.; Sabaratnam, V. Hericium Erinaceus (Bull.: Fr) Pers. Cultivated under Tropical Conditions: Isolation of Hericenones and Demonstration of NGF-Mediated Neurite Outgrowth in PC12 Cells via MEK/ERK and PI3K-Akt Signaling Pathways. *Food Funct.* **2014**, *5* (12), 3160–3169.

(48) Malerba, F.; Paoletti, F.; Cattaneo, A. NGF and ProNGF Reciprocal Interference in Immunoassays: Open Questions, Criticalities, and Ways Forward. *Front. Mol. Neurosci.* **2016**, *9* (AUG), 63.

(49) Soligo, M.; Albini, M.; Bertoli, F. L.; Marzano, V.; Protto, V.; Bracci-Laudiero, L.; Minnone, G.; De Benedetti, F.; Chiaretti, A.; Mantuano, E.; Manni, L. Different Responses of PC12 cells to Different Pro-Nerve Growth Factor Protein Variants. *Neurochem. Int.* **2019**, *129*, 104498.

(50) Boutilier, J.; Ceni, C.; Pagdala, P. C.; Forgie, A.; Neet, K. E.; Barker, P. A. Proneurotrophins Require Endocytosis and Intracellular Proteolysis to Induce TrkA Activation. *J. Biol. Chem.* **2008**, *283* (19), 12709–12716.

(51) Masoudi, R.; Ioannou, M. S.; Coughlin, M. D.; Pagadala, P.; Neet, K. E.; Clewes, O.; Allen, S. J.; Dawbarn, D.; Fahnestock, M. Biological Activity of Nerve Growth Factor Precursor Is Dependent upon Relative Levels of Its Receptors *. *J. Biol. Chem.* **2009**, *284* (27), 18424–18433.

(52) Fahnestock, M.; Shekari, A. ProNGF and Neurodegeneration in Alzheimer's Disease. *Front. Neurosci.* **2019**, *13* (FEB), 129.

(53) Nykjaer, A.; Willnow, T. E. Sortilin: A Receptor to Regulate Neuronal Viability and Function. *Trends Neurosci.* **2012**, *35* (4), 261–270.

(54) Ioannou, M. S.; Fahnestock, M. ProNGF, but Not NGF, Switches from Neurotrophic to Apoptotic Activity in Response to Reductions in TrkA Receptor Levels. *Int. J. Mol. Sci.* **2017**, *18* (3).

(55) Marlin, M. C.; Li, G. Biogenesis and Function of the NGF/TrkA Signaling Endosome. *Int. Rev. Cell Mol. Biol.* **2015**, *314*, 239.

(56) Berndt, N.; Yang, H.; Trinczek, B.; Betzi, S.; Zhang, Z.; Wu, B.; Lawrence, N. J.; Pellecchia, M.; Schönbrunn, E.; Cheng, J. Q.; Sebti, S. M. The Akt Activation Inhibitor TCN-P Inhibits Akt Phosphorylation by Binding to the PH Domain of Akt and Blocking Its Recruitment to the Plasma Membrane. *Cell Death Differ.* **2010**, *17* (11), 1795–1804.

(57) Young, L. H.; Balin, B. J.; Weis, M. T. Gö 6983: A Fast Acting Protein Kinase C Inhibitor That Attenuates Myocardial Ischemia/Reperfusion Injury. *Cardiovasc. Drug Rev.* **2005**, *23* (3), 255–272.

(58) Morris, E. J.; Jha, S.; Restaino, C. R.; Dayananth, P.; Zhu, H.; Cooper, A.; Carr, D.; Deng, Y.; Jin, W.; Black, S.; Long, B.; Liu, J.; DiNunzio, E.; Windsor, W.; Zhang, R.; Zhao, S.; Angagaw, M. H.; Pinheiro, E. M.; Desai, J.; Xiao, L.; Shipps, G.; Hruza, A.; Wang, J.; Kelly, J.; Paliwal, S.; Gao, X.; Babu, B. S.; Zhu, L.; Daublain, P.; Zhang, L.; Lutterbach, B. A.; Pelletier, M. R.; Philippar, U.; Siliphaivanh, P.; Witter, D.; Kirschmeier, P.; Robert Bishop, W.; Hicklin, D.; Gary Gillil, D.; Jayaraman, L.; Zawel, L.; Fawell, S.; Samatar, A. A. Discovery of a Novel ERK Inhibitor with Activity in Models of Acquired Resistance to

BRAF and MEK Inhibitors. *Cancer Discov.* **2013**, *3* (7), 742–750.

(59) Lee, S. R.; Park, J. H.; Park, E. K.; Chung, C. H.; Kang, S. S.; Bang, O. S. Akt-Induced Promotion of Cell-Cycle Progression at G2/M Phase Involves Upregulation of NF-Y Binding Activity in PC12 Cells. *J. Cell. Physiol.* **2005**, *205* (2), 270–277.

(60) Bennison, S. A.; Blazejewski, S. M.; Smith, T. H.; Toyo-oka, K. Protein Kinases: Master Regulators of Neuritogenesis and Therapeutic Targets for Axon Regeneration. *Cell. Mol. Life Sci.* **2020**, *77* (8), 1511–1530.

(61) Read, D. E.; Gorman, A. M. Involvement of Akt in Neurite Outgrowth. *Cell. Mol. Life Sci.* **2009**, *66* (18), 2975–2984.

(62) Klesse, L.; Meyers, K.; Marshall, C.; Parada, L. Nerve Growth Factor Induces Survival and Differentiation through Two Distinct Signaling Cascades in PC12 Cells. *Oncogene* **1999**, *18* (12), 2055–2068.

Chapter 4: Development of a new fluorescent protein-based FRET pair

4.1 Introduction

The biological processes that occur inside and outside a cell form a highly dynamic and complex network that encompasses all of the essential cellular functions for sustaining life. Understanding these biological processes requires tools that can monitor the dynamic movement of various molecules in an extremely heterogenous cellular environment. Fluorescent proteins (FPs), either on their own or as components of biosensors, are indispensable tools to probe these molecular dynamics and interactions.[1]

4.1.1 Fluorescent protein-based biosensors

A biosensor for an analyte or a cellular event typically consists of a recognition domain, which recognizes the binding of an analyte or occurrence of an event, and an indicator domain, which subsequently generates a measurable signal. Fluorescent proteins are popular indicator domains for biosensor development as they generate a fluorescent signal which can be modulated in terms of intensity or wavelength. Coupled with microscopy technology, FP-based fluorescent biosensors enable quantitative measurement and real-time imaging of biomolecules and cellular processes with high spatiotemporal resolution.[2] Different hues of FPs have provided opportunities for constructing various genetically encodable biosensors categorized into two classes based on their response mechanism. The first class consists of intensiometric biosensors in which a conformational change in the recognition domain is relayed to an attached single FP, leading to a modulation of the fluorescence. The second class is based on recognition domain-dependent modulation of Förster resonance energy transfer (FRET) between two FPs that emit different fluorescent colours, leading to a ratiometric change in fluorescence emission.[3]

4.1.2 FRET theory for FP-based biosensor development

FRET is a photophysical phenomenon by which energy is transferred non-radiatively from a higher energy fluorophore (the donor) to a lower energy fluorophore (the acceptor) by means of an intermolecular dipole-dipole coupling interaction.[4] The efficiency of FRET is dependent on several parameters, including the distance between the donor and the acceptor.

This inherent dependence on distance enables measurements of proximity between the donor and acceptor fluorophores at angstrom distances (10–100 Å). FRET efficiency (E) can be defined by **equation 1**, where r is the distance between donor and acceptor and R_0 is the Förster distance. R_0 is defined as the distance at which half the excitation energy of the donor is transferred to the acceptor. R_0 depends on various factors (**equation 2**) such as the degree of overlap between the emission spectrum of the donor and the absorption spectrum of the acceptor (J), the quantum yield of the donor (Φ_D), the spatial orientation of the donor and acceptor dipoles $(\kappa)^2$ and the refractive index of the medium (n).[4,5]

Equation 1 $$E = \frac{1}{1 + \left({}^{r}/_{R_0}\right)^6}$$

Equation 2 $$R_0^6 = 0.021 J \kappa^2 \Phi_D n^{-4}$$

In genetically encodable FRET-based biosensors, the recognition domain is typically a protein, and the indicator domain consists of a pair of FPs that can provide a FRET response. The selection and the development of FPs for forming a FRET pair must take into consideration the photophysical properties described by **equation 1 and 2**. The most important requirement for FRET is the spectral overlap between the donor emission and acceptor absorption. The spectral overlap is quantified by **equation 3** where $\overline{I_D}$ is the normalized donor emission intensity, ε_A is the molar extinction coefficient of the acceptor and λ is the wavelength.[4,5]

Equation 3 $$J = \int \overline{I_D} \varepsilon_A \lambda^4 d\lambda$$

The molar extinction coefficient (EC) is a wavelength dependent property, which measures how strongly a substance absorbs light at a particular wavelength. Quantum yield (QY) is the probability that excitation of a chromophore by a photon would lead to emission of a photon instead of the energy being dissipated in a non-radiative manner. The product of the extinction coefficient and the quantum yield determines the molecular brightness of a FP.[6]

Based on **equations 1, 2 and 3** it can be concluded that for a biosensor to have the highest FRET efficiency change, it is essential to optimize the photophysical properties of FP pairs, the distance between them, and potentially how the FPs interact with each other.

4.1.3 Mechanism of FRET-based biosensors

FRET-based biosensors function through the modulation of inter-fluorophore distance or orientation between the two FPs. This modulation can occur either by a conformational change in the recognition domain upon binding of an analyte or upon enzymatic activity on a substrate-based recognition domain.[2] An example of this is shown in **figure 4-1**. When the donor and acceptor are within an acceptable *r*, the excitation of the donor fluorophore would result in FRET and cause emission from the acceptor. Upon proteolysis, the donor and acceptor would no longer be in proximity to each other, and this increased distance would cause a decrease or complete loss of FRET and an increase in the donor emission intensity.

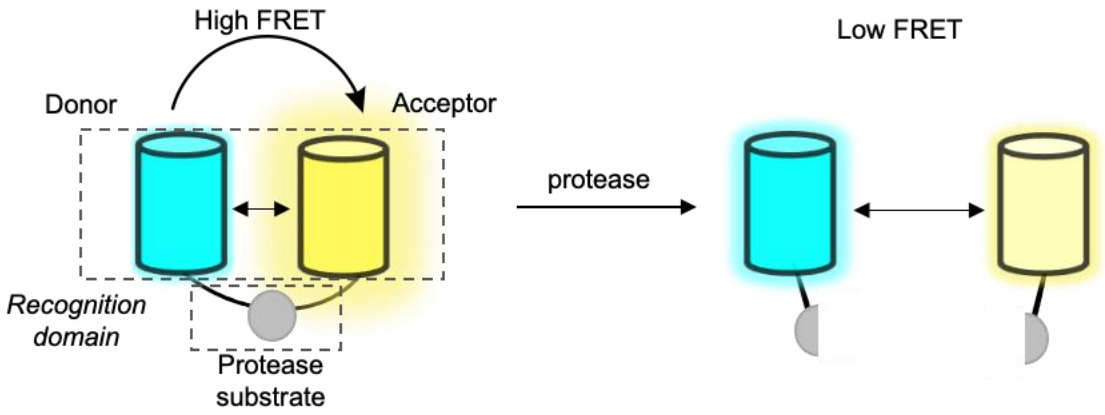

Figure 4-1. Representative design of a FRET-based biosensor for detecting protease activity. With the protease substrate uncut, efficient FRET occurs between donor and acceptor. After protease activity, FRET efficiency reduces with increasing distance.

Experimentally, when studying analyte changes using a FRET-based biosensor, FRET efficiency increases (or decreases) leading to a decrease (or increase) in the fluorescent intensity of the donor (I_D) and an increase (or decrease) in the fluorescent intensity of the acceptor (I_A). The change in FRET efficiency can be assessed as the change in the ratio of acceptor intensity to donor intensity ($R = I_A/I_D$). Since a FRET-based biosensor has two

different states, a change in ratio ($\Delta R = R_{max} - R_{min}$) can be calculated.[7] ΔR is sometimes referred to as the "ratiometric response" or "dynamic range" of a biosensor and a normalised value of $\Delta R/R_{min}$ is used as a proxy to represent changes in FRET efficiency.

Numerous FRET-based biosensors have been designed for the purpose of studying various intracellular processes such as enzyme activity, ion dynamics, post-translational modifications and protein-protein interactions.[2] These FRET-based biosensors are powerful molecular tools as they allow quantitative (ratiometric), noninvasive, live cell imaging in various model systems with high spatial and temporal resolution.[7]

4.1.4 Fluorescent proteins as FRET indicators

The performance of a FRET-based biosensor is highly dependent on the photophysical properties of its component FPs (**equations 2-3**). FPs in a FRET pair should ideally have substantial spectral overlap (**figure 4-2**), a donor with high quantum yield, and an acceptor with a high EC.

Apart from the photophysical properties of FPs, other factors such as maturation and pH stability of a FP also affect its utility for use in a FRET pair. The maturation of a FP refers to all of the steps necessary to form a correctly folded protein that has a functional fluorescent chromophore. If there is incomplete maturation of a FP, it leads to an unequal stoichiometry of donor and acceptor which would result in fewer functional FRET pairs. pH stability of a FP refers to apparent change in QY or EC of a FP upon varying pH. Since cellular events can alter pH and most FPs get quenched at acidic pH, if the pK_a of a FP is close to physiological pH it can lead to a decrease in fluorescence. This would result in a FRET signal change that is challenging to interpret.

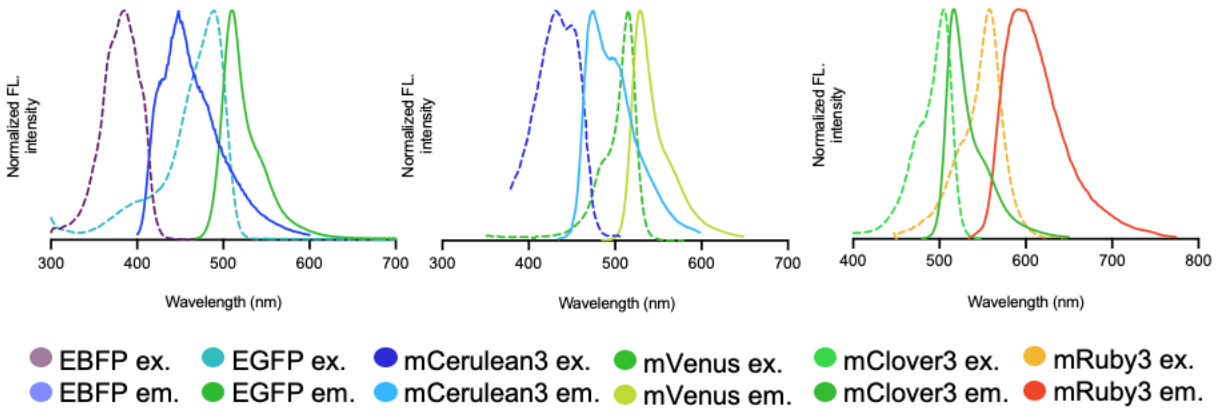

Figure 4-2. Spectral overlap of common FRET pairs. Normalized fluorescence (FL.) intensity represented on y axis, ex.= excitation and em. = emission.

The first FPs to be used in a FRET-based biosensor were the green fluorescent protein (GFP) and the blue fluorescent protein (BFP). BFPs were not ideal FRET donors, given their low QY, sensitivity to photobleaching, and near-UV excitation which can be harmful to cells.[8,9] These shortcomings led to the development of cyan fluorescent proteins (CFPs) and yellow fluorescent proteins (YFPs), which remain the most effective and most commonly used FRET pair to date.[2,10–12] CFPs are popular as FRET donors given the exceptionally good quantum yields of modern variants (mTurquoise2 QY = 0.93) and long fluorescence lifetimes (mTurquoise2 lifetime = 3.8 ns).[13]

Despite their popularity, CFP-YFP pairs have certain properties that can be problematic for FRET analysis. CFPs and YFPs can be reversibly photobleached, YFPs can be photoconverted to CFP-like FPs, phototoxicity and autofluorescence can be induced by violet light excitation of CFP, and CFP-YFP pairs have significant spectral cross-talk.[10,14]

To overcome these issues, alternative FRET pairs with GFPs as the donor and an orange or red fluorescent protein (OFP or RFP) as an acceptor have been explored. The GFP-RFP pairing leads to reduced phototoxicity and improves spectral separation.[10,14–17] The first red FPs to be used as FRET acceptors were DsRed (a tetramer) and tdimer2 (a tandem dimer) with EGFP as the FRET donor. They were challenging to use in a FRET pair due to their tendency to oligomerize and their slow maturation.[18,19] Monomeric RFPs such as mRFP1 and mCherry do not suffer from these same issues and have been paired with EGFP to

develop FRET-based biosensors for analysis by fluorescence-lifetime imaging microscopy (FLIM). However, these red monomeric FPs have low brightness and are typically not well-suited for ratiometric FRET analysis.[17,20,21] To overcome the issue of low brightness, TagRFP was developed as a FRET acceptor with increased brightness (brightness = 48 $M^{-1}cm^{-1}$). When paired with TagGFP it resulted in more efficient FRET compared to that with mCherry (brightness = 16 $M^{-1}cm^{-1}$).[22]

Further advancement in green-red FRET pairs for ratiometric imaging came from the development of Clover-mRuby2, and the further improved version mClover3-mRuby3, which had better photostability compared to existing GFP-RFP and CFP-YFP FRET pairs.[14,23] These FPs were developed to have photophysical properties that favour higher FRET efficiencies such as improved quantum yield of the donor, large Stokes shift, fast maturation and high photostability. For comparison, the calculated R_0 for mClover3-mRuby3 is 6.5 nm and for ECFP-EYFP the R_0 is 4.9 nm. This high R_0 is a result of high QY of mClover3 (0.78 vs 0.4 for ECFP) and high EC of mRuby3 (128,000 $M^{-1}cm^{-1}$ vs 83,000 $M^{-1}cm^{-1}$ for EYFP).[10] Before the development of mClover and mRuby, the reported green-red FRET pairs did not have improved FRET efficiencies compared to CFP-YFP pairs. The improvement in FRET efficiency by swapping CFP-YFP in a biosensor with green-red FP was demonstrated in Camuiα, a FRET-based biosensor that reports CaMKIIα activity. Swapping Venus and ECFP in this biosensor with Clover-mRuby2 resulted in a 62% increase in $\Delta R/R_{min}$.[14]

With the development of new FPs, the diversity of FP-based FRET pairs is ever increasing. As seen from the examples above, the development of new FPs and FRET pairs is highly interdependent. Each new FRET pair utilizes and provides a fluorescent readout from a slightly different region of the spectrum. For example, the CFP mTurquoise2 has been used as an efficient FRET donor to YFPs, GFPs (mNeonGreen), and RFPs (mScarlet-I).[24] There are FRET pairs with more red shifted acceptor FPs such as mPlum (a far-red FP, excitation λ_{max} = 590 nm) and long Stokes shift FPs which result in reduced spectral crosstalk between the donor and the acceptor.[10]

FRET pair development is also driven by the need to develop new pairs with improved properties for specific types of applications. For example, NowGFP has been utilised as a donor for red FPs tdTomato or mRuby2 and has led to development of FRET pairs with large FRET efficiency based on fluorescence lifetime analysis.[25] Circularly permuted GFPs have been used as a donor for mScarlet-I and one such pair (cpGFP175–mScarlet) has been used to develop the best existing ratiometric calcium ion (Ca^{2+}) biosensor.[26] mOrange-mCherry biosensors have been used in combination with a CFP-YFP pair for multiplexed imaging.[27–29]

4.1.5 Improving dynamic range of FRET-based biosensors

Improving the photophysical properties of FPs in a FRET pair is one way of improving FRET efficiency. Another way of increasing FRET efficiency is to adjust the interactions of the two FPs, and the distance between them. Since FRET is dependent on the orientation and distance between two FPs, these two factors can be modulated to obtain higher FRET efficiency leading to better ΔR (dynamic range).[7,30] A high dynamic range enables the measurement of more subtle changes through FRET.

One way to adjust the distance between two FPs is to optimize the connecting junctions (commonly referred to as linkers) between the FPs and recognition domain. Most biosensor development involves a critical step of optimizing the length and the molecular composition of these linkers.[7,30] A second approach is to change the topology by incorporating a circularly permuted fluorescent protein (cpFP) as an acceptor or donor. A cpFP can be described as a rearranged protein where the topology has been changed by genetically joining the original C- and N-termini of the FP and generating new C- and N-termini elsewhere in the protein structure.[7,30] This strategy was used to develop Twitch Ca^{2+} indicators which used cpCitrine as an acceptor and exhibited a 30% increase in dynamic range as compared to when a regular FP (not a cpFP) was used as an acceptor (**figure 4-3a**).[26]

A third approach is to adjust how the two FPs physically interact with each other by increasing the association between the two FPs such that a higher R_{max} can be achieved. This would ideally require an association that is fine-tuned such that the FRET-based biosensor can still form high FRET and low FRET states, depending on the conformational changes

brought about by binding of an analyte. The association should not be so strong that the FP's are perpetually bound and lose their ability to transduce any analyte binding changes. Examples of different ways in which FPs have been associated to increase the dynamic range of biosensors are explained in this section.

The CyPet-YPet FRET pair can be considered the first example where optimized intramolecular association between the two FPs increased FRET dynamic range. CyPet and YPet were evolved from CFP and YFP respectively through random mutagenesis to form a highly efficient FRET pair. The CyPet-YPet caspase biosensor had a 7-fold enhancement in FRET signal as compared to a CFP-YFP-based caspase biosensor.[31] Out of the 18 mutations collectively found in CyPet and YPet, the increased intramolecular association was attributed to two mutations S208F and V224L.[32] These two mutations synergistically increased I_A/I_D and established a design principle of utilising FP to FP association to increase the dynamic range of FRET pairs.[33,34]

Lindenburg and co-workers used a similar strategy to promote intramolecular interactions between mOrange-mCherry (**figure 4-3b**).[29] They engineered a FP to FP dimerization by introducing hydrophobic amino acids on the interacting interface of these two FPs. mOrange and mCherry were originally both derived by breaking the hydrophobic interfaces of DsRed which is an obligate tetramer.[35] The hydrophobic amino acids introduced to restore dimerization were the same ones that were mutated while monomerizing DsRed. Lindenburg and co-workers designed a protease biosensor based on mOrange-mCherry that had a $\Delta R/R_{min}$ of 23%. Upon introduction of the dimerization-inducing R125I mutation on both FPs, the $\Delta R/R_{min}$ increased to 174%. They also designed a zinc biosensor called redCALWY which exhibited an increase in FRET efficiency when R125I was introduced on mOrange and mCherry. However, the observed improvement was smaller than the one seen with the protease biosensor ($\Delta R/R_{min}$ improvement ~50% for Zn^{2+} versus 150% for protease). The authors suggest that this design principle of introducing weak dimerizing residues on the interface of FPs can be extended to many FPs belonging to the same family.

The strategies described above have all been demonstrated in unimolecular FRET detection. In contrast, modulating FP interactions based on dimerization is not typically

applicable to bimolecular FRET for detection of protein-protein interactions, as this would lead to undesirable homodimerization of acceptor or donor FPs. Grünberg and co-workers used a similar concept of increasing interaction between FRET pair FPs for bimolecular FRET. However, instead of modifying FP surfaces, they attached a protein domain (the WW domain of human YAP65 or the SH3 domain from *Saccharomyces cerevisiae* protein Sho1) to one FP and a cognate binding peptide to the other FP (**figure 4-3c**). This design strategy relies on weak protein-domain interactions to increase FRET efficiency. They used this system on mCitrine-mCherry, mTFP1-mCherry and mTurquoise2-mCitrine to study protein-protein interactions between full-length H-Ras and Raf1 as well as the drug-induced interaction between Raf1 and B-Raf.[36]

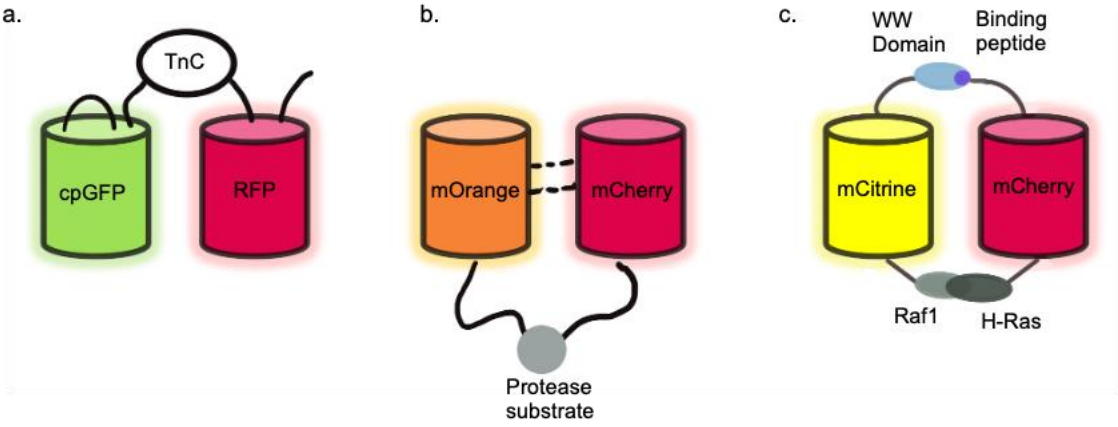

Figure 4-3. Examples of techniques to improve FRET efficiency. (a) Topology modification by inserting a cpFP, TnC = Troponin C (a Ca^{2+} binding protein). (b) Intramolecular interface association between FPs. (c) Bimolecular FRET pair with helper domain and binding peptide.

4.2 Development of a new green-red FRET pair

Based on these examples of FRET pairs, it is evident that there is still a need to develop and optimize new FRET pairs with the potential to achieve high signal-to-noise ratios. The overall objective of the project described in this chapter was to create a new green-red FP-based FRET pair that could serve as an improved alternative to the existing CFP-YFP pairs. To achieve this objective, I planned to optimize the dimer interface between the two FPs

such that they would form a weak heterodimeric complex, that exhibited high FRET efficiency, when in close proximity.

4.2.1 mScarlet-I as the FRET acceptor

As seen from the development of mRuby3, a favourable FRET acceptor needs to be as bright as possible in order to give a strong sensitized emission signal. Currently, mScarlet is the brightest red FP (brightness = 70 $M^{-1}cm^{-1}$) with a fast maturation time. A variant of mScarlet called mScarlet-I matures faster although it has a moderate decrease in brightness (brightness = 56 $M^{-1}cm^{-1}$).[37] Both mScarlet and mScarlet-I have been used as red FRET acceptors. Given the enhanced maturation of mScarlet-I, I selected it as the preferred FRET acceptor for the green-red FRET pair.[26,38]

4.2.2 Development of a green FRET donor

With mScarlet-I selected as the FRET acceptor, I next had to identify a green FP that could be a high efficiency FRET donor. Since the objective was to study the effect of interface interactions on FRET efficiency, this green FP would need to interact with the interface of mScarlet-I. Self-associating dimeric interactions are usually found in monomeric FPs that originate from the same family.[29,39] For this reason, I used a green FP that was engineered from mScarlet-I by Dr. Yi Shen in our lab. This green FP is referred to as green Scarlet (gScarlet) throughout this chapter. The development of gScarlet started with the random mutagenesis of position M67, the first residue of the chromophore forming tripeptide, which led to a dim green FP. This was followed by five rounds of directed evolution which resulted in a green FP that was bright enough to be used as a FRET donor.

a.

Version	0.1	0.2	0.3	0.4	0.5	0.6
Mutation	+ M67G	+ Y121H	+ F178C	+ V8L/F12Y	+ Q43H/K139R	+ N24D

b.

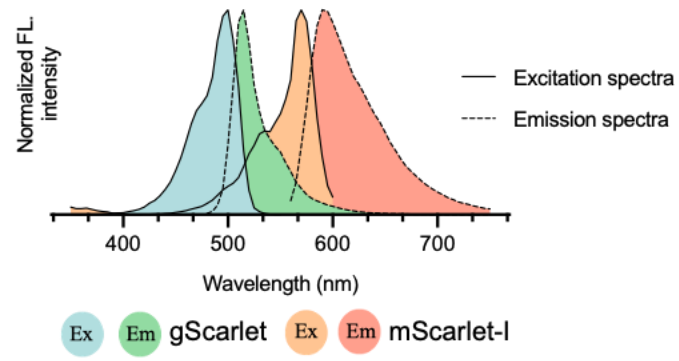

c.

	gScarlet	mScarlet-I
Ex max (nm)	500	570
Em max (nm)	515	590
QY	0.47	0.54
EC (M^{-1} cm^{-1})	87,600	104,000
pKa	5.2	5.4

Figure 4-4. Development and properties of gScarlet. (a) Evolution chart of gScarlet. (b) Excitation and emission spectra of gScarlet and mScarlet-I. (c) Key properties of gScarlet compared to mScarlet-I. QY = quantum yield and EC = Extinction coefficient

This transformation of a red FP to a green FP is possible due to the proposed branched mechanism of chromophore formation in DsRed (**scheme 4-1**) which can lead to either a green chromophore species **4-5** or a red chromophore species **4-10**.[40] FP chromophores are produced through a series of autocatalytic reactions. The chromophore of DsRed is formed from three sequential amino acids: Gln65, Tyr66, and Gly67. The proposed mechanism starts with a cyclization where the amide nitrogen of Gly67 attacks the carbonyl of Gln65 forming a 5-membered ring intermediate **4-2**. This 5-membered ring intermediate undergoes oxidation to form a hydroxylated cyclic imine (**4-3**) which is in equilibrium with the cyclic imine **(4-6)**. This equilibrium is the branching point where dehydration of **4-3** leads to the formation of the green chromophore. On the other hand, the cyclic imine **4-6** can undergo irreversible oxidation to form the blue chromophore intermediate **4-7** which can subsequently undergo hydroxylation and dehydration to form the neutral red chromophore **4-9**. This phenol chromophore exists in equilibrium with the anionic chromophore **4-10** which gives rise to the characteristic red fluorescence of DsRed. Inhibiting the oxidation of **4-6** can lead to the preferred formation of the green chromophore over the red chromophore.[41]

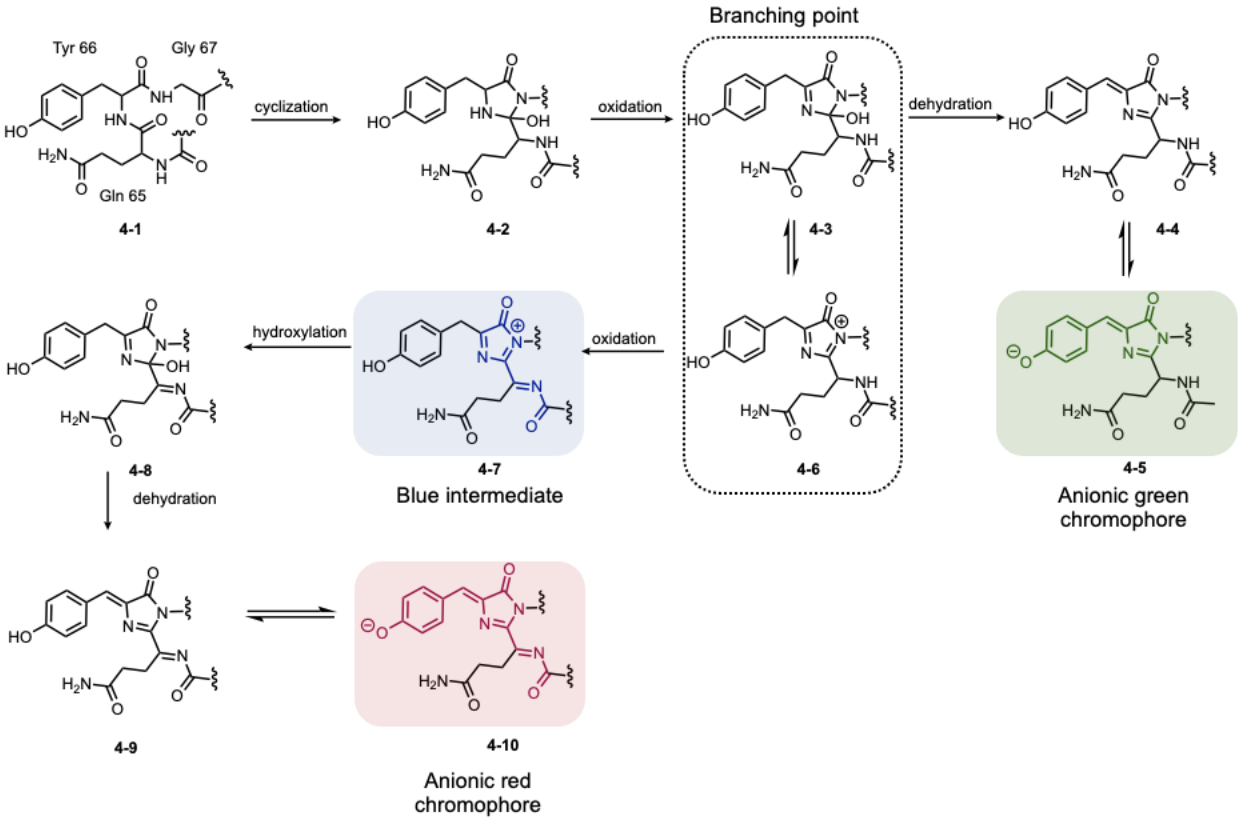

Scheme 4-1. Proposed mechanism for chromophore formation in DsRed. Adapted from reference [41].

A previous example of the development of a FP with a hypsochromic shift in excitation and emission is mTagBFP, which was developed from TagRFP by structure-based directed evolution to trap the blue intermediate in the chromophore formation pathway and prevent its further maturation.[42] Another example is the development of ddGFP from ddRFP which relied on two key mutations which were previously known to convert DsRed into a green FP.[43,44]

From the mutations listed in **figure 4-4a**; it is apparent that the M67G mutation changes the chromophore-forming tripeptide from MYG to GYG. Many yellow and orange FPs have GYG as their chromophore forming tripeptide.[45] F178C, Y121H and Q43H face towards the chromophore and are most likely to affect the chromophore environment (**figure 4-5**). During the evolution of mScarlet, the introduction of bulky F178 was believed to induce an upward movement of residue M164, which in turn forces the chromophore phenolate to

adopt a planar conformation.[37] Substituting phenylalanine with cysteine would reduce this co-planarity of the tyrosine ring and the N-acylimine which would result in less effective conjugation, causing a blue shift in the chromophore.[40] These three mutations also increase the hydrophilicity around the chromophore.

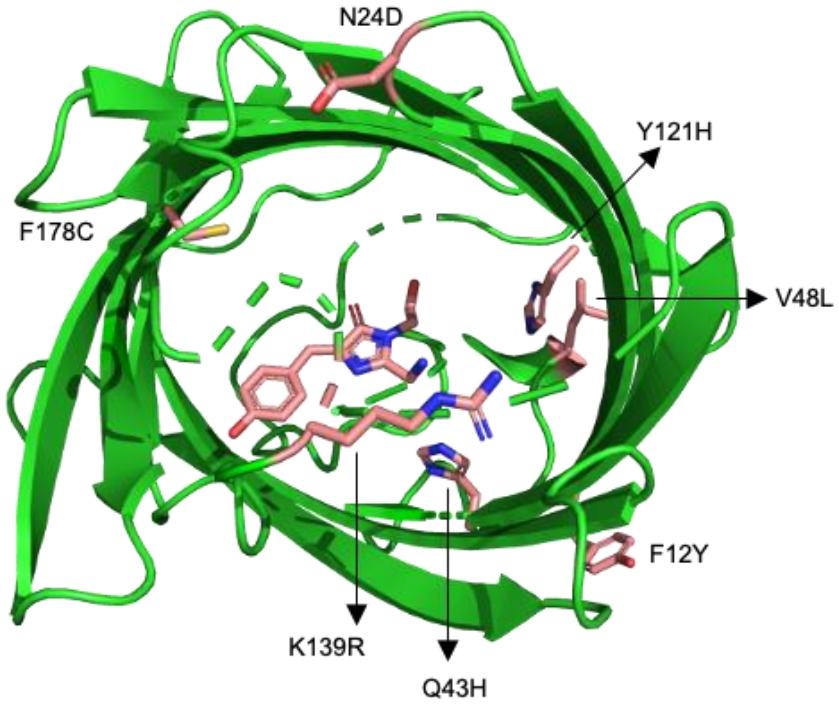

Figure 4-5. gScarlet protein structure model predicted by AlphaFold2.[46] Chromophore placed by superimposing with the structure of the Clover GFP (PDB id. 5WJ2).[46]

4.3 Green-red FP-based protease indicators

In order to determine the FRET efficiency between gScarlet and mScarlet-I, I decided to develop a protease indicator as a test system. gScarlet and mScarlet-I were attached to a WELQut protease recognition sequence (W- E- L- Q↓X) through a 16 amino acid flexible linker on either side of the recognition sequence (**figure 4-6**). First, the effect of donor and acceptor position in the indicator was determined. In an attempt to reduce the distance between the donor and the acceptor, the FP on the N- terminus of the indicator had six residues deleted from the C terminus of the FP and the FP on the C-terminus of the indicator had four residues deleted from the N-terminus of the FP. The first topological arrangement

tested had the donor gScarlet on the N-terminus (indicator named GWS, for gScarlet-WELQut-mScarlet-I). The proteolysis of GWS resulted in a $\Delta R/R_{min}$ of 2.56. Switching the positions of gScarlet and mScarlet-I (indicator named SWG) led to an increase in $\Delta R/R_{min}$ from 2.56 to 3.18.

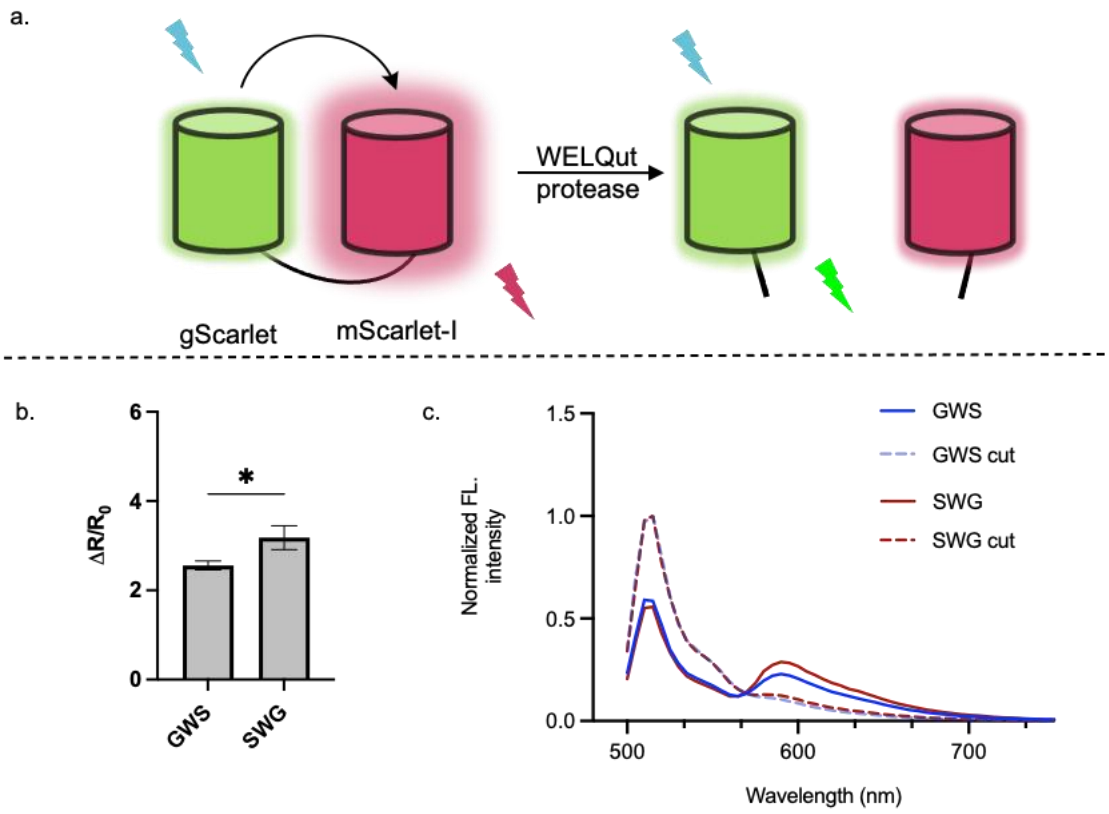

Figure 4-6. Effect of FP topology on a FRET-based protease indicator. (a) Schematic representation of the indicator constructs before and after being cleaved by WELQut protease. (b) FRET efficiency and (c) Normalized emission spectrum of protease indicators gScarlet-WELQ-mScarlet (GWS) and mScarlet-WELQ-gScarlet (SWG). Bar graph shows data ± S.D. for n = 3. p-value measured by unpaired t-test, *p < 0.05.

I decided to next determine if $\Delta R/R_{min}$ could be improved by following an intramolecular association strategy similar to that reported by Lindenburg and co-workers.[29] I focused on introducing weak dimeric interactions within the A-C interacting interface by reversing the mutations originally made in DsRed to break this interface. There were eleven mutations introduced in order to break the A-C dimer interface of DsRed. Nine of these mutations exist in mScarlet-I whereas two of the residues (A164, L174D; residues numbered as found in mScarlet-I) match DsRed. I selected seven residues to reverse: E154R, K163H, R173H, A193Y, N195Y, S223H and T224L (**figure 4-7a**). These reversions were systematically introduced by site directed mutagenesis on both gScarlet and mScarlet-I followed by measuring the change in dynamic range. The K163H mutation was made in all variants because of its positioning at the centre of the A-C interface. Finally, all these mutations were included on both FPs leading to a fully dimeric mScarlet-I and gScarlet protease indicator designated as "dimeric SWG".

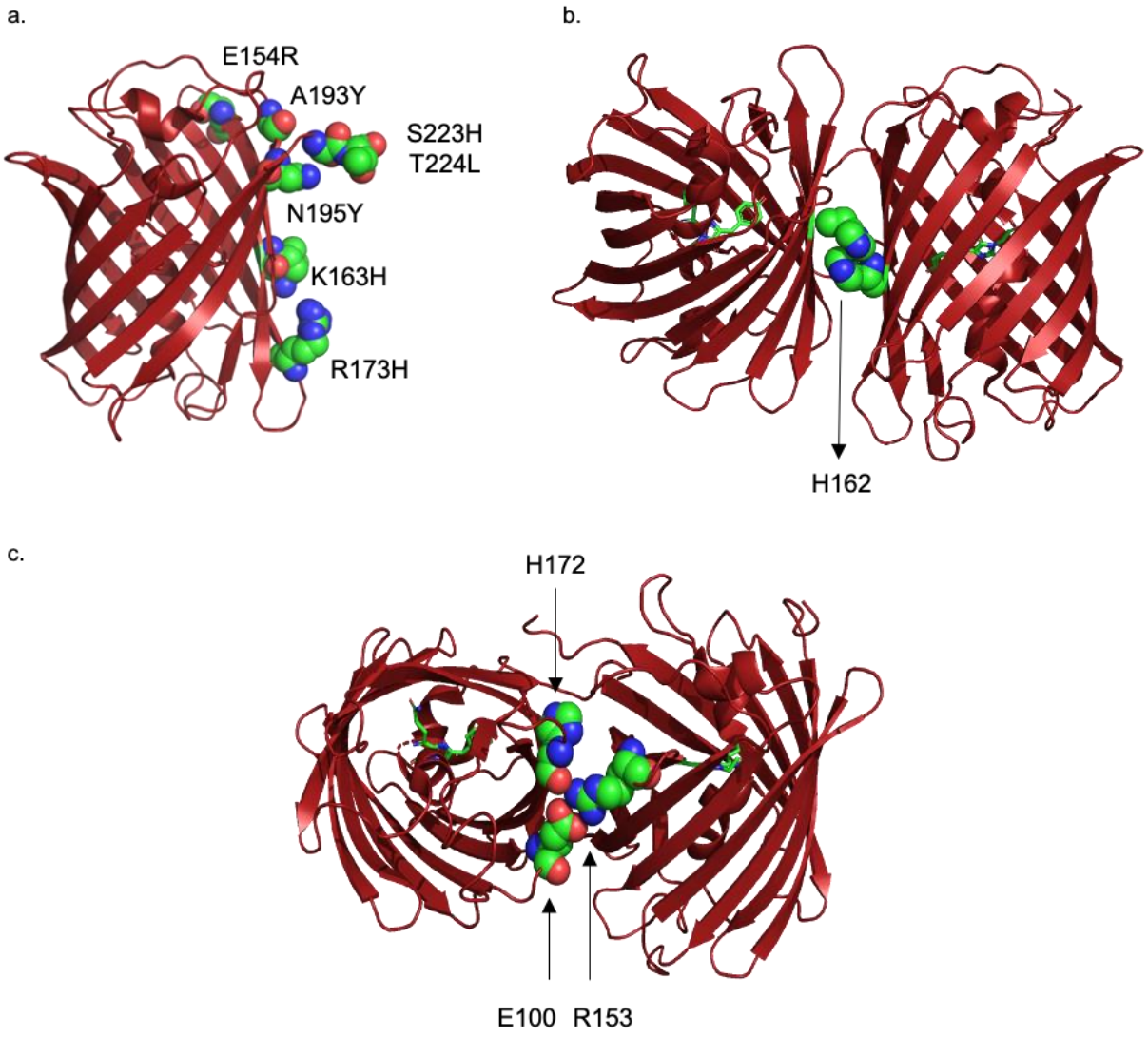

Figure 4-7. Intramolecular interface interactions. (a) Structure of mScarlet (PDB id. 5LK4)[37] showing key residues reversed on the interface. (b) Interaction of H162 (corresponding to K163 on m-Scarlet) on the A-C interface of DsRed (PDB id. 1G7K).[46] (c) Interaction of R153 with residues E100 and H172 on DsRed.

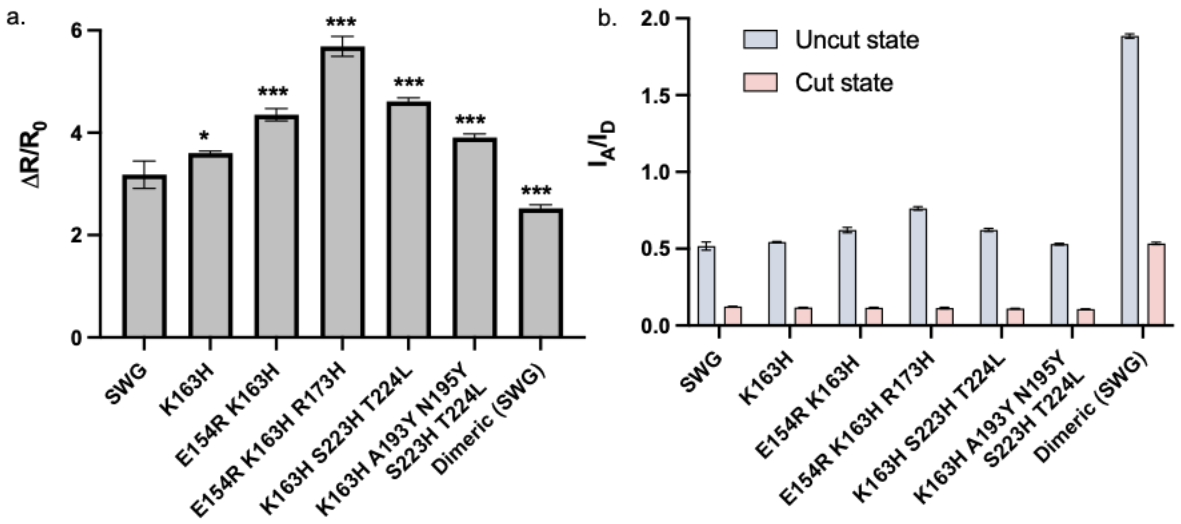

Figure 4-8. Effect of introducing intramolecular interactions on dynamic range of FRET based protease indicator. (a) Ratio change and (b) FRET ratio before and after proteolysis of mScarlet-WELQ-gScarlet (SWG) and variants with various combinations of mutations. Bar graph shows data ± S.D. for n = 3. p-value measured by one way ANOVA followed by Dunnett's multiple comparison test vs. SWG *$p < 0.05$, ***$p < 0.001$.

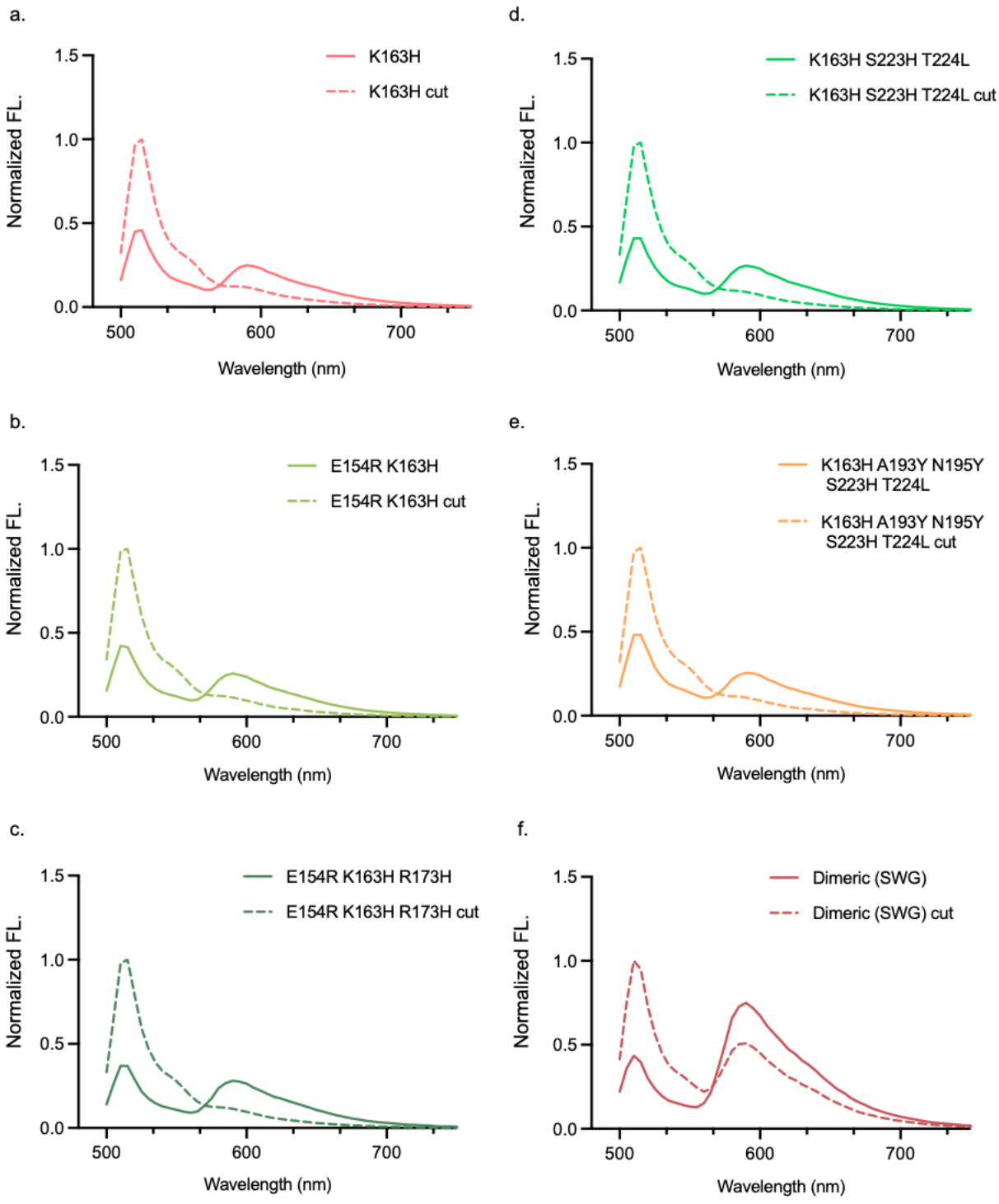

Figure 4-9. Normalized emission spectra of protease indicators (n = 3) mScarlet-WELQ-gScarlet (SWG) with mutations as listed on both FPs. (a) K163H. (b) E154R K163H. (c) E154R K163H R173H. (d) K163H S223H T224L. (e) K163H A193Y N195Y S223H

T224L. (f) E154R K163H R173H A193Y N195Y S223H T224L. Y-axis represents normalized fluorescence intensity. Spectra have been colour coded according to the indicators $\Delta R/R_{min}$ change with dark green as the highest and dark red as the lowest change.

As seen in **figure 4-8a**, all variants with different reversion, except dimeric SWG, had higher ratio changes compared to the original indicator. In all variants, the FRET ratio (I_A/I_D) is higher in the uncut state as compared to original SWG (**figure 4-8b**). The FRET ratio in the cut state should be the same for all variants as it depends primarily on the emission peak shape of the donor (**figure 4-9**), and this is observed for all variants except dimeric (SWG) where the FRET ratio is higher than original SWG. The variant with E154R, K163H, and R173H reversions on both FPs had the highest FRET response of 568% as compared to 318% of the original SWG. The increase in FRET efficiency for most variants can be attributed to the increase in FRET ratio in the bound state which is an indication that promoting intramolecular interactions helps. The increase in bound state FRET for variants with E154R can potentially be explained by favorable intramolecular interactions of R154 on one FP (either gScarlet or mScarlet-I) with E101 on the other FP (**figure 4-7c**). Interestingly a change in FRET ratio is observed between the bound and cut state of dimeric SWG, indicating the possibility of weakened intramolecular association between dimeric mScarlet-I and dimeric gScarlet post proteolysis.

4.4 gScarlet – mScarlet-I-based Ca^{2+} and K^+ indicators

Given the good performance of gScarlet-mScarlet-I as a FRET pair for protease indicator, next I expanded its application to develop indicators for Ca^{2+} and potassium ion (K^+). Similar to the protease indicators, I introduced mutations that would increase intramolecular association between the FPs with the aim of increasing FRET dynamic range.

4.4.1 gScarlet-mScarlet-I-based Ca^{2+} indicator

The calcium ion (Ca^{2+}) is an important and multi-functional secondary messenger involved in regulating various cellular processes such as growth, proliferation, transcription etc.[47] It also plays an important role in disease pathologies, and dysregulation of intracellular Ca^{2+}

homeostasis has been proposed as an early hallmark of neurodegenerative disorders such as Alzheimer's.[48] Given the importance of Ca^{2+}, many FP-based indicators have been designed to study its dynamics.[49] Currently some of the best ratiometric Ca^{2+} indicators employing green-red FPs are the Twitch biosensors (**figure 4-3a**). These biosensors have mScarlet as the FRET acceptor and cpGFP175, cpNeon174, cpClover175 or cpVenus175 as the FRET donor. These biosensors have FRET efficiencies as high as 40% *in vitro* in mammalian cells with Ca^{2+} binding affinities near the neuronal Ca^{2+} concentration. These properties allow for their use to image Ca^{2+} dynamics both *in vitro* and *in vivo* with high signal to noise ratios.[26]

Likewise, I designed a Ca^{2+} indicator with gScarlet–mScarlet-I pair as the FRET indicator domain. The recognition domain consisted of calmodulin (CaM) along with the CaM-binding peptide of myosin light-chain kinase (M13). CaM-M13 was fused in between the two FPs. When Ca^{2+} binds to CaM an intramolecular interaction is initiated which changes the CaM-M13 conformation from extended to compact. In this Ca^{2+}-bound compact state, an increase in FRET between gScarlet and mScarlet-I is expected to be observed. This Ca^{2+} based response is reversible and upon decrease in Ca^{2+} concentration or chelation of Ca^{2+} by an external additive, the recognition domain should revert to its extended state causing a decrease in FRET response (**figure 4-10a**).[49]

Similar to the protease indicator, I wanted to establish which relative arrangement of mScarlet-I and gScarlet on the N- or C-terminus of the indicator provided better response. These indicators are labelled as SCG or GCS based on the positioning of the FP (S = mScarlet-I, C = CaM-M13 and G = gScarlet). As seen in **figure 4-10b**, having mScarlet-I on the N-terminus increased FRET efficiency by 17 ± 5 %.

With the favoured FP arrangement established, the mutations E154R, K163H, R173H, A193Y, N195Y, S223H and T224L were introduced systematically on both gScarlet and mScarlet-I followed by measuring the change in dynamic range. When all these mutations were included on both FPs, the corresponding indicator is labelled as "dimeric SCG".

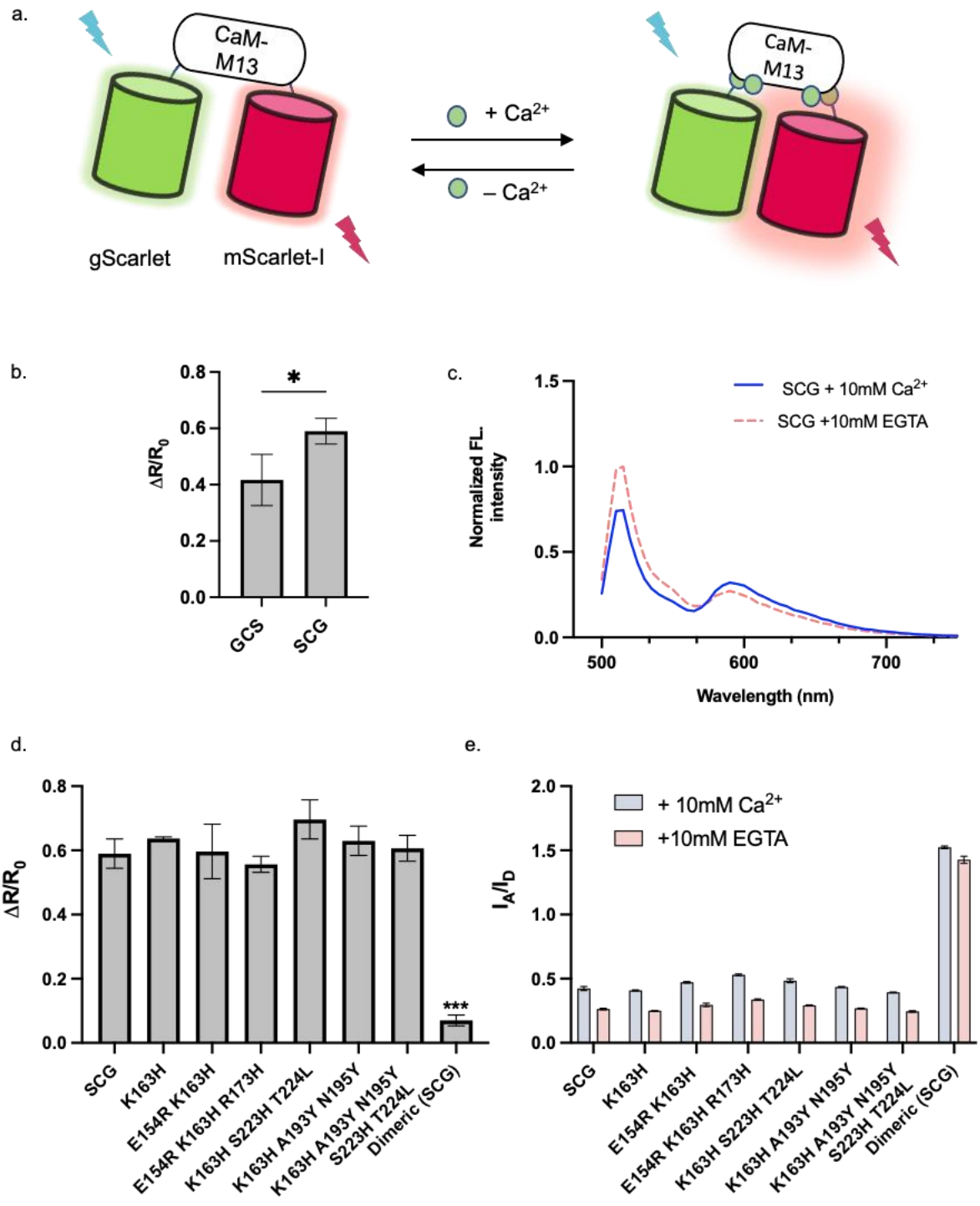

Figure 4-10. Design and response of gScarlet – mScarlet-I-based Ca^{2+} indicator. (a) Schematic representation of the mechanism of FRET-based Ca^{2+} indicator. (b) FRET efficiency of Ca^{2+} indicators gScarlet-CaM-M13-mScarlet (GCS) and mScarlet-CaM-M13-gScarlet (SCG) (c) Normalised emission spectra of SCG with added Ca^{2+} and EGTA. (d)

FRET efficiency and (e) FRET ratio of SCG indicator variants with mutations as listed on the x-axis. Bar graphs show data ± S.D. for n = 3. p-value measured by unpaired t-test for (b), and one way ANOVA followed by Dunnett's multiple comparison test for (c) vs. SCG, *p < 0.05, ***p < 0.001.

Unlike in the case of protease indicators, there was no substantial increase in FRET efficiency observed in all variants with different mutations as compared to the original indicator with no reversions (**figure 4-10d**). In most variants, any marginal increase in FRET ratio (I_A/I_D) in the presence of 10 mM Ca^{2+} was accompanied by an increase in FRET ratio in the presence of 10 mM EGTA. With the dimeric SCG, the two FPs seem to be tightly bound in both the presence and absence of Ca^{2+}, with the interaction solely driven by the intramolecular association of the FPs.

These results suggest that introducing mutations associated with increasing intramolecular association of the FPs does not always lead to an improvement in FRET efficiency. The protease indicator and the Ca^{2+} indicator function through very different mechanisms. In protease indicators the FPs are closely held together with a flexible linker which would allow them to freely orient to maximize interface interactions, leading to a higher FRET. Also, after the irreversible cleavage of the substrate holding the FPs together, the FPs are disconnected and can diffuse without being affected by intramolecular attractions. Whereas in the case of Ca^{2+} indicators the intramolecular interactions of the two FPs are limited by the presence of CaM-M13 domain which may not allow the same level of orientation flexibility. Further upon Ca^{2+} release the FPs are still held together in the construct and their interfaces can still interact, which drives the FRET increase in both Ca^{2+} bound and free state. The dimeric SCG indicator shows constitutive dimerization, restricting its dynamic range. Unfortunately, a balanced equilibrium between a Ca^{2+} bound and unbound state was not achieved with these reversions.

4.4.2 gScarlet-mScarlet-I-based K^+ indicator

The potassium ion (K^+) is one of the most abundant cation in the human body and is critical for maintaining cellular functions. Most of the K^+ pool is present intracellularly at a concentration of 140-150 mM and the remaining is present extracellularly at a concentration of 3.5-5 mM. Maintenance of K^+ gradient across cell membranes is responsible for the excitability of neuronal and muscular tissue. Dysregulation of K^+ homeostasis can affect cardiovascular, neurological and the renal systems leading to pathological conditions.[49]

The identification of *Escherichia coli* K^+ binding protein (Kbp) has led to the development of genetically encoded K^+ indicators. Kbp was reported to undergo large conformational changes due to K^+ binding. Kbp is a 16 kDa protein consisting of a LysM (lysin motif) domain at the N-terminus and BON (bacterial OsmY and nodulation) at the C-terminus. When Kbp binds to K^+ it undergoes a conformational change and the LysM and the BON domain come close together. The mechanism of K^+ binding of Kbp is similar to the mechanism of Ca^{2+} binding of CaM-M13. Currently, there are only two ratiometric indicators for K^+: KIRINs [(K) ion ratiometric indicator] and GEPIIs (genetically encoded potassium ion indicators). Both of these indicators use Kbp as the K^+ recognition domain. The indicator domain of both is CFP-YFP-based, KIRIN1 utilised mCerulean3-cpVenus173 and GEPII has mseCFP-cpVenus. KIRIN1-GR is variant which has a green-red FRET pair of Clover-mRuby2. Out of the three, GEPII has the highest *in vitro* $\Delta R/R_{min}$ of 220%, followed by 130% of KIRIN 1 and KIRIN1-GR has the lowest at 20%.[50,51]

Given the scope of development for a new green-red K^+ indicator, I tested out gScarlet-mScarlet-I as a FRET pair for a Kbp-based indicator. Unlike the protease and Ca^{2+} indicator, the order of FP had a minimal effect on FRET efficiency of K^+ indicators. Gratifyingly, mScarlet-I– Kbp–gScarlet (SKG) showed an increase in response by 37 ± 9% over KIRIN1-GR (**figure 4-11a**).

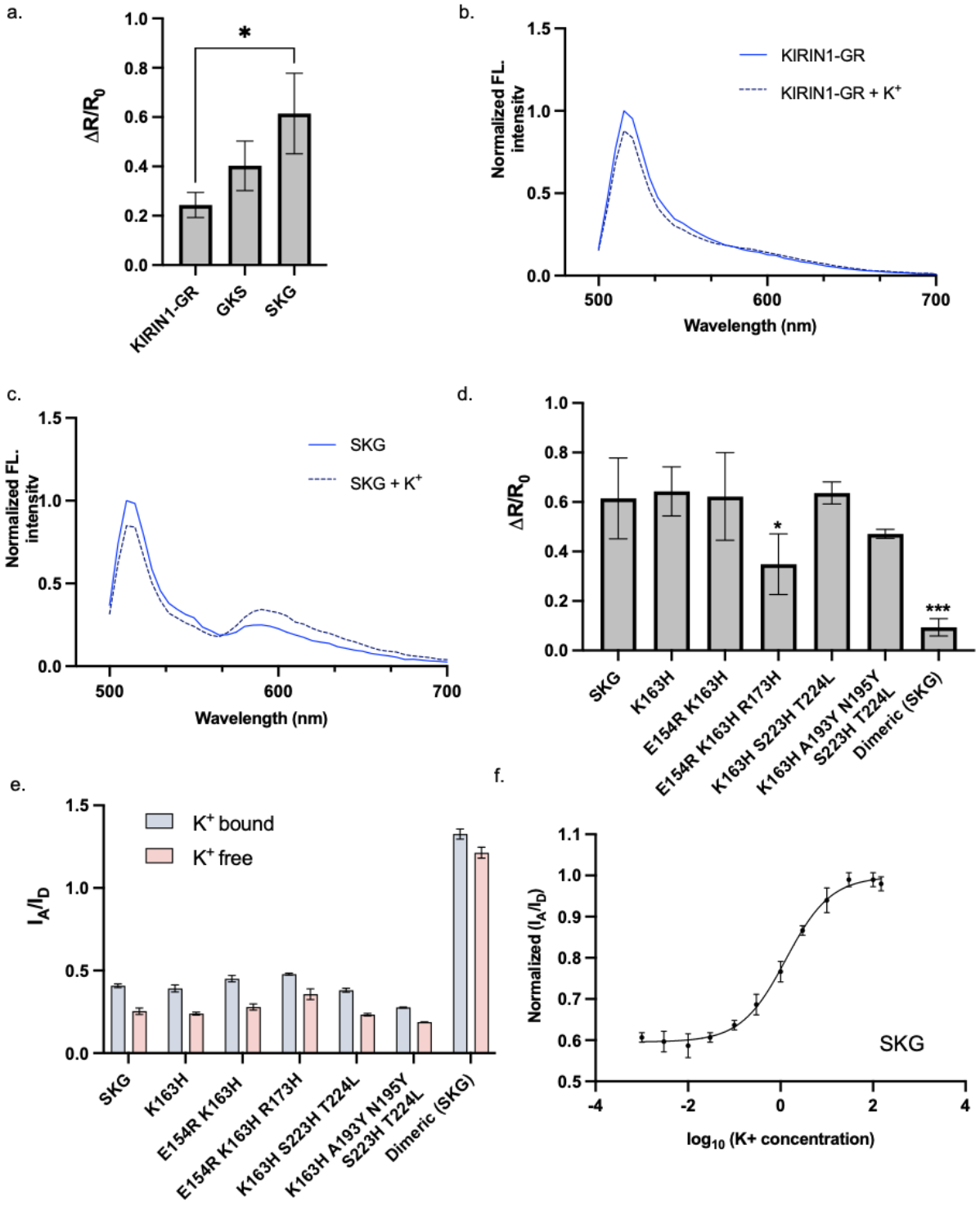

Figure 4-11. Response of gScarlet – mScarlet-I-based K^+ indicators. (a) FRET efficiency of K^+ indicators gScarlet-Kbp-mScarlet (GKS), mScarlet-Kbp-gScarlet (SKG) and KIRIN1-

GR. (b) Normalised emission spectra of KIRIN1-GR and (c) SKG in the presence and absence of K^+ (150 mM). (d) FRET efficiency and (e) FRET ratio of SKG indicator variants with mutations as listed on the x-axis. (f) K^+ titration curve of SKG vs. acceptor-to-donor fluorescence ratio (F_{590}/F_{515}), data expressed as mean ± S.D. Bar graphs show data ± S.D. for n = 3. p-value measured by unpaired t- test for (a) and one way ANOVA followed by Dunnett's multiple comparison test for (c) vs. SCG, *p < 0.05, ***p < 0.001.

Similar to the Ca^{2+} indicators, there was no substantial increase in FRET efficiency observed in all variants with different reversion as compared to the original indicator with no reversions (**figure 4-11d**). In the variant that has E154R, K163H and R173H the FRET ratio (I_A/I_D) increases both in the presence of 150 mM K^+ and absence of K^+ resulting in a lower FRET efficiency similar to the dimeric SKG. Although the dynamic range of SKG could not be improved further, mScarlet-I and gScarlet provide a good alternative to KIRIN1-GR. SKG exhibits a K_d of 1.31 ± 0.40 mM for K^+ (**figure 4-11e**) which is similar to the K_d of KIRIN1-GR (2.56 ± 0.01 mM for K^+).

4.5 Comparison of gScarlet-mScarlet-I to other FRET pairs

After establishing that gScarlet-mScarlet-I can be used to develop FRET indicators for detecting protease activity, Ca^{2+} and K^+, its performance was benchmarked against two existing FRET FP pairs. mClover3–mRuby3 (C-R) pair was selected since it is the best existing green-red FP pair.[23] cpVenus175–mScarlet-I (cpV-S) pair was selected as it would be most similar to the FRET pair in the highly responsive Twitch-VR Ca^{2+} indicator.[26] Protease, Ca^{2+} and K^+ indicators were developed by substituting gScarlet–mScarlet-I with these FRET pairs. For consistency, in all the indicators the FRET donor was positioned on the N- terminus. mClover3-mRuby3 had the same number of residues deleted on the C terminus and N terminus respectively as gScarlet–mScarlet-I.

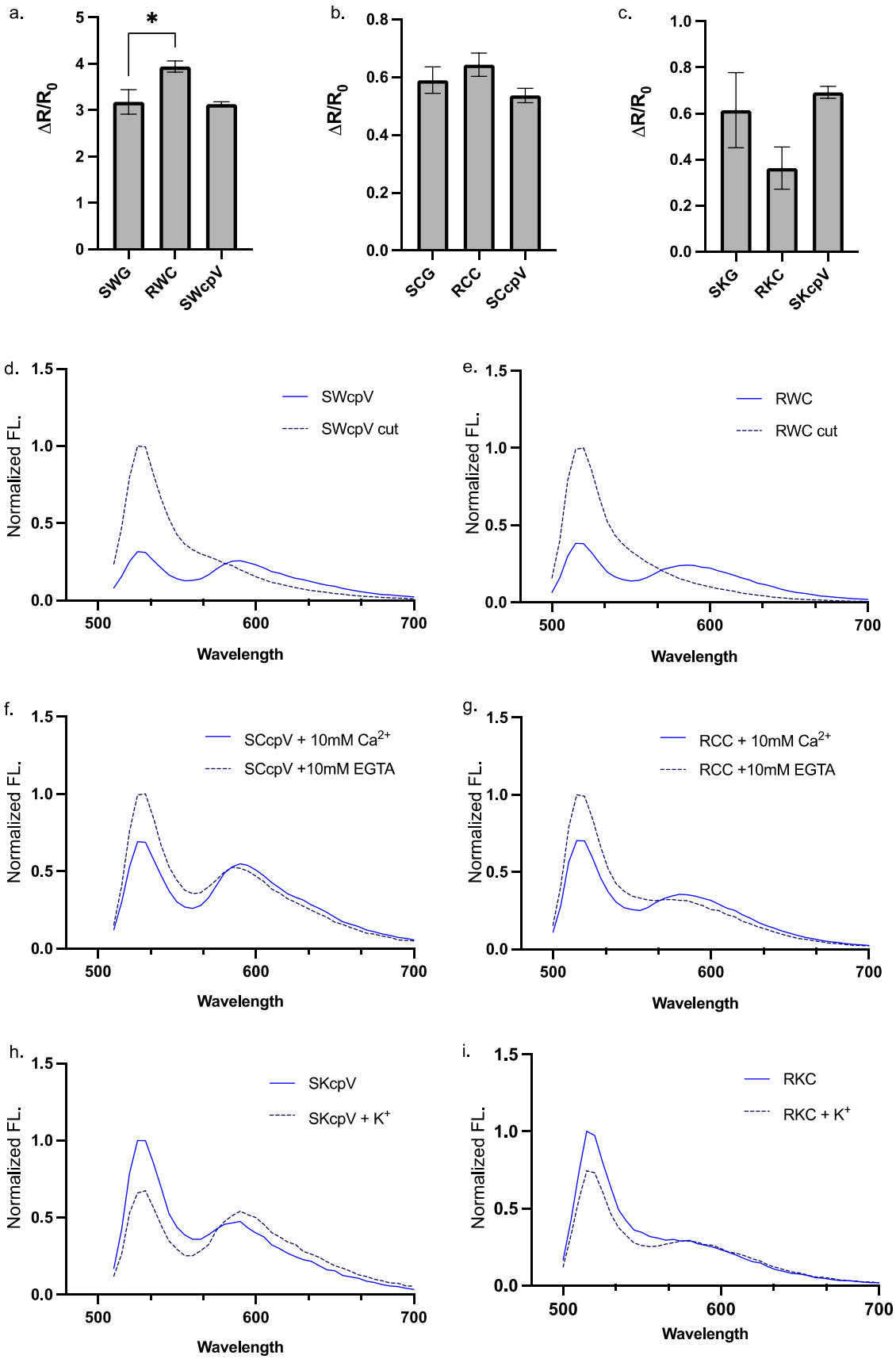
a.
b.
c.
ΔR/R0
SWG
RWC
SWcpV
SCG
RCC
SCcpV
SKG
RKC
SKcpV
d.
e.
f.
g.
h.
i.
Normalized FL.
Wavelength
SWcpV
SWcpV cut
RWC
RWC cut
SCcpV + 10mM Ca2+
SCcpV +10mM EGTA
RCC + 10mM Ca2+
RCC +10mM EGTA
SKcpV
SKcpV + K+
RKC
RKC + K+

Figure 4-12. Benchmarking the performance of gScarlet – mScarlet-I indicator. FRET efficiency of (a) protease indicators (b) Ca^{2+} indicators (c) K^+ indicators. Normalised emission spectra (d,f,h) of mScarlet-I and cpVenus containing indicators, and (e,g,i) mRuby3 and mClover 3 containing indicators. Bar graphs show data ± S.D. for n = 3. p-value measured by unpaired t-test, *p < 0.05.

As seen in **figure 4-12a-c**, indicators with mScarlet-I – gScarlet have similar response to mScarlet-I- cpVenus. mRuby3-mClover 3 performs better than mScarlet-I – gScarlet as a FRET pair in the protease indicator. The response of mRuby3–CaM-M13–mClover3 is similar to mScarlet-I–CaM-M13–gScarlet. In contrast, for the K^+ indicator there is a marginal decrease in the indicator with mRuby3-mClover 3 as compared to mScarlet-I-gScarlet. This comparison shows that all three FP pairs are good potential alternatives to CFP-YFP pairs, and they all show a good response.

From these screens it is observed that the green-red K^+ indicators have the most substantial improvement over KIRIN1-GR. mScarlet-I –Kbp– cpVenus exhibits a K_d of 0.88 ± 0.46 mM and mRuby3-Kbp-mClover3 exhibits a K_d of 1.27 ± 0.29 mM for K^+ (**figure 4-13**).

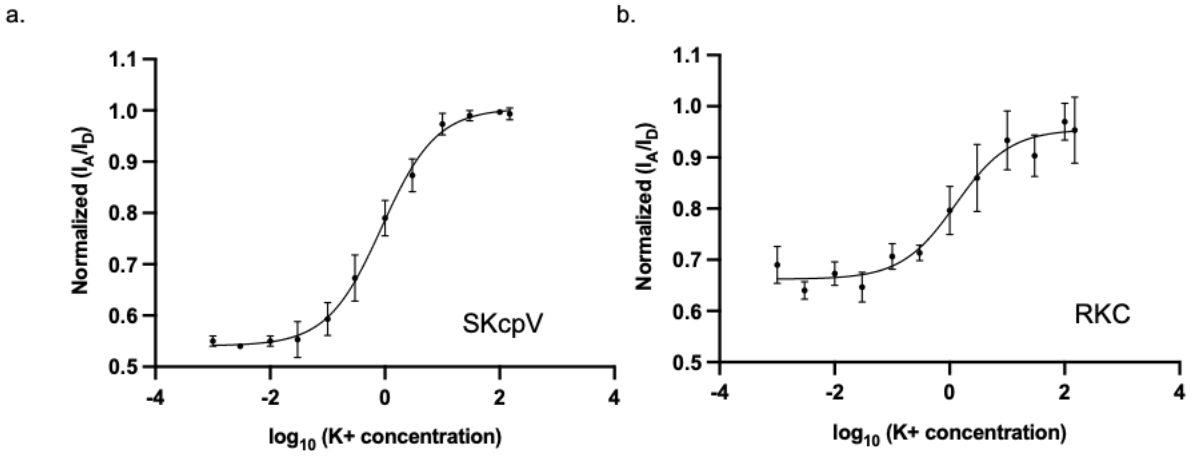

Figure 4-13. K^+ titration curves of (a) SKcpV and (b) RKC versus normalized acceptor-to-donor fluorescence ratio. Data expressed as mean ± S.D for n = 3.

4.6 Further characterization of FRET-based indicators

Since FRET measurements are dependent on the proper expression and maturation of both FPs forming a pair, it was important to validate that both FPs were formed properly in these indicators. A two-step validation was set up, first these indicators were analysed through a modified SDS-PAGE (polyacrylamide gel electrophoresis) where the samples were loaded without being denatured by boiling in SDS. This modification was done in order to understand the oligomeric interactions of FPs in the indicators. Secondly, an absorbance spectrum was recorded for all these indicators. This spectrum would indicate the presence of a functional chromophore and the relative amounts of donor to acceptor FP. For these validation experiments, all proteins were expressed in parallel with identical culture conditions and purification methods.

The SDS-PAGE analysis showed that the correct band sizes for protease indicators (~54 kDa), Ca^{2+} indicators (~ 71 kDa), and K^{+} indicators (~ 68 kDa), are present (**figure 4-14**). However, there are also bands with molecular weights 2.5-3.5 times higher than the expected molecular weight. These higher molecular weight bands indicate the presence of some inter-molecular interactions in these indicators. This can be expected in the variants which have mutations to increase interface interactions, for instance gScarlet on one molecule of an indicator can interact with a gScarlet or mScarlet-I on another molecule and this would lead to higher molecular weight aggregates. Surprisingly, these higher molecular weight bands are also observed in the original indicators. This suggests that even original gScarlet and mScarlet-I can have intermolecular interactions. In the right panel of **figure 4-14** where these gels are visualised under cyan light illumination, lower molecular weight red and green bands are visible, suggesting that partial proteolysis of the indicators occurred during cell lysis and purification. Possibly, these proteolyzed segments interact with the intact protein to form the multiple bands greater than 25 kDa.

The SDS PAGE analysis also helps visualize the issue of relatively low protein expression of indicators with mRuby3-mClover3 and mScarlet-I-cpVenus.

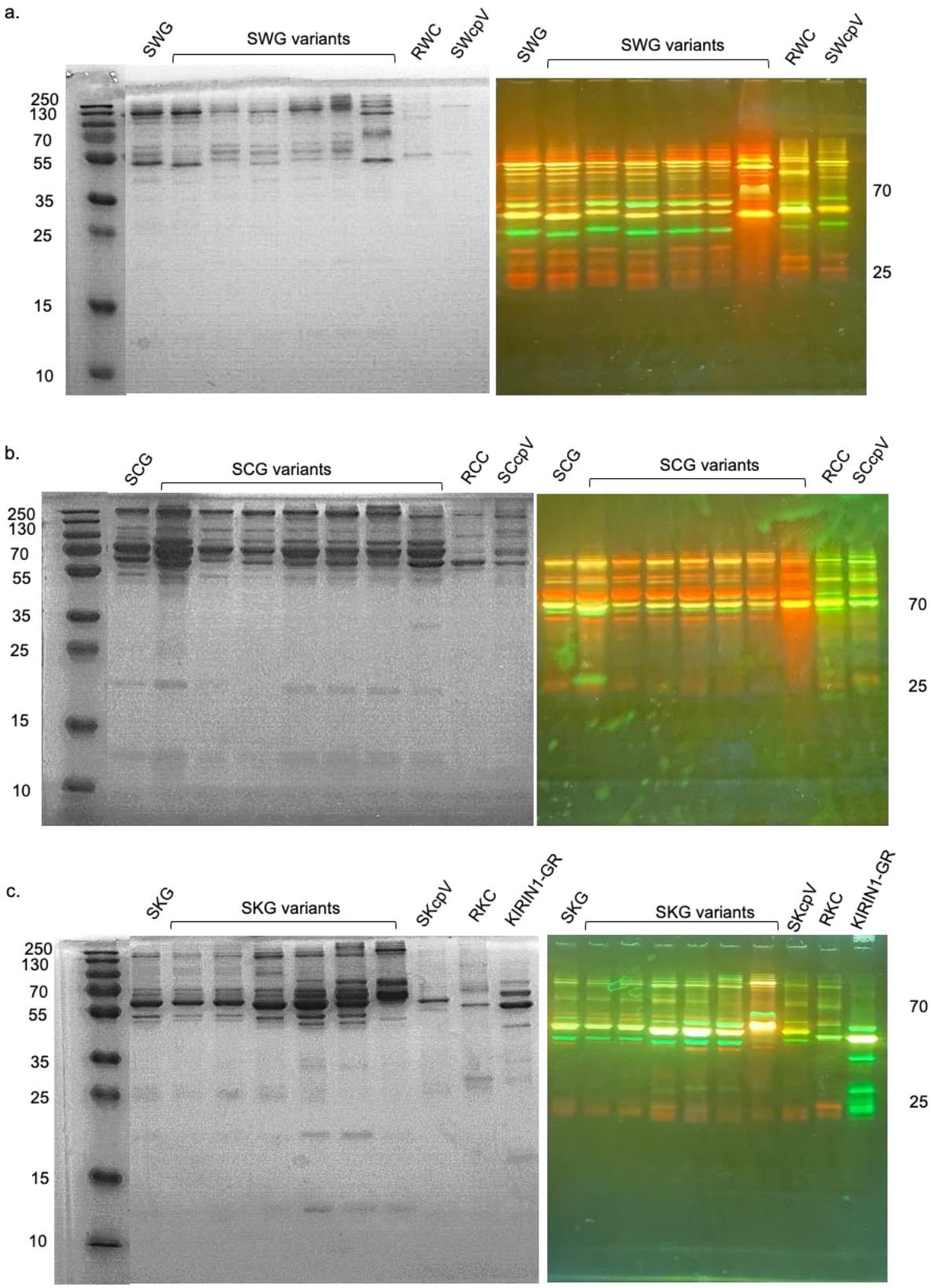
a.
SWG
SWG variants
RWC
SWcpV
250
130
70
55
35
25
15
10
70
25
b.
SCG
SCG variants
RCC
SCcpV
c.
SKG
SKG variants
SKcpV
RKC
KIRIN1-GR

Figure 4-14. SDS-PAGE (without heat denaturation) analysis of mScarlet-I–gScarlet and variants, mRuby3-mClover3, and mScarlet-I–cpVenus indicators. (a) Protease indicators (expected molecular weight = 54 kDa). (b) Ca^{2+} indicators (expected molecular weight = 71 kDa). (c) K^{+} indicators (expected molecular weight = 68 kDa). Left panel shows Coomassie stained bands and right panel shows gels excited by a Xenon-Arc lamp with a 470/40 nm bandpass filter, and the emission was collected through a 500 nm long pass filter.

The absorbance spectrum from all indicators shows peaks from both FPs. The absorbance spectra of indicators containing variants of mScarlet-I–gScarlet were deconvoluted with a Python script based on absorbance spectra of single FPs (gScarlet and mScarlet-I). The stoichiometry of folded gScarlet to mScarlet-I in a pair was determined through the deconvoluted spectra and is around 1 for all indicators **(figure 4-15).**

The low protein expression of mRuby3-mClover3 and mScarlet-I-cpVenus is evident from the absorbance spectra which reveals that the total integrated absorbance is lower than mScarlet-I-gScarlet.

Overall, both the SDS-PAGE and the absorbance spectra indicate the presence of functional donor and acceptor FPs that are responsible for the observed FRET.

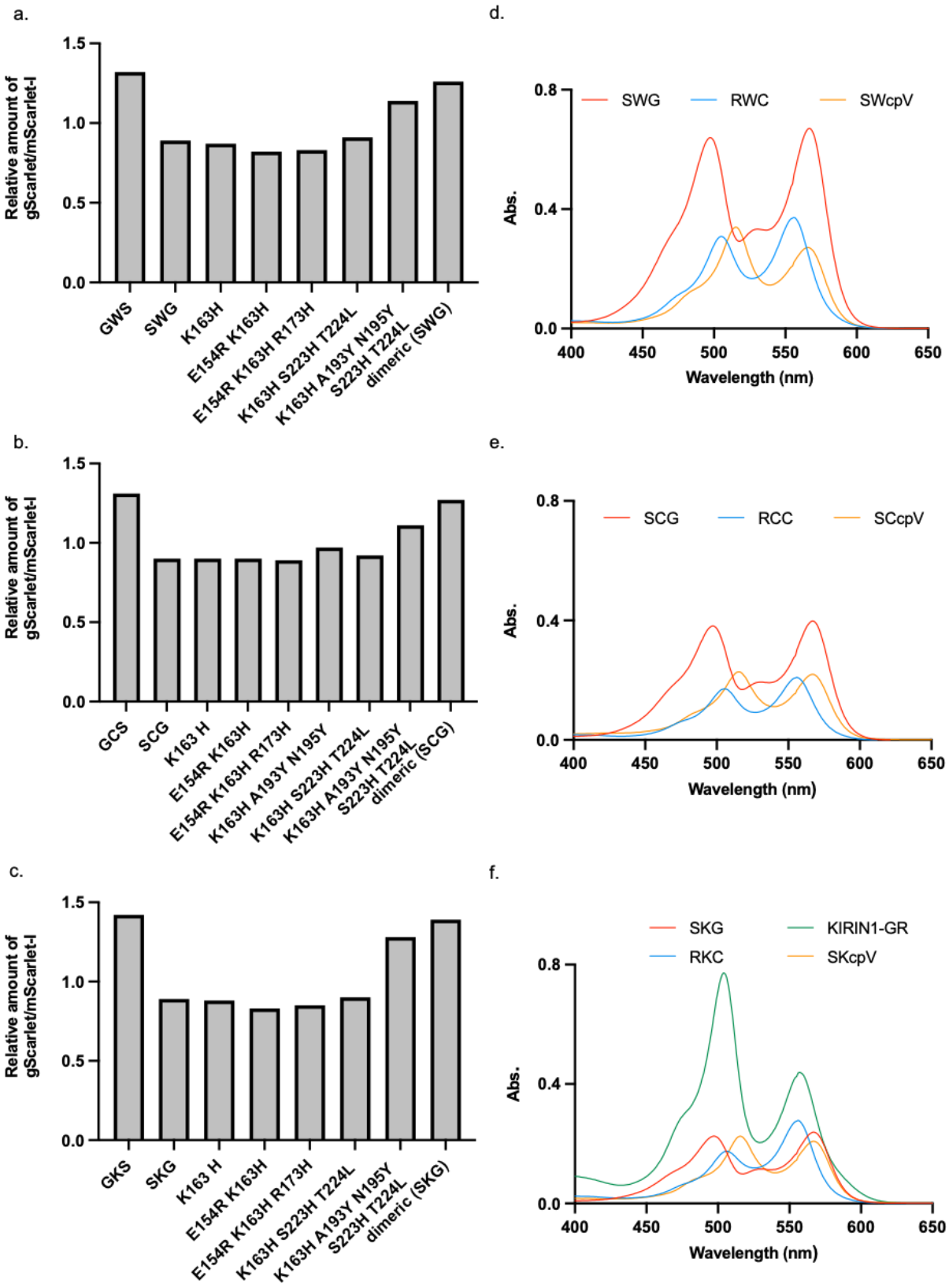
a.
Relative amount of gScarlet/mScarlet-I
1.5
1.0
0.5
0.0
GWS
SWG
K163H
E154R K163H
E154R K163H R173H
K163H S223H T224L
K163H A193Y N195Y S223H T224L
dimeric (SWG)
d.
SWG
RWC
SWcpV
Abs.
0.8
0.4
0.0
400
450
500
550
600
650
Wavelength (nm)
b.
Relative amount of gScarlet/mScarlet-I
GCS
SCG
K163 H
E154R K163H
E154R K163H R173H
K163H A193Y N195Y
K163H S223H T224L
K163H A193Y N195Y S223H T224L
dimeric (SCG)
e.
SCG
RCC
SCcpV
Abs.
Wavelength (nm)
c.
Relative amount of gScarlet/mScarlet-I
GKS
SKG
K163 H
E154R K163H
E154R K163H R173H
K163H S223H T224L
K163H A193Y N195Y S223H T224L
dimeric (SKG)
f.
SKG
KIRIN1-GR
RKC
SKcpV
Abs.
Wavelength (nm)

Figure 4-15. Absorbance of mScarlet-I–gScarlet and variants, mRuby3-mClover3 and mScarlet-I–cpVenus indicators. (a-c) Relative amounts of gScarlet to mScarlet-I in various indicators. (d-e) Representative absorbance spectra of protease, Ca^{2+} and K^+ indicators.

4.7 Summary and conclusions

This chapter describes the development of a new green-red FRET pair with mScarlet-I as the FRET acceptor and gScarlet (a blue-shifted version of mScarlet-I) as the FRET donor. The potential of this FP pair has been established by developing FRET-based indicators to detect protease activity, Ca^{2+}, and K^+. This pair can serve as a good alternative to the existing cyan-yellow FRET pair for construction of ratiometric biosensors.

An attempt was made to improve the dynamic range of mScarlet-I–gScarlet indicators by introducing hydrophobic mutations which would allow for weak hetero-dimerization of mScarlet-I and gScarlet to occur. Although this strategy proved useful in improving FRET efficiency for our protease indicator, it did not improve the FRET efficiency for our Ca^{2+} and K^+ indicators. This suggests that the strategy can be useful when mScarlet-I and gScarlet are closer in proximity and are joined together by flexible linkers that allows the orientational flexibility to form intramolecular interactions. When mScarlet-I and gScarlet are fused along with a comparatively rigid binding domain, their conformational mobility is more limited, and they may not be able to adopt the orientation required for intramolecular interactions to occur. The aim was to identify a set of mutations that increases FRET efficiency universally across different indicators employing gScarlet and mScarlet-I. Unfortunately, these experiments strongly suggest that indicators need to be optimized individually based on their own unique binding domains.

In the cases where intramolecular interactions did help, introduction of charged interactions (e.g., the interaction of E154R on one FP with residue E101 on the other FP) seem to influence the dynamic range more than the introduction of hydrophobic interactions. Constitutive high affinity dimerization, as seen in dimeric (SWG/SCG and SKG), locks the two FPs in a bound state, essentially rendering the indicator unable to respond to any changes in the recognition domain. A finely balanced equilibrium is required to ensure that FP interactions are driven primarily by the change in conformation brought about by the binding

domains and that any other enhancement to FP interactions are weak enough to improve FRET efficiency in bound state but do not affect the un-bound state.

The mScarlet-I–gScarlet pair led to responses similar to those observed for mRuby3-mClover3 and mScarlet-I–cpVenus. All three FP pairs are similarly effective and reasonable starting points for development of FRET-based indicators. As demonstrated in this work, Ca^{2+} and K^{+} indicators were successfully developed simply by substituting FPs in existing indicators. Indicators with better responses could potentially be developed by further optimizing the linkers connecting them or by improving the photophysical properties of these FPs. Overall, mScarlet-I and gScarlet seem to be a reliable FRET FP pair that could be utilised to create FRET indicators for various cellular applications.

4.8 Experimental methods

4.8.1 General methods and material

All DNA primers for cloning and mutagenesis were purchased from Integrated DNA Technologies. Genes encoding individual components of indicators were synthesised by polymerase chain reaction (PCR) using Q5® High-Fidelity DNA Polymerase from New England Biolabs. Site directed mutagenesis was performed by Quikchange lightning mutagenesis kit (Agilent) or by CloneAmp HiFi PCR Premix (Takara Bio). PCR products and products of restriction digests were purified using GeneJET gel extraction kit (Thermo Fisher). Restriction enzymes and ligases were purchased from New England Biolabs or ThermoFisher. Absorbance spectra were recorded with a DU-800 UV-visible spectrophotometer (Beckman). The fluorescence spectra were measured using a Tecan Safire2 microplate reader.

4.8.2 Plasmid DNA construction

The initial protease indicator was constructed by amplifying the gene encoding gScarlet and mScarlet-I by PCR and overlapping these PCR products one at a time with a DNA oligomer that encodes for the synthesised linker and WELQ protease substrate. Ca^{2+} and K^{+} indicators were constructed similarly.

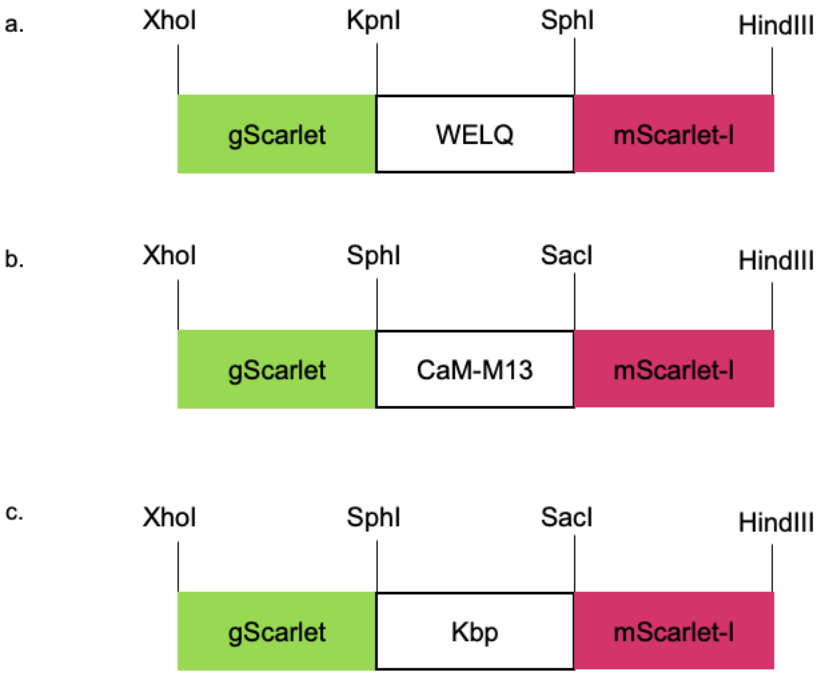

Figure 4-16. Design and restrictions sites introduced in (a) protease indicators, (b) Ca^{2+} indicators, and (c) K^+ indicators

All other genes encoding the FP variants of gScarlet, variants of mScarlet-I, cpVenus, mRuby3 and mClover3 were amplified by PCR and inserted into these initial constructs by restriction digestion followed by ligation of one FP gene at a time (restriction digestion sites shown in **figure 4-16**). These constructed DNA encoding various indicators were then assembled into a pBAD expression vector. All indicator constructs were verified by DNA sequencing.

4.8.3 Protein purification and *in vitro* characterization

The assembled pBAD plasmids were then used to transform *E. coli* strain DH10B by electroporation. The transformed DH10B cells were plated onto agar with LB medium containing 0.4 mg/ml ampicillin and 0.02% w/v L-arabinose and grown overnight at 37 °C. A single colony for each indicator was picked and cultured in 150 mL LB medium containing 0.1 mg/ml ampicillin and 0.02% w/v L-arabinose and incubated in a shaker (225 rpm) at 25 °C for 48 hours.

Bacteria were harvested at 10,000 rpm, 4 °C for 10 min and cell pellet was then resuspended in 25 mL of 1× Tris buffered saline (TBS). Halt™ protease inhibitor cocktail was added to the resuspended pellet and the cells were then lysed using sonication. The lysate was clarified by centrifugation at 10,000 rpm for 30 min. All the indicator proteins had a His tag which allowed for their purification from the supernatant by affinity chromatography using Ni-NTA agarose resin. The eluted protein solution was then buffer exchanged using a PD-10 (GE Healthcare Life Sciences) desalting column.

Extinction coefficient of purified gScarlet protein was determined by alkali denaturation method. The absorption spectrum was measured with and without 1M NaOH. The extinction coefficient was calculated with the assumption that in 1M NaOH solution GFP-type chromophores have an extinction coefficient of 44,000 $M^{-1}cm^{-1}$ at their absorption peaks near 450 nm.

Quantum yield of purified gScarlet protein was determined by using mGreenLantern as a standard. The emission fluorescence spectrum of a dilution series of gScarlet/mGreenLantern (absorbance corresponding to 0.01 to 0.1) was measured. The emission fluorescence was integrated and plotted against the absorbance. The slope from this plot was used to calculate the quantum yield of gScarlet.

The relative amounts of gScarlet and mScarlet-I present in various indicators was calculated from the measured absorbance spectra of the indicators. First, gScarlet and mScarlet-I spectra were deconvoluted from the indicator's absorbance spectra. Then the relative amount of FP was calculated by dividing the peak absorbance by the EC of the FP. The code for the spectral deconvolution and FP stoichiometry calculation was written by Dr. Wu and is available at :
https://github.com/shengyi2/spectrum_analysis/blob/main/Heterodimer_absorbance_curve_deconvolution_colab.ipynb
https://github.com/shengyi2/spectrum_analysis/blob/main/Calculation_of_stoichiometry_calculation.ipynb

4.8.4 Fluorescence response measurement of indicators

The protease indicator proteins (approximately 25 μg) were incubated with WELQut protease (final concentration of 0.1 unit in TBS) at 25 °C for 12 hours. The emission spectrum was measured for both uncut and proteolyzed indicators. The fluorescence spectrum for Ca^{2+} indicator proteins was measured in the presence of 39μM free Ca^{2+} (10mM CaEGTA in 100 mM KCl, 30mM MOPS, pH 7.2) and zero free Ca^{2+} buffer (10 mM EGTA in 100 mM KCl, 30 mM MOPS, pH 7.2). The fluorescence spectrum for K^+ indicator proteins was measured in the presence and absence of 150 mM K^+. For K^+ K_d determination, purified protein was diluted into a series of buffers with K^+ concentration ranging from 0 to 150 mM.

The indicators that have gScarlet or mClover3 were excited at 470 nm and the emission spectra were scanned from 500-750 nm whereas the indicators that had cpVenus were excited at 480 nm and emission spectra were scanned from 510-750 nm.

4.8.5 Statistical analysis

All data are expressed as individual data points or mean ± SD. Sample sizes (*n*) are listed for each experiment. Statistical analyses and graphing were done using GraphPad Prism version 9.2.0. p-values were determined by one-way ANOVA followed by Dunnett's multiple comparisons test or unpaired t-tests as mentioned in figure captions. K_d curves were simulated by GraphPad Prism using a dose-response curve model with variable slope (four parameters) with least squares fit.

4.9 References

(1) Sciences, N. R. C. (US) C. on R. at the I. of the P. and L. Enabling Technologies and Tools for Research. **2010**.

(2) Tamura, T.; Hamachi, I. Recent Progress in Design of Protein-Based Fluorescent Biosensors and Their Cellular Applications. *ACS Chem. Biol.* **2014**, *9* (12), 2708–2717.

(3) Nasu, Y.; Shen, Y.; Kramer, L.; Campbell, R. E. Structure- and Mechanism-Guided Design of Single Fluorescent Protein-Based Biosensors. *Nat. Chem. Biol.* **2021**, *17* (5), 509–518.

(4) Cardullo, R. A. Chapter 19 - Theoretical Principles and Practical Considerations for Fluorescence Resonance Energy Transfer Microscopy. In *Digital Microscopy*; Sluder, G., Wolf, D. E. B. T.-M. in *C. B., Eds.; Academic Press*, **2013**; *114*, 441–456.

(5) Algar, W. R.; Hildebrandt, N.; Vogel, S. S.; Medintz, I. L. FRET as a Biomolecular Research Tool — Understanding Its Potential While Avoiding Pitfalls. *Nat. Methods* **2019**, *16* (9), 815–829.

(6) Cranfill, P. J.; Sell, B. R.; Baird, M. A.; Allen, J. R.; Lavagnino, Z.; De Gruiter, H. M.; Kremers, G. J.; Davidson, M. W.; Ustione, A.; Piston, D. W. Quantitative Assessment of Fluorescent Proteins. *Nat. Methods* **2016**, *13* (7), 557–562.

(7) Campbell, R. E. Fluorescent-Protein-Based Biosensors: Modulation of Energy Transfer as a Design Principle. *Anal. Chem.* **2009**, *81* (15), 5972–5979.

(8) Kremers, G. J.; Goedhart, J.; Van Den Heuvel, D. J.; Gerritsen, H. C.; Gadella, T. W. J. Improved Green and Blue Fluorescent Proteins for Expression in Bacteria and Mammalian Cells. *Biochemistry* **2007**, *46* (12), 3775–3783.

(9) Heim, R.; Tsien, R. Y. Engineering Green Fluorescent Protein for Improved Brightness, Longer Wavelengths and Fluorescence Resonance Energy Transfer. *Curr. Biol.* **1996**, *6* (2), 178–182.

(10) Bajar, B. T.; Wang, E. S.; Zhang, S.; Lin, M. Z.; Chu, J. A Guide to Fluorescent Protein FRET Pairs. *Sensors (Basel)*. **2016**, *16* (9).

(11) Carlson, H. J.; Campbell, R. E. Genetically Encoded FRET-Based Biosensors for Multiparameter Fluorescence Imaging. *Curr. Opin. Biotechnol.* **2009**, *20* (1), 19–27.

(12) Miyawaki, A.; Llopis, J.; Heim, R.; Michael McCaffery, J.; Adams, J. A.; Ikura, M.; Tsien, R. Y. Fluorescent Indicators for Ca2+based on Green Fluorescent Proteins and Calmodulin. *Nat.* **1997**, *388* (6645), 882–887.

(13) Goedhart, J.; Von Stetten, D.; Noirclerc-Savoye, M.; Lelimousin, M.; Joosen, L.; Hink, M. A.; Van Weeren, L.; Gadella, T. W. J.; Royant, A. Structure-Guided Evolution of Cyan Fluorescent Proteins towards a Quantum Yield of 93%. *Nat. Commun.* **2012**, *3* (1), 1–9.

(14) Lam, A. J.; St-Pierre, F.; Gong, Y.; Marshall, J. D.; Cranfill, P. J.; Baird, M. A.; McKeown, M. R.; Wiedenmann, J.; Davidson, M. W.; Schnitzer, M. J.; Tsien, R. Y.; Lin, M. Z. Improving FRET Dynamic Range with Bright Green and Red Fluorescent Proteins. *Nat. Methods* **2012**, *9* (10), 1005.

(15) Karasawa, S.; Araki, T.; Nagai, T.; Mizuno, H.; Miyawaki, A. Cyan-Emitting and Orange-Emitting Fluorescent Proteins as a Donor/Acceptor Pair for Fluorescence Resonance Energy Transfer. *Biochem. J.*

2004, *381* (1), 307.

(16) Tsutsui, H.; Karasawa, S.; Okamura, Y.; Miyawaki, A. Improving Membrane Voltage Measurements Using FRET with New Fluorescent Proteins. *Nat. Methods* **2008**, *5* (8), 683–685.

(17) Kwok, S.; Lee, C.; Sánchez, S. A.; Hazlett, T. L.; Gratton, E.; Hayashi, Y. Genetically Encoded Probe for Fluorescence Lifetime Imaging of CaMKII Activity. *Biochem. Biophys. Res. Commun.* **2008**, *369* (2), 519.

(18) Yang, X.; Xu, P.; Xu, T. A New Pair for Inter- and Intra-Molecular FRET Measurement. *Biochem. Biophys. Res. Commun.* **2005**, *330* (3), 914–920.

(19) Liu, R.; Ren, D.; Liu, Y.; Deng, Y.; Sun, B.; Zhang, Q.; Guo, X. Biosensors of DsRed as FRET Partner with CFP or GFP for Quantitatively Imaging Induced Activation of Rac, Cdc42 in Living Cells. *Mol. imaging Biol.* **2011**, *13* (3), 424–431.

(20) Yasuda, R.; Harvey, C. D.; Zhong, H.; Sobczyk, A.; Van Aelst, L.; Svoboda, K. Supersensitive Ras Activation in Dendrites and Spines Revealed by Two-Photon Fluorescence Lifetime Imaging. *Nat. Neurosci.* **2006**, *9* (2), 283–291.

(21) Goedhart, J.; Vermeer, J. E. M.; Adjobo-Hermans, M. J. W.; van Weeren, L.; Gadella, T. W. J. Sensitive Detection of P65 Homodimers Using Red-Shifted and Fluorescent Protein-Based FRET Couples. *PLoS One* **2007**, *2* (10), e1011.

(22) Shcherbo, D.; Souslova, E. A.; Goedhart, J.; Chepurnykh, T. V.; Gaintzeva, A.; Shemiakina, I. I.; Gadella, T. W. J.; Lukyanov, S.; Chudakov, D. M. Practical and Reliable FRET/FLIM Pair of Fluorescent Proteins. *BMC Biotechnol.* **2009**, *9* (1), 1–6.

(23) Bajar, B. T.; Wang, E. S.; Lam, A. J.; Kim, B. B.; Jacobs, C. L.; Howe, E. S.; Davidson, M. W.; Lin, M. Z.; Chu, J. Improving Brightness and Photostability of Green and Red Fluorescent Proteins for Live Cell Imaging and FRET Reporting. *Sci. Reports* **2016**, *6* (1), 1–12.

(24) Mastop, M.; Bindels, D. S.; Shaner, N. C.; Postma, M.; Gadella, T. W. J.; Goedhart, J. Characterization of a Spectrally Diverse Set of Fluorescent Proteins as FRET Acceptors for MTurquoise2. *Sci. Reports* **2017**, *7* (1), 1–18.

(25) Abraham, B. G.; Sarkisyan, K. S.; Mishin, A. S.; Santala, V.; Tkachenko, N. V.; Karp, M. Fluorescent Protein Based FRET Pairs with Improved Dynamic Range for Fluorescence Lifetime Measurements. *PLoS One* **2015**, *10* (8), e0134436.

(26) Zhang, D.; Redington, E.; Gong, Y. Rational Engineering of Ratiometric Calcium Sensors with Bright Green and Red Fluorescent Proteins. *Commun. Biol.* **2021**, *4* (1), 1–12.

(27) Piljic, A.; Schultz, C. Simultaneous Recording of Multiple Cellular Events by FRET. *ACS Chem. Biol.* **2008**, *3* (3), 156–160.

(28) Ouyang, M.; Huang, H.; Shaner, N. C.; Remacle, A. G.; Shiryaev, S. A.; Strongin, A. Y.; Tsien, R. Y.; Wang, Y. Simultaneous Visualization of Protumorigenic Src and MT1-MMP Activities with Fluorescence Resonance Energy Transfer. *Cancer Res.* **2010**, *70* (6), 2204–2212.

(29) Lindenburg, L. H.; Hessels, A. M.; Ebberink, E. H. T. M.; Arts, R.; Merkx, M. Robust Red FRET Sensors Using Self-Associating Fluorescent Domains. *ACS Chem. Biol.* **2013**, *8* (10), 2133–2139.

(30) VanEngelenburg, S. B.; Palmer, A. E. Fluorescent Biosensors of Protein Function. *Curr. Opin. Chem. Biol.* **2008**, *12* (1), 60–65.

(31) Nguyen, A. W.; Daugherty, P. S. Evolutionary Optimization of Fluorescent Proteins for Intracellular FRET. *Nat. Biotechnol.* **2005**, *23* (3), 355–360.

(32) Zacharias, D. A.; Violin, J. D.; Newton, A. C.; Tsien, R. Y. Partitioning of Lipid-Modified Monomeric GFPs into Membrane Microdomains of Live Cells. *Science (80-.).* **2002**, *296* (5569), 913–916.

(33) Vinkenborg, J. L.; Evers, T. H.; Reulen, S. W. A.; Meijer, E. W.; Merkx, M. Enhanced Sensitivity of FRET-Based Protease Sensors by Redesign of the GFP Dimerization Interface. *ChemBioChem* **2007**, *8* (10), 1119–1121.

(34) Ohashi, T.; Galiacy, S. D.; Briscoe, G.; Erickson, H. P. An Experimental Study of GFP-Based FRET, with Application to Intrinsically Unstructured Proteins. *Protein Sci.* **2007**, *16* (7), 1429.

(35) Campbell, R. E.; Tour, O.; Palmer, A. E.; Steinbach, P. A.; Baird, G. S.; Zacharias, D. A.; Tsien, R. Y. A Monomeric Red Fluorescent Protein. *Proc. Natl. Acad. Sci. U. S. A.* **2002**, *99* (12), 7877–7882.

(36) Grünberg Raik; Burnier, J. V.; Ferrar, T.; Beltran-Sastre, V.; Stricher, F.; Van Der Sloot, A. M.; Garcia-Olivas, R.; Mallabiabarrena, A.; Sanjuan, X.; Zimmermann, T.; Serrano, L. Engineering of Weak Helper Interactions for High-Efficiency FRET Probes. *Nat. Methods* **2013**, *10* (10), 1021–1027.

(37) Bindels, D. S.; Haarbosch, L.; Van Weeren, L.; Postma, M.; Wiese, K. E.; Mastop, M.; Aumonier, S.; Gotthard, G.; Royant, A.; Hink, M. A.; Gadella, T. W. J. MScarlet: A Bright Monomeric Red Fluorescent Protein for Cellular Imaging. *Nat. Methods* **2016**, *14* (1), 53–56.

(38) McCullock, T. W.; MacLean, D. M.; Kammermeier, P. J. Comparing the Performance of MScarlet-I, MRuby3, and MCherry as FRET Acceptors for MNeonGreen. *PLoS One* **2020**, *15* (2).

(39) Kotera, I.; Iwasaki, T.; Imamura, H.; Noji, H.; Nagai, T. Reversible Dimerization of Aequorea Victoria Fluorescent Proteins Increases the Dynamic Range of FRET-Based Indicators. *ACS Chem. Biol.* **2010**, *5* (2), 215–222.

(40) Subach, F. V.; Verkhusha, V. V. Chromophore Transformations in Red Fluorescent Proteins. *Chem. Rev.* **2012**, *112* (7), 4308.

(41) Strack, R. L.; Strongin, D. E.; Mets, L.; Glick, B. S.; Keenan, R. J. Chromophore Formation in DsRed Occurs by a Branched Pathway. *J. Am. Chem. Soc.* **2010**, *132* (24), 8496–8505.

(42) Subach, O. M.; Gundorov, I. S.; Yoshimura, M.; Subach, F. V.; Zhang, J.; Grüenwald, D.; Souslova, E. A.; Chudakov, D. M.; Verkhusha, V. V. Conversion of Red Fluorescent Protein into a Bright Blue Probe. *Chem. Biol.* **2008**, *15* (10), 1116.

(43) Terskikh, A. V.; Fradkov, A. F.; Zaraisky, A. G.; Kajava, A. V.; Angres, B. Analysis of DsRed Mutants: SPACE AROUND THE FLUOROPHORE ACCELERATES FLUORESCENCE DEVELOPMENT *. *J. Biol. Chem.* **2002**, *277* (10), 7633–7636.

(44) Alford, S. C.; Ding, Y.; Simmen, T.; Campbell, R. E. Dimerization-Dependent Green and Yellow Fluorescent Proteins. *ACS Synth. Biol.* **2012**, *1* (12), 569.

(45) Shaner, N. C.; Patterson, G. H.; Davidson, M. W. Advances in Fluorescent Protein Technology. *J. Cell Sci.*

2007, *120* (24), 4247–4260.

(46) Jumper, J.; Evans, R.; Pritzel, A.; Green, T.; Figurnov, M.; Ronneberger, O.; Tunyasuvunakool, K.; Bates, R.; Žídek, A.; Potapenko, A.; Bridgland, A.; Meyer, C.; Kohl, S. A. A.; Ballard, A. J.; Cowie, A.; Romera-Paredes, B.; Nikolov, S.; Jain, R.; Adler, J.; Back, T.; Petersen, S.; Reiman, D.; Clancy, E.; Zielinski, M.; Steinegger, M.; Pacholska, M.; Berghammer, T.; Bodenstein, S.; Silver, D.; Vinyals, O.; Senior, A. W.; Kavukcuoglu, K.; Kohli, P.; Hassabis, D. Highly Accurate Protein Structure Prediction with AlphaFold. *Nat.* **2021**, *596* (7873), 583–589.

(47) Berridge, M. J.; Bootman, M. D.; Roderick, H. L. Calcium Signalling: Dynamics, Homeostasis and Remodelling. *Nat. Rev. Mol. Cell Biol.*, **2003**, *4* (7), 517–529.

(48) Honarnejad, K.; Kirsch, A. K.; Daschner, A.; Szybinska, A.; Kuznicki, J.; Herms, J. FRET-Based Calcium Imaging: A Tool for High-Throughput/Content Phenotypic Drug Screening in Alzheimer Disease. *J. Biomol. Screen.* **2013**, *18* (10), 1309–1320.

(49) Greenwald, E. C.; Mehta, S.; Zhang, J. Genetically Encoded Fluorescent Biosensors Illuminate the Spatiotemporal Regulation of Signaling Networks. *Chem. Rev.* **2018**, *118* (24), 11707–11794.

(50) Bischof, H.; Rehberg, M.; Stryeck, S.; Artinger, K.; Eroglu, E.; Waldeck-Weiermair, M.; Gottschalk, B.; Rost, R.; Deak, A. T.; Niedrist, T.; Vujic, N.; Lindermuth, H.; Prassl, R.; Pelzmann, B.; Groschner, K.; Kratky, D.; Eller, K.; Rosenkranz, A. R.; Madl, T.; Plesnila, N.; Graier, W. F.; Malli, R. Novel Genetically Encoded Fluorescent Probes Enable Real-Time Detection of Potassium in Vitro and in Vivo. *Nat. Commun.* **2017**, *8* (1).

(51) Shen, Y.; Wu, S. Y.; Rancic, V.; Aggarwal, A.; Qian, Y.; Miyashita, S. I.; Ballanyi, K.; Campbell, R. E.; Dong, M. Genetically Encoded Fluorescent Indicators for Imaging Intracellular Potassium Ion Concentration. *Commun. Biol.* **2019**, *2* (1).

Chapter 5: Summary and future perspectives

This thesis describes two different research projects - the first is the assessment of neurotrophic activity of banglenes (chapter 1-3) and second is the development of a new green and red fluorescent protein (FP) based FRET pair (chapter 4).

5.1 Assessment of neurotrophic activity of banglenes

Neurotrophin signaling is central to neuronal survival and function and is naturally antithetical to neurodegenerative progression. The neuroprotective and neuro-regenerative ability of neurotrophins is highly desirable as this can allow for a pathway to restore damaged neuronal tissue. Despite their favourable biological effects, the translation of neurotrophin proteins into a clinical setting has been challenging. This has been attributed to their suboptimal pharmacological properties such as poor oral bioavailability, short serum half-lives, limited penetration of the blood brain barrier, poor receptor selectivity and their pleiotropic pro-survival and pro-death activities. [1–4]

Small molecules which are functionally analogous to neurotrophins can help overcome the pharmacological drawbacks of neurotrophins. A number of structurally diverse neurotrophic small molecules have been discovered, yet except for some notable examples, the elucidation of their detailed mechanism of action has happened at a pace that is frustratingly slower than the discovery of these molecules.[5] Elucidation of the mechanism of actions and the cellular binding partners of these neurotrophic molecule would help discover targets for which therapeutics could then be developed through a more rational approach.

Banglenes extracted from Javanese ginger are neurotrophic molecules which have demonstrated neurotrophic activity *in vitro* and *in vivo*. To understand the activity of its different stereoisomers and its mechanism of action, I synthesised different stereoisomers of banglenes and its derivatives (chapter 2). These molecules were then subjected to a phenotypic assay with PC-12 cells to assess their neuritogenic ability. In Chapter 3, I elucidated the important structural features of banglenes, established (–) *trans*-banglene (*t*-BG) as the active stereoisomer, and obtained further insight on its mode of action.

(–) *t*-BG caused modest neuritogenesis on its own and substantially potentiated NGF neuritogenesis in PC-12 cells. The structure-activity relationship studies revealed the degree of potentiating activity for banglene derivatives was not proportional to neurotrophic activity in the absence of NGF. This lack of correlation provides evidence of dual function and further, may be the result of a dual mechanism of (–) *t*-BG.

The inherent complexity of studying the modulation of neurotrophic signalling pathways is reflected in my studies aimed at uncovering the mechanism of action of (–) *t*-BG. One such complexity I faced was to assess whether expressed pro-NGF or NGF is detected upon combined treatment of PC-12 cells with (–) *t*-BG and NGF and if they are responsible for the increase observed in NGF-induced neuritogenesis. The fact that inhibiting key kinases involved in TrkA mediated signalling pathways did not affect the NGF potentiating ability of (–) *t*-BG hints that mechanism may not be as simple as activation of TrkA. It is possible that (–) *t*-BG functions independently by binding to p75 NTR and further affects neuritogenesis by modulating RhoA activation. One way of assessing the involvement of p75 NTR would be to use the specific p75 NTR inhibitor LM11A-31 (**figure 5-1a**).[6] Soligo and co-workers have demonstrated that treatment of PC-12 cells with LM11A-31 increases cell viability and decreases NGF induced neuritogenesis.[7] If (–) *t*-BG acts by binding to p75 NTR, LM11A-31 and (–) *t*-BG will compete for binding and the maximum neuritogenesis and cell viability should be nearly the same as that caused by using LM11A-31 and (–) *t*-BG individually in the presence of NGF.

Although the PC-12 cell line is a relatively easy-to-use model to study neurotrophic activity, it may not provide a full picture of the banglenes mechanism of action. In the future it will be important to carry out studies to understand its mechanism of action in a complementary cell line such as SH-SY5Y or in primary cultured neurons. This would help to understand if (–) *t*-BG interacts with other Trk receptors and if it can potentiate the activity of other neurotrophins.

While the exact details of the mechanism of (–) *t*-BG remain unclear, this work has established derivative (±) **36** as an important starting point for developing a mechanistic probe which can be used to enrich a cellular binding partner (**figure 5-1b-d**). The molecule

could be attached covalently to a solid support, and then be used in a standard pull down protocol with PC-12 or any other cell lysate. Any enriched protein can then be identified by tryptic digestion followed by mass spectrometric analysis.

Alternatively, a photolabile cross-linker such as a diazirine with an alkyne tag could be conjugated to (±) **36 (Figure 5-1-d).** When irradiated, the diazirine would generate a carbene intermediate which could then covalently link the probe molecule to nearby cellular moieties which would likely include a cellular binding partner. The cellular partner bound to the probe could then be enriched by performing a click reaction with an azide functionalized biotin followed by a pull down with Streptavidin. Both strategies would require another similarly modified inactive banglene derivative which would serve as a control to reduce enriched false-positive targets.

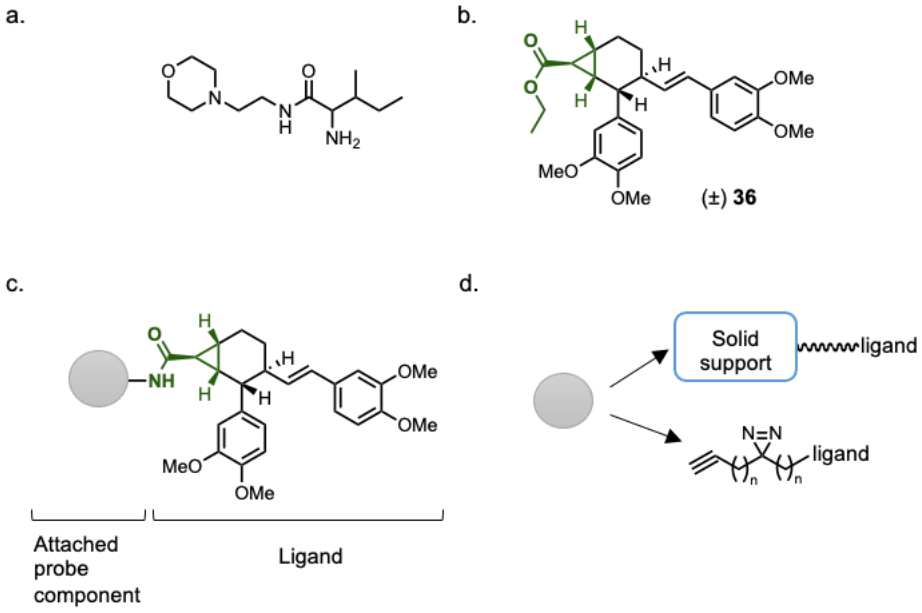

Figure 5-1. Further tools to understand the mechanism of action of banglenes (a) Structure of p75 NTR inhibitor LM11A-31. (b) Banglene derivative best suited for probe development. (c) and (d) Representation of probe components, banglene derivative **(±) 36** would serve as the ligand and can be attached to a solid support through a linker or can be attached to a photo-labile crosslinker.

The current understanding of neurotrophins, their receptors, their downstream signalling pathways, and their effects on normal and pathological brain, is rapidly evolving and with this our understanding of key drivers of neurotrophic effects is also increasing. Annotating the mechanism of action for neurotrophic molecules like (–) *t*-BG will allow for their use as tools to further neurotrophic signaling investigations. I believe that (–) *t*-BG is best suited to function as a probe and not as a therapeutic. Although clinical safety studies have been performed by the Fukuyama group for extracts containing banglenes, (–) *t*-BG still needs to be optimized for better potency and physiochemical properties.

5.2 Green and red fluorescent protein (FP) based FRET pair

The second part of this thesis (chapter 4) describes the development of a new green-red FRET pair with mScarlet-I as the FRET acceptor and gScarlet (a blue-shifted version of mScarlet-I) as the FRET donor. The FP pair was then used to develop FRET-based indicators to detect protease activity, Ca^{2+}, and K^{+}. I attempted to improve the dynamic range of these mScarlet-I–gScarlet indicators by rationally introducing mutations that could potentially allow for weak hetero-dimerization of mScarlet-I and gScarlet to occur. This strategy proved useful in improving the response of the protease indicator, but it did not improve the response of the Ca^{2+} and K^{+} indicators. This suggests that it might not be possible to identify a set of interactions that increases FRET efficiency universally across different indicators employing gScarlet and mScarlet-I, and that each indicator needs to be optimized individually based on their own unique binding domains. Finally, I demonstrate that this pair can serve as a good alternative to the existing cyan-yellow FRET pair for construction of ratiometric biosensors.

Although the mutations I made did not result in the anticipated improvements in Ca^{2+} and K^{+} indicators, there is still a scope to utilize this strategy to fine tune the response. For example, different amino acid substitutions can be screened at a particular position. One of the changes I made was E154R, but it is possible that substitution with a different amino acid such as aspartic acid, histidine or even leucine would give a different result. The changes that I made were symmetric on both FPs in an indicator, and so unsymmetric changes on both FPs can also be explored.

Another way of improving the response of these indicators independent of the dimerization strategy would be to develop a bright circularly permuted version of gScarlet to function as the FRET donor. This strategy was demonstrated to be effective in the latest Twitch-GR series of Ca^{2+} indicators. There also remains the possibility to optimize the linkers joining the FPs to the recognition domains for increasing the response of these indicators.

FRET based indicators are versatile and powerful tools to analyze biological processes and interactions. Each existing FRET based indicator has its own unique advantages and disadvantages. Developing new FRET based indicators expands the existing choices and allows researchers to select the tool best suited for use in their system. gScarlet–mScarlet-I based indicators are a useful addition to this growing toolbox and the performance of these indicators should be assessed for various cellular applications.

References

(1) Rodrigues, T. M.; Jerónimo-Santos, A.; Outeiro, T. F.; Sebastião, A. M.; Diógenes, M. J. Challenges and Promises in the Development of Neurotrophic Factor-Based Therapies for Parkinson's Disease. *Drugs and Aging* **2014**, *31* (4), 239–261.

(2) Saragovi, H. U.; Galan, A.; Levin, L. A. Neuroprotection: Pro-Survival and Anti-Neurotoxic Mechanisms as Therapeutic Strategies in Neurodegeneration. *Front. Cell. Neurosci.* **2019**, *13*, 231.

(3) Houlton, J.; Abumaria, N.; Hinkley, S. F. R.; Clarkson, A. N. Therapeutic Potential of Neurotrophins for Repair after Brain Injury: A Helping Hand from Biomaterials. *Front. Genet.* **2019**, *10* (JUL), 790.

(4) Weissmiller, A. M.; Wu, C. Current Advances in Using Neurotrophic Factors to Treat Neurodegenerative Disorders. *Transl. Neurodegener.* **2012**, *1*, 14.

(5) Xu, J.; Lacoske, M. H.; Theodorakis, E. A. Neurotrophic Natural Products: Chemistry and Biology. *Angew. Chem. Int. Ed. Engl.* **2014**, *53* (4), 956.

(6) Simmons, D. A.; Knowles, J. K.; Belichenko, N. P.; Banerjee, G.; Finkle, C.; Massa, S. M.; Longo, F. M. A Small Molecule P75NTR Ligand, LM11A-31, Reverses Cholinergic Neurite Dystrophy in Alzheimer's Disease Mouse Models with Mid- to Late-Stage Disease Progression. *PLoS One* **2014**, *9* (8).

(7) Soligo, M.; Albini, M.; Bertoli, F. L.; Marzano, V.; Protto, V.; Bracci-Laudiero, L.; Minnone, G.; De Benedetti, F.; Chiaretti, A.; Mantuano, E.; Manni, L. Different Responses of PC12 cells to Different Pro-Nerve Growth Factor Protein Variants. *Neurochem. Int.* **2019**, *129*, 104498.

Bibliography

(1) Abraham, B. G.; Sarkisyan, K. S.; Mishin, A. S.; Santala, V.; Tkachenko, N. V.; Karp, M. Fluorescent Protein Based FRET Pairs with Improved Dynamic Range for Fluorescence Lifetime Measurements. *PLoS One* **2015**, *10* (8), e0134436.

(2) Al-Qudah, M. A.; Al-Dwairi, A. Mechanisms and Regulation of Neurotrophin Synthesis and Secretion. *Neurosci. J.* **2016**, *21* (4), 306–313.

(3) Alford, S. C.; Ding, Y.; Simmen, T.; Campbell, R. E. Dimerization-Dependent Green and Yellow Fluorescent Proteins. *ACS Synth. Biol.* **2012**, *1* (12), 569.

(4) Algar, W. R.; Hildebrandt, N.; Vogel, S. S.; Medintz, I. L. FRET as a Biomolecular Research Tool — Understanding Its Potential While Avoiding Pitfalls. *Nat. Methods* **2019**, *16* (9), 815–829.

(5) Amatayakul, T.; C, J. R.; Dechatiwongse, T.; F Giles, R. G.; Ku, K.; ast ton, C. L.; WhiteB, A. H. Chemistry and Crystal Structures of Some Constituents of Zingiber Cassumunar*. *Aust. J. Chem* **1979**, *32*, 71–88.

(6) Amatayakul, T.; Cannon, J. R.; Dampawan, P.; Dechatiwongse, T.; Giles, R. G. F.; Huntrakul, C.; Kusamran, K.; Mokkhasamit, M.; Raston, C. L.; Reutrakul, V.; White, A. H. Syntheses of Some Constituents of Zingiber Cassumunar. *Aust. J. Chem* **1980**, *33*, 2756.

(7) Arevalo, J. C.; Conde, B.; Hempstead, B. L.; Chao, M. V.; Martin-Zanca, D.; Perez, P. TrkA Immunoglobulin-Like Ligand Binding Domains Inhibit Spontaneous Activation of the Receptor. *Mol. Cell. Biol.* **2000**, *20* (16), 5908–5916.

(8) Azari, H.; Reynolds, B. A. In Vitro Models for Neurogenesis. *Cold Spring Harb. Perspect. Biol.* **2016**, *8* (6).

(9) Bajar, B. T.; Wang, E. S.; Lam, A. J.; Kim, B. B.; Jacobs, C. L.; Howe, E. S.; Davidson, M. W.; Lin, M. Z.; Chu, J. Improving Brightness and Photostability of Green and Red Fluorescent Proteins for Live Cell Imaging and FRET Reporting. *Sci. Reports* **2016**, *6* (1), 1–12.

(10) Bajar, B. T.; Wang, E. S.; Zhang, S.; Lin, M. Z.; Chu, J. A Guide to Fluorescent Protein FRET Pairs. *Sensors (Basel).* **2016**, *16* (9).

(11) Balon, K.; Wiatrak, B. PC12 and THP-1 Cell Lines as Neuronal and Microglia Model in Neurobiological Research. *Appl. Sci.,* **2021**, *11* (9), 3729.

(12) Bannister, A. J.; Kouzarides, T. Regulation of Chromatin by Histone Modifications. *Cell Res.* **2011**, *21* (3), 381–395.

(13) Barbosa, D. J.; Capela, J. P.; De Lourdes Bastos, M.; Carvalho, F. In Vitro Models for Neurotoxicology Research. *Toxicol. Res. (Camb).* **2015**, *4* (4), 801–842.

(14) Bennison, S. A.; Blazejewski, S. M.; Smith, T. H.; Toyo-oka, K. Protein Kinases: Master Regulators of Neuritogenesis and Therapeutic Targets for Axon Regeneration. *Cell. Mol. Life Sci.* **2020**, *77* (8), 1511–1530.

(15) Berndt, N.; Yang, H.; Trinczek, B.; Betzi, S.; Zhang, Z.; Wu, B.; Lawrence, N. J.; Pellecchia, M.;

Schönbrunn, E.; Cheng, J. Q.; Sebti, S. M. The Akt Activation Inhibitor TCN-P Inhibits Akt Phosphorylation by Binding to the PH Domain of Akt and Blocking Its Recruitment to the Plasma Membrane. *Cell Death Differ.* **2010**, *17* (11), 1795–1804.

(16) Berridge, M. J.; Bootman, M. D.; Roderick, H. L. Calcium Signalling: Dynamics, Homeostasis and Remodelling. *Nat. Rev. Mol. Cell Biol.* **2003**, *4* (7), 517–529.

(17) Bindels, D. S.; Haarbosch, L.; Van Weeren, L.; Postma, M.; Wiese, K. E.; Mastop, M.; Aumonier, S.; Gotthard, G.; Royant, A.; Hink, M. A.; Gadella, T. W. J. MScarlet: A Bright Monomeric Red Fluorescent Protein for Cellular Imaging. *Nat. Methods* **2016**, *14* (1), 53–56.

(18) Bischof, H.; Rehberg, M.; Stryeck, S.; Artinger, K.; Eroglu, E.; Waldeck-Weiermair, M.; Gottschalk, B.; Rost, R.; Deak, A. T.; Niedrist, T.; Vujic, N.; Lindermuth, H.; Prassl, R.; Pelzmann, B.; Groschner, K.; Kratky, D.; Eller, K.; Rosenkranz, A. R.; Madl, T.; Plesnila, N.; Graier, W. F.; Malli, R. Novel Genetically Encoded Fluorescent Probes Enable Real-Time Detection of Potassium in Vitro and in Vivo. *Nat. Commun.* **2017**, *8* (1).

(19) Bothwell, M. NGF, BDNF, NT3, and NT4. *Handb. Exp. Pharmacol.* **2014**, *220*, 3–15.

(20) Boutilier, J.; Ceni, C.; Pagdala, P. C.; Forgie, A.; Neet, K. E.; Barker, P. A. Proneurotrophins Require Endocytosis and Intracellular Proteolysis to Induce TrkA Activation. *J. Biol. Chem.* **2008**, *283* (19), 12709–12716.

(21) Burch, P.; Binaghi, M.; Scherer, M.; Wentzel, C.; Bossert, D.; Eberhardt, L.; Neuburger, M.; Scheiffele, P.; Gademann, K. Total Synthesis of Gelsemiol. *Chem. – A Eur. J.* **2013**, *19* (8), 2589–2591.

(22) Cai, J.; Hua, F.; Yuan, L.; Tang, W.; Lu, J.; Yu, S.; Wang, X.; Hu, Y. Potential Therapeutic Effects of Neurotrophins for Acute and Chronic Neurological Diseases. *Biomed Res. Int.* **2014**, *2014*.

(23) Campbell, R. E. Fluorescent-Protein-Based Biosensors: Modulation of Energy Transfer as a Design Principle. *Anal. Chem.* **2009**, *81* (15), 5972–5979.

(24) Campbell, R. E.; Tour, O.; Palmer, A. E.; Steinbach, P. A.; Baird, G. S.; Zacharias, D. A.; Tsien, R. Y. A Monomeric Red Fluorescent Protein. *Proc. Natl. Acad. Sci. U. S. A.* **2002**, *99* (12), 7877–7882.

(25) Cao, C. Y.; Zhang, C. C.; Shi, X. W.; Li, D.; Cao, W.; Yin, X.; Gao, J. M. Sarcodonin G Derivatives Exhibit Distinctive Effects on Neurite Outgrowth by Modulating NGF Signaling in PC12 Cells. *ACS Chem. Neurosci.* **2018**, *9* (7), 1607–1615.

(26) Cardullo, R. A. Chapter 19 - Theoretical Principles and Practical Considerations for Fluorescence Resonance Energy Transfer Microscopy. In *Digital Microscopy*; Sluder, G., Wolf, D. E. B. T.-M. in *C. B., Eds.; Academic Press,* **2013**; *114*, 441–456.

(27) Carlson, H. J.; Campbell, R. E. Genetically Encoded FRET-Based Biosensors for Multiparameter Fluorescence Imaging. *Curr. Opin. Biotechnol.* **2009**, *20* (1), 19–27.

(28) Ceni, C.; Kommaddi, R. P.; Thomas, R.; Vereker, E.; Liu, X.; McPherson, P. S.; Ritter, B.; Barker, P. A. The P75NTR Intracellular Domain Generated by Neurotrophin-Induced Receptor Cleavage Potentiates Trk Signaling. *J. Cell Sci.* **2010**, *123* (13), 2299–2307.

(29) Chan, G. K. L.; Hu, W. W. H.; Zheng, Z. X.; Huang, M.; Lin, Y. X. Y.; Wang, C. Y.; Gong, A. G. W.;

Yang, X. Y.; Tsim, K. W. K.; Dong, T. T. X. Quercetin Potentiates the NGF-Induced Effects in Cultured PC 12 Cells: Identification by HerboChips Showing a Binding with NGF. *Evid. Based. Complement. Alternat. Med.* **2018**.

(30) Cho, J. Y.; Katz, D. R.; Skubitz, K. M.; Chain, B. M. Conventional Protein Kinase C Plays a Critical Role in Negative Regulation of CD98-Induced Homotypic Aggregation. *Tissue Antigens* **2010**, *75* (1), 19–29.

(31) Cho, Y. S.; Carcache, D. A.; Tian, Y.; Li, Y. M.; Danishefsky, S. J. Total Synthesis of (±)-Jiadifenin, a Non-Peptidyl Neurotrophic Modulator. *J. Am. Chem. Soc.* **2004**, *126* (44), 14358–14359.

(32) Chu, J.; Suh, D. H.; Lee, G.; Han, A. R.; Chae, S. W.; Lee, H. J.; Seo, E. K.; Lim, H. J. Synthesis and Biological Activity of Optically Active Phenylbutenoid Dimers. *J. Nat. Prod.* **2011**, *74* (8), 1817–1821.

(33) Clement, C. M.; Dandepally, S. R.; Williams, A. L.; Ibeanu, G. C. A Synthetic Analog of Verbenachalcone Potentiates NGF-Induced Neurite Outgrowth and Enhances Cell Survival in Neuronal Cell Models. *Neurosci. Lett.* **2009**, *459* (3), 157–161.

(34) Cranfill, P. J.; Sell, B. R.; Baird, M. A.; Allen, J. R.; Lavagnino, Z.; De Gruiter, H. M.; Kremers, G. J.; Davidson, M. W.; Ustione, A.; Piston, D. W. Quantitative Assessment of Fluorescent Proteins. *Nat. Methods* **2016**, *13* (7), 557–562.

(35) Das, K. P.; Freudenrich, T. M.; Mundy, W. R. Assessment of PC12 Cell Differentiation and Neurite Growth: A Comparison of Morphological and Neurochemical Measures. *Neurotoxicol. Teratol.* **2004**, *26* (3), 397–406.

(36) Davenport, E.; Fernandez, E. Transition-Metal-Free Synthesis of Vicinal Triborated Compounds and Selective Functionalisation of the Internal C–B Bond. *Chem. Commun.* **2018**, *54* (72), 10104–10107.

(37) Deinhardt, K.; Chao, M. V. Trk Receptors. *Handb. Exp. Pharmacol.* **2014**, *220*, 103–119.

(38) Diaz-Muñoz, G.; Isidorio, R. G.; Miranda, I. L.; de Souza Dias, G. N.; Diaz, M. A. N. A Concise and Efficient Synthesis of Tetrahydroquinoline Alkaloids Using the Phase Transfer Mediated Wittig Olefination Reaction. *Tetrahedron Lett.* **2017**, *58* (33), 3311–3315.

(39) Díaz, E.; Reyes, E.; Uria, U.; Carrillo, L.; Tejero, T.; Merino, P.; Vicario, J. L. Carboxylates as Nucleophiles in the Enantioselective Ring-Opening of Formylcyclopropanes under Iminium Ion Catalysis. *Chem. – A Eur. J.* **2018**, *24* (35), 8764–8768.

(40) Duque, A.; Arellano, J. I.; Rakic, P. An Assessment of the Existence of Adult Neurogenesis in Humans and Value of Its Rodent Models for Neuropsychiatric Diseases. *Mol. Psychiatry.* **2021**, 1–6.

(41) Fahnestock, M.; Shekari, A. ProNGF and Neurodegeneration in Alzheimer's Disease. *Front. Neurosci.* **2019**, *13* (FEB), 129.

(42) Fillion, E.; Dumas, A. M.; Hogg, S. A. Modular Synthesis of Tetrahydrofluorenones from 5-Alkylidene Meldrum's Acids. *J. Org. Chem.* **2006**, *71* (26), 9899–9902.

(43) Franco, M. L.; Nadezhdin, K. D.; Goncharuk, S. A.; Mineev, K. S.; Arseniev, A. S.; Vilar, M. Structural Basis of the Transmembrane Domain Dimerization and Rotation in the Activation Mechanism of the TRKA Receptor by Nerve Growth Factor. *J. Biol. Chem.* **2020**, *295* (1), 275–286.

(44) Franco, M. L.; Nadezhdin, K. D.; Light, T. P.; Goncharuk, S. A.; Soler-Lopez, A.; Ahmed, F.; Mineev, K.

S.; Hristova, K.; Arseniev, A. S.; Vilar, M. Interaction between the Transmembrane Domains of Neurotrophin Receptors P75 and TrkA Mediates Their Reciprocal Activation. *J. Biol. Chem.* **2021**, *297* (2), 100926.

(45) Fuchs, M.; Schober, M.; Pfeffer, J.; Kroutil, W.; Birner-Gruenberger, R.; Faber, K. Homoallylic Alcohols via a Chemo-Enzymatic One-Pot Oxidation–Allylation Cascade. *Adv. Synth. Catal.* **2011**, *353* (13), 2354–2358.

(46) Fukuyama, Y.; Otoshi, Y.; Miyoshi, K.; Nakamura, K.; Kodama, M.; Nagasawa, M.; Hasegawa, T.; Okazaki, H.; Sugawara, M. Neurotrophic Sesquiterpene-Neolignans from Magnolia Obovata: Structure and Neurotrophic Activity. *Tetrahedron* **1992**, *48* (3), 377–392.

(47) Gao, L.; Zhang, Y.; Sterling, K.; Song, W. Brain-Derived Neurotrophic Factor in Alzheimer's Disease and Its Pharmaceutical Potential. *Transl. Neurodegener.* **2022**, *11* (1), 1–34.

(48) Gaub, P.; Tedeschi, A.; Puttagunta, R.; Nguyen, T.; Schmandke, A.; Di Giovanni, S. HDAC Inhibition Promotes Neuronal Outgrowth and Counteracts Growth Cone Collapse through CBP/P300 and P/CAF-Dependent P53 Acetylation. *Cell Death Differ.* **2010**, *17* (9), 1392–1408.

(49) Goedhart, J.; Vermeer, J. E. M.; Adjobo-Hermans, M. J. W.; van Weeren, L.; Gadella, T. W. J. Sensitive Detection of P65 Homodimers Using Red-Shifted and Fluorescent Protein-Based FRET Couples. *PLoS One* **2007**, *2* (10), e1011.

(50) Goedhart, J.; Von Stetten, D.; Noirclerc-Savoye, M.; Lelimousin, M.; Joosen, L.; Hink, M. A.; Van Weeren, L.; Gadella, T. W. J.; Royant, A. Structure-Guided Evolution of Cyan Fluorescent Proteins towards a Quantum Yield of 93%. *Nat. Commun.* **2012**, *3* (1), 1–9.

(51) Greene, L. A. Nerve Growth Factor Prevents the Death and Stimulates the Neuronal Differentiation of Clonal PC12 Pheochromocytoma Cells in Serum-Free Medium. *J. Cell Biol.* **1978**, *78* (3), 747.

(52) Greene, L. A.; Tischler, A. S. Establishment of a Noradrenergic Clonal Line of Rat Adrenal Pheochromocytoma Cells Which Respond to Nerve Growth Factor. *Proc. Natl. Acad. Sci.* **1976**, *73* (7), 2424–2428.

(53) Greenwald, E. C.; Mehta, S.; Zhang, J. Genetically Encoded Fluorescent Biosensors Illuminate the Spatiotemporal Regulation of Signaling Networks. *Chem. Rev.* **2018**, *118* (24), 11707–11794.

(54) Grünberg Raik; Burnier, J. V.; Ferrar, T.; Beltran-Sastre, V.; Stricher, F.; Van Der Sloot, A. M.; Garcia-Olivas, R.; Mallabiabarrena, A.; Sanjuan, X.; Zimmermann, T.; Serrano, L. Engineering of Weak Helper Interactions for High-Efficiency FRET Probes. *Nat. Methods* **2013**, *10* (10), 1021–1027.

(55) Guroff, G. PC12 Cells as a Model of Neuronal Differentiation. *Cell Cult. Neurosci.* **1985**, 245–272.

(56) Han, A.-R.; Kim, H.; Piao, D.; Jung, C.-H.; Seo, E. K.; Jung, D. ; Seo, C.-H. ; Phytochemicals, E. K.; Of Zingiber, B.; Molecules, R.; Sülsen, P. Phytochemicals and Bioactivities of Zingiber Cassumunar Roxb. Mol. **2021**, *26* (8), 2377.

(57) Hao, Y.; Creson, T.; Zhang, L.; Li, P.; Du, F.; Yuan, P.; Gould, T. D.; Manji, H. K.; Chen, G. Mood Stabilizer Valproate Promotes ERK Pathway-Dependent Cortical Neuronal Growth and Neurogenesis. *J. Neurosci.* **2004**, *24* (29), 6590–6599.

(58) Harada, K.; Kubo, M.; Fukuyama, Y. Chemistry and Neurotrophic Activities of (–)-Talaumidin and Its Derivatives. *Front. Chem.* **2020**, *8*, 301.

(59) Harada, K.; Kubo, M.; Horiuchi, H.; Ishii, A.; Esumi, T.; Hioki, H.; Fukuyama, Y. Systematic Asymmetric Synthesis of All Diastereomers of (-)-Talaumidin and Their Neurotrophic Activity. *J. Org. Chem.* **2015**, *80* (14), 7076–7088.

(60) Harrill, J. A.; Mundy, W. R. Quantitative Assessment of Neurite Outgrowth in PC12 Cells. *Methods Mol. Biol.* **2011**, *758*, 331–348.

(61) Hasan, M. R.; Kim, J. H.; Kim, Y. J.; Kwon, K. J.; Shin, C. Y.; Kim, H. Y.; Han, S. H.; Choi, D. H.; Lee, J. Effect of HDAC Inhibitors on Neuroprotection and Neurite Outgrowth in Primary Rat Cortical Neurons Following Ischemic Insult. *Neurochem. Res.* **2013**, *38* (9), 1921–1934.

(62) Heim, R.; Tsien, R. Y. Engineering Green Fluorescent Protein for Improved Brightness, Longer Wavelengths and Fluorescence Resonance Energy Transfer. *Curr. Biol.* **1996**, *6* (2), 178–182.

(63) Hempstead, B. L. Deciphering Proneurotrophin Actions. *Handb. Exp. Pharmacol.* **2014**, *220*, 17–32.

(64) Hines, J.; Groll, M.; Fahnestock, M.; Crews, C. M. Proteasome Inhibition by Fellutamide B Induces Nerve Growth Factor Synthesis. *Chem. Biol.* **2008**, *15* (5), 501.

(65) Honarnejad, K.; Kirsch, A. K.; Daschner, A.; Szybinska, A.; Kuznicki, J.; Herms, J. FRET-Based Calcium Imaging: A Tool for High-Throughput/Content Phenotypic Drug Screening in Alzheimer Disease. *J. Biomol. Screen.* **2013**, *18* (10), 1309–1320.

(66) Houlton, J.; Abumaria, N.; Hinkley, S. F. R.; Clarkson, A. N. Therapeutic Potential of Neurotrophins for Repair after Brain Injury: A Helping Hand from Biomaterials. *Front. Genet.* **2019**, *10* (JUL), 790.

(67) Hu, R.; Cao, Q.; Sun, Z.; Chen, J.; Zheng, Q.; Xiao, F. A Novel Method of Neural Differentiation of PC12 Cells by Using Opti-MEM as a Basic Induction Medium. *Int. J. Mol. Med.* **2018**, *41* (1), 195.

(68) Huang, X. R.; Pan, X. H.; Lee, G. H.; Chen, C. C2-Symmetrical Bipyridyldiols as Promising Enantioselective Catalysts in Nozaki–Hiyama Allylation. *Adv. Synth. Catal.* **2011**, *353* (11–12), 1949–1954.

(69) Imagawa, H.; Saijo, H.; Kurisaki, T.; Yamamoto, H.; Kubo, M.; Fukuyama, Y.; Nishizawa, M. Total Synthesis of(±)-Neovibsanin B. *Org. Lett.* **2009**, *11* (6), 1253–1255.

(70) Ioannou, M. S.; Fahnestock, M. ProNGF, but Not NGF, Switches from Neurotrophic to Apoptotic Activity in Response to Reductions in TrkA Receptor Levels. *Int. J. Mol. Sci.* **2017**, *18* (3).

(71) Ishiuchi, K.; Kubota, T.; Ishiyama, H.; Hayashi, S.; Shibata, T.; Mori, K.; Obara, Y.; Nakahata, N.; Kobayashi, J. Lyconadins D and E, and Complanadine E, New Lycopodium Alkaloids from Lycopodium Complanatum. *Bioorg. Med. Chem.* **2011**, *19* (2), 749–753.

(72) Jang, S. W.; Okada, M.; Sayeed, I.; Xiao, G.; Stein, D.; Jin, P.; Ye, K. Gambogic Amide, a Selective Agonist for TrkA Receptor That Possesses Robust Neurotrophic Activity, Prevents Neuronal Cell Death. *Proc. Natl. Acad. Sci. U. S. A.* **2007**, *104* (41), 16329.

(73) Jessen, H. J.; Barbaras, D.; Hamburger, M.; Gademann, K. Total Synthesis and Neuritotrophic Activity of Farinosone C and Derivatives. *Org. Lett.* **2009**, *11* (15), 3446–3449.

(74) Jumper, J.; Evans, R.; Pritzel, A.; Green, T.; Figurnov, M.; Ronneberger, O.; Tunyasuvunakool, K.; Bates, R.; Žídek, A.; Potapenko, A.; Bridgland, A.; Meyer, C.; Kohl, S. A. A.; Ballard, A. J.; Cowie, A.; Romera-Paredes, B.; Nikolov, S.; Jain, R.; Adler, J.; Back, T.; Petersen, S.; Reiman, D.; Clancy, E.; Zielinski, M.; Steinegger, M.; Pacholska, M.; Berghammer, T.; Bodenstein, S.; Silver, D.; Vinyals, O.; Senior, A. W.; Kavukcuoglu, K.; Kohli, P.; Hassabis, D. Highly Accurate Protein Structure Prediction with AlphaFold. *Nat. 2021 5967873* **2021**, *596* (7873), 583–589.

(75) Karasawa, S.; Araki, T.; Nagai, T.; Mizuno, H.; Miyawaki, A. Cyan-Emitting and Orange-Emitting Fluorescent Proteins as a Donor/Acceptor Pair for Fluorescence Resonance Energy Transfer. *Biochem. J.* **2004**, *381* (1), 307.

(76) Kato, E.; Kubo, M.; Okamoto, Y.; Matsunaga, Y.; Kyo, H.; Suzuki, N.; Uebaba, K.; Fukuyama, Y. Safety Assessment of Bangle (Zingiber Purpureum Rosc.) Rhizome Extract: Acute and Chronic Studies in Rats and Clinical Studies in Human. *ACS Omega* **2018**, *3* (11), 15879-15889.

(77) Kawagishi, H.; Shimada, A.; Hosokawa, S.; Mori, H.; Sakamoto, H.; Ishiguro, Y.; Sakemi, S.; Bordner, J.; Kojima, N.; Furukawa, S. Erinacines E, F, and G, Stimulators of Nerve Growth Factor (NGF)-Synthesis, from the Mycelia of Hericium Erinaceum. *Tetrahedron Lett.* **1996**, *37* (41), 7399–7402.

(78) Kawagishi, H.; Shimada, A.; Shirai, R.; Okamoto, K.; Ojima, F.; Sakamoto, H.; Ishiguro, Y.; Furukawa, S. Erinacines A, B and C, Strong Stimulators of Nerve Growth Factor (NGF)-Synthesis, from the Mycelia of Hericium Erinaceum. *Tetrahedron Lett.* **1994**, *35* (10), 1569–1572.

(79) Kawagishi, H.; Simada, A.; Shizuki, K.; Mori, H.; Okamoto, K.; Sakamoto, H.; Furukawa, S. Erinacine D, a Stimulator of NGF-Synthesis, from the Mycelia of Hericium Erinaceum. *Heterocycl. Commun.* **1996**, *2* (1), 51–54.

(80) Khaing, Z.; Kang, D.; Camelio, A. M.; Schmidt, C. E.; Siegel, D. Hippocampal and Cortical Neuronal Growth Mediated by the Small Molecule Natural Product Clovanemagnolol. *Bioorg. Med. Chem. Lett.* **2011**, *21* (16), 4808–4812.

(81) Kim, S. S.; Fang, Y.; Park, H. Synthesis and Anti-Inflammatory Activity of Phenylbutenoid Dimer Analogs. *Bull. Korean Chem. Soc.* **2015**, *36* (6), 1676–1680.

(82) Kinarivala, N.; Shah, K.; Abbruscato, T. J.; Trippier, P. C. Passage Variation of PC12 Cells Results in Inconsistent Susceptibility to Externally Induced Apoptosis. *ACS Chem. Neurosci.* **2017**, *8* (1), 82.

(83) Klesse, L.; Meyers, K.; Marshall, C.; Parada, L. Nerve Growth Factor Induces Survival and Differentiation through Two Distinct Signaling Cascades in PC12 Cells. *Oncogene* **1999**, *18* (12), 2055–2068.

(84) Koriyama, Y.; Furukawa, A.; Sugitani, K.; Kubo, M.; Harada, K.; Fukuyama, Y. Talaumidin Promotes Neurite Outgrowth of Staurosporine-Differentiated RGC-5 Cells Through PI3K/Akt-Dependent Pathways. *Adv. Exp. Med. Biol.* **2018**, *1074*, 649–653.

(85) Kotera, I.; Iwasaki, T.; Imamura, H.; Noji, H.; Nagai, T. Reversible Dimerization of Aequorea Victoria Fluorescent Proteins Increases the Dynamic Range of FRET-Based Indicators. *ACS Chem. Biol.* **2010**, *5* (2), 215–222.

(86) Kovalevich, J.; Langford, D. Considerations for the Use of SH-SY5Y Neuroblastoma Cells in Neurobiology. *Methods Mol. Biol.* **2013**, *1078*, 9.

(87) Kraemer, B. R.; Yoon, S. O.; Carter, B. D. The Biological Functions and Signaling Mechanisms of the P75 Neurotrophin Receptor. *Handb. Exp. Pharmacol.* **2014**, *220*, 121–164.

(88) Kremers, G. J.; Goedhart, J.; Van Den Heuvel, D. J.; Gerritsen, H. C.; Gadella, T. W. J. Improved Green and Blue Fluorescent Proteins for Expression in Bacteria and Mammalian Cells. *Biochemistry* **2007**, *46* (12), 3775–3783.

(89) Kubo, M.; Kaga, S.; Harada, K.; Okamoto, Y.; Kato, E.; Hosoda, S.; Fukuyama, Y. Studies on Extraction Conditions to Increase the Content of Neurotrophic Compounds in the Bangle (Zingiber Purpureum) Extract.*Nat. Prod. Commun.* **2017**, *12* (8), 1934578X1701200835.

(90) Kwok, S.; Lee, C.; Sánchez, S. A.; Hazlett, T. L.; Gratton, E.; Hayashi, Y. Genetically Encoded Probe for Fluorescence Lifetime Imaging of CaMKII Activity. *Biochem. Biophys. Res. Commun.* **2008**, *369* (2), 519.

(91) Lam, A. J.; St-Pierre, F.; Gong, Y.; Marshall, J. D.; Cranfill, P. J.; Baird, M. A.; McKeown, M. R.; Wiedenmann, J.; Davidson, M. W.; Schnitzer, M. J.; Tsien, R. Y.; Lin, M. Z. Improving FRET Dynamic Range with Bright Green and Red Fluorescent Proteins. *Nat. Methods* **2012**, *9* (10), 1005.

(92) Latina, V.; Caioli, S.; Zona, C.; Ciotti, M. T.; Amadoro, G.; Calissano, P. Impaired NGF/TrKA Signaling Causes Early AD-Linked Presynaptic Dysfunction in Cholinergic Primary Neurons. *Front. Cell. Neurosci.* **2017**, *11*, 68.

(93) Le, A. P.; Friedman, W. J. Matrix Metalloproteinase-7 Regulates Cleavage of pro-Nerve Growth Factor and Is Neuroprotective Following Kainic Acid-Induced Seizures. *J. Neurosci.* **2012**, *32* (2), 703–712.

(94) Lee, F. S.; Rajagopal, R.; Kim, A. H.; Chang, P. C.; Chao, M. V. Activation of Trk Neurotrophin Receptor Signaling by Pituitary Adenylate Cyclase-Activating Polypeptides *. *J. Biol. Chem.* **2002**, *277* (11), 9096–9102.

(95) Lee, S. R.; Park, J. H.; Park, E. K.; Chung, C. H.; Kang, S. S.; Bang, O. S. Akt-Induced Promotion of Cell-Cycle Progression at G2/M Phase Involves Upregulation of NF-Y Binding Activity in PC12 Cells. *J. Cell. Physiol.* **2005**, *205* (2), 270–277.

(96) Lin, C. W.; Wu, M. J.; Liu, I. Y. C.; Su, J. D.; Yen, J. H. Neurotrophic and Cytoprotective Action of Luteolin in PC12 Cells through ERK-Dependent Induction of Nrf2-Driven HO-1 Expression. *J. Agric. Food Chem.* **2010**, *58* (7), 4477–4486.

(97) Lindenburg, L. H.; Hessels, A. M.; Ebberink, E. H. T. M.; Arts, R.; Merkx, M. Robust Red FRET Sensors Using Self-Associating Fluorescent Domains. *ACS Chem. Biol.* **2013**, *8* (10), 2133–2139.

(98) Liu, L.; Shi, X. W.; Zong, S. C.; Tang, J. J.; Gao, J. M. Scabronine M, a Novel Inhibitor of NGF-Induced Neurite Outgrowth from PC12 Cells from the Fungus Sarcodon Scabrosus. *Bioorg. Med. Chem. Lett.* **2012**, *22* (7), 2401–2406.

(99) Liu, R.; Ren, D.; Liu, Y.; Deng, Y.; Sun, B.; Zhang, Q.; Guo, X. Biosensors of DsRed as FRET Partner with CFP or GFP for Quantitatively Imaging Induced Activation of Rac, Cdc42 in Living Cells. *Mol.*

imaging Biol. **2011**, *13* (3), 424–431.

(100) Lording, W. J.; Fallon, T.; Sherburn, M. S.; Paddon-Row, M. N. The Simplest Diels–Alder Reactions Are Not Endo -Selective. *Chem. Sci.* **2020**, *11* (43), 11915–11926.

(101) Ma, B. J.; Shen, J. W.; Yu, H. Y.; Ruan, Y.; Wu, T. T.; Zhao, X. Hericenones and Erinacines: Stimulators of Nerve Growth Factor (NGF) Biosynthesis in Hericium Erinaceus. *Mycology* **2010**, *1* (2), 92–98.

(102) Ma, T.; Gong, K.; Yan, Y.; Zhang, L.; Tang, P.; Zhang, X.; Gong, Y. Huperzine A Promotes Hippocampal Neurogenesis in Vitro and in Vivo. *Brain Res.* **2013**, *1506*, 35–43.

(103) Makkerh, J. P. S.; Ceni, C.; Auld, D. S.; Vaillancourt, F.; Dorval, G.; Barker, P. A. P75 Neurotrophin Receptor Reduces Ligand-Induced Trk Receptor Ubiquitination and Delays Trk Receptor Internalization and Degradation. *EMBO Rep.* **2005**, *6* (10), 936–941.

(104) Malerba, F.; Paoletti, F.; Cattaneo, A. NGF and ProNGF Reciprocal Interference in Immunoassays: Open Questions, Criticalities, and Ways Forward. *Front. Mol. Neurosci.* **2016**, *9* (AUG), 63.

(105) Mansoury, M.; Hamed, M.; Karmustaji, R.; Al Hannan, F.; Safrany, S. T. The Edge Effect: A Global Problem. The Trouble with Culturing Cells in 96-Well Plates. *Biochem. Biophys. Reports* **2021**, *26*, 100987.

(106) Marlin, M. C.; Li, G. Biogenesis and Function of the NGF/TrkA Signaling Endosome. *Int. Rev. Cell Mol. Biol.* **2015**, *314*, 239.

(107) Masoudi, R.; Ioannou, M. S.; Coughlin, M. D.; Pagadala, P.; Neet, K. E.; Clewes, O.; Allen, S. J.; Dawbarn, D.; Fahnestock, M. Biological Activity of Nerve Growth Factor Precursor Is Dependent upon Relative Levels of Its Receptors *. *J. Biol. Chem.* **2009**, *284* (27), 18424–18433.

(108) Mastop, M.; Bindels, D. S.; Shaner, N. C.; Postma, M.; Gadella, T. W. J.; Goedhart, J. Characterization of a Spectrally Diverse Set of Fluorescent Proteins as FRET Acceptors for MTurquoise2. *Sci. Reports* **2017**, *7* (1), 1–18.

(109) Matsui, N.; Kido, Y.; Okada, H.; Kubo, M.; Nakai, M.; Fukuishi, N.; Fukuyama, Y.; Akagi, M. Phenylbutenoid Dimers Isolated from Zingiber Purpureum Exert Neurotrophic Effects on Cultured Neurons and Enhance Hippocampal Neurogenesis in Olfactory Bulbectomized Mice. *Neurosci. Lett.* **2012**, *513* (1), 72–77.

(110) McCullock, T. W.; MacLean, D. M.; Kammermeier, P. J. Comparing the Performance of MScarlet-I, MRuby3, and MCherry as FRET Acceptors for MNeonGreen. *PLoS One* **2020**, *15* (2).

(111) Mi, S.; Lee, X.; Shao, Z.; Thill, G.; Ji, B.; Relton, J.; Levesque, M.; Allaire, N.; Perrin, S.; Sands, B.; Crowell, T.; Cate, R. L.; McCoy, J. M.; Pepinsky, R. B. LINGO-1 Is a Component of the Nogo-66 Receptor/P75 Signaling Complex. *Nat. Neurosci. 2004 73* **2004**, *7* (3), 221–228.

(112) Miranda, M.; Morici, J. F.; Zanoni, M. B.; Bekinschtein, P. Brain-Derived Neurotrophic Factor: A Key Molecule for Memory in the Healthy and the Pathological Brain. *Front. Cell. Neurosci.* **2019**, *13*, 363.

(113) Miyawaki, A.; Llopis, J.; Heim, R.; Michael McCaffery, J.; Adams, J. A.; Ikura, M.; Tsien, R. Y. Fluorescent Indicators for Ca2+based on Green Fluorescent Proteins and Calmodulin. *Nat.* **1997**, *388* (6645), 882–887.

(114) Moghaddam, F. M.; Farimani, M. M. A Simple and Efficient Total Synthesis of (±)-Danshexinkun A, a Bioactive Diterpenoid from Salvia Miltiorrhiza. *Tetrahedron Lett.* **2010**, *51* (3), 540–542.

(115) Mohideen, M.; Zulkepli, S.; Nik-Salleh, N. S.; Zulkefeli, M.; Weber, J. F. F. A.; Rahman, A. F. M. M. Design, Synthesis, in Vitro Cytotoxicity Evaluation and Structure-Activity Relationship of Goniothalamin Analogs. *Arch. Pharm. Res.* **2013**, *36* (7), 812–831.

(116) Montgomery, T. P.; Grandner, J. M.; Houk, K. N.; Grubbs, R. H. Synthesis and Evaluation of Sterically Demanding Ruthenium Dithiolate Catalysts for Stereoretentive Olefin Metathesis. *Organometallics* **2017**, *36* (20), 3940–3953.

(117) Morales-Medina, J. C.; Iannitti, T.; Freeman, A.; Caldwell, H. K. The Olfactory Bulbectomized Rat as a Model of Depression: The Hippocampal Pathway. *Behav. Brain Res.* **2017**, *317*, 562–575.

(118) Morris, E. J.; Jha, S.; Restaino, C. R.; Dayananth, P.; Zhu, H.; Cooper, A.; Carr, D.; Deng, Y.; Jin, W.; Black, S.; Long, B.; Liu, J.; DiNunzio, E.; Windsor, W.; Zhang, R.; Zhao, S.; Angagaw, M. H.; Pinheiro, E. M.; Desai, J.; Xiao, L.; Shipps, G.; Hruza, A.; Wang, J.; Kelly, J.; Paliwal, S.; Gao, X.; Babu, B. S.; Zhu, L.; Daublain, P.; Zhang, L.; Lutterbach, B. A.; Pelletier, M. R.; Philippar, U.; Siliphaivanh, P.; Witter, D.; Kirschmeier, P.; Robert Bishop, W.; Hicklin, D.; Gary Gillil, D.; Jayaraman, L.; Zawel, L.; Fawell, S.; Samatar, A. A. Discovery of a Novel ERK Inhibitor with Activity in Models of Acquired Resistance to BRAF and MEK Inhibitors. *Cancer Discov.* **2013**, *3* (7), 742–750.

(119) Mufson, E. J.; Counts, S. E.; Ginsberg, S. D.; Mahady, L.; Perez, S. E.; Massa, S. M.; Longo, F. M.; Ikonomovic, M. D. Nerve Growth Factor Pathobiology During the Progression of Alzheimer's Disease. *Front. Neurosci.* **2019**, *13* (JUL).

(120) Nakai, M.; Iizuka, M.; Matsui, N.; Hosogi, K.; Imai, A.; Abe, N.; Shiraishi, H.; Hirata, A.; Yagi, Y.; Jobu, K.; Yokota, J.; Kato, E.; Hosoda, S.; Yoshioka, S.; Harada, K.; Kubo, M.; Fukuyama, Y.; Miyamura, M. Bangle (Zingiber Purpureum) Improves Spatial Learning, Reduces Deficits in Memory, and Promotes Neurogenesis in the Dentate Gyrus of Senescence-Accelerated Mouse P8. *J. Med. Food* **2016**, *19* (5), 435–441.

(121) Nakamura, S.; Iwami, J.; Matsuda, H.; Wakayama, H.; Pongpiriyadacha, Y.; Yoshikawa, M. Structures of New Phenylbutanoids and Nitric Oxide Production Inhibitors from the Rhizomes of Zingiber Cassumunar Chart 1. Structures of New Constituents from the Rhizomes of Zingiber Cassumunar. *Chem. Pharm. Bull* **2009**, *57* (11), 1267–1272.

(122) Nasu, Y.; Shen, Y.; Kramer, L.; Campbell, R. E. Structure- and Mechanism-Guided Design of Single Fluorescent Protein-Based Biosensors. *Nat. Chem. Biol.* **2021**, *17* (5), 509–518.

(123) Nguyen, A. W.; Daugherty, P. S. Evolutionary Optimization of Fluorescent Proteins for Intracellular FRET. *Nat. Biotechnol.* **2005**, *23* (3), 355–360.

(124) Ngwendson, J. N.; Schultze, C. M.; Bollinger, J. W.; Banerjee, A. Effect of Base on Alkyltriphenylphosphonium Salts in Polar Aprotic Solvents. *Can. J. Chem.* **2011**, *86* (7), 668–675.

(125) Nykjaer, A.; Willnow, T. E. Sortilin: A Receptor to Regulate Neuronal Viability and Function. *Trends Neurosci.* **2012**, *35* (4), 261–270.

(126) Obara, Y.; Hoshino, T.; Marcotullio, M. C.; Pagiotti, R.; Nakahata, N. A Novel Cyathane Diterpene, Cyrneine A, Induces Neurite Outgrowth in a Rac1-Dependent Mechanism in PC12 Cells. *Life Sci.* **2007**, *80* (18), 1669–1677.

(127) Obara, Y.; Kobayashi, H.; Ohta, T.; Ohizumi, Y.; Nakahata, N. Scabronine G-Methylester Enhances Secretion of Neurotrophic Factors Mediated by an Activation of Protein Kinase C-ζ. *Mol. Pharmacol.* **2001**, *59* (5), 1287–1297.

(128) Obara, Y.; Nakahata, N.; Kita, T.; Takaya, Y.; Kobayashi, H.; Hosoi, S.; Kiuchi, F.; Ohta, T.; Oshima, Y.; Ohizumi, Y. Stimulation of Neurotrophic Factor Secretion from 1321N1 Human Astrocytoma Cells by Novel Diterpenoids, Scabronines A and G. *Eur. J. Pharmacol.* **1999**, *370* (1), 79–84.

(129) Ohashi, T.; Galiacy, S. D.; Briscoe, G.; Erickson, H. P. An Experimental Study of GFP-Based FRET, with Application to Intrinsically Unstructured Proteins. *Protein Sci.* **2007**, *16* (7), 1429.

(130) Orlowska, A.; Perera, P. T.; Al Kobaisi, M. A.; Dias, A.; Nguyen, H. K. D.; Ghanaati, S.; Baulin, V.; Crawford, R. J.; Ivanova, E. P. The Effect of Coatings and Nerve Growth Factor on Attachment and Differentiation of Pheochromocytoma Cells. *Mater.* **2017**, *11* (1), 60.

(131) Ouyang, M.; Huang, H.; Shaner, N. C.; Remacle, A. G.; Shiryaev, S. A.; Strongin, A. Y.; Tsien, R. Y.; Wang, Y. Simultaneous Visualization of Protumorigenic Src and MT1-MMP Activities with Fluorescence Resonance Energy Transfer. *Cancer Res.* **2010**, *70* (6), 2204–2212.

(132) Paoletti, F.; Chiara, C. de; Kelly, G.; Covaceuszach, S.; Malerba, F.; Yan, R.; Lamba, D.; Cattaneo, A.; Pastore, A. Conformational Rigidity within Plasticity Promotes Differential Target Recognition of Nerve Growth Factor. *Front. Mol. Biosci.* **2016**, *3* (DEC), 83.

(133) PC-12 | ATCC https://www.atcc.org/products/crl-1721 (accessed 2022 -01 -10).

(134) Phan, C. W.; Lee, G. S.; Hong, S. L.; Wong, Y. T.; Brkljača, R.; Urban, S.; Abd Malek, S. N.; Sabaratnam, V. Hericium Erinaceus (Bull.: Fr) Pers. Cultivated under Tropical Conditions: Isolation of Hericenones and Demonstration of NGF-Mediated Neurite Outgrowth in PC12 Cells via MEK/ERK and PI3K-Akt Signaling Pathways. *Food Funct.* **2014**, *5* (12), 3160–3169.

(135) Piljic, A.; Schultz, C. Simultaneous Recording of Multiple Cellular Events by FRET. *ACS Chem. Biol.* **2008**, *3* (3), 156–160.

(136) Radio, N. M.; Breier, J. M.; Shafer, T. J.; Mundy, W. R. Assessment of Chemical Effects on Neurite Outgrowth in PC12 Cells Using High Content Screening. *Toxicol. Sci.* **2008**, *105* (1), 106–118.

(137) Read, D. E.; Gorman, A. M. Involvement of Akt in Neurite Outgrowth. *Cell. Mol. Life Sci.* **2009**, *66* (18), 2975–2984.

(138) Reichardt, L. F. Neurotrophin-Regulated Signalling Pathways. *Philos. Trans. R. Soc. B Biol. Sci.* **2006**, *361* (1473), 1545–1564.

(139) Rodrigues, T. M.; Jerónimo-Santos, A.; Outeiro, T. F.; Sebastião, A. M.; Diógenes, M. J. Challenges and Promises in the Development of Neurotrophic Factor-Based Therapies for Parkinson's Disease. *Drugs and Aging* **2014**, *31* (4), 239–261.

(140) Saragovi, H. U.; Galan, A.; Levin, L. A. Neuroprotection: Pro-Survival and Anti-Neurotoxic Mechanisms

as Therapeutic Strategies in Neurodegeneration. *Front. Cell. Neurosci.* **2019**, *13*, 231.

(141) Schmid, P.; Maier, M.; Pfeiffer, H.; Belz, A.; Henry, L.; Friedrich, A.; Schönfeld, F.; Edkins, K.; Schatzschneider, U. Catalyst-Free Room-Temperature IClick Reaction of Molybdenum(Ii) and Tungsten(Ii) Azide Complexes with Electron-Poor Alkynes: Structural Preferences and Kinetic Studies. *Dalt. Trans*. **2017**, *46* (39), 13386–13396.

(142) Sciences, N. R. C. (US) C. on R. at the I. of the P. and L. Enabling Technologies and Tools for Research. **2010**.

(143) Seow, S. L. S.; Hong, S. L.; Lee, G. S.; Malek, S. N. A.; Sabaratnam, V. 6-Shogaol, a Neuroactive Compound of Ginger (Jahe Gajah) Induced Neuritogenic Activity via NGF Responsive Pathways in PC-12 Cells. *BMC Complement. Altern. Med.* **2017**, *17* (1), 1–11.

(144) Shaner, N. C.; Patterson, G. H.; Davidson, M. W. Advances in Fluorescent Protein Technology. *J. Cell Sci.* **2007**, *120* (24), 4247–4260.

(145) Shcherbo, D.; Souslova, E. A.; Goedhart, J.; Chepurnykh, T. V.; Gaintzeva, A.; Shemiakina, I. I.; Gadella, T. W. J.; Lukyanov, S.; Chudakov, D. M. Practical and Reliable FRET/FLIM Pair of Fluorescent Proteins. *BMC Biotechnol.* **2009**, *9* (1), 1–6.

(146) Shen, J.; Maruyama, I. N. Nerve Growth Factor Receptor TrkA Exists as a Preformed, yet Inactive, Dimer in Living Cells. *FEBS Lett.* **2011**, *585* (2), 295–299.

(147) Shen, Y.; Wu, S. Y.; Rancic, V.; Aggarwal, A.; Qian, Y.; Miyashita, S. I.; Ballanyi, K.; Campbell, R. E.; Dong, M. Genetically Encoded Fluorescent Indicators for Imaging Intracellular Potassium Ion Concentration. *Commun. Biol.* **2019**, *2* (1).

(148) Shi, X. W.; Liu, L.; Gao, J. M.; Zhang, A. L. Cyathane Diterpenes from Chinese Mushroom Sarcodon Scabrosus and Their Neurite Outgrowth-Promoting Activity. *Eur. J. Med. Chem.* **2011**, *46* (7), 3112–3117.

(149) Shimbo, M.; Kawagishi, H.; Yokogoshi, H. Erinacine A Increases Catecholamine and Nerve Growth Factor Content in the Central Nervous System of Rats. *Nutr. Res.* **2005**, *25* (6), 617–623.

(150) Shukla, S.; Shariat-Madar, Z.; Walker, L. A.; Tekwani, B. L. Mechanism for Neurotropic Action of Vorinostat, a Pan Histone Deacetylase Inhibitor. *Mol. Cell. Neurosci.* **2016**, *77*, 11–20.

(151) Shukla, S.; Tekwani, B. L. Histone Deacetylases Inhibitors in Neurodegenerative Diseases, Neuroprotection and Neuronal Differentiation. *Front. Pharmacol.* **2020**, *11*, 537.

(152) Simmons, D. A.; Knowles, J. K.; Belichenko, N. P.; Banerjee, G.; Finkle, C.; Massa, S. M.; Longo, F. M. A Small Molecule P75NTR Ligand, LM11A-31, Reverses Cholinergic Neurite Dystrophy in Alzheimer's Disease Mouse Models with Mid- to Late-Stage Disease Progression. *PLoS One* **2014**, *9* (8).

(153) Skaper, S. D. The Neurotrophin Family of Neurotrophic Factors: An Overview. *Methods Mol. Biol.* **2012**, *846*, 1–12.

(154) Skeldal, S.; Sykes, A. M.; Glerup, S.; Matusica, D.; Palstra, N.; Autio, H.; Boskovic, Z.; Madsen, P.; Castrén, E.; Nykjaer, A.; Coulson, E. J. Mapping of the Interaction Site between Sortilin and the P75 Neurotrophin Receptor Reveals a Regulatory Role for the Sortilin Intracellular Domain in P75

Neurotrophin Receptor Shedding and Apoptosis *. *J. Biol. Chem.* **2012**, *287* (52), 43798–43809.

(155) Soligo, M.; Albini, M.; Bertoli, F. L.; Marzano, V.; Protto, V.; Bracci-Laudiero, L.; Minnone, G.; De Benedetti, F.; Chiaretti, A.; Mantuano, E.; Manni, L. Different Responses of PC12 cells to Different Pro-Nerve Growth Factor Protein Variants. *Neurochem. Int.* **2019**, *129*, 104498.

(156) Strack, R. L.; Strongin, D. E.; Mets, L.; Glick, B. S.; Keenan, R. J. Chromophore Formation in DsRed Occurs by a Branched Pathway. *J. Am. Chem. Soc.* **2010**, *132* (24), 8496–8505.

(157) Subach, F. V.; Verkhusha, V. V. Chromophore Transformations in Red Fluorescent Proteins. *Chem. Rev.* **2012**, *112* (7), 4308.

(158) Subach, O. M.; Gundorov, I. S.; Yoshimura, M.; Subach, F. V.; Zhang, J.; Grüenwald, D.; Souslova, E. A.; Chudakov, D. M.; Verkhusha, V. V. Conversion of Red Fluorescent Protein into a Bright Blue Probe. *Chem. Biol.* **2008**, *15* (10), 1116.

(159) Tamura, T.; Hamachi, I. Recent Progress in Design of Protein-Based Fluorescent Biosensors and Their Cellular Applications. *ACS Chem. Biol.* **2014**, *9* (12), 2708–2717.

(160) Tang, G.; Dong, X.; Huang, X.; Huang, X. J.; Liu, H.; Wang, Y.; Ye, W. C.; Shi, L. A Natural Diarylheptanoid Promotes Neuronal Differentiation via Activating ERK and PI3K-Akt Dependent Pathways. *Neuroscience* **2015**, *303*, 389–401.

(161) Tang, L. L.; Wang, R.; Tang, X. C. Effects of Huperzine A on Secretion of Nerve Growth Factor in Cultured Rat Cortical Astrocytes and Neurite Outgrowth in Rat PC12 Cells. *Acta Pharmacol. Sin.* **2005**, *26* (6), 673–678.

(162) Tang, L. L.; Wang, R.; Tang, X. C. Huperzine A Protects SHSY5Y Neuroblastoma Cells against Oxidative Stress Damage via Nerve Growth Factor Production. *Eur. J. Pharmacol.* **2005**, *519* (1–2), 9–15.

(163) Tang, W.; Hioki, H.; Harada, K.; Kubo, M.; Fukuyama, Y. Clerodane Diterpenoids with NGF-Potentiating Activity from Ptychopetalum Olacoides. *J. Nat. Prod.* **2008**, *71* (10), 1760–1763.

(164) Teng, K. K.; Angelastro, J. M.; Cunningham, M. E.; Greene, L. A. Cultured PC12 Cells: A Model for Neuronal Function, Differentiation, and Survival. *Cell Biol. Four-Volume Set* **2006**, *1*, 171–176.

(165) Terskikh, A. V.; Fradkov, A. F.; Zaraisky, A. G.; Kajava, A. V.; Angres, B. Analysis of DsRed Mutants: SPACE AROUND THE FLUOROPHORE ACCELERATES FLUORESCENCE DEVELOPMENT *. *J. Biol. Chem.* **2002**, *277* (10), 7633–7636.

(166) Tomaselli, K. J.; Damsky, C. H.; Reichardt, L. F. Purification and Characterization of Mammalian Integrins Expressed by a Rat Neuronal Cell Line (PC12): Evidence That They Function as Alpha/Beta Heterodimeric Receptors for Laminin and Type IV Collagen. *J. Cell Biol.* **1988**, *107* (3), 1241–1252.

(167) Tremblay, R. G.; Sikorska, M.; Sandhu, J. K.; Lanthier, P.; Ribecco-Lutkiewicz, M.; Bani-Yaghoub, M. Differentiation of Mouse Neuro 2A Cells into Dopamine Neurons. *J. Neurosci. Methods* **2010**, *186* (1), 60–67.

(168) Tsuji, M.; Inanami, O.; Kuwabara, M. Induction of Neurite Outgrowth in PC12 Cells by α-Phenyl-N-Tert-Butylnitron through Activation of Protein Kinase C and the Ras-Extracellular Signal-Regulated

Kinase Pathway *. *J. Biol. Chem.* **2001**, *276* (35), 32779–32785.

(169) Tsutsui, H.; Karasawa, S.; Okamura, Y.; Miyawaki, A. Improving Membrane Voltage Measurements Using FRET with New Fluorescent Proteins. *Nat. Methods 2008 58* **2008**, *5* (8), 683–685.

(170) Van Bergeijk, J.; Haastert, K.; Grothe, C.; Claus, P. Valproic Acid Promotes Neurite Outgrowth in PC12 Cells Independent from Regulation of the Survival of Motoneuron Protein. *Chem. Biol. Drug Des.* **2006**, *67* (3), 244–247.

(171) VanEngelenburg, S. B.; Palmer, A. E. Fluorescent Biosensors of Protein Function. *Curr. Opin. Chem. Biol.* **2008**, *12* (1), 60–65.

(172) Vauzour, D.; Vafeiadou, K.; Rodriguez-Mateos, A.; Rendeiro, C.; Spencer, J. P. E. The Neuroprotective Potential of Flavonoids: A Multiplicity of Effects. *Genes Nutr.* **2008**, *3* (3–4), 115–126.

(173) Venkatesan, R.; Ji, E.; Kim, S. Y. Phytochemicals That Regulate Neurodegenerative Disease by Targeting Neurotrophins: A Comprehensive Review. *Biomed Res. Int.* **2015**.

(174) Venkatesan, R.; Shim, W. S.; Yeo, E. J.; Kim, S. Y. Lactucopicrin Potentiates Neuritogenesis and Neurotrophic Effects by Regulating Ca2+/CaMKII/ATF1 Signaling Pathway. *J. Ethnopharmacol.* **2017**, *198*, 174–183.

(175) Vinkenborg, J. L.; Evers, T. H.; Reulen, S. W. A.; Meijer, E. W.; Merkx, M. Enhanced Sensitivity of FRET-Based Protease Sensors by Redesign of the GFP Dimerization Interface. *ChemBioChem* **2007**, *8* (10), 1119–1121.

(176) Weber, S.; Fernández-Cachón, M. L.; Nascimento, J. M.; Knauer, S.; Offermann, B.; Murphy, R. F.; Boerries, M.; Busch, H. Label-Free Detection of Neuronal Differentiation in Cell Populations Using High-Throughput Live-Cell Imaging of PC12 Cells. *PLoS One* **2013**, *8* (2), e56690.

(177) Weissmiller, A. M.; Wu, C. Current Advances in Using Neurotrophic Factors to Treat Neurodegenerative Disorders. *Transl. Neurodegener.* **2012**, *1*, 14.

(178) Westerink, R. H. S.; Ewing, A. G. The PC12 Cell as Model for Neurosecretion. *Acta Physiol. (Oxf).* **2008**, *192* (2), 273.

(179) Wiatrak, B.; Kubis-Kubiak, A.; Piwowar, A.; Barg, E. PC12 Cell Line: Cell Types, Coating of Culture Vessels, Differentiation and Other Culture Conditions. *Cells* **2020**, *9* (4).

(180) Williams, B.; Dwyer, D. S. Structure-Based Discovery of Low Molecular Weight Compounds That Stimulate Neurite Outgrowth and Substitute for Nerve Growth Factor. *J. Neurochem.* **2009**, *110* (6), 1876.

(181) Wlesmann, C.; Ultsch, M. H.; Bass, S. H.; De Vos, A. M. Crystal Structure of Nerve Growth Factor in Complex with the Ligand-Binding Domain of the TrkA Receptor. *Nat. 1999 4016749* **1999**, *401* (6749), 184–188.

(182) Xu, J.; Lacoske, M. H.; Theodorakis, E. A. Neurotrophic Natural Products: Chemistry and Biology. *Angew. Chem. Int. Ed. Engl.* **2014**, *53* (4), 956.

(183) Yamashita, N.; Kuruvilla, R. Neurotrophin Signaling Endosomes: Biogenesis, Regulation, and Functions. *Curr. Opin. Neurobiol.* **2016**, *39*, 139–145.

(184) Yamashita, T.; Tucker, K. L.; Barde, Y. A. Neurotrophin Binding to the P75 Receptor Modulates Rho Activity and Axonal Outgrowth. *Neuron* **1999**, *24* (3), 585–593.

(185) Yanagimoto, T.; Kishimoto, S.; Kasai, Y.; Matsui, N.; Kubo, M.; Yamamoto, H.; Fukuyama, Y.; Imagawa, H. Design and Synthesis of Dual Active Neovibsanin Derivatives Based on a Chemical Structure Merging Method. *Bioorg. Med. Chem. Lett.* **2020**, *30* (20), 127497.

(186) Yang, G.; Wang, Y.; Tian, J.; Liu, J. P. Huperzine A for Alzheimer's Disease: A Systematic Review and Meta-Analysis of Randomized Clinical Trials. *PLoS One* **2013**, *8* (9).

(187) Yang, X.; Xu, P.; Xu, T. A New Pair for Inter- and Intra-Molecular FRET Measurement. *Biochem. Biophys. Res. Commun.* **2005**, *330* (3), 914–920.

(188) Yasuda, R.; Harvey, C. D.; Zhong, H.; Sobczyk, A.; Van Aelst, L.; Svoboda, K. Supersensitive Ras Activation in Dendrites and Spines Revealed by Two-Photon Fluorescence Lifetime Imaging. *Nat. Neurosci.* **2006**, *9* (2), 283–291.

(189) Young, L. H.; Balin, B. J.; Weis, M. T. Gö 6983: A Fast Acting Protein Kinase C Inhibitor That Attenuates Myocardial Ischemia/Reperfusion Injury. *Cardiovasc. Drug Rev.* **2005**, *23* (3), 255–272.

(190) Zacharias, D. A.; Violin, J. D.; Newton, A. C.; Tsien, R. Y. Partitioning of Lipid-Modified Monomeric GFPs into Membrane Microdomains of Live Cells. *Science (80-.).* **2002**, *296* (5569), 913–916.

(191) Zhang, C. C.; Cao, C. Y.; Kubo, M.; Harada, K.; Yan, X. T.; Fukuyama, Y.; Gao, J. M. Chemical Constituents from Hericium Erinaceus Promote Neuronal Survival and Potentiate Neurite Outgrowth via the TrkA/Erk1/2 Pathway. *Int. J. Mol. Sci.* **2017**, *18* (8).

(192) Zhang, D.; Redington, E.; Gong, Y. Rational Engineering of Ratiometric Calcium Sensors with Bright Green and Red Fluorescent Proteins. *Commun. Biol.* **2021**, *4* (1), 1–12.

(193) Zlotkowski, K.; Eliasen, A. M.; Mitra, A.; Siegel, D. Small-Molecule Mechanism of Action Studies in Caenorhabditis Elegans. *Chembiochem* **2013**, *14* (17), 2338–2344.

Appendix 1: Selected copies of NMR spectra

Figure S1: ^{1}H NMR spectrum of compound **2-39a** ($CDCl_3$, 400 MHz)

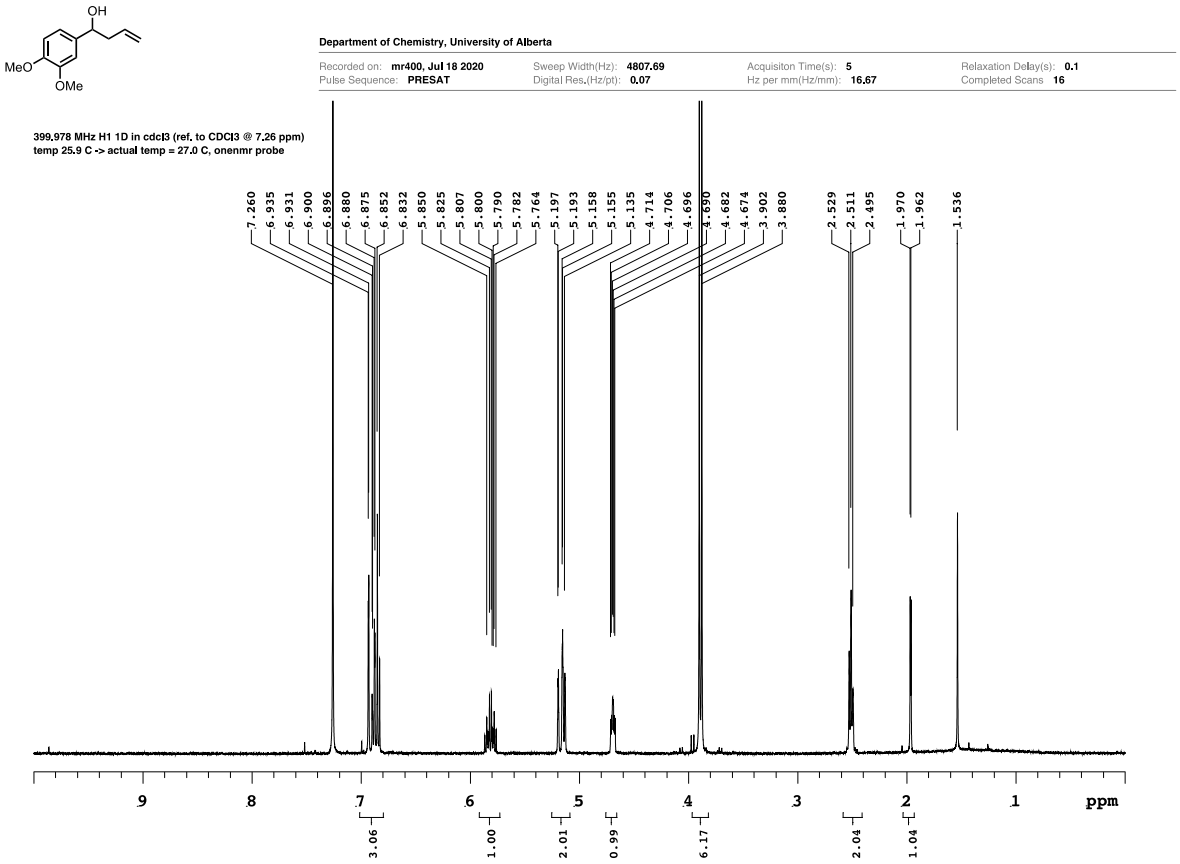

Figure S2: ^{13}C NMR spectrum of compound **2-39a** ($CDCl_3$, 176 MHz)

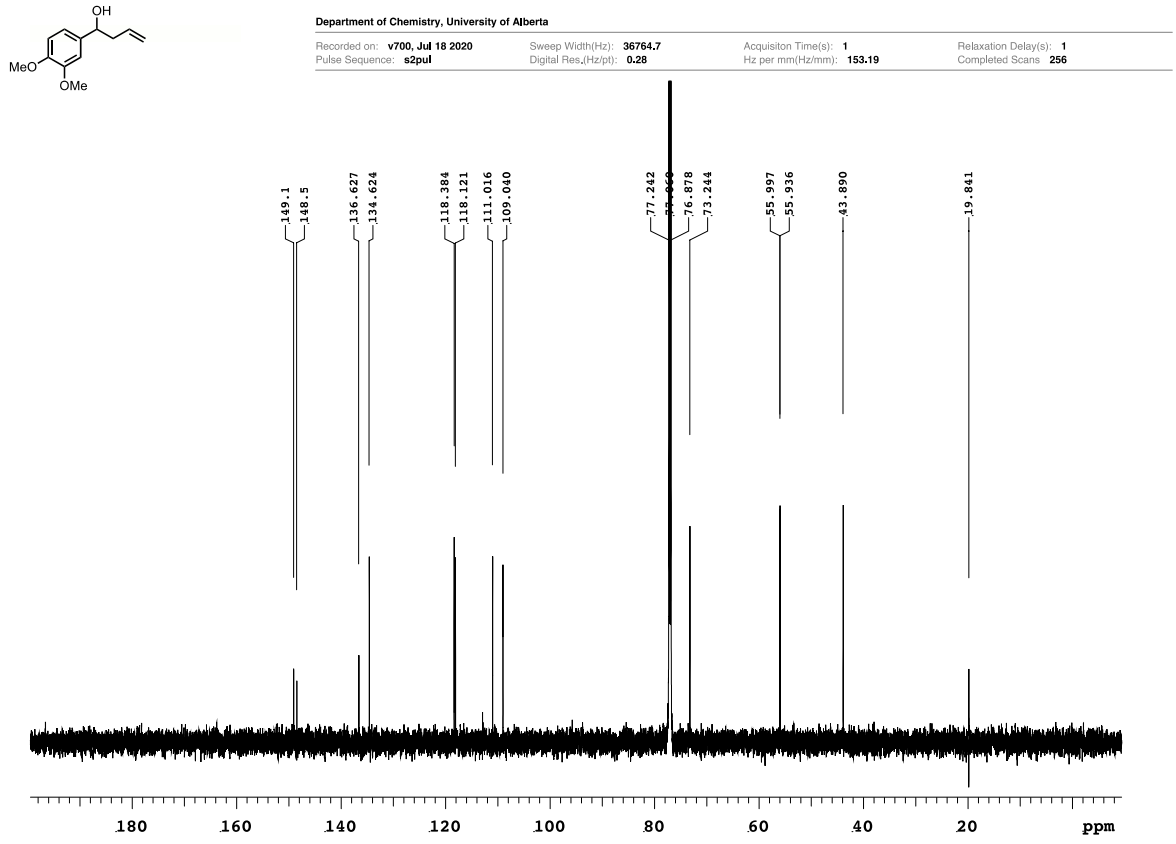

Figure S3: ^{1}H NMR spectrum of compound **2-1a** ($CDCl_3$, 500 MHz)

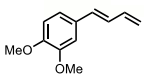

Recorded on: u500, Jul 3 2018	Sweep Width(Hz): 6009.62	Acquisiton Time(s): 5	Relaxation Delay(s): 0.1
Pulse Sequence: PRESAT	Digital Res.(Hz/pt): 0.09	Hz per mm(Hz/mm): 20.82	Completed Scans 8

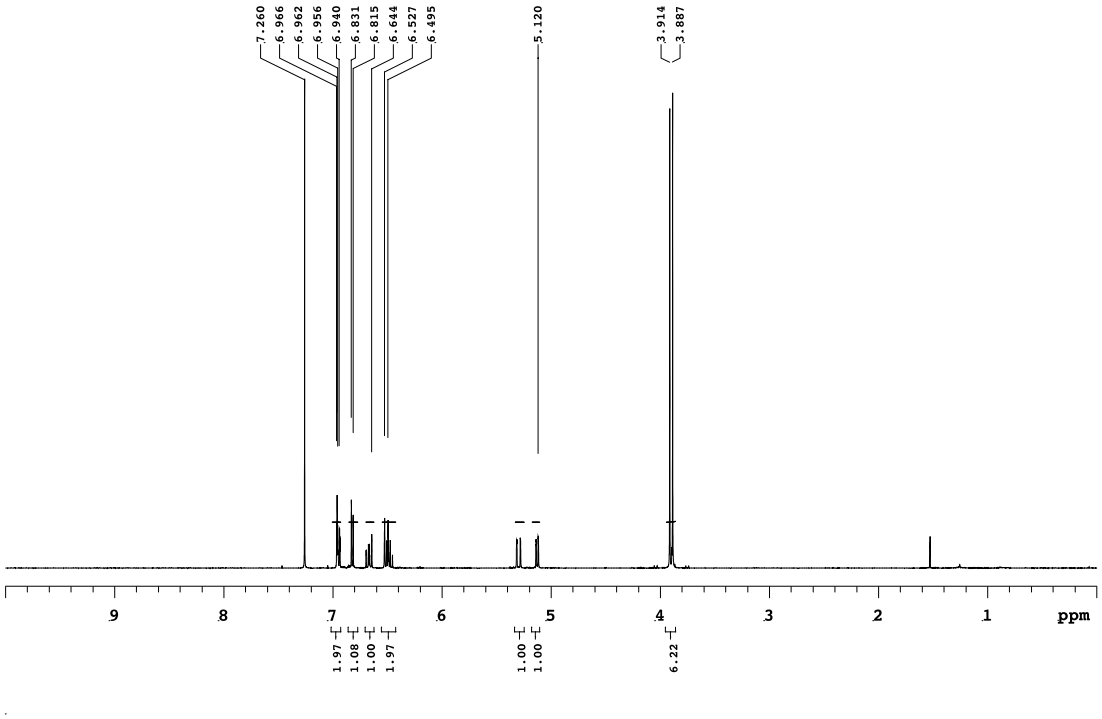

Figure S1: ^{13}C NMR spectrum of compound **2-1a** ($CDCl_3$, 126 MHz)

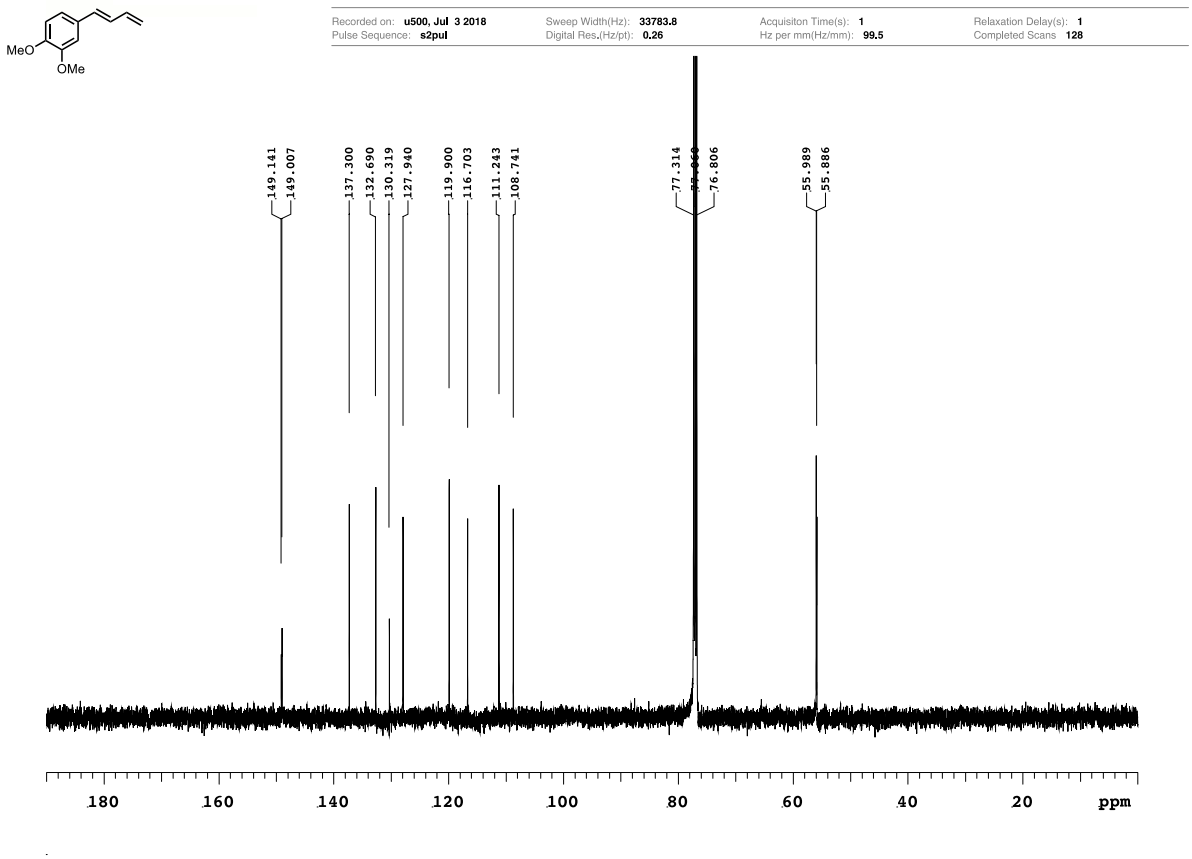

Figure S5: ^{1}H NMR spectrum of compound ***c*–BG** ($CDCl_3$, 700 MHz)

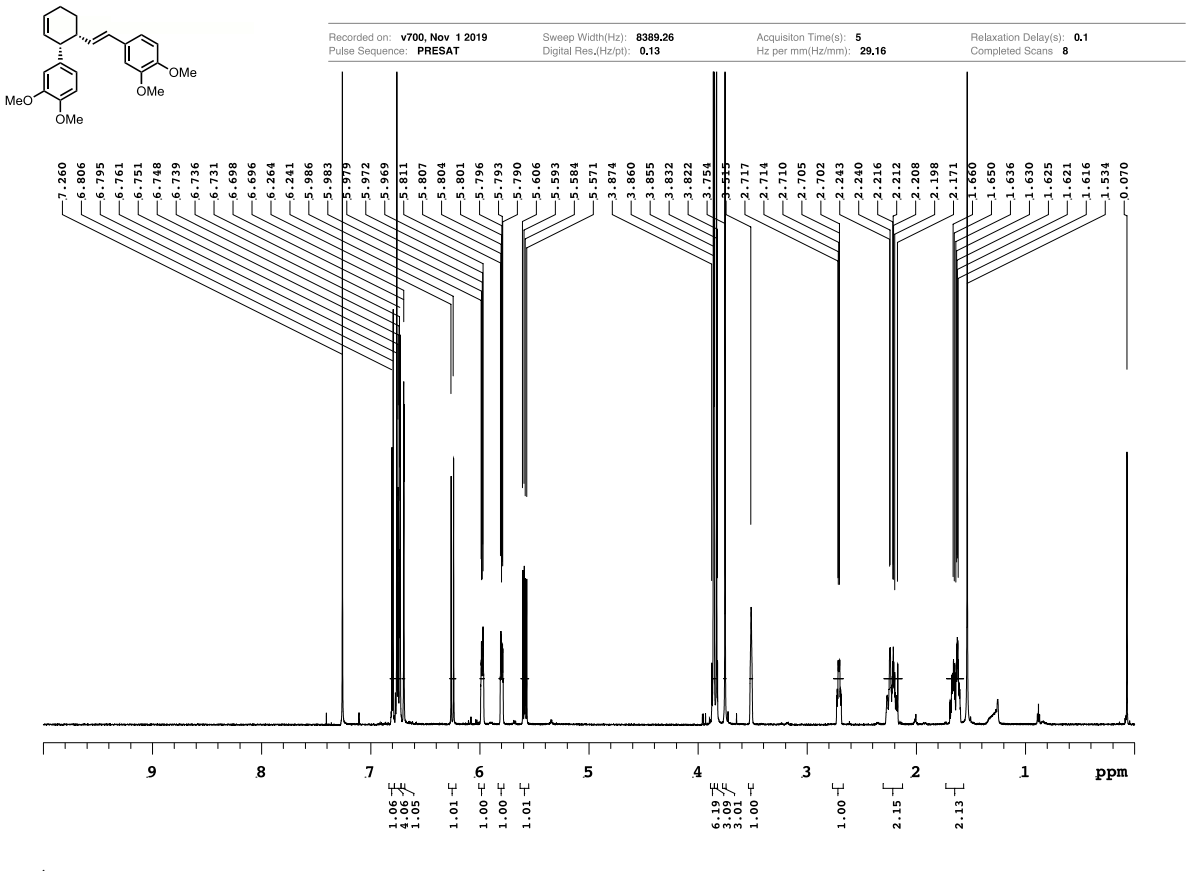

Figure S6: ^{1}H NMR magnified spectrum of compound ***c*–BG** ($CDCl_3$, 700 MHz)

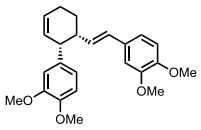

Recorded on: **v700, Nov 1 2019**	Sweep Width(Hz): **8389.26**	Acquisiton Time(s): **5**	Relaxation Delay(s): **0.1**
Pulse Sequence: **PRESAT**	Digital Res.(Hz/pt): **0.13**	Hz per mm(Hz/mm): **29.16**	Completed Scans **8**

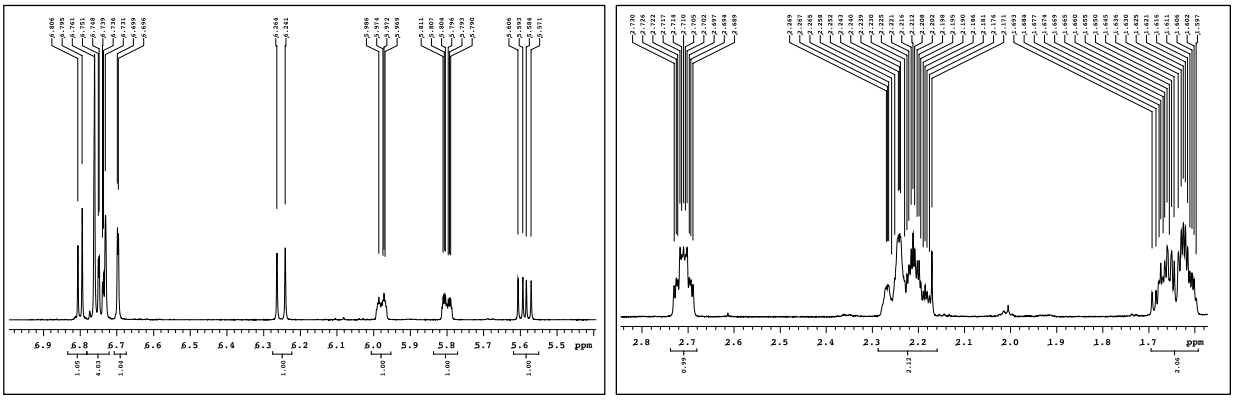

Figure S7: ^{13}C NMR spectrum of compound ***c*–BG** ($CDCl_3$, 176 MHz)

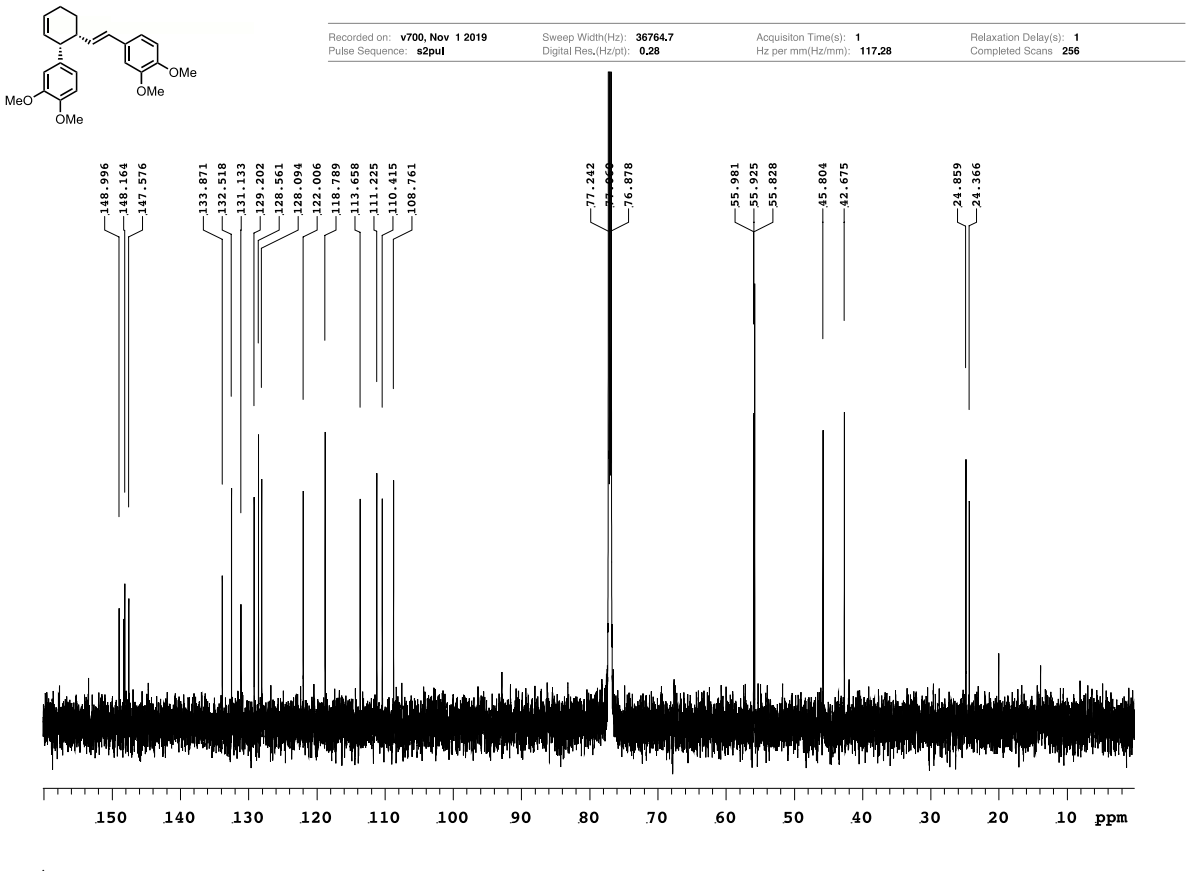

Figure S8: ^{1}H NMR spectrum of compound ***t*–BG** ($CDCl_3$, 700 MHz)

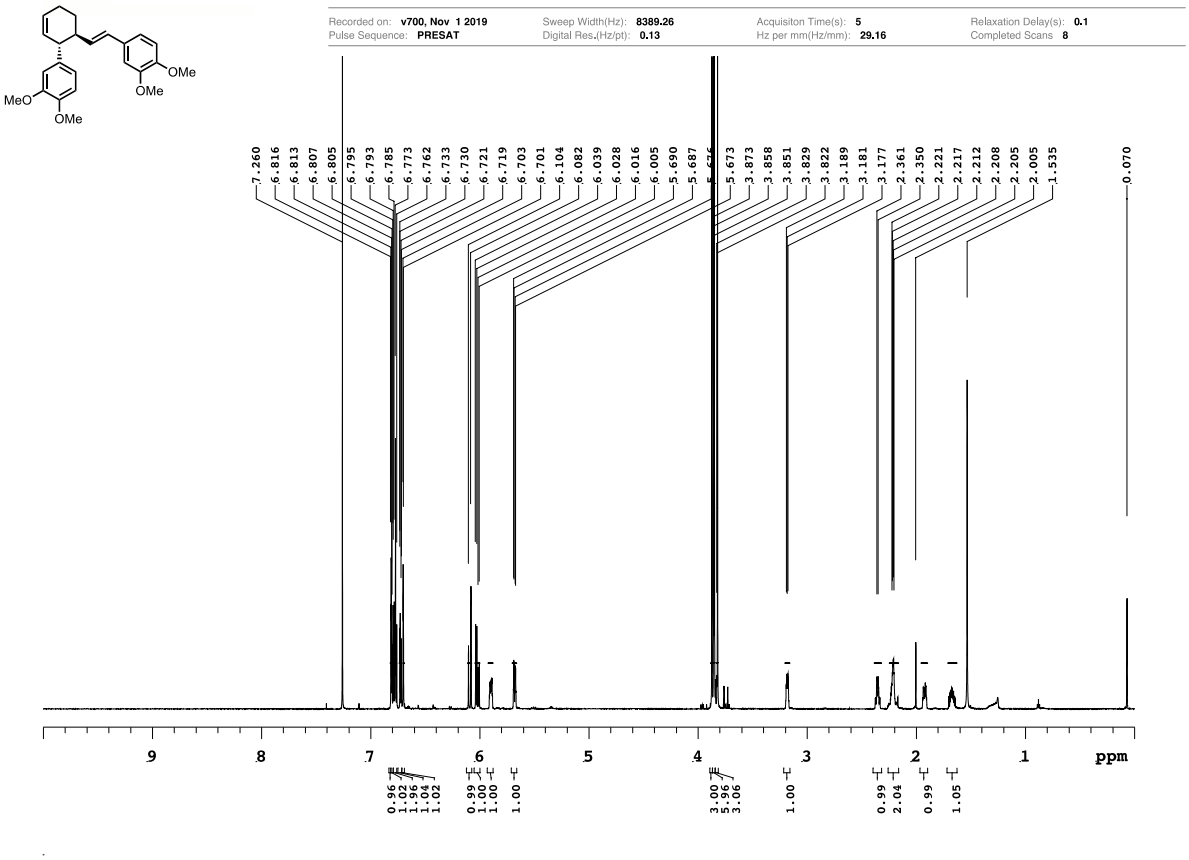

Figure S9: ^{1}H NMR magnified spectrum of compound ***t*–BG** ($CDCl_3$, 700 MHz)

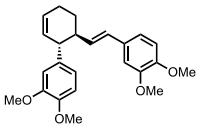

Recorded on: **v700, Nov 1 2019**	Sweep Width(Hz): **8389.26**	Acquisiton Time(s): **5**	Relaxation Delay(s): **0.1**
Pulse Sequence: **PRESAT**	Digital Res.(Hz/pt): **0.13**	Hz per mm(Hz/mm): **29.16**	Completed Scans **8**

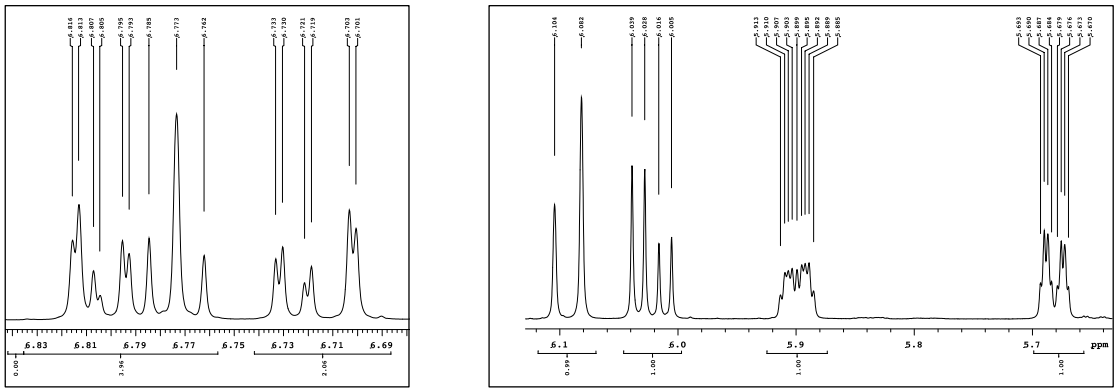

Figure S10: ^{1}H NMR magnified spectrum of compound ***t*–BG** ($CDCl_3$, 700 MHz)

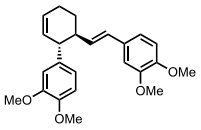

Recorded on: **v700, Nov 1 2019**	Sweep Width(Hz): **8389.26**	Acquisiton Time(s): **5**	Relaxation Delay(s): **0.1**
Pulse Sequence: **PRESAT**	Digital Res.(Hz/pt): **0.13**	Hz per mm(Hz/mm): **29.16**	Completed Scans **8**

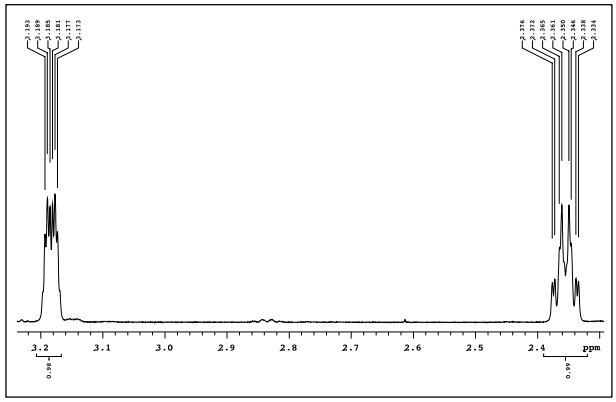

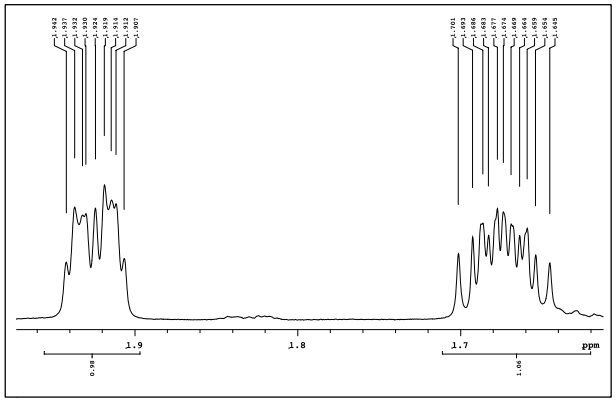

Figure S11: ^{13}C NMR spectrum of compound ***t*–BG** ($CDCl_3$, 176 MHz)

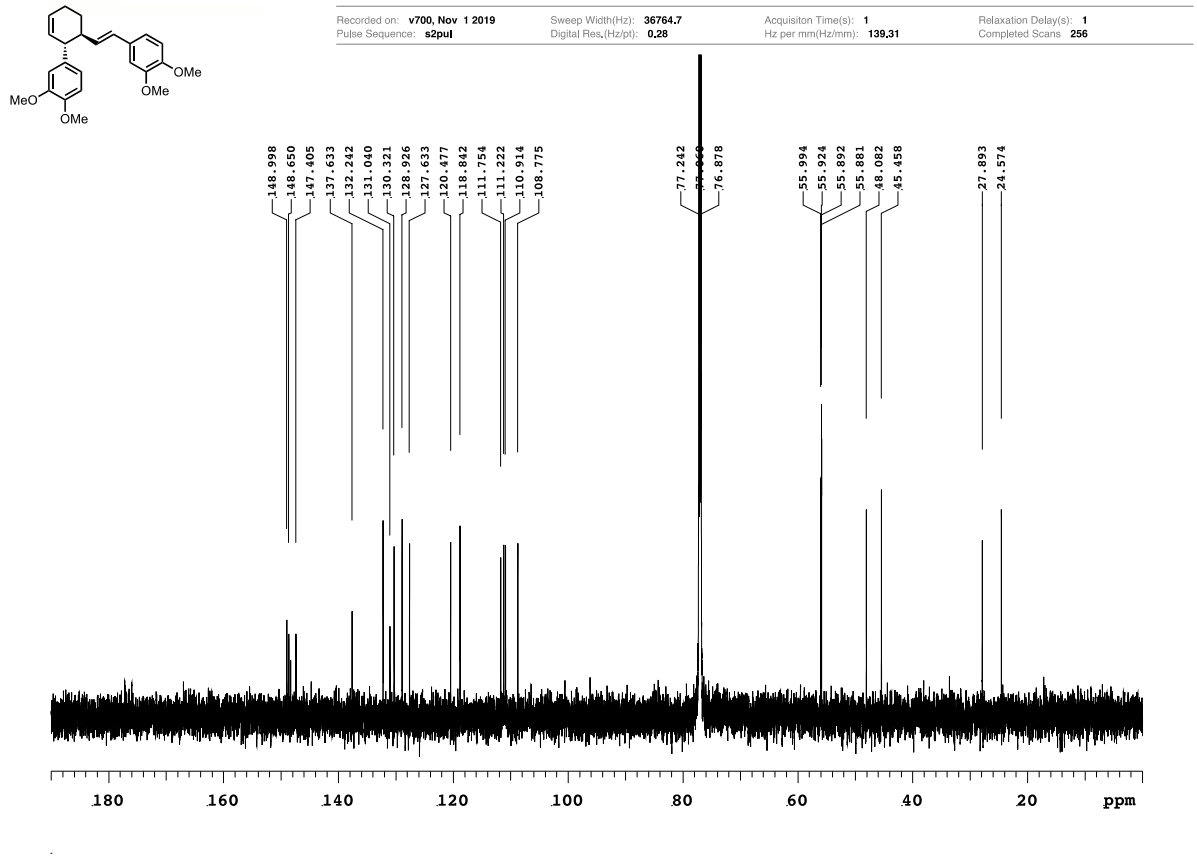

Figure S12: ^{1}H NMR spectrum of compound **2-20** ($CDCl_3$, 700 MHz)

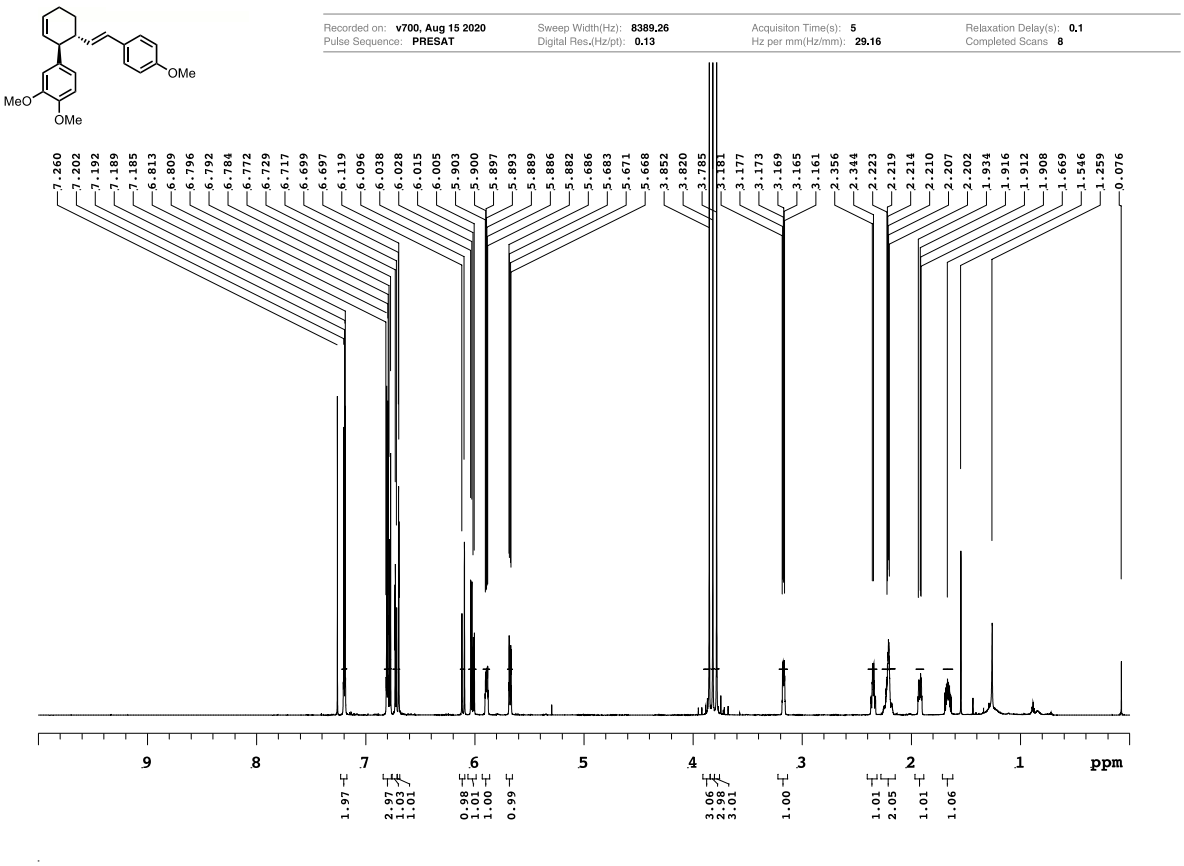

Figure S13: ^{13}C NMR spectrum of compound **2-20** ($CDCl_3$, 176 MHz)

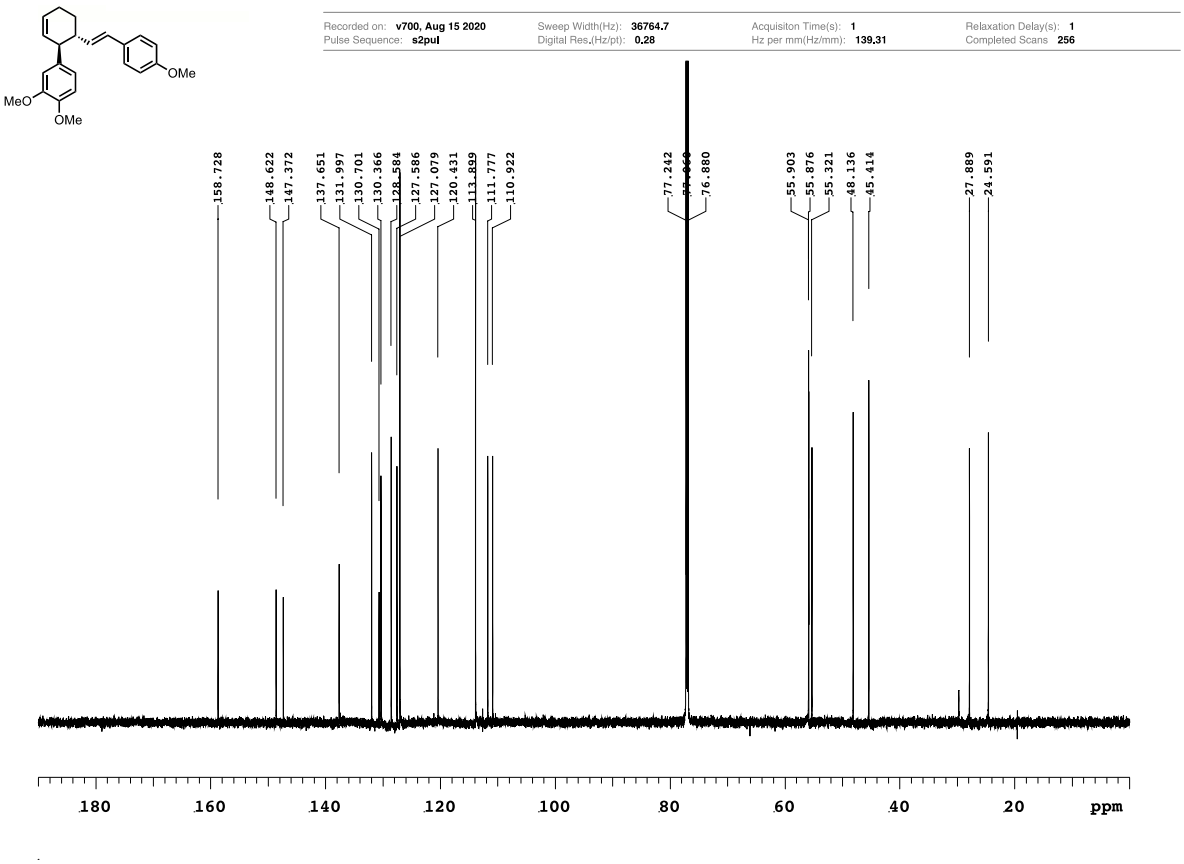

Figure S14: ^{1}H NMR spectrum of compound **2-23** ($CDCl_3$, 700 MHz)

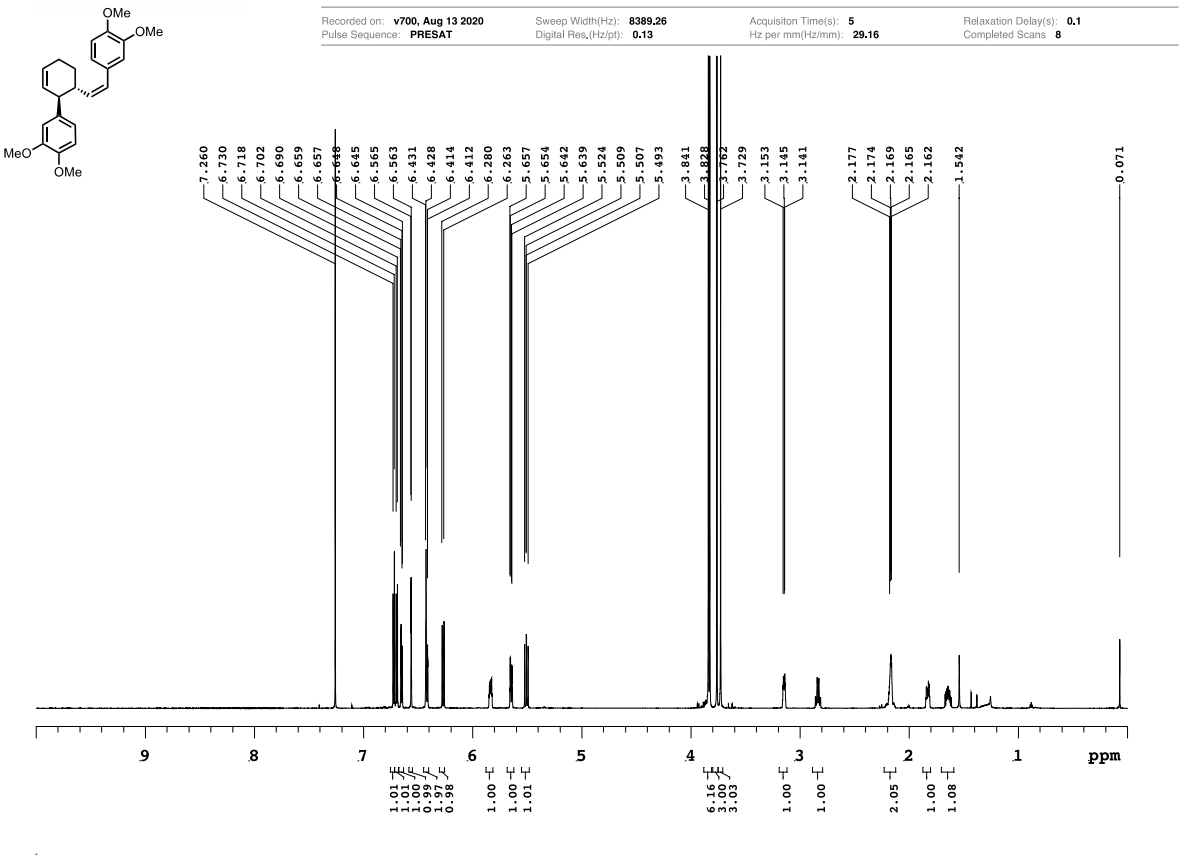

Figure S15: ^{1}H NMR magnified spectrum of compound **2-23** ($CDCl_3$, 700 MHz)

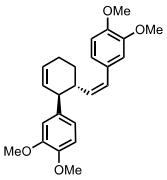

Recorded on: **v700, Aug 13 2020**	Sweep Width(Hz): **8389.26**	Acquisiton Time(s): **5**	Relaxation Delay(s): **0.1**
Pulse Sequence: **PRESAT**	Digital Res.(Hz/pt): **0.13**	Hz per mm(Hz/mm): **29.16**	Completed Scans **8**

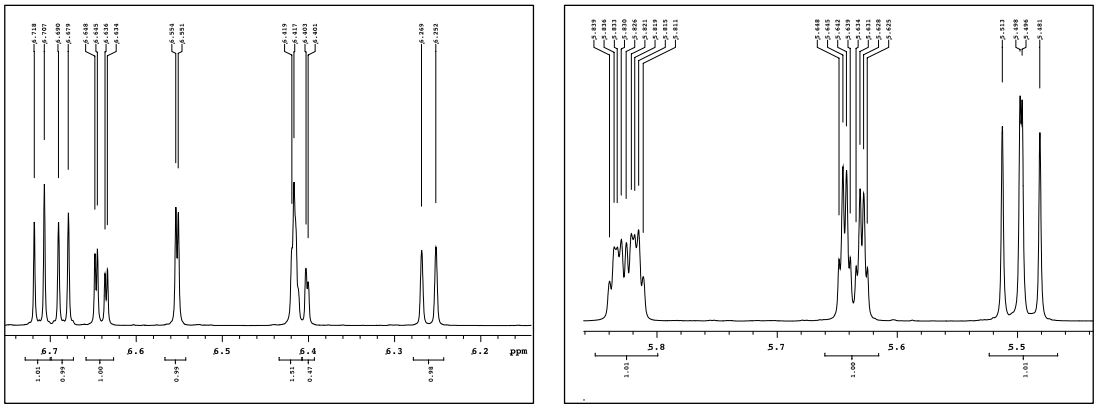

Figure S16: ^{1}H NMR magnified spectrum of compound **2-23** ($CDCl_3$, 700 MHz)

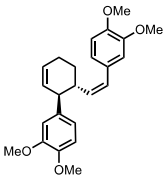

Recorded on: **v700, Aug 13 2020**	Sweep Width(Hz): **8389.26**	Acquisiton Time(s): **5**	Relaxation Delay(s): **0.1**
Pulse Sequence: **PRESAT**	Digital Res.(Hz/pt): **0.13**	Hz per mm(Hz/mm): **29.16**	Completed Scans **8**

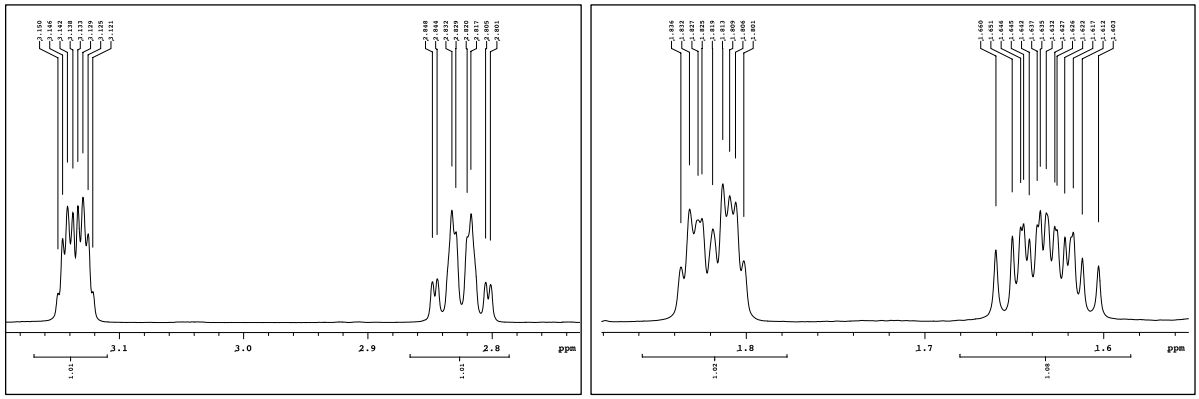

Figure S17: ^{13}C NMR spectrum of compound **2-23** ($CDCl_3$, 176 MHz)

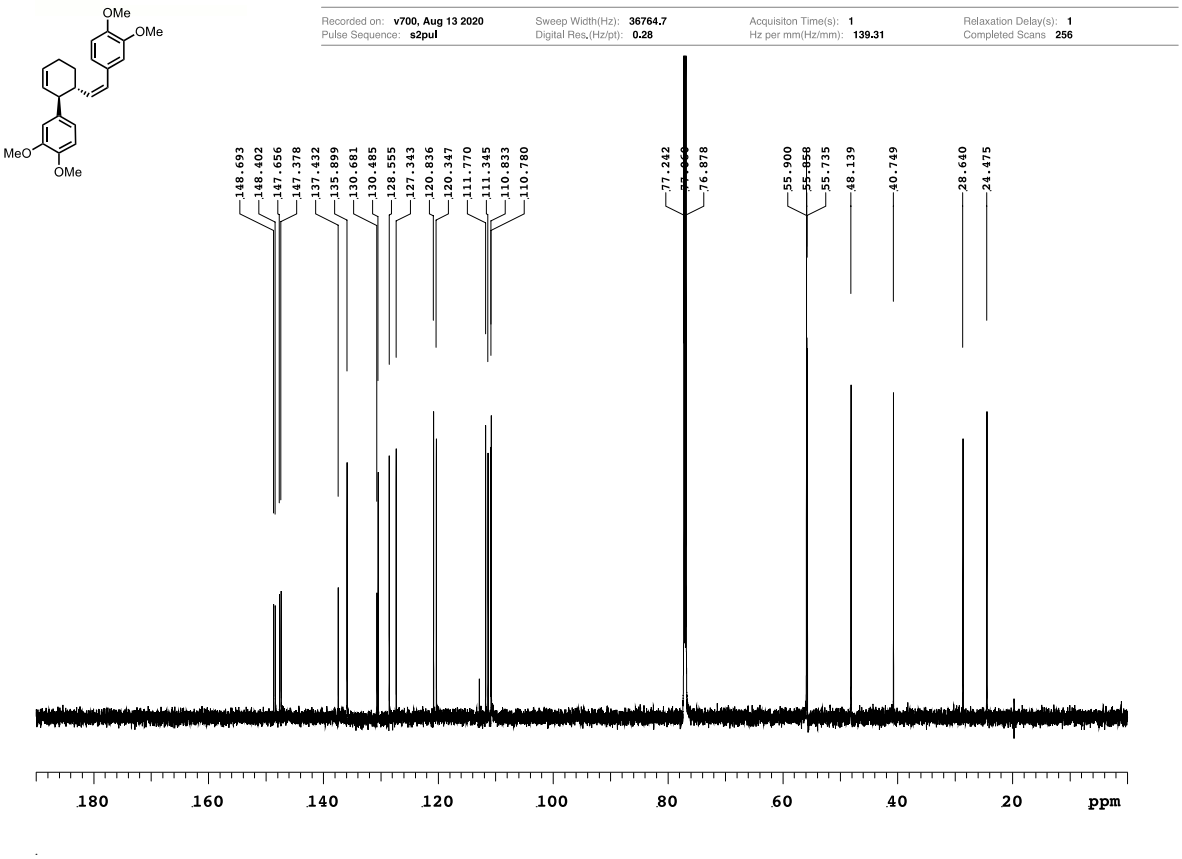

Figure S18: ^{1}H NMR spectrum of compound **2-36** ($CDCl_3$, 700 MHz)

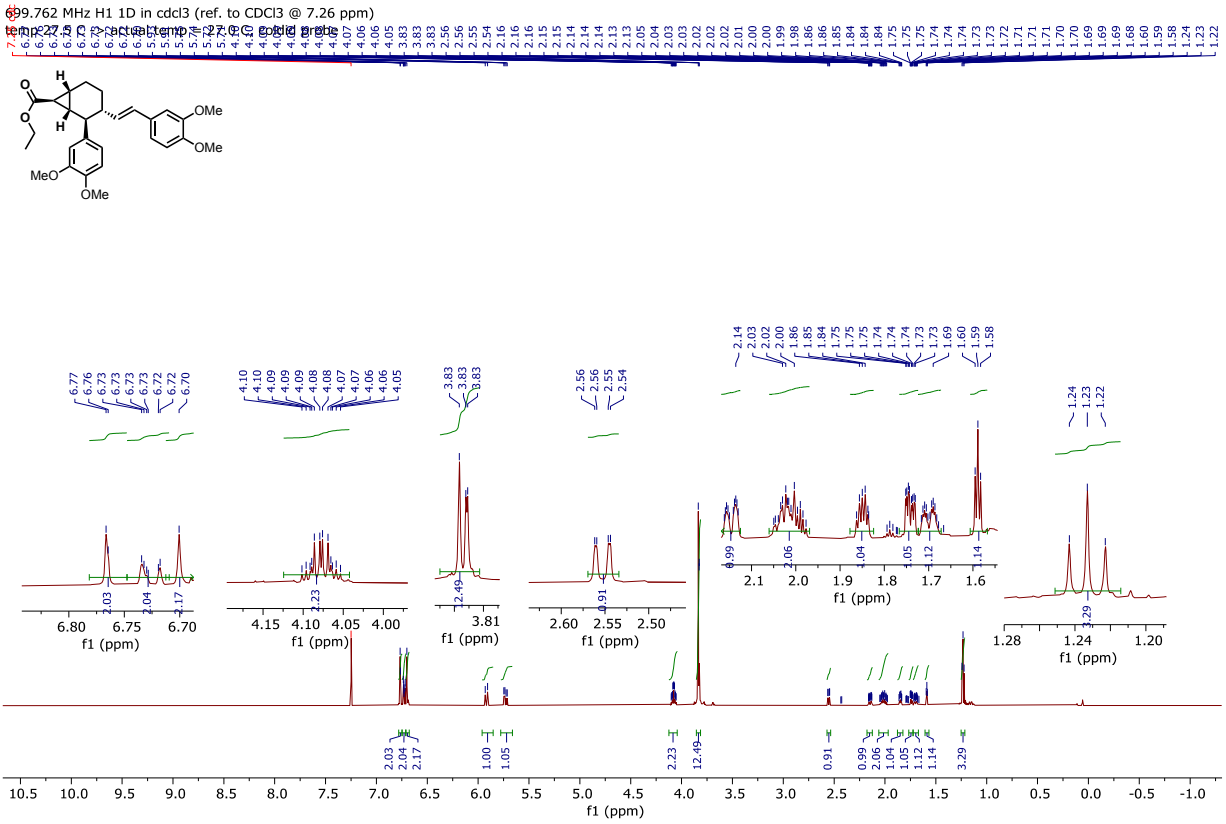

Figure S19: ^{13}C NMR spectrum of compound **2-36** ($CDCl_3$, 176 MHz)

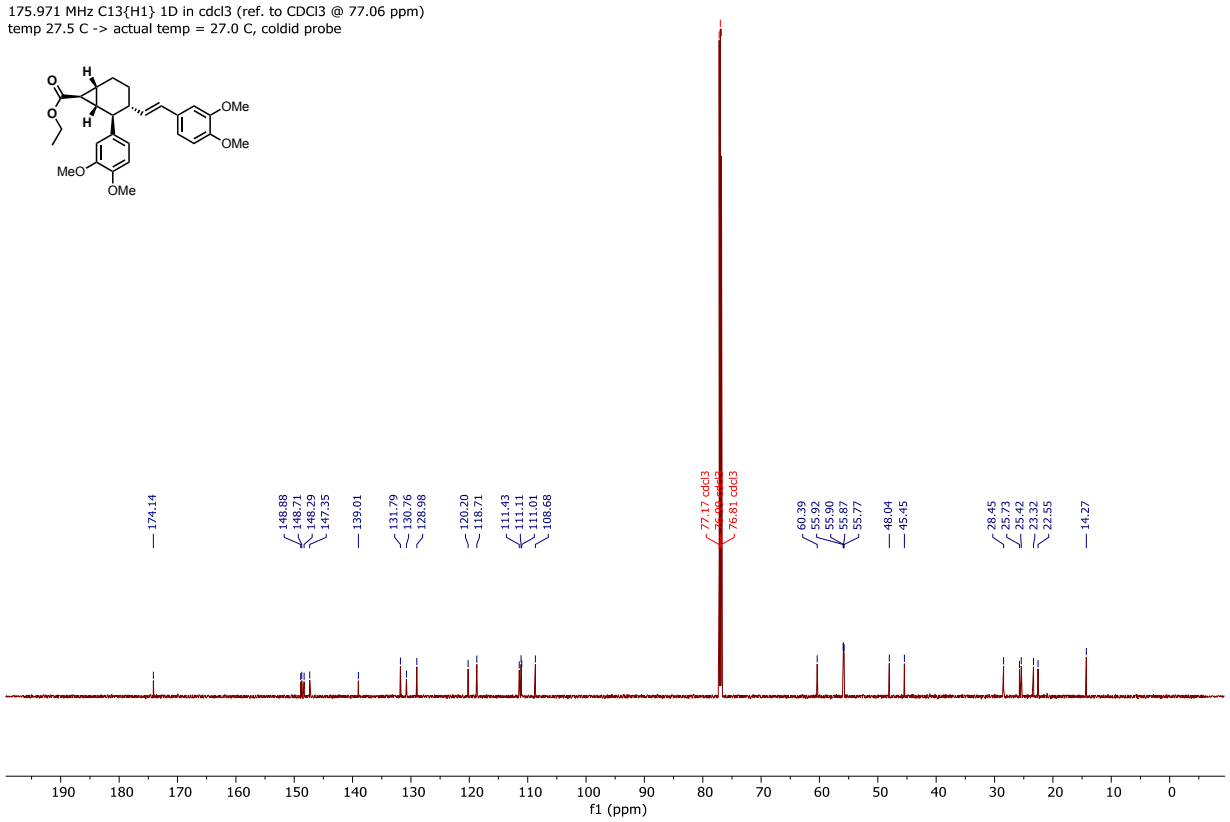

Appendix 2: Chromatograms for assessment of optical purity

Optical Purity Data

Enantiomeric excess (% ee) was determined by chiral HPLC analysis, with one of the following methods:

(a) 5% IPA: Hexane. Daicel CHIRALPAK IG column.

(b) 20% isopropanol/CO_2, 100 bar. Daicel CHIRALPAK AD-H column.

(c) 10% IPA: Hexane. Daicel CHIRALPAK IC column.

* *Absolute stereochemistry was assigned according to published data in* "Chu, J.; Suh, D.; Lee, G.; Han, A.; Chae, S.; Lee, H.; Seo, E.; Lim, H. Synthesis and Biological Activity of Optically Active Phenylbutenoid Dimers. J. Nat. Prod. 2011, 74 (8), 1817–1821."

2-18. 3(*S/R*)-(3,4-dimethoxyphenyl)-4(*R/S*)-[(*E*)-styryl]cyclohex-1-ene: (Method a)

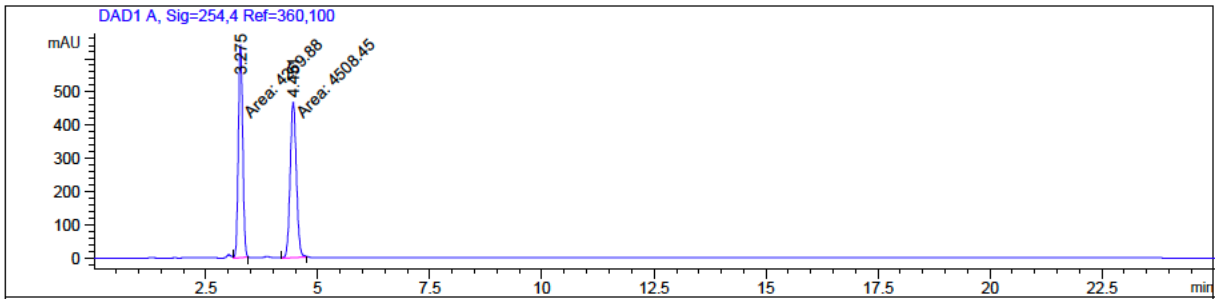

Signal 1: DAD1 A, Sig=254,4 Ref=360,100

Peak #	RetTime [min]	Type	Width [min]	Area [mAU*s]	Height [mAU]	Area %
1	3.275	MM	0.1110	4269.88037	640.98907	48.6412
2	4.451	MM	0.1608	4508.44580	467.26389	51.3588
Totals :				8778.32617	1108.25296	

(+) 2-18. 3(*S*)-(3,4-dimethoxyphenyl)-4(*R*)-[(*E*)-styryl]cyclohex-1-ene (99% ee): (Method a)

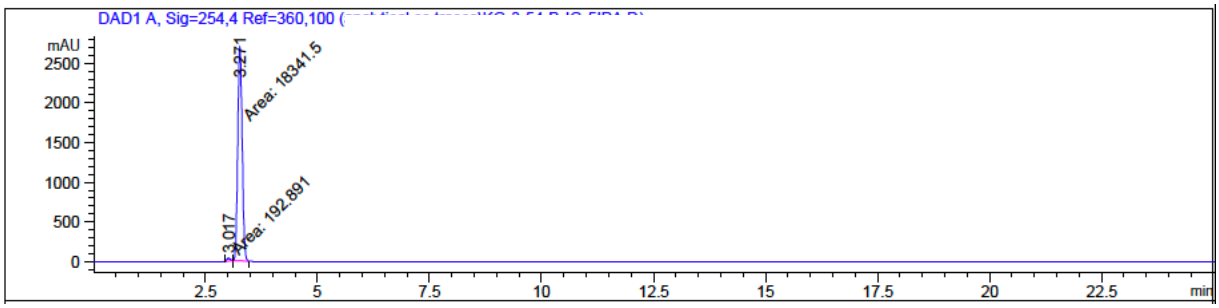

Signal 1: DAD1 A, Sig=254,4 Ref=360,100

Peak #	RetTime [min]	Type	Width [min]	Area [mAU*s]	Height [mAU]	Area %	Description
1	3.017	MM	0.0932	192.89052	34.49250	1.0407	Impurity (+)8
2	3.271	MM	0.1134	1.83415e4	2694.58887	98.9593	
Totals :				1.85344e4	2729.08137		

(–) 2-18. 3(*R*)-(3,4-dimethoxyphenyl)-4(*S*)-[(*E*)-styryl]cyclohex-1-ene (> 99% ee): (Method a)

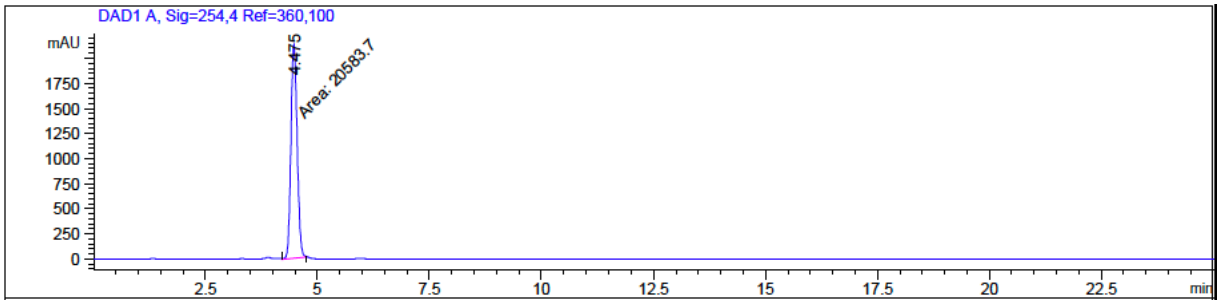

Signal 1: DAD1 A, Sig=254,4 Ref=360,100

Peak #	RetTime [min]	Type	Width [min]	Area [mAU*s]	Height [mAU]	Area %	Description
1	4.475	MM	0.1612	2.05837e4	2128.18555	100.0000	(–)8
Totals :				2.05837e4	2128.18555		

2-19. 3(*S/R*)-(3,4-dimethoxyphenyl)-4(*R/S*)-[(*E*)-3-methoxystyryl]cyclohex-1-ene: (Method a)

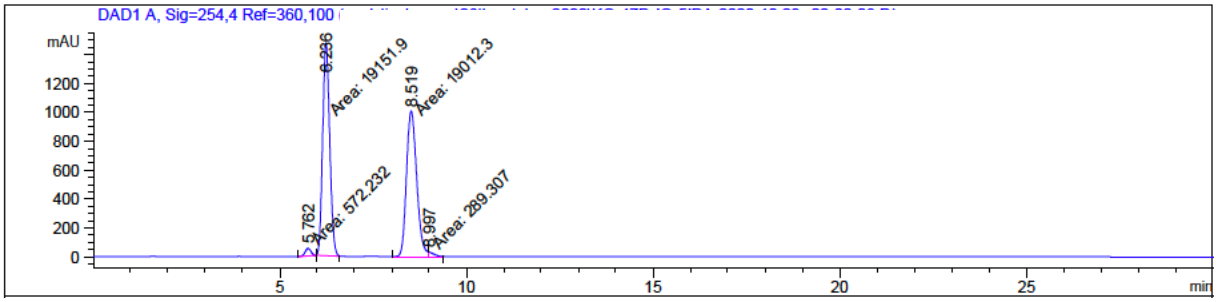

Signal 1: DAD1 A, Sig=254,4 Ref=360,100

Peak #	RetTime [min]	Type	Width [min]	Area [mAU*s]	Height [mAU]	Area %
1	5.762	MM	0.1832	572.23199	52.04971	1.4663
2	6.236	MM	0.2170	1.91519e4	1471.11340	49.0750
3	8.519	MF	0.3142	1.90123e4	1008.52759	48.7173
4	8.997	FM	0.1510	289.30722	31.94090	0.7413
Totals :				3.90258e4	2563.63160	

(+) 2-19. 3(*S*)-(3,4-dimethoxyphenyl)-4(*R*)-[(*E*)-3-methoxystyryl]cyclohex-1-ene(>99% ee): (Method a)

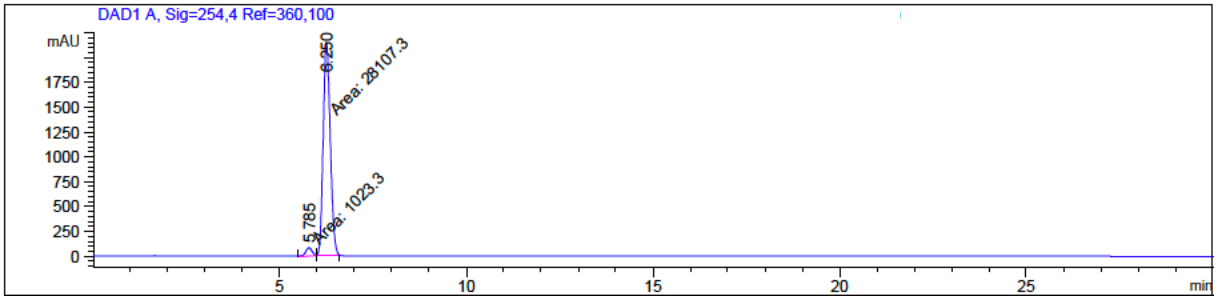

Signal 1: DAD1 A, Sig=254,4 Ref=360,100

Peak #	RetTime [min]	Type	Width [min]	Area [mAU*s]	Height [mAU]	Area %	Description
1	5.785	MM	0.2057	1023.30310	82.91499	3.5128	Impurity
2	6.250	MM	0.2190	2.81073e4	2139.51660	96.4872	(+)9
Totals :				2.91306e4	2222.43159		

(–) 2-19. 3(*R*)-(3,4-dimethoxyphenyl)-4(*S*)-[(*E*)-3-methoxystyryl]cyclohex-1-ene(>99% ee): (Method a)

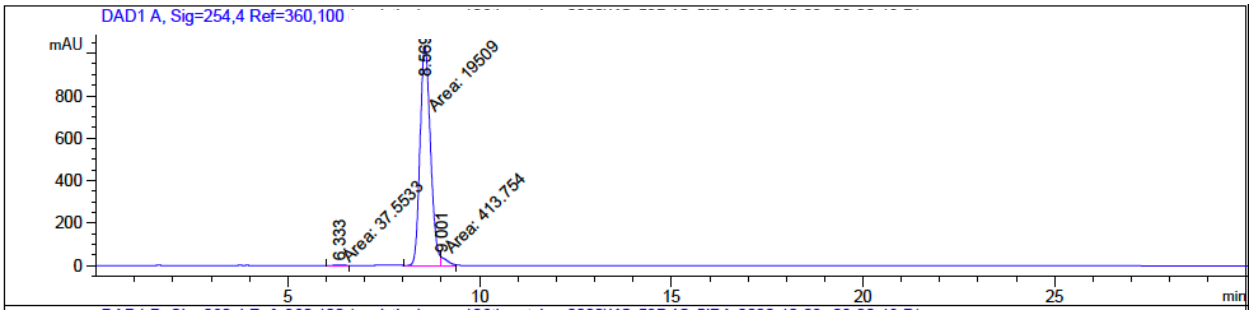

Signal 1: DAD1 A, Sig=254,4 Ref=360,100

Peak #	RetTime [min]	Type	Width [min]	Area [mAU*s]	Height [mAU]	Area %	Description
1	6.333	MM	0.2538	37.55331	2.46581	0.1881	(+)9
2	8.569	MF	0.3149	1.95090e4	1032.60400	97.7390	(–)9
3	9.001	FM	0.1763	413.75418	39.11983	2.0729	Impurity
Totals :				1.99603e4	1074.18965		

2-24. 3(*S/R*)-(3,4-dimethoxyphenyl)-4(*R/S*)-[(*Z*)-3-methoxystyryl]cyclohex-1-ene: (Method a)

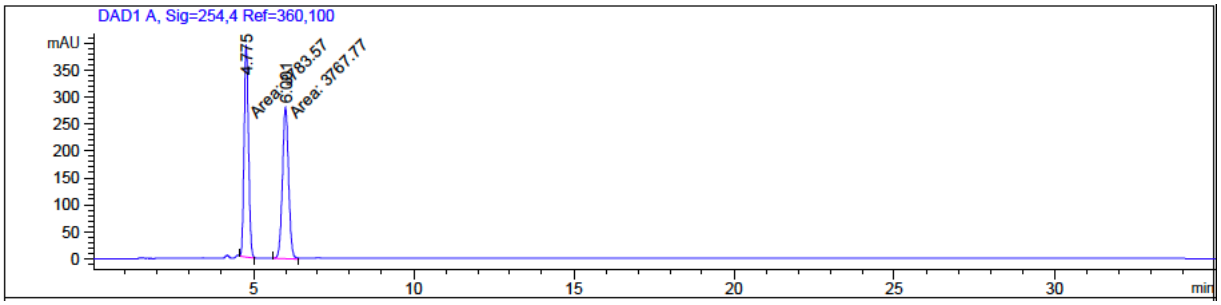

Signal 1: DAD1 A, Sig=254,4 Ref=360,100

Peak #	RetTime [min]	Type	Width [min]	Area [mAU*s]	Height [mAU]	Area %
1	4.775	MM	0.1600	3783.56592	394.04947	50.1046
2	6.001	MM	0.2238	3767.76880	280.64569	49.8954
Totals :				7551.33472	674.69516	

(+) 2-24. 3(*S*)-(3,4-dimethoxyphenyl)-4(*R*)-[(*Z*)-3-methoxystyryl]cyclohex-1-ene (>99% ee): (Method a)

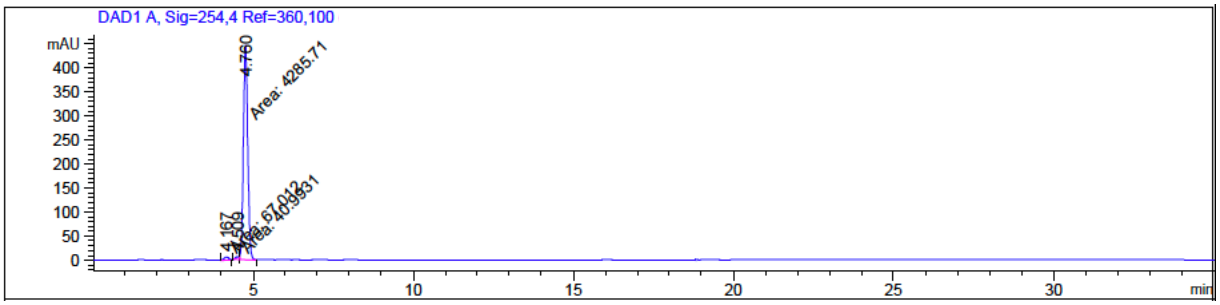

Signal 1: DAD1 A, Sig=254,4 Ref=360,100

Peak #	RetTime [min]	Type	Width [min]	Area [mAU*s]	Height [mAU]	Area %	Description
1	4.167	MM	0.1578	67.01202	7.07963	1.5252	Impurity
2	4.509	MF	0.1259	40.99306	5.42767	0.9330	Impurity
3	4.760	FM	0.1605	4285.70508	444.97592	97.5418	(+)14
Totals :				4393.71016	457.48322		

(–) 2-24. 3(*R*)-(3,4-dimethoxyphenyl)-4(*S*)-[(*Z*)-3-methoxystyryl]cyclohex-1-ene (>99% ee): (Method a)

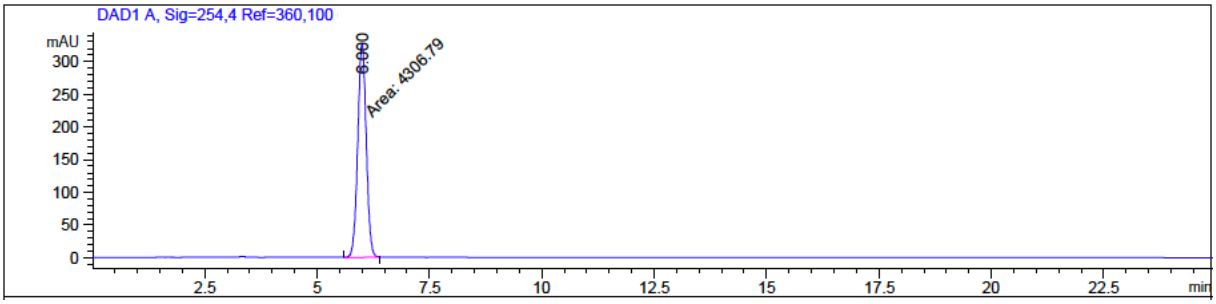

Signal 1: DAD1 A, Sig=254,4 Ref=360,100

Peak #	RetTime [min]	Type	Width [min]	Area [mAU*s]	Height [mAU]	Area %	Description
1	6.000	MM	0.2197	4306.78857	326.78674	100.0000	(–)14
Totals :				4306.78857	326.78674		

2-20. 3(*S/R*)-(3,4-dimethoxyphenyl)-4(*R/S*)-[(*E*)-4-methoxystyryl]cyclohex-1-ene: (Method a)

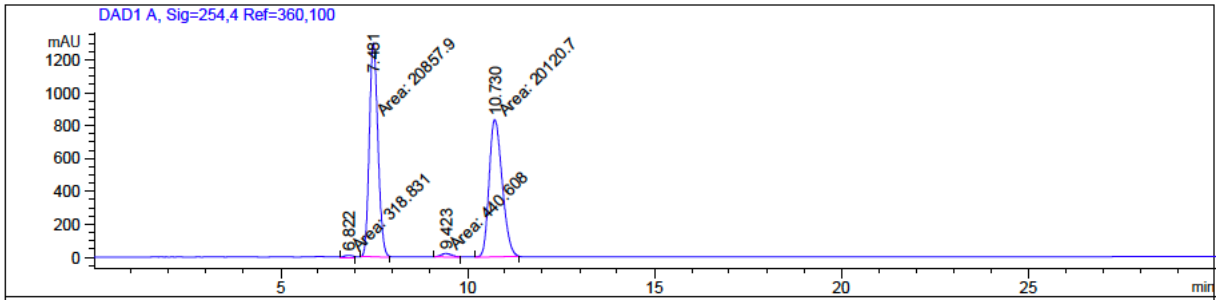

Signal 1: DAD1 A, Sig=254,4 Ref=360,100

Peak #	RetTime [min]	Type	Width [min]	Area [mAU*s]	Height [mAU]	Area %
1	6.822	MM	0.2920	318.83115	18.19932	0.7639
2	7.481	MM	0.2679	2.08579e4	1297.71582	49.9733
3	9.423	MM	0.3424	440.60825	21.44956	1.0557
4	10.730	MM	0.4021	2.01207e4	833.89203	48.2072
Totals :				4.17381e4	2171.25673	

(+) 2-20. 3(*S*)-(3,4-dimethoxyphenyl)-4(*R*)-[(*E*)-4-methoxystyryl]cyclohex-1-ene (>99% ee): (Method a)

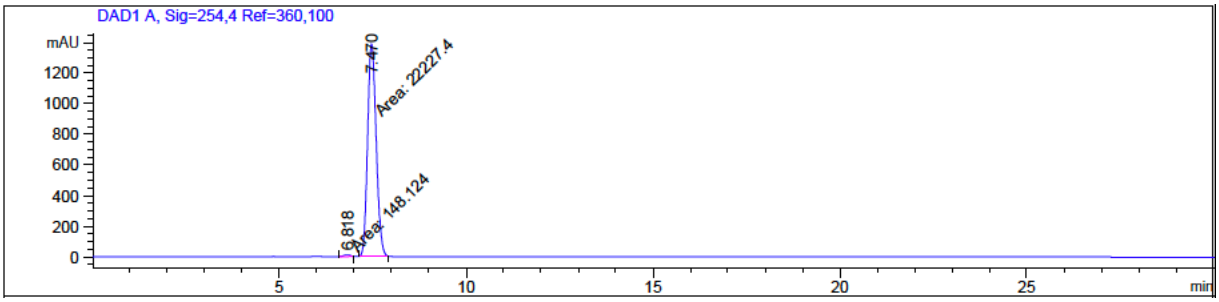

Signal 1: DAD1 A, Sig=254,4 Ref=360,100

Peak #	RetTime [min]	Type	Width [min]	Area [mAU*s]	Height [mAU]	Area %	Description
1	6.818	MM	0.2138	148.12431	11.54741	0.6620	Impurity
2	7.470	MM	0.2671	2.22274e4	1386.85339	99.3380	(+)10
Totals :				2.23755e4	1398.40080		

(–) 2-20. 3(*R*)-(3,4-dimethoxyphenyl)-4(*S*)-[(*E*)-4-methoxystyryl]cyclohex-1-ene (99% ee): (Method a)

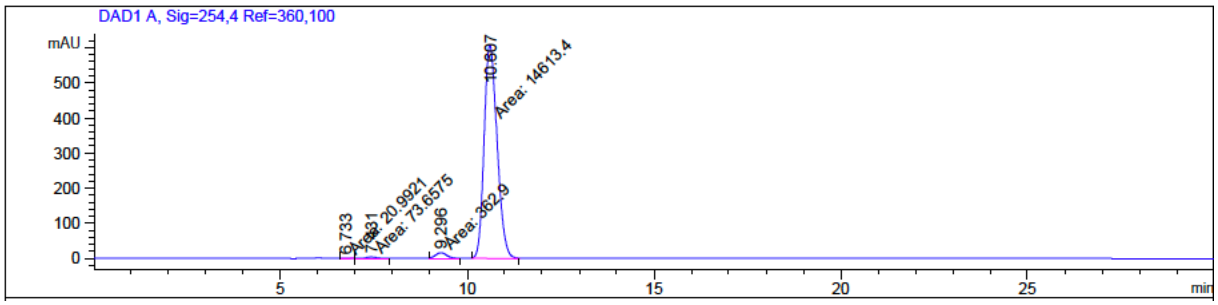

Signal 1: DAD1 A, Sig=254,4 Ref=360,100

Peak #	RetTime [min]	Type	Width [min]	Area [mAU*s]	Height [mAU]	Area %	Description
1	6.733	MM	0.2292	20.99214	1.10117	0.1393	Impurity
2	7.431	MM	0.3088	73.65749	3.97611	0.4887	(+)10
3	9.296	MM	0.3646	362.90045	16.59074	2.4080	Impurity
4	10.607	MM	0.4010	1.46134e4	607.34192	96.9640	(–)10
Totals :				1.50709e4	629.00994		

2-25. 3(*S/R*)-(3,4-dimethoxyphenyl)-4(*R/S*)-[(*Z*)-4-methoxystyryl]cyclohex-1-ene: (Method a)

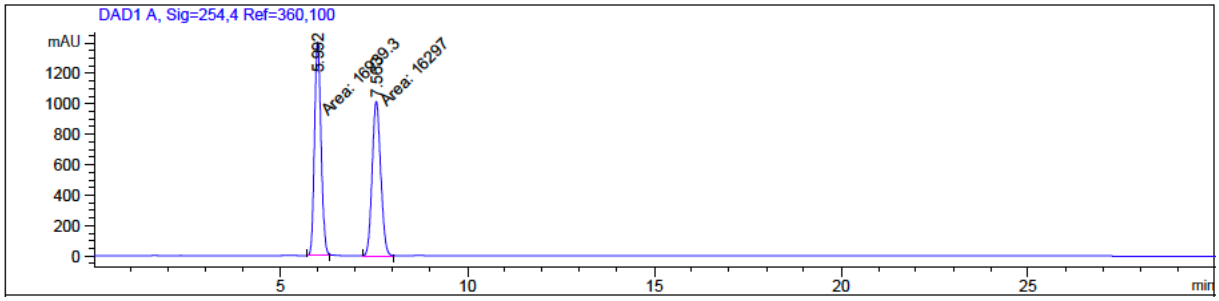

Signal 1: DAD1 A, Sig=254,4 Ref=360,100

Peak #	RetTime [min]	Type	Width [min]	Area [mAU*s]	Height [mAU]	Area %
1	5.992	MM	0.2023	1.69393e4	1395.22888	50.9662
2	7.563	MM	0.2668	1.62970e4	1017.92480	49.0338
Totals :				3.32363e4	2413.15369	

(+) 2-25. 3(*S*)-(3,4-dimethoxyphenyl)-4(*R*)-[(*Z*)-4-methoxystyryl]cyclohex-1-ene (98% ee): (Method a)

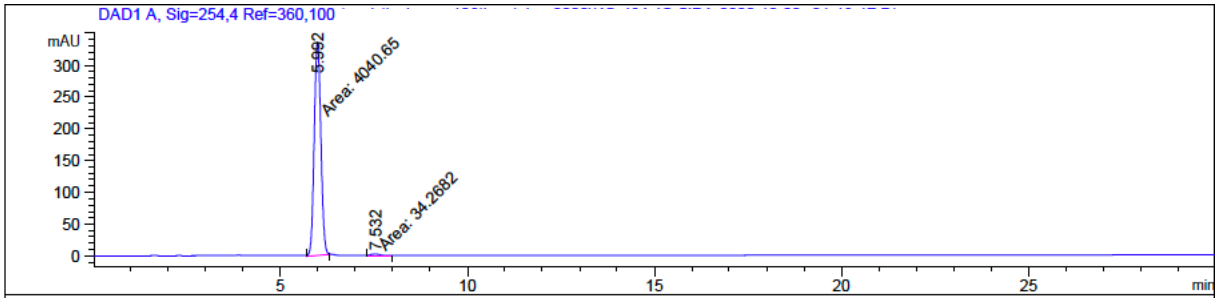

Signal 1: DAD1 A, Sig=254,4 Ref=360,100

Peak #	RetTime [min]	Type	Width [min]	Area [mAU*s]	Height [mAU]	Area %	Description
1	5.992	MM	0.2014	4040.65259	334.44958	99.1590	(–)15
2	7.532	MM	0.2558	34.26825	2.23308	0.8410	(+)15
Totals :				4074.92084	336.68266		

(–) 2-25. 3(*R*)-(3,4-dimethoxyphenyl)-4(*S*)-[(*Z*)-4-methoxystyryl]cyclohex-1-ene (99% ee): (Method a)

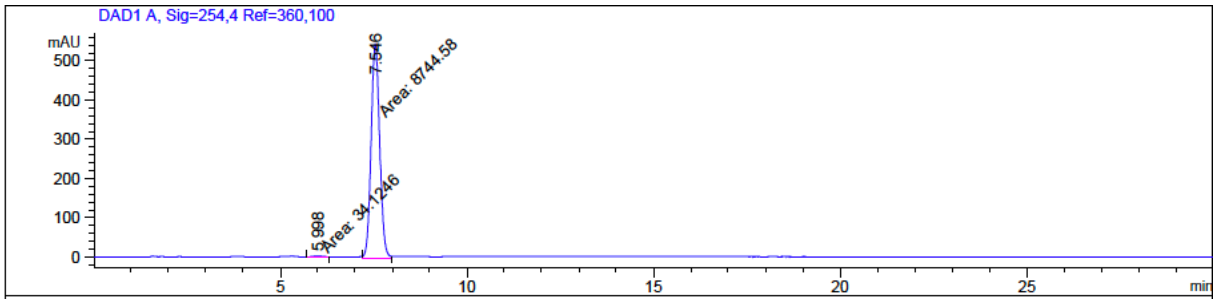

Signal 1: DAD1 A, Sig=254,4 Ref=360,100

Peak #	RetTime [min]	Type	Width [min]	Area [mAU*s]	Height [mAU]	Area %	Description
1	5.998	MM	0.2191	34.12463	2.59597	0.3887	(–)15
2	7.546	MM	0.2669	8744.57520	546.10803	99.6113	(+)15
Totals :				8778.69983	548.70400		

2-21. 3(*S/R*)-(3,4-dimethoxyphenyl)-4(*R/S*)-[(*E*)-2-methylstyryl]cyclohex-1-ene: (Method a)

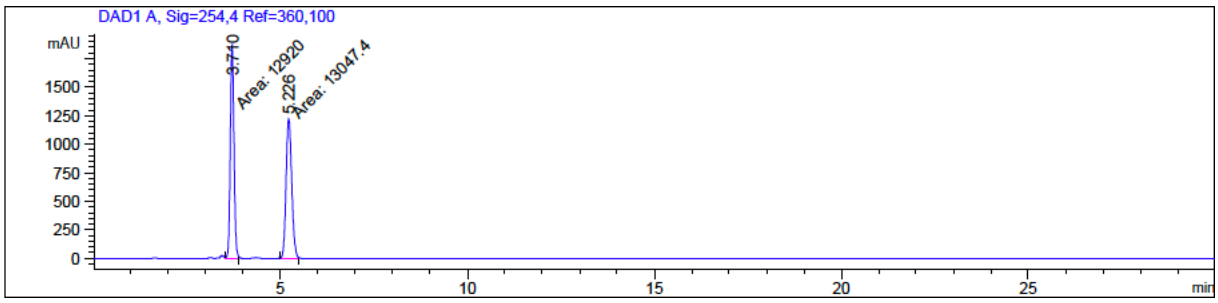

Signal 1: DAD1 A, Sig=254,4 Ref=360,100

Peak #	RetTime [min]	Type	Width [min]	Area [mAU*s]	Height [mAU]	Area %
1	3.710	MM	0.1154	1.29200e4	1865.38831	49.7547
2	5.226	MM	0.1773	1.30474e4	1226.50244	50.2453
Totals :				2.59673e4	3091.89075	

(+) 2-21. 3(*S*)-(3,4-dimethoxyphenyl)-4(*R*)-[(*E*)-2-methylstyryl]cyclohex-1-ene (98%ee): (Method a)

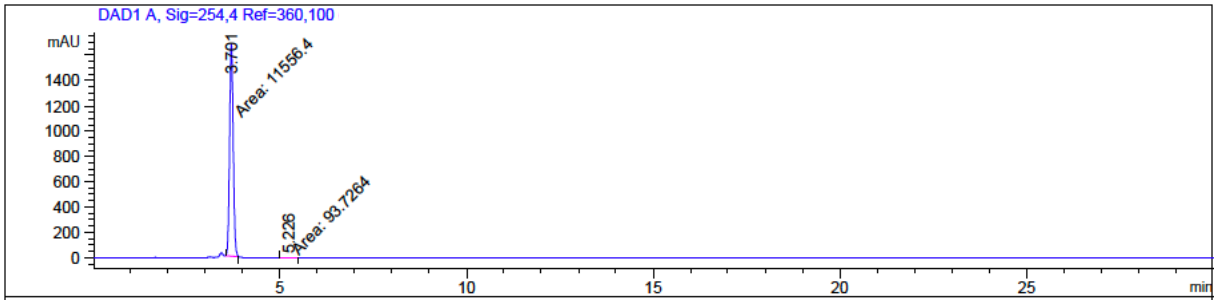

Signal 1: DAD1 A, Sig=254,4 Ref=360,100

Peak #	RetTime [min]	Type	Width [min]	Area [mAU*s]	Height [mAU]	Area %	Description
1	3.701	MM	0.1144	1.15564e4	1684.34827	99.1955	(+)11
2	5.226	MM	0.4766	93.72644	3.27791	0.8045	(–)11
Totals :				1.16501e4	1687.62618		

(–) 2-21. 3(*R*)-(3,4-dimethoxyphenyl)-4(*S*)-[(*E*)-2-methylstyryl]cyclohex-1-ene (99%ee): (Method a)

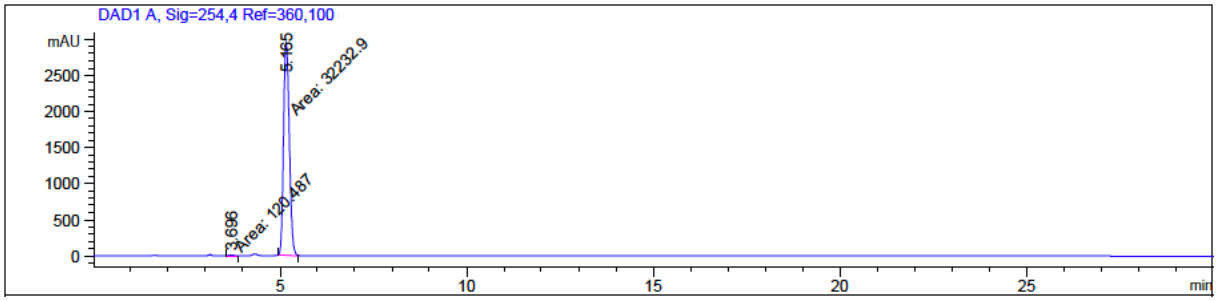

Signal 1: DAD1 A, Sig=254,4 Ref=360,100

Peak #	RetTime [min]	Type	Width [min]	Area [mAU*s]	Height [mAU]	Area %	Description
1	3.696	MM	0.1361	120.48663	14.74946	0.3724	(+)11
2	5.165	MM	0.1827	3.22329e4	2940.39087	99.6276	(–)11
Totals :				3.23534e4	2955.14033		

2-26. 3(*S/R*)-(3,4-dimethoxyphenyl)-4(*R/S*)-[(*Z*)-2-methylstyryl]cyclohex-1-ene: (Method a)

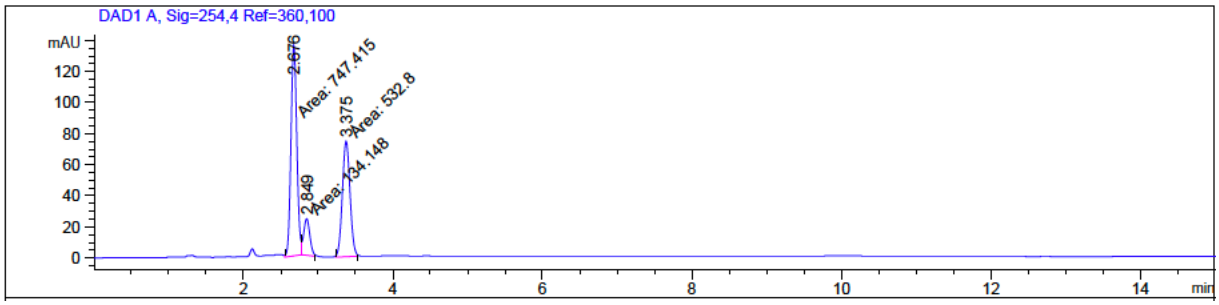

Signal 1: DAD1 A, Sig=254,4 Ref=360,100

Peak #	RetTime [min]	Type	Width [min]	Area [mAU*s]	Height [mAU]	Area %
1	2.676	MM	0.0916	747.41486	135.98724	52.8446
2	2.849	MM	0.0947	134.14784	23.60262	9.4847
3	3.375	MM	0.1194	532.80042	74.35267	37.6707
Totals :				1414.36311	233.94253	

(+) 2-26. 3(*S*)-(3,4-dimethoxyphenyl)-4(*R*)-[(*Z*)-2-methylstyryl]cyclohex-1-ene (99% ee): (Method a)

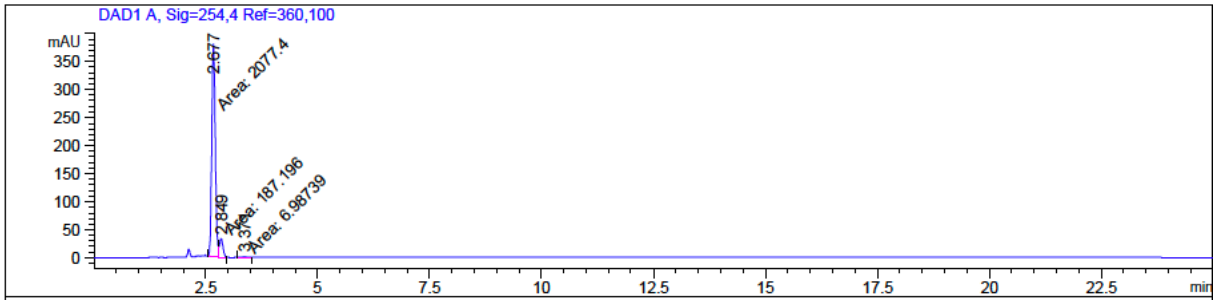

Signal 1: DAD1 A, Sig=254,4 Ref=360,100

Peak #	RetTime [min]	Type	Width [min]	Area [mAU*s]	Height [mAU]	Area %	Description
1	2.677	MM	0.0911	2077.39697	380.17612	91.4516	(+)16
2	2.849	MM	0.0947	187.19553	32.93308	8.2408	impurity
3	3.371	MM	0.1600	6.98739	7.27885e-1	0.3076	(–)16
Totals :				2271.57989	413.83708		

(–) 2-26. 3(*R*)-(3,4-dimethoxyphenyl)-4(*S*)-[(*Z*)-2-methylstyryl]cyclohex-1-ene (99% ee): (Method a)

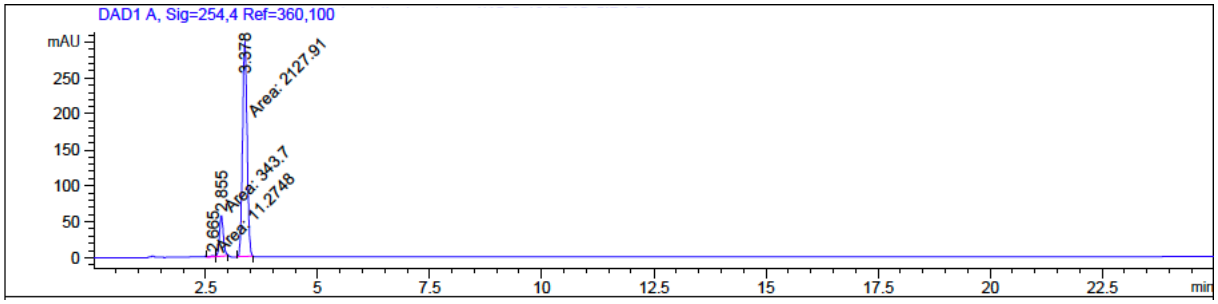

Signal 1: DAD1 A, Sig=254,4 Ref=360,100

Peak #	RetTime [min]	Type	Width [min]	Area [mAU*s]	Height [mAU]	Area %	Description
1	2.665	MM	0.1076	11.27477	1.74601	0.4541	(+)16
2	2.855	MM	0.1014	343.70029	56.51110	13.8428	impurity
3	3.378	MM	0.1196	2127.91309	296.63055	85.7031	(–)16
Totals :				2482.88815	354.88767		

2-22. 3(*S/R*)-(3,4-dimethoxyphenyl)-4(*R/S*)-[(*E*)-2-bromostyryl]cyclohex-1-ene: (Method a)

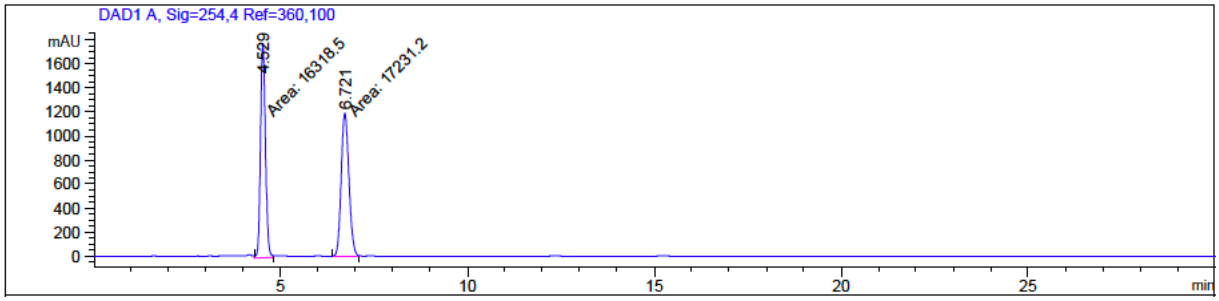

Signal 1: DAD1 A, Sig=254,4 Ref=360,100

Peak #	RetTime [min]	Type	Width [min]	Area [mAU*s]	Height [mAU]	Area %
1	4.529	MM	0.1522	1.63185e4	1787.35388	48.6397
2	6.721	MM	0.2411	1.72312e4	1191.35974	51.3603
Totals :				3.35496e4	2978.71362	

(+) 2-22. 3(*S*)-(3,4-dimethoxyphenyl)-4(*R*)-[(*E*)-2-bromostyryl]cyclohex-1-ene (>99% ee): (Method a)

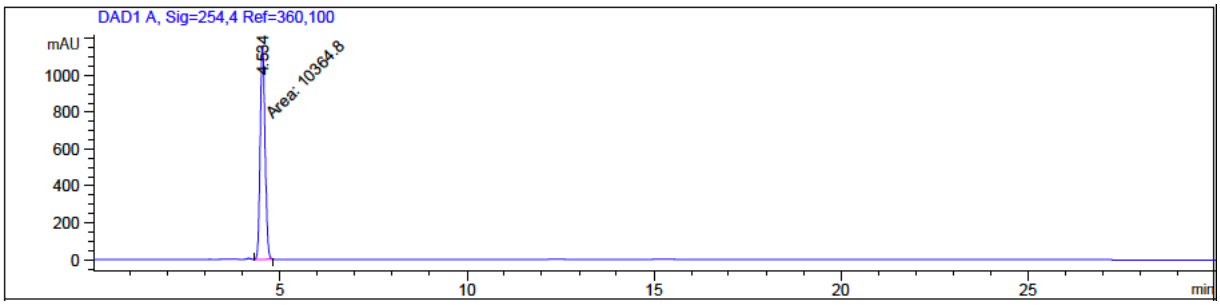

Signal 1: DAD1 A, Sig=254,4 Ref=360,100

Peak #	RetTime [min]	Type	Width [min]	Area [mAU*s]	Height [mAU]	Area %	Description
1	4.534	MM	0.1487	1.03648e4	1161.68628	100.0000	(+)12
Totals :				1.03648e4	1161.68628		

(–) 2-22. 3(*R*)-(3,4-dimethoxyphenyl)-4(*S*)-[(*E*)-2-bromostyryl]cyclohex-1-ene (99% ee): (Method a)

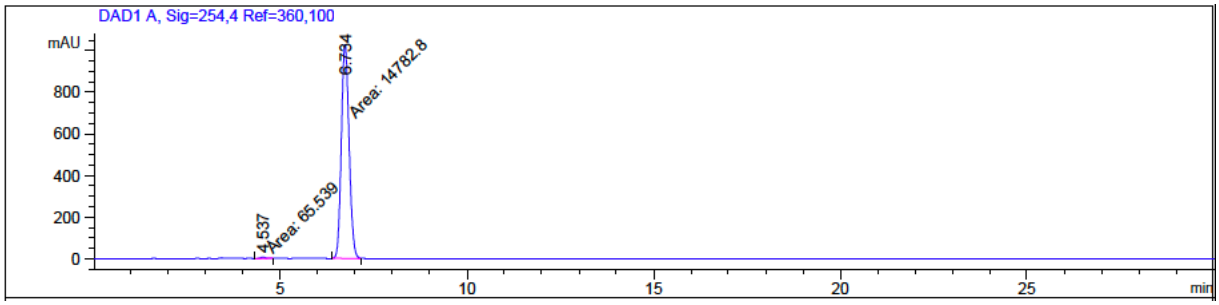

Signal 1: DAD1 A, Sig=254,4 Ref=360,100

Peak #	RetTime [min]	Type	Width [min]	Area [mAU*s]	Height [mAU]	Area %	Description
1	4.537	MM	0.1676	65.53897	6.51827	0.4414	(+)12
2	6.734	MM	0.2394	1.47828e4	1029.02100	99.5586	(–)12
Totals :				1.48483e4	1035.53927		

2-23. 3(*S/R*)-(3,4-dimethoxyphenyl)-4(*R/S*)-[(*Z*)-3,4-dimethoxystyryl]cyclohex-1-ene: (Method b)

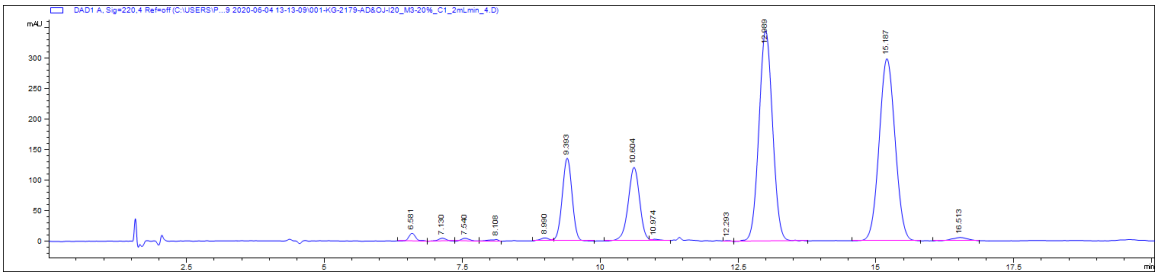

(+) 2-23. 3(*S*)-(3,4-dimethoxyphenyl)-4(*R*)-[(*Z*)-3,4-dimethoxystyryl]cyclohex-1-ene: (Method b)

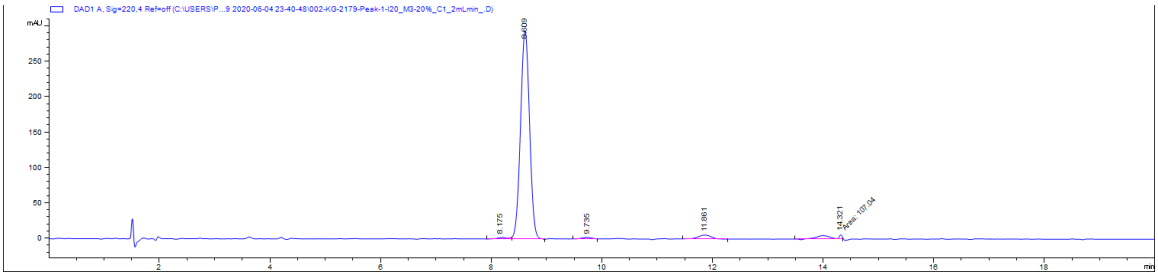

Index	Time (min)	Area (%) 220 nm
impurity	8.18	0.715
(+)2-23	8.61	93.027
(–)2-23	9.74	0.717
(+) *t*-BG	11.86	2.579
(–) *t*-BG	14.32	2.961
Total		100.00

(–) 2-23. 3(*R*)-(3,4-dimethoxyphenyl)-4(S)-[(*Z*)-3,4-dimethoxystyryl]cyclohex-1-ene: (Method b)

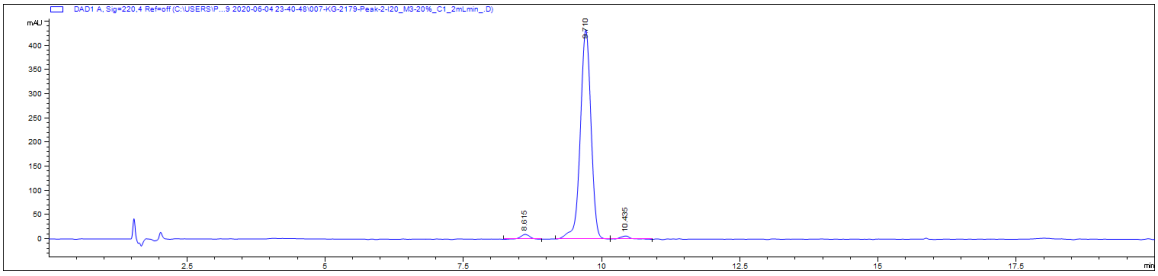

Index	Time (min)	Area (%) 220 nm
(+)2-23	8.82	2.051
(–)2-23	9.71	96.518
impurity	10.43	1.368
Total		100.00

Since this analytical method led to different retention times for (+) **13** and (–) **13** as compared to the trace **13** (which is a mixture of (+) **13**, (–) **13**, (+) **t-BG** and (–) **t-BG**) another round of analytical validation was done to establish the enantiomeric purity (spectra shown below). Due to limited material remaining, a mixture containing 85:15 of the two enantiomers was prepared. These enantiomers were dissolved in DMSO which results in a solvent peak at ~1.6 min, this peak was ignored while integrating these spectra.

15:85 of (+) 2-23: (–) 2-23: (Method b)

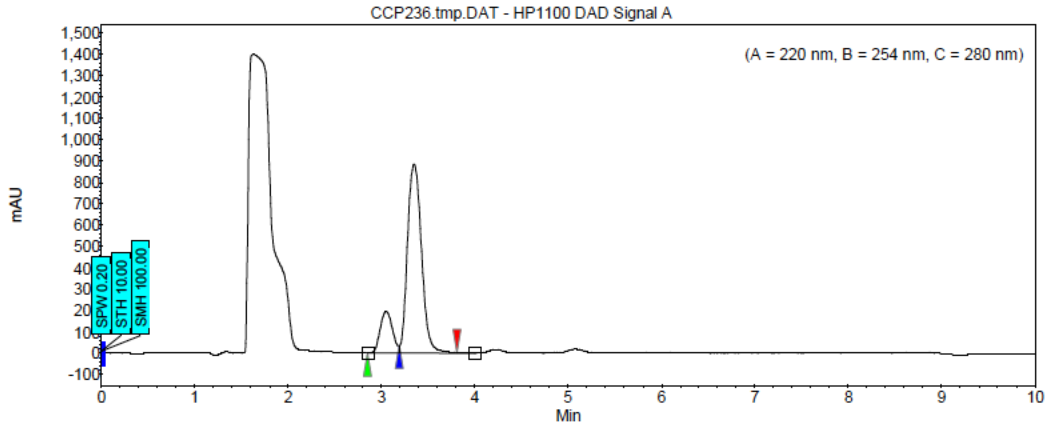

	Index	Name	Start	Time	End	RT Offset	Quantity	Height	Area	Area
			[Min]	[Min]	[Min]	[Min]	[% Area]	[µV]	[µV.Min]	[%]
(+) 2-23	1	UNKNOWN	2.85	3.05	3.19	0.00	15.95	192.6	29.1	15.946
(–) 2-23	2	UNKNOWN	3.19	3.35	3.81	0.00	84.05	883.9	153.3	84.054
	Total						100.00	1076.5	182.4	100.000

(+) 2-23. 3(*S*)-(3,4-dimethoxyphenyl)-4(*R*)-[(*Z*)-3,4-dimethoxystyryl]cyclohex-1-ene (96% ee):
(Method b-round 2)

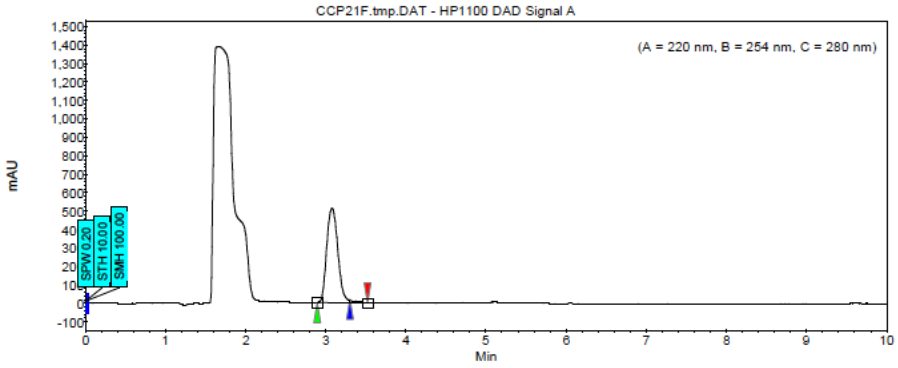

	Index	Name	Start [Min]	Time [Min]	End [Min]	RT Offset [Min]	Quantity [% Area]	Height [µV]	Area [µV.Min]	Area [%]
(+) 2-23	1	UNKNOWN	2.90	3.08	3.30	0.00	98.31	511.5	82.2	98.311
(–)2-23	2	UNKNOWN	3.30	3.30	3.52	0.00	1.69	13.3	1.4	1.689
	Total						100.00	524.8	83.6	100.000

(–) 2-23. 3(*R*)-(3,4-dimethoxyphenyl)-4(S)-[(*Z*)-3,4-dimethoxystyryl]cyclohex-1-ene (95% ee) :
(Method b-round 2)

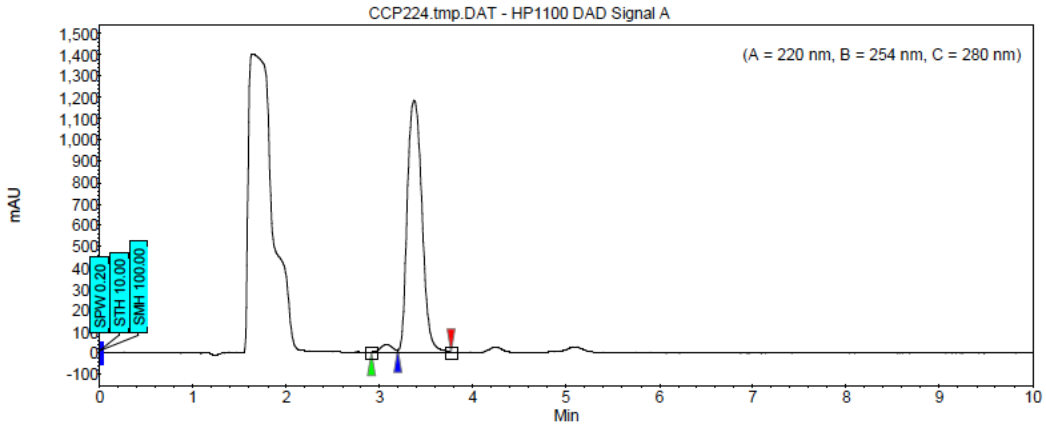

	Index	Name	Start [Min]	Time [Min]	End [Min]	RT Offset [Min]	Quantity [% Area]	Height [µV]	Area [µV.Min]	Area [%]
(+)13	1	UNKNOWN	2.92	3.08	3.20	0.00	2.42	36.2	5.3	2.416
(–)13	2	UNKNOWN	3.20	3.37	3.77	0.00	97.58	1182.0	213.9	97.584
	Total						100.00	1218.2	219.2	100.000

***t*–BG– 3(*S/R*)-(3,4-Dimethoxyphenyl)-4(*R/S*)-[(*E*)-3,4-dimethoxystyryl]cyclohex-1-ene: (Method c)**

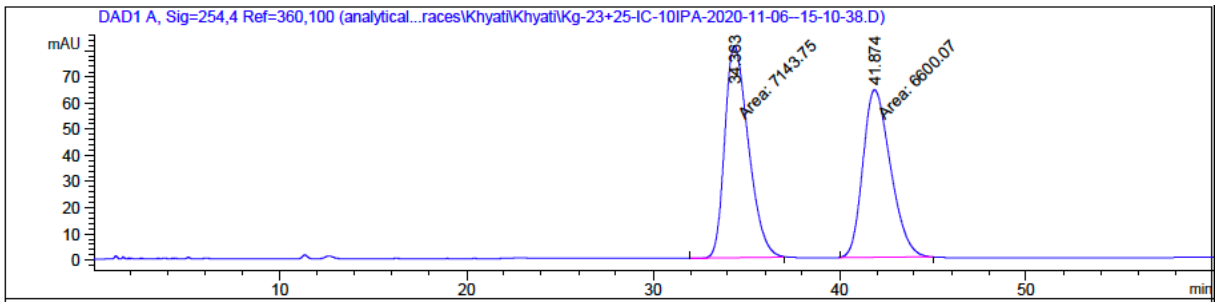

Signal 1: DAD1 A, Sig=254,4 Ref=360,100

Peak #	RetTime [min]	Type	Width [min]	Area [mAU*s]	Height [mAU]	Area %
1	34.363	MM	1.4701	7143.75244	80.99113	51.9779
2	41.874	MM	1.7187	6600.07324	64.00153	48.0221
Totals :				1.37438e4	144.99266	

(+)*t*–BG– 3(*S*)-(3,4-Dimethoxyphenyl)-4(*R*)-[(*E*)-3,4-dimethoxystyryl]cyclohex-1-ene (99% ee):
(Method c)

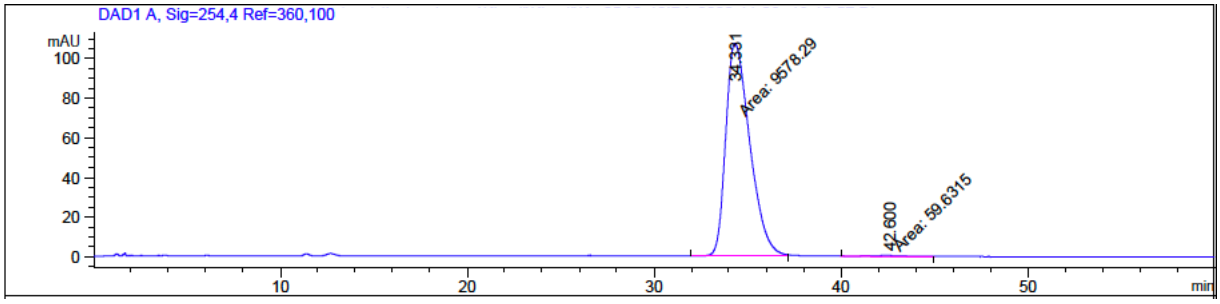

Signal 1: DAD1 A, Sig=254,4 Ref=360,100

Peak #	RetTime [min]	Type	Width [min]	Area [mAU*s]	Height [mAU]	Area %	Description
1	34.331	MM	1.4894	9578.29492	107.18334	99.3813	+*t*-BG
2	42.600	MM	2.3143	59.63152	4.29444e-1	0.6187	-*t*-BG
Totals :				9637.92644	107.61279		

(–) *t*–BG– 3(*R*)-(3,4-Dimethoxyphenyl)-4(*S*)-[(*E*)-3,4-dimethoxystyryl]cyclohex-1-ene (93% ee):
(Method c)

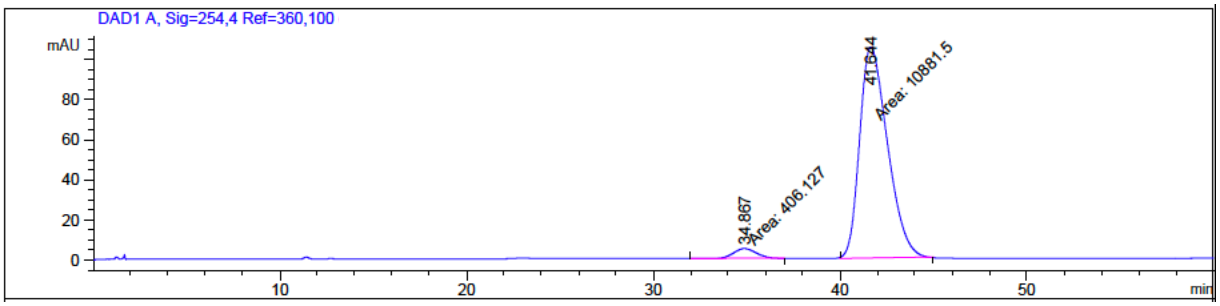

Signal 1: DAD1 A, Sig=254,4 Ref=360,100

Peak #	RetTime [min]	Type	Width [min]	Area [mAU*s]	Height [mAU]	Area %	Description
1	34.867	MM	1.3973	406.12741	4.84431	3.5980	(+)*t*-BG
2	41.644	MM	1.7276	1.08815e4	104.97392	96.4020	(–)*t*-BG
Totals :				1.12876e4	109.81823		

Appendix 3: Select images of PC-12 neuritogenesis and additional data

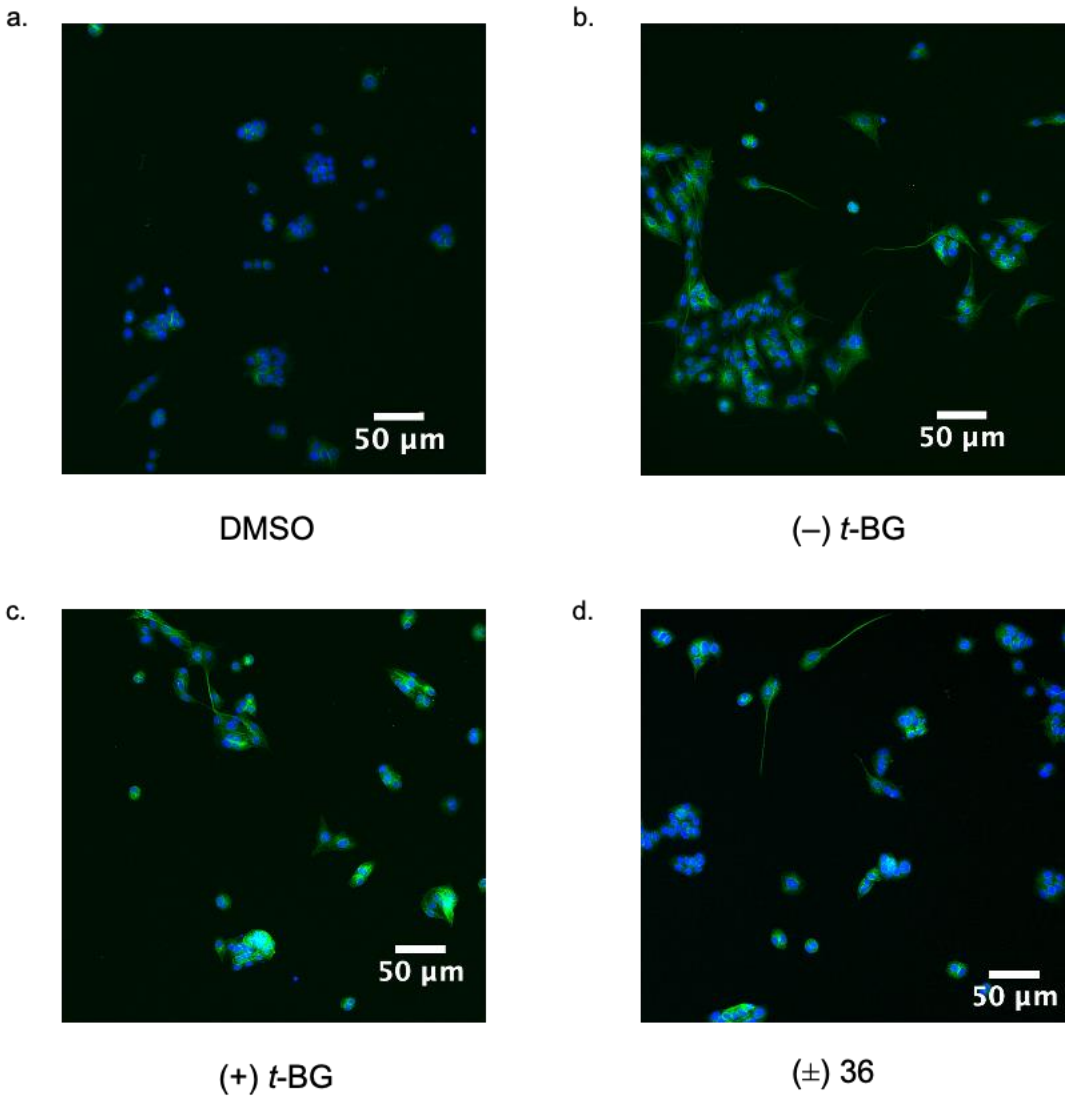

Figure S20. Images showing neuritogenesis in PC-12 cells after 48h incubation with 0.6% DMSO or 30 µM compound. Assay procedure as shown in figure 3-2. Nucleus = blue and cell body = green

a.

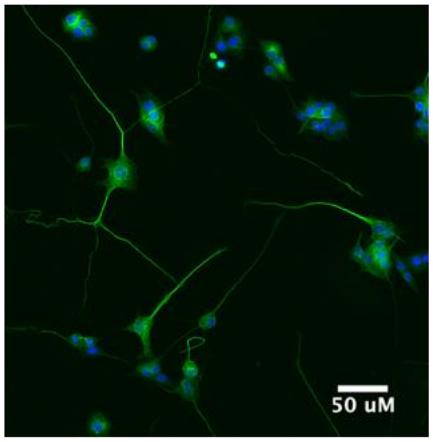

NGF+DMSO

b.

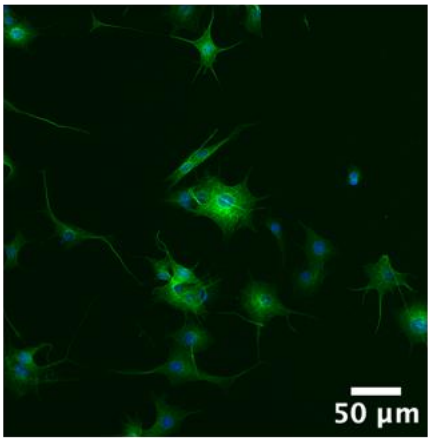

(–) *t*-BG+NGF

c.

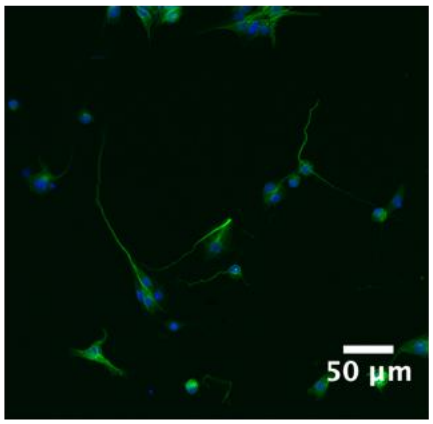

(+) *t*-BG+NGF

d.

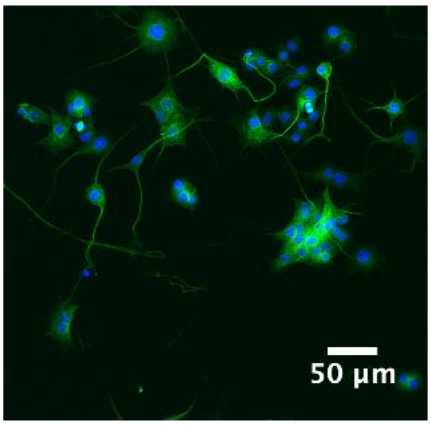

(±) 36+NGF

e.

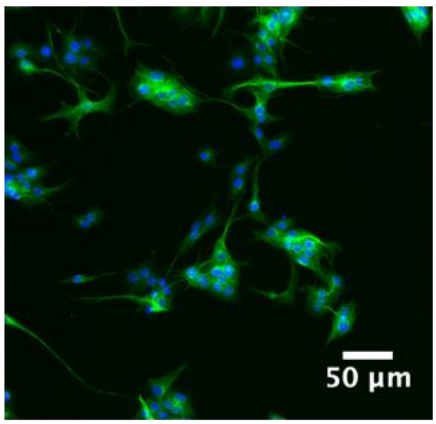

(±) 20+NGF

f.

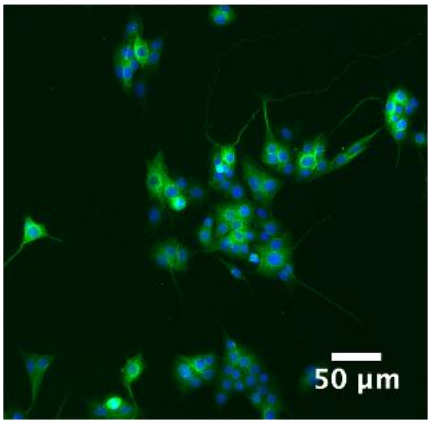

Resveratrol+ NGF

Figure S21. Images showing neuritogenesis in PC-12 cells after 48h incubation with 10 ng/mL of NGF+ 0.6% DMSO or 10 ng/mL of NGF + 30 µM compound. Assay procedure as shown in figure 3-2. Nucleus = blue and cell body = green

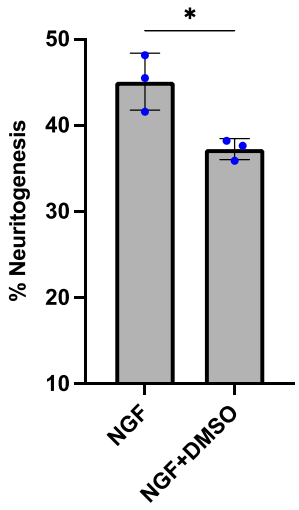

Figure S22. Effect of 0.6% DMSO on neuritogenesis induced by 10 ng/mL of NGF. % Neuritogenesis was calculated as a percentage of total number of cells that had neurites > 5 µm. p-value measured by unpaired t-test, *p < 0.05.

Treatments compared	Figure ref.	p-Value
Vitamin E vs NGF + 0.6% DMSO	3-16b	0.8440
(–) 23 vs DMSO	3-8c	0.3061
(+) 23 vs DMSO	3-8c	0.4437
(+) *t*-BG vs NGF + 0.6% DMSO	3-8d	0.0788
(–) 20 vs DMSO	3-15	0.4035
(±) 28 vs DMSO	3-15	0.3440

Table S1. p-Values for key treatment comparisons which were not statistically significant